

AD-A267 293



PL-TR-92-2225

Environmental Research Papers, No. 1108

**PHILLIPS LABORATORY GLOBAL SPECTRAL
NUMERICAL WEATHER PREDICTION MODEL**

**Donald C. Norquist
Chien-hsiung Yang
Sam Chang
Douglas C. Hahn**

11 September 1992

Approved for public release; distribution unlimited



**PHILLIPS LABORATORY
Directorate of Geophysics
AIR FORCE MATERIEL COMMAND
HANSCOM AIR FORCE BASE, MA 01731-5000**

93-15424



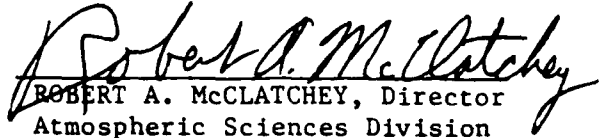
03 008

"This technical report has been reviewed and is approved for publication"

FOR THE COMMANDER



DONALD A. CHISHOLM, Chief
Atmospheric Prediction Branch



ROBERT A. McCLATCHEY, Director
Atmospheric Sciences Division

This document has been reviewed by the ESC Public Affairs Office (PA) and is releasable to the National Technical Information Service (NTIS).

Qualified requestors may obtain additional copies from the Defense Technical Information Center. All others should apply to the National Technical Information Service.

If your address has changed, or if you wish to be removed from the mailing list, or if the addressee is no longer employed by your organization, please notify PL/DAA, Hanscom AFB, MA 01731. This will assist us in maintaining a current mailing list.

REPORT DOCUMENTATION PAGE

Form Approved
OMB No 0704-0188

Public reporting burden for this collection of information is estimated to average 1 hour per response, including the time for reviewing instructions, searching existing data sources, gathering and maintaining the data needed, and completing and reviewing the collection of information. Send comments regarding this burden estimate or any other aspect of this collection of information, including suggestions for reducing the burden, to Washington Headquarters Service, Directorate for Information Operations and Reports, 1215 Jefferson Davis Highway, Suite 1204, Arlington, VA 22202-4302, and to the Office of Management and Budget, Paperwork Project Director, Paperwork Project, Washington, DC 20503.

1. AGENCY USE ONLY (Leave blank)	2. REPORT DATE 11 September 1992	3. REPORT TYPE AND DATES COVERED Final Report Oct 88 to Sep 91	
4. TITLE AND SUBTITLE Phillips Laboratory Global Spectral Numerical Weather Prediction Model		5. FUNDING NUMBERS PE 61102F PR 2310 TA G7 WU 11	
6. AUTHOR(S) Norquist, Donald C. Yang, Chien-hsiung		Chang, Sam Hahn, Douglas C.	
7. PERFORMING ORGANIZATION NAME(S) AND ADDRESS(ES) Phillips Laboratory (GPAP) Hanscom Air Force Base Massachusetts 01731-5000		8. PERFORMING ORGANIZATION REPORT NUMBER PL-TR-92-2225 ERP, No. 1108	
9. SPONSORING / MONITORING AGENCY NAME(S) AND ADDRESS(ES)		10. SPONSORING / MONITORING AGENCY REPORT NUMBER	
11. SUPPLEMENTARY NOTES			
12a. DISTRIBUTION / AVAILABILITY STATEMENT Approved for public release; distribution unlimited		12b. DISTRIBUTION CODE	
13. ABSTRACT (Maximum 200 words) This report documents the ten-year (1981-91) development of the Phillips Laboratory Global Spectral Model (PL GSM). Beginning with the National Meteorological Center Model of 1980, the hydrodynamics of the model were recoded and new physical parameterizations were developed for radiation, planetary boundary layer, cumulus convection, and gravity wave drag effects on the large-scale forecast fields. A sequence of tests and parameterization refinements were carried out to arrive ultimately at the current version of the PL GSM, termed PL-91. The report describes its performance with respect to that of the operational AFGWC GSM in a series of six January and June forecasts. The PL-91 version appears to produce better forecasts of virtually all parameters, producing smaller systematic errors and slower error growth. The model is envisioned to serve as a research tool to develop techniques for global cloud forecasting.			
14. SUBJECT TERMS Atmospheric models Numerical weather prediction		Physical parameterization Forecast evaluation	
		15. NUMBER OF PAGES 166	
		16. PRICE CODE	
17. SECURITY CLASSIFICATION OF REPORT Unclassified	18. SECURITY CLASSIFICATION OF THIS PAGE Unclassified	19. SECURITY CLASSIFICATION OF ABSTRACT Unclassified	20. LIMITATION OF ABSTRACT SAR

DTIC QUALITY INSPECTED 8

Accession For	
NTIS CRA&I	<input checked="" type="checkbox"/>
DTIC TAB	<input type="checkbox"/>
Unannounced	<input type="checkbox"/>
Justification	
By	
Distribution /	
Availability Codes	
Dist	Avail and/or Special
A-1	

Contents

1. BACKGROUND	1
2. SUMMARY OF PL GSM DESIGN	7
3. EXPERIMENTAL DESIGN	12
4. EXPERIMENTAL RESULTS	14
4.1 Direct Comparisons of Forecasts With FGGE III-b Analyses	14
4.1.1 Hemispheric Statistics	14
4.1.2 Zonal Average Statistics	38
4.1.3 Hemispheric Map Comparisons	38
4.1.4 Regional Statistics	61
4.2 Evaluation of Forecasts in the Planetary Boundary Layer	71
4.2.1 Regional Comparisons With FGGE III-b Analyses	71
4.2.2 Performance of the PBL Predictions at Model Gridpoints	71
4.3 Patterns of Weather Prediction	85
4.4 Forecast Precipitation, Evaporation, and Cloud Results	122
5. ANALYSIS AND CONCLUSIONS	131
6. SUMMARY AND RECOMMENDATIONS	145
REFERENCES	149
APPENDIX A - TOPOGRAPHY REPRESENTATIONS	153

Illustrations

1.	Flow Chart of PL-91 Version of PL GSM.	9
2.	Vertical Structures of N12 Model, N18 Model, and FGGE III-b Analysis.	11
3.	Northern Hemisphere Temperature Bias of (a) GWC84 January, (b) GL-89 January, (c) PL-91 January, (d) GWC84 June, (e) GL-89 June, and (f) PL-91 June.	16
4.	Northern Hemisphere Temperature RMSE of (a) GWC84 January, (b) GL-89 January, (c) PL-91 January, (d) GWC84 June, (e) GL-89 June, and (f) PL-91 June.	17
5.	Northern Hemisphere Wind RMSE of 850 mb January Forecasts of (a) GWC84, Zonal Component, (b) GWC84, Meridional Component, (c) GL-89, Zonal Component, (d) GL-89, Meridional Component, (e) PL-91, Zonal Component, (f) PL-91, Meridional Component.	18
6.	Same as in Figure 5 for 500 mb.	19
7.	Same as in Figure 5 for 200 mb.	20
8.	Same as in Figure 5 for June Forecasts.	21
9.	Same as in Figure 6 for June Forecasts.	22
10.	Same as in Figure 7 for June Forecasts.	23
11.	Northern Hemisphere Temperature Bias, RMSE of 850 mb January Forecasts of (a) GWC84, Bias, (b) GWC84, RMSE, (c) GL-89, Bias, (d) GL-89, RMSE, (e) PL-91, Bias, (f) PL-91, RMSE.	24

12. Same as in Figure 11 for 500 mb.	25
13. Same as in Figure 11 for 250 mb.	26
14. Same as in Figure 11 for June Forecasts.	27
15. Same as in Figure 12 for June Forecasts.	28
16. Same as in Figure 13 for June Forecasts.	29
17. Northern Hemisphere Relative Humidity Bias, RMSE of 850 mb January Forecast: of (a) GWC84, Bias, (b) GWC84, RMSE, (c) GL-89, Bias, (d) GL-89, RMSE, (e) PL-91, Bias, (f) PL-91, RMSE.	30
18. Same as in Figure 17 for 500 mb.	31
19. Same as in Figure 17 for 300 mb.	32
20. Same as in Figure 17 for June Forecasts.	33
21. Same as in Figure 18 for June Forecasts.	34
22. Same as in Figure 19 for June Forecasts.	35
23. Anomaly Correlation for January 500 mb Geopotential Height Forecasts (Models G, 1, 2 are GWC84, GL-89, PL-91 respectively).	36
24. Same as in Figure 23 for June Forecasts.	37
25. Latitude-Pressure Distributions of Zonal Bias of Zonal Wind Component at Days 3, 5, and 10 of the January Forecasts for (a) GWC84, (b) GL-89, (c) PL-91.	39
26. Same as in Figure 25 for June Forecasts.	40
27. Latitude-Pressure Distributions of Zonal RMSE of Zonal Wind Component at Days 3, 5, and 10 of January Forecasts for (a) GWC84, (b) GL-89, (c) PL-91.	41
28. Same as in Figure 27 for June Forecasts.	42
29. Latitude-Pressure Distributions of Zonal Bias of Temperature at Days 3, 5, and 10 of the January Forecasts for (a) GWC84, (b)GL-89, (c) PL-91.	43
30. Same as in Figure 29 for June Forecasts.	44
31. Latitude-Pressure Distributions of Zonal RMSE of Temperature at Days 3, 5, and 10 of the January Forecasts for (a) GWC84, (b) GL-89, (c) PL-91.	45
32. Same as in Figure 31 for June Forecasts.	46
33. Latitude-Pressure Distributions of Zonal Bias of Relative Humidity at Days 3, 5, and 10 of the January Forecasts for (a) GWC84, (b) GL-89, (c) PL-91.	47

34. Same as in Figure 33 for June Forecasts.	48
35. Hemispheric Maps of PL-91 60-120 Hour January Forecast Error of Wind Speed: (a) Western Hemisphere (WH), 950 mb Mean Error (ME), (b) WH, 950 mb Standard Deviation of Error (SDE), (c) WH, 850 mb ME, (d) WH, 850 mb SDE.	50
36. Hemispheric Maps of PL-91 60-120 Hour January Forecast Error of Wind Speed: (a) Eastern Hemisphere (EH), 200 mb ME, (b) EH, 200 mb SDE, (c) WH, 200 mb ME, (d) WH, 200 mb SDE.	51
37. Hemispheric Maps of PL-91 60-120 Hour June Forecast Error of Wind Speed: (a) WH, 850 mb ME, (b) WH, 850 mb SDE, (c) WH, 700 mb ME, (d) WH 700 mb SDE.	52
38. Same as in Figure 36 for June Forecast.	53
39. Hemispheric Maps of PL-91 60-120 Hour January Forecast Error of Temperature: (a) WH, 950 mb ME, (b) WH, 950 mb SDE, (c) EH, 950 mb ME, (d) EH, 950 mb SDE.	55
40. Same as in Figure 39 for 850 mb.	56
41. Same as in Figure 39 for 200 mb.	57
42. Same as in Figure 39 for June Forecasts.	58
43. Hemispheric Maps of PL-91 60-120 Hour June Forecast Error of Temperature: (a) EH, 850 mb ME, (b) EH, 850 mb SDE, (c) EH, 700 mb ME, (d) EH, 700 mb SDE.	59
44. Hemispheric Maps of PL-91 60-120 Hour June Forecast Error of 500 mb Temperature: (a) EH ME, (b) EH SDE, (c) WH ME, (d) WH SDE.	60
45. Domain of the (a) Central Pacific Window, and (b) North American Window.	62
46. Central Pacific Temperature Bias of January and June Forecasts of (a) 850 mb, (b) 700 mb, (c) 500 mb, and (d) 300 mb.	63-64
47. Same as in Figure 46 for RMSE.	65-66
48. Same as in Figure 46 for the North American Window.	67-68
49. Same as in Figure 48 for RMSE.	69-70
50. Spatial Correlation of Temperature and Geopotential Height Forecasts with FGGE III-b Analyses for North American (NA) and Central Pacific (CP) Windows at 850, 500, and 300 mb: (a)-(c) January, and (d)-(f) June.	72-77
51. Central Pacific Relative Humidity Bias of January and June Forecasts at (a) 850 mb, (b) 700 mb, (c) 500 mb, and (d) 300 mb.	78-79
52. Same as in Figure 51 for the North American Window.	80-81

53. Map of Forecast - Analysis Temperature Differences at 900 mb for 24-Hour Forecasts Valid 1200 UTC 13 January 1979: (a) RAD-0, and (b) PBL-2G.	82
54. Same as in Figure 53 for 48-Hour Forecast Valid 1200 UTC 14 January 1979.	83
55. Time Series of $\sigma = 0.960$ FGGE III-b (Solid) and PL-91 (Dash) Temperature (C) at Gridpoint Near Denver for Six January Cases (Abscissa is Integer Number of 12-Hour Intervals in 10-Day Forecast).	86
56. Same as in Figure 55 for June Cases.	87
57. Same as in Figure 55 for Specific Humidity (g/kg).	88
58. Same as in Figure 57 for June Cases.	89
59. Time Series of $\sigma = 0.960$ FGGE III-b (Solid) and PL-91 (Dash) Wind Speed (m/s) and (b) Wind Direction (degrees) at Gridpoint Near Denver for Six January Cases.	90-91
60. Same as in Figure 59 for June Cases.	92-93
61. Time Series of $\sigma = 0.995$ FGGE III-b (Solid) and PL-91 (Dash) Temperature (C) at Gridpoint Near Hawaii for Six January Cases.	94
62. Same as in Figure 61 for June Cases.	95
63. Same as in Figure 61 for Specific Humidity (g/kg).	96
64. Same as in Figure 63 for June Cases.	97
65. Time Series of $\sigma = 0.995$ FGGE III-b (Solid) and PL-91 (Dash) (a) Wind Speed (m/s), and (b) Wind Direction (degrees) at Gridpoint Near Hawaii for Six January Cases.	98-99
66. Same as in Figure 65 for June Cases.	100-101
67. Time Series of $\sigma = 0.960$ FGGE III-b (Solid) and PL-91 (Dash) Temperature (C) at Gridpoint Near Alert for Six January Cases.	102
68. Same as in Figure 67 for June Cases.	103
69. Same as in Figure 67 for Specific Humidity (g/kg).	104
70. Same as in Figure 69 for June Cases.	105
71. Time Series of $\sigma = 0.960$ FGGE III-b (Solid) and PL-91 (Dash) (a) Wind Speed (m/s), and (b) Wind Direction (degrees) at Gridpoint Near Alert for Six January Cases.	106-107
72. Same as in Figure 71 for June Cases.	108-109
73. Northern Hemisphere (a) Mean Sea Level Pressure (Contour Interval - 4 mb) and (b) 500 mb Geopotential Height (Contour Interval - 6 decameters) for 72-Hour GWC84 and PL-91 1200 UTC 12 January 1979 Forecasts, and Verifying FGGE III-b Analysis.	110-113

74. Northern Hemisphere (a) 850 mb Relative Humidity (Contour Interval = 20 percent) and (b) 850 mb Specific Humidity (Contour Interval = 2 g/kg for 72 Hour GWC84 and PL-91 1200 UTC 12 January 1979 Forecasts, and Verifying FGGE III-b Analysis.	112-113
75. Northern Hemisphere (a) 300 mb Relative Humidity (Contour Interval = 20 percent) and (b) 200 mb Wind Speed (Contour Interval = 10 m/s) for 72 Hour GWC84 and PL-91 1200 UTC 12 January 1979 Forecasts, and Verifying FGGE III-b Analysis.	114-115
76. Eastern Hemisphere Tropical (30S to 30N) Mean Sea Level Pressure (Contour Interval = 4mb) for 72-Hour GWC84 and PL-91 1200 UTC 10 June 1979 Forecasts and Verifying FGGE III-b Analysis.	116
77. Same as in Figure 76 for 850 mb Wind.	117
78. Same as in Figure 76 for 850 mb Specific Humidity (Contour Interval = 2 g/kg).	118
79. Same as in Figure 76 for 850 mb Relative Humidity (Contour Interval = 20 percent).	119
80. Same as in Figure 79 for 700 mb.	120
81. Same as in Figure 79 for 400 mb.	121
82. Global Average (a) and (b) Precipitation Rate (mm/day) and (c) and (d) Evaporation Rate (mm/day) Averaged Over Six January [(a) and (c)] and June [(b) and (d)] Forecasts.	124-125
83. Zonal Average of Accumulated Total Precipitation (mm) Over Days 2-6 of Six (a) January and (b) June Forecasts, Compared with Climatology.	127
84. Global Maps of Accumulated Total Precipitation (mm) Over Days 2-6 of Six January Forecasts for (a) GWC84, (b) GL-89, and (c) PL-91 (Contour Interval = 150 mm).	128
85. Same as in Figure 84 for Six June Forecasts.	129
86. Zonal Time Average of Cloud Amounts From (a) Three 10-Day January 1979 PL-91 Forecasts, and (b) Climatology Based on January 1979 3DNEPH Data [from Schattel ¹⁵].	130

Tables

1. Comparison of Model Features.	10
2. Geographical Location of Five Gridpoints for the Evaluation of PBL Prediction.	84
3. Global Average Precipitation and Evaporation Rates.	123
4. A Score Card on NH Error Statistics.	135
5. Number of Cases Where a Version is Selected as Best Temperature Forecast.	138
6. Height and Pressure Data for the Five Reference Gridpoints.	140

Acknowledgement

This ten-year effort has involved a number of people who, over the years, have been affiliated with the Atmospheric Prediction Branch. Two of our former colleagues, Drs Stephen Brenner and Kenneth Mitchell, played major roles in the foundational technical and software development which remains the basis for our model. Throughout the lifetime of the project, Donald Aiker, has ably assisted us in data set development, auxiliary software design and implementation, and generation of computer graphics for analysis. Captain John Schattel was responsible for the adaptation and testing of a broad-band radiation scheme that interacted with model clouds. As our branch chief, Donald Chubbuck kept us focused and encouraged to continue to strive towards continued improvement in model performance. Audrey Campana and Anna Tortorici patiently performed the word processing tasks for several of the model-related reports including this one. Finally, our thanks go to the four university groups who contributed physical parameterization schemes, and to Michael Tiedtke of the ECMWF, for supplying us with the mass flux scheme.

Phillips Laboratory Global Spectral Numerical Weather Prediction Model

1. BACKGROUND

The Atmospheric Prediction Branch of the Phillips Laboratory (PL/GPAP) has developed and tested a global spectral numerical weather prediction model, which will be referred to as the Phillips Laboratory Global Spectral Model (PL GSM). This effort took place over a ten-year period (1981-1991) and involved PL/GPAP personnel and several supporting contract efforts. The model was developed in response to the USAF Air Weather Service (AWS) Geophysical Requirement (GR-3-80), Improved Cloud Forecast Technology, to provide the platform for improved global cloud forecasts. The goal was to develop a state-of-the-art global weather forecast model with physical parameterization schemes that would forecast the atmospheric state (winds, geopotential heights, temperature, pressure, and humidity). The horizontal and vertical cloud distribution could then be deduced on scales practical in global

Received for publication 1 September 1992

models [grid resolutions of $O(100 \text{ km})$] using diagnostic methods that relate cloud amount to forecasted variables. The model might eventually be adapted to a prognostic cloud forecasting capability, in which cloud water would be an additional prognostic variable within the model.

The purpose of this report is to briefly review the developmental history of the PL GSM, discuss its current components, and document its present performance in forecasting the atmospheric state. The balance of Section 1 is devoted to the history of the PL GSM development. Section 2 describes the individual components of the various versions of the PL GSM. Section 3 details the design used in the forecast experiments, while Section 4 includes a discussion of the experimental results. In Section 5, we present our analysis and conclusions on the current model's forecast performance. Section 6 presents our recommendations for further improvement, testing, and evaluation of the PL GSM.

The original form of the PL (formerly the Air Force Geophysics Laboratory) GSM was developed from the National Meteorological Center's global spectral model¹ acquired from NMC in 1981. The model was adapted for installation on the local computer system, and in doing so the hydrodynamics of the model were completely re-coded. The physics of the model (parameterizations of moist processes, dry adiabatic adjustment, and planetary boundary layer fluxes) were retained in the form described in Sela.¹ We refer to this version of the PL GSM as NMC80. The original implementation and studies of the expanded resolution (to 30 rhomboidal spectral truncation) are described in Brenner et al.^{2,3} The nonlinear normal mode initialization procedure used to remove fast gravity modes from the gridded initial

¹Sela, J. (1980) Spectral Modeling at the National Meteorological Center, *Mon. Wea. Rev.*, 108:1279-1292.

²Brenner, S., Yang, C., and Yee, S. (1982) *The AFGL Spectral Model of the Moist Global Atmosphere: Documentation of the Baseline Version*, AFGL-TR-82-0393, Air Force Geophysics Laboratory, Hanscom AFB, MA. AD129283.

³Brenner, S., Yang, C., and Mitchell, K (1984) *The AFGL Global Spectral Model: Expanded Resolution Baseline Version*, AFGL-TR-84-0308, Air Force Geophysics Laboratory, Hanscom AFB, MA. ADA160370.

conditions was also acquired from NMC.⁴ Its impact on model performance was discussed by Brenner et al.³

In 1984, we acquired from NMC, by way of the Air Force Global Weather Central (AFGWC), the version of the physical parameterizations resident in the NMC model that was made operational at AFGWC in 1984. Upon replacing the NMC80 physics with this version of the physics in our baseline model, we termed this version of the GSM GWC84. The differences between NMC80 and GWC84 versions of the GSM are presented by Yang et al.⁵ GWC84 is essentially the form of the global spectral model currently employed operationally at AFGWC. Because of its status as the operational Air Force model, we use it as a reference in this report to measure any improvement in forecast skill that might be attributed to PL GSM development.

Several university research groups, under AFGL sponsorship, developed new parameterization schemes for physical processes not resolved or explicitly handled by the hydrodynamics of the model. Between 1982 and 1986, three university groups developed first installments of software for preliminary testing of a new version of the PL GSM. Mahrt and others⁶ at Oregon State University developed a planetary boundary layer scheme that parameterizes surface effects on the atmosphere (fluxes of heat, moisture, and momentum). Ogura and Soong⁷ at the University of Illinois investigated and modified two methods of parameterizing moist convective processes.

⁴Ballish, B.A. (1980) *Initialization Theory and Application to the NMC Spectral Model*, Ph.D. Thesis, Dept of Meteorology, Univ. of Maryland.

⁵Yang, C.-H., Mitchell, K., Norquist, D., and Yee, S.Y.K. (1989) *Diagnostics for and Evaluation of New Physical Parameterization Schemes for Global NWP Models*, GL-TR-89-0158, Geophysics Laboratory (AFSC), Hanscom AFB, MA. ADA228033.

⁶Mahrt, L., Pan, H., Paumier, J., and Troen, Ib (1984) *A Boundary Layer Parameterization for a General Circulation Model*, AFGL-TR-84-0063, Air Force Geophysics Laboratory, Hanscom AFB, MA. ADA144224.

⁷Soong, S.-T., Ogura, Y., and Kau, W.-S (1985) *A Study of Cumulus Parameterization in a Global Circulation Model*, AFGL-TR-85-0160, Air Force Geophysics Laboratory, Hanscom AFB, MA. ADA170137.

They recommended their modified Kuo⁸ method for implementation in the new version of the PL GSM. Liou and others⁹ at the University of Utah developed a scheme to parameterize atmospheric radiative transfer that was based on broad-band emissivity calculations. Yang et al.⁵ reported in detail on the individual and collective impacts of these preliminary versions of the new physical parameterizations on the GSM performance. They conducted a limited number of prediction experiments to measure the effects that the delivered schemes had on forecast performance with respect to both NMC80 and GWC84. Later, more extensive prediction experiments with this version (called GL-87) confirmed the conclusions of Yang et al.⁵

As the packages delivered by the university groups were considered preliminary, the period 1987-1989 saw the continued improvement of the packages to eliminate shortcomings or over-simplifications. Mahrt et al.¹⁰ focused their efforts on interactions between the soil and the atmosphere, as well as on performance of the boundary layer package under very stable conditions and development of a formulation for boundary layer cumulus. Ou and Liou¹¹ extended the radiative parameterization scheme to variable resolution in the vertical in the accommodation of up to three cloudy layers. Norquist and Yang¹² sought to overcome shortcomings in the modified Kuo convective scheme by extensive refinement of the physical

⁸Kuo, H.-L. (1974) Further Studies of the Parameterization of the Influence of Cumulus Convection on Large-Scale Flow, *J. Atmos. Sci.*, 31:1232-1240.

⁹Liou, K.-N., Ou, S.-C., Kinne, S., and Koenig, G. (1984) *Radiation Parameterization Programs for Use in General Circulation Models*, AFGL-TR-84-0217, Air Force Geophysics Laboratory, Hanscom AFB, MA. ADA148015.

¹⁰Mahrt, L., Pan, H.-L., Ruscher, P., and Chu, C.-T. (1987) *Boundary Layer Parameterization for a Global Spectral Model*, AFGL-TR-87-0246, Air Force Geophysics Laboratory, Hanscom AFB, MA. ADA199440.

¹¹Ou, S.-C., and Liou, K.-N. (1988) *Development of Radiation and Cloud Parameterization Programs for AFGL Global Models*, AFGL-TR-88-0018, Air Force Geophysics Laboratory, Hanscom AFB, MA. ADA202020.

¹²Norquist, D. and Yang, C.-H. (1990) *Refinement and Testing of the Moist Convection Parameterization in the GL Global Spectral Model*, GL-TR-90-0285, Geophysics Laboratory (AFSC), Hanscom AFB, MA. ADA241684.

processes parameterized in the package as delivered by the University of Illinois.⁷ These efforts culminated in another round of testing the newly developed schemes. Individual tests showed that the effect of the modified PBL parameterization differed little from the previous version. A significant mid-tropospheric cooling resulted from the three-cloud-deck radiative scheme. A more modest tropical cooling replaced a warm bias in the tropics. The relatively cooler tropical forecast was attributed to a significant reduction in precipitation (thus latent heat) in the refined convective scheme. The reduction brought the model's precipitation rate in line with the climatological precipitation value. Because the convective package was the only one of the three enhanced physics packages that showed clear improvement in the realism of its performance, it was the only modified package included in the next series of extensive forecast experiments. These experiments, conducted in 1989 (the GSM version thus termed GL-89), showed modest overall improvements in forecast skill over GWC84. The combination of the originally-delivered PBL and one-cloud-deck radiation schemes along with the GL-refined modified Kuo scheme¹² resulted in a tropical cold bias and a modest mid-latitude wintertime warm bias. These results were in contrast with the prevalent warm bias present in the radiation-less GWC84 model.

The final round of physical parameterization development efforts (1990-1991) has led to the current version of the PL GSM, referred to as PL-91. Hahn and Chang¹³ have documented the changes they have made to the surface fields (soil type, vegetation type) that are provided to this version's PBL parameterization. Vernekar and others¹⁴ at the University of Maryland formulated and tested a gravity wave drag parameterization designed to simulate the effect that topographically induced gravity waves have on winds. A silhouette orography field replaces the smoothed FGGE III-b (1.875° latitude-longitude) topography when the model incorporates the

¹³Hahn, D. and Chang, S. (1992) *Land-Surface Parameterization in the Phillips Laboratory Global Spectral Model*, to be published as a Phillips Laboratory Technical Report.

¹⁴Vernekar, A.D., Zhou, J., and Kirtman, B. (1991) *A Comparison of Systematic Errors in AFGL and COLA Forecast Models*, PL-TR-91-2164, Phillips Laboratory, Hanscom AFB, MA. ADA244458.

gravity wave drag scheme. Appendix A describes the representations of topography commonly used in global models. Schattell¹⁵ has modified the cloud configuration and specification algorithms in the three-deck-cloud Utah radiation scheme. A significant reduction in the mid-tropospheric cooling resulted from this effort. Finally, the mass flux convective parameterization scheme of the current ECMWF NWP model¹⁶ was acquired and has replaced the refined, modified Kuo scheme.¹² This was motivated by the shortcomings of the latter formulation as investigated by Norquist and Yang.^{12,17} Although Mahrt et al.¹⁸ developed a boundary layer cloud diagnostic scheme and a gravity wave drag parameterization in their most recent work on the PBL package, neither of these two enhancements were implemented in the PL-91 version of the PBL scheme. The ultimate selection of the physics packages for the PL-91 version of the PL GSM was based on extensive experimentation with various candidate versions of each physical parameterization.

Concurrent to the global model development was the formulation of a cloud-diagnosis technique by Mitchell and Hahn¹⁹ known as the cloud curve algorithm. This procedure makes use of two-week samples of the most current GWC84 forecasts and AFGWC RTNEPH cloud analyses. From these samples, a statistical relationship is developed between forecast relative humidity from GWC84 and concurrent cloud amounts from RTNEPH at each of several isobaric levels, forecast lengths, and geographic regions. These relationships are then used to infer cloud amount from

¹⁵Schattell, J. (1992) *Refinement and Testing of the Radiative Transfer Parameterization in the PL Global Spectral Model*, PL-TR-92-2169, Phillips Laboratory, Hanscom AFB, MA.

¹⁶Tiedtke, M. (1989) A Comprehensive Mass Flux Scheme for Cumulus Parameterization in Large-Scale Models, *Mon. Wea. Rev.*, **117**: 1779-1800.

¹⁷Norquist, D., and Yang, C. (1992) Comparing Model-produced Convective Cloudiness with Observations, *Mon. Wea. Rev.*, **120**: 770-786.

¹⁸Mahrt, L., Ek, M., Kim, J., and Holtslag, A.A.M. (1991) *Boundary Layer Parameterization for a Global Spectral Model*, PL-TR-91-2031, Phillips Laboratory, Hanscom AFB, MA. ADA235310.

¹⁹Mitchell, K., and Hahn, D. (1989) *Development of a Cloud Forecast Scheme for the GL Baseline Global Spectral Model*, GL-TR-89-0343, Geophysics Laboratory, Hanscom AFB, MA. ADA231595.

forecast relative humidity for the ensuing two weeks. Trapnell²⁰ has tested the scheme in several variations and found that the method is competitive with (and in some cases superior to) the trajectory-based forecasts produced by AFGWC's operational 5LAYER model²¹ beyond 24 hours of forecast time.

Nehrkorn et al.^{22,23} have designed and tested a computationally optimized version of the PL GSM. Beginning with a generalized truncation version of the GSM hydrodynamics, they have redesigned the computer code of the model to allow the Cray-2 FORTRAN compiler to vectorize the computations more fully. Then for the hydrodynamics only, they have installed multitasking directives to perform parallel processing of most of what used to be serial computations. As a result, they have achieved speed-ups of approximately two times from the vectorization and of 3.6 times due to multitasking on the four CPU Cray-2. This translates to a 6-7 times reduction in the elapsed execution ("wall clock") time of a forecast on a dedicated Cray-2. In addition to the timing tests, Nehrkorn et al.²³ discuss the results of forecast comparisons of a pre-PL-91 version of the PL GSM at 40R, 80R, and 120R truncation horizontal resolutions.

2. SUMMARY OF PL GSM DESIGN

Brenner et al.²³ have described the design of the PL GSM hydrodynamics. Their discussion includes the horizontal spectral representation, vertical discretization, and the time-stepping utilized in the model. This design was reconfigured by Nehrkorn

²⁰Trapnell, R. (1992) *Cloud Curve Algorithm Test Program*, PL-TR-92-2052, Phillips Laboratory, Hanscom AFB, MA. ADA253918.

²¹Crum, T.D. (1987) *AFGWC Cloud Forecast Models*, AFGWC Tech Note 87/001, AFGWC, Air Weather Service (MAC), Offutt AFB, NE.

²²Nehrkorn, T., Hoffman, R.N., and Louis, J.-F. (1990) *Design of an Enhanced Global Spectral Model*, GL-TR-90-0309, Geophysics Laboratory (AFSC), Hanscom AFB, MA. ADA232123.

²³Nehrkorn, T., Hoffman, R.N., Louis, J.-F., and Zivkovic, M. (1992) *An Enhanced Global Spectral Model*, PL-TR-92-2011, Phillips Laboratory, Hanscom AFB, MA. ADA251242.

et al.^{22,23} to allow multitasking and vectorization, as well as in generalized (rhomboidal or triangular) truncation form. Figure 1 is a flow chart showing the order of processing during a single model time step. The sections of code represented by boxes in Figure 1 "Spectral to Grid Transform," "Sub-grid Scale Diffusion," "Time Stepping," and "Large-Scale Precip. and Dry Convective Adj." are virtually unchanged between the versions of PL GSM mentioned in Section 1. Differences in these routines between "NMC80" and "GWC84" versions of PL GSM are shown in Table 2 of Yang et al.⁵ In all but PL-91, the box "Convective Tendencies" would be labeled "Moist Convective Adjustment" and would appear just after "Time-Stepping" in the flow diagram. Thus, Figure 1 is only strictly applicable to the PL-91 version of PL GSM, with all other versions departing from Figure 1 in either content, order, or both.

Table 1 summarizes the differences between the five versions of PL GSM developed and tested over the period 1981-1991. Footnotes noted in Table 1 will direct the reader to relevant references. This table shows the evolution of the PL GSM over the 10-year development period. It is obvious that we have tried to improve the parameterization of physical effects of sub-grid scale processes that have an important impact on large-scale variables.

The goal of implementing these new schemes was to improve the accuracy of model forecasts. The change from the simple bulk aerodynamic planetary boundary layer (PBL) formulation of NMC80 and GWC84 to the sophisticated PBL scheme of Mahrt et al.^{6,10} in later versions necessitated a change in vertical resolution of the model. Figure 2 shows the N12 and N18 (both devised by NMC) vertical structures referred to in Table 1. Also shown are the isobaric levels (in bars) where data are available in the FGGE III-b analyses from which initial and verification fields for the model were generated (discussed further in Section 3).

All versions of the model have been tested extensively at the same horizontal resolution (rhomboidal 30, or "R30") to isolate the effects of the various schemes on the model forecasts. Only with the recent multitasking and optimization upgrade will it now be feasible to run the PL GSM at significantly higher horizontal resolutions.

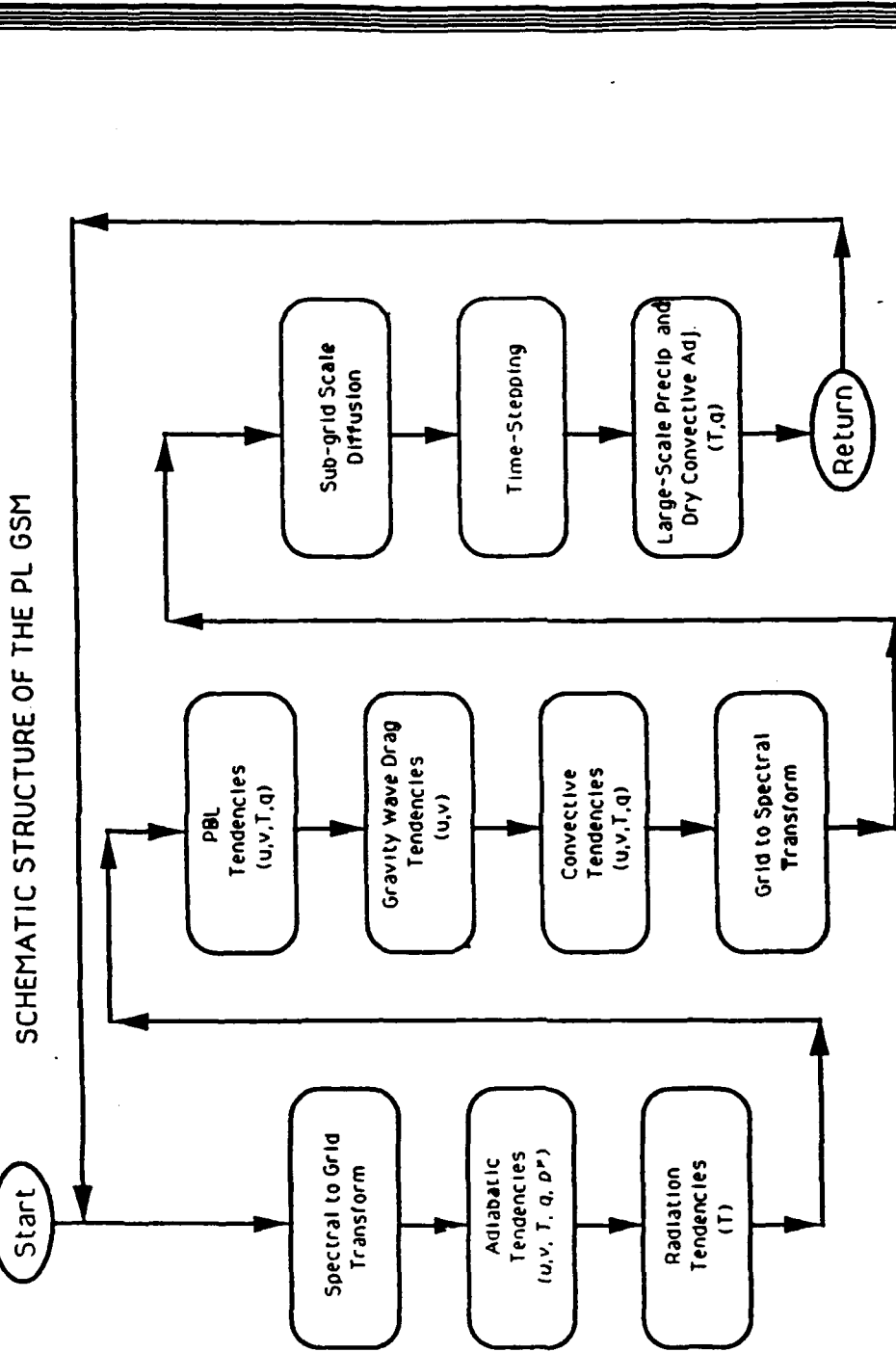


Figure 1. Flow Chart of PL-91 Version of PL GSM.

Table 1. Comparison of Model Features

	NMC80	GWC84	GL-87	GL-89	PL-91
Vertical Resolution	N12	N12	N18	N18	N18
Radiation Scheme	none	none	Utah 1-deck ⁹	Utah 1-deck ⁹	Utah-PL 3-Deck ¹⁶
PBL Scheme	bulk	bulk	OSU PBL ⁶	OSU PBL ⁶	OSU PBL ¹⁰
Moist Convective Scheme	Kuo ¹	Kuo with modifications ⁵	Illinois MODKuo ⁷	GL-Refined MODKuo ¹²	ECMWF ¹⁶
Gravity Wave Drag	none	none	none	none	U. Maryland ¹⁴
Orography	smoothed mean ³	same as NMC80	same as NMC80	same as NMC80	silhouette ¹⁴
Specified Initial Surface Fields	SST, drag coeff.	SST, drag coeff.	roughness length, albedo, snow depth, soil temp., T _s , uniform soil and veg. type ⁶	same as GL-87, ⁶ plus sea ice and corrected T _s	same as GL-89 plus varying soil, vegetation types ¹³
Specified Ozone	none	none	universal profile	universal profile	monthly latitude-varying profile ¹⁶
Layers of moisture carried in GSM	7 lowest	7 lowest	18	18	18

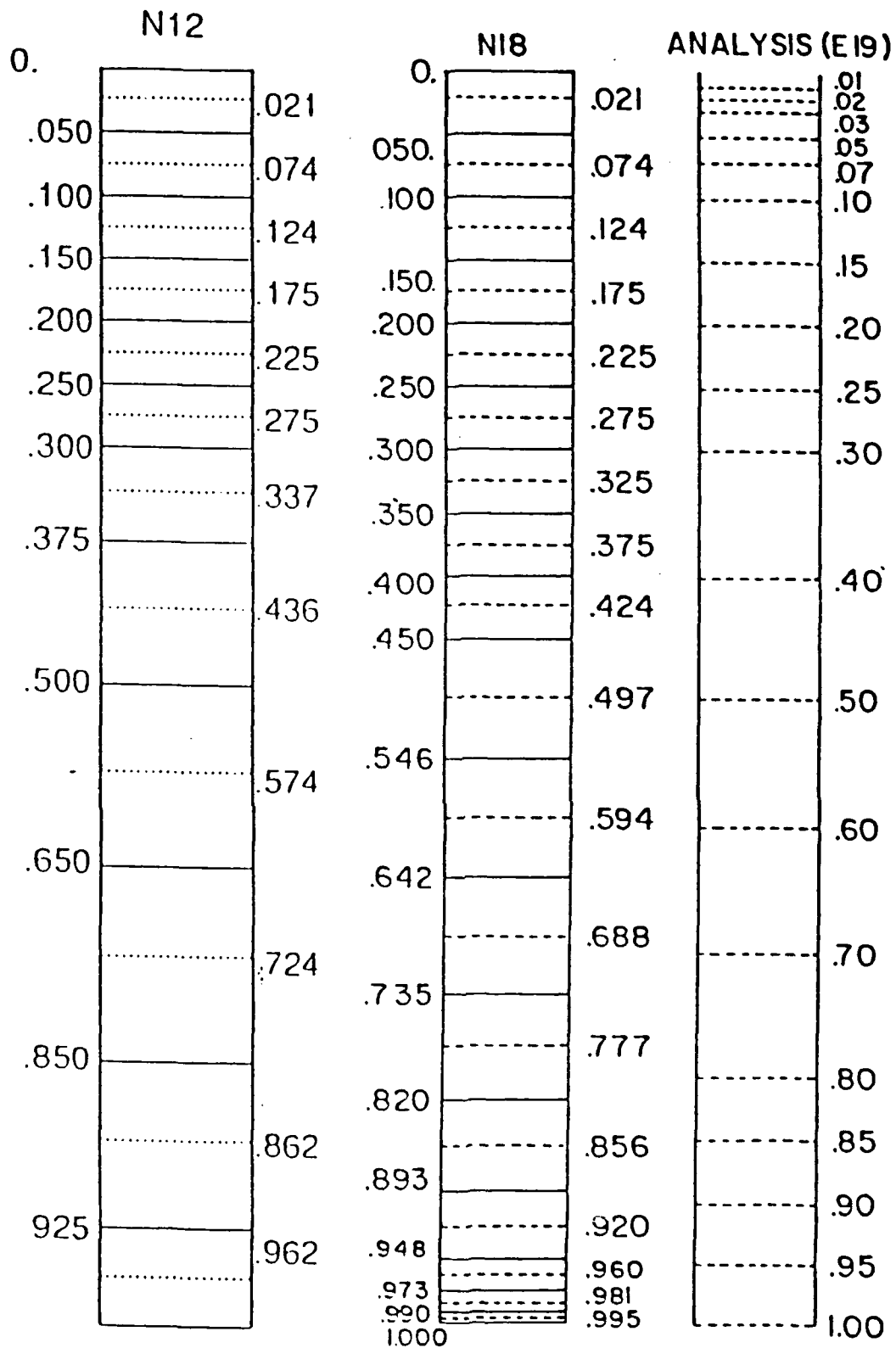


Figure 2. Vertical Structures of N12 Model, N18 Model, and FGGE III-b Analysis.

Indeed, a single case from a pre-PL-91 version of the PL GSM has been run at R80 and R120.²² However, all forecast experiments described in this report were conducted at R30.

3. EXPERIMENTAL DESIGN

We conducted a series of 10-day experiments to determine the extent of improvement resulting from inclusion of the advanced physical parameterizations. Unless otherwise stated, we will refer to an individual 10-day prediction as a "case", and a "forecast" will refer to a case evaluated at a specific time. Experimental results from GWC84, GL-89, and PL-91 are included in this report. Global meteorological analyses from the First GARP (Global Atmospheric Research Program) Global Experiment (FGGE) are employed as initial conditions and verifying analyses in the experiments. These were the "final" (1985/86) FGGE III-b initialized analyses (Uppala²⁴), reanalyzed using corrected and additional data and new mass and wind (Shaw et al.²⁵) and humidity (Illari²⁶) analysis algorithms. Because of the augmented global data observing systems during the special observing periods (SOP-I, 5 January 1979 - 5 March 1979; SOP-II, 5 May 1979 - 5 July 1979), these global analyses are among the most comprehensive observation-based analyses available. Geopotential height, horizontal wind, vertical velocity, temperature, and relative humidity are available at 19 mandatory pressure levels (see Figure 2), along with mean sea level pressure. All of these fields are available on a 1.875° latitude - longitude grid at six-hour intervals.

²⁴Uppala, S. (1986) The Assimilation of the Final Level IIB Data Set at ECMWF, Part I. *Preprints, Scientific Results of the First GARP Global Experiment*, 14-17 January, 1986, Miami, FL. *Amer. Meteor. Soc.*, 24-29.

²⁵Shaw, D.B., Lonnerberg, P., Hollingsworth, A., and Uden, P. (1987) The 1984/1985 Revisions of the ECMWF Assimilation System, *Quart. J. Roy. Meteor. Soc.*, 113:533-566.

²⁶Illari, L. (1989) The Quality of Satellite Precipitable Water Content Data and Their Impact on Analyzed Moisture Fields, *Tellus*, 41A: 319-337.

We pre-processed the FGGE III-b initialized final analyses for 1200 UTC on 2, 7, 12, 17, 22, 27 January, and 31 May, 5, 10, 15, 20, 25 June 1979. The pre-processing algorithm linearly interpolated height, wind, and humidity values on the 97 latitude sets (192 longitude points in each set) to 96 Gaussian latitudes of the 30R GSM transform grid. The 19 levels of height (Z) at each of the 192×96 gridpoints were used to hydrostatically calculate temperature (T), then perform a quadratic extrapolation or interpolation between mandatory levels to obtain the model terrain surface pressure (p^*) at each gridpoint, based on model terrain height (Z^*). With p^* thus obtained and the $\sigma = p/p^*$ specified on Figure 2 (N12 for GWC84, N18 for GL-89 and PL-91), we computed the pressure at σ -levels and -layers at each gridpoint. We then interpolated the mandatory level values of horizontal wind (u, v), temperature, and relative humidity (RH) linearly in the logarithm of pressure to the σ layers. After conversion of RH to specific humidity (q), T , u , v , q , p^* , and Z^* were transformed to coefficients of the spherical harmonics (spectral form) at each σ layer. The resulting spectral fields of divergence (D), absolute vorticity (η), T , q , natural logarithm of p^* , and $\Phi^* = gZ^*$ on σ -layers served as initial conditions for all of the PL GSM.

Each version of the PL GSM was integrated using 20-minute time steps out to 10 days of forecast time. Spectral forecast fields and accumulated precipitation were saved at 12-hour intervals for evaluation. The post-processing of the forecast fields to the FGGE III-b analysis grid proceeded as follows. First, we performed a backward transform from spectral coefficients to grid-point values (on the 1.875° grid) at each σ -layer. After conversion of q to RH, we performed a linear (in logarithm of pressure) interpolation of u , v , T , and RH from σ -layer pressures to the 19 mandatory levels at each gridpoint. In instances where mandatory levels lie below the model terrain, an extrapolation was necessary. The σ -layer T were used to construct σ -level Z (hydrostatically) and σ -level T (linear interpolation). Then the σ -level Z , T values bounding a mandatory level were used to quadratically interpolate (in logarithm of pressure) to obtain Z at the mandatory level. Finally, mandatory level T was calculated from mandatory level Z . The result was values of Z , T , u , v , RH on the

1.875° grid at the 19 mandatory levels. These fields were compared directly with verifying FGGE III-b analyses at verifying times of the forecasts.

4. EXPERIMENTAL RESULTS

4.1 Direct Comparisons of Forecasts With FGGE III-b Analyses

In this report, we have chosen to use the FGGE III-b analyses to be our only reference for verification of the prognostic variables. Yang et al.⁵ also verified individual forecasts of earlier versions of the PL GSM against rawinsonde observations. However, they found that inferences from the statistics of comparison with the two references generally agreed with each other. We will limit our evaluation to the use of the analysis as a reference. Future evaluations should extend the scrutiny to observational data as a reference.

4.1.1 HEMISPHERIC STATISTICS

We choose to employ hemispheric statistics as collective measures of model performance as a natural follow-on to the decision to group the January and June cases separately for seasonal differences. In the following figures, we show profiles and time series of the bias and root-mean-square errors (RMSE) for the six January and six June 1979 cases. Bias is defined as the area-weighted average of differences between the forecast and analysis at analysis gridpoints in a hemisphere at each analysis level. RMSE is the square root of the area-weighted average of squares of the difference between the forecast and analysis at analysis gridpoints in a hemisphere at each analysis level. At each analysis grid pressure level and latitude in the post-processed forecasts and corresponding analyses (both on the 1.875° grid), we computed the average of the fields (zonal averages), the average of the difference of the fields (zonal mean error), and the square root of the average squared difference of the fields (zonal RMSE). The area-weighted average of the zonal statistics over

each hemisphere are the hemispheric statistics discussed in this section. The results shown here are restricted to the variables T, u, v, and RH, given the predicted variables T, D, η , and q and analysis values of Z, u, v, and RH. The previous section discussed how the prognostic variables were post-processed to the analysis variables. Analysis values of T are derived from analysis values of Z hydrostatically.

Figures 3 and 4 show profiles of the temperature bias and RMSE respectively for the Northern Hemisphere. Results for the six January cases are shown in the upper row, and for the six June cases in the lower row. Each data point on the profile corresponds to one of the 16 analysis levels from 1000 to 50 mb. The width of each individual box (between successive forecast days) represents 5K in bias and 10K in RMSE. The corresponding Southern Hemisphere profiles reveal trends similar to their Northern Hemisphere season counterparts. Therefore, we show only the Northern Hemisphere profiles for the error trends in both hemispheres. These plots illustrate the consistency of the temperature error from case to case for each version of the model. Because we found it difficult to differentiate between the similar error statistics for the various model versions in the wind and humidity, they were not shown in this format.

We present Figures 5-22 in an attempt to bring out the differences among cases and contrasts between versions of the time evolution of the hemispheric error statistics. Plots are shown of RMSE for u, v at 850, 500, and 200 mb (Figures 5-10), bias and RMSE for T at 850, 500, and 250 mb (Figures 11-16), and bias and RMSE for RH at 850, 500, and 300 mb (Figures 17-22). Note that the ordinate scale can vary from frame to frame, so care should be exercised when comparing various versions of the model.

Another commonly used measure of forecast accuracy is the 500 mb height anomaly correlation. This is the spatial correlation between the forecast/climatology difference and the analysis/climatology difference. Figures 23 and 24 show the results for the Northern Hemisphere (north of 20°N) for January and June cases respectively. The curves join the means of the six cases for each model version, while a pair of symbols designates one standard deviation on each side of the group mean at a given day.

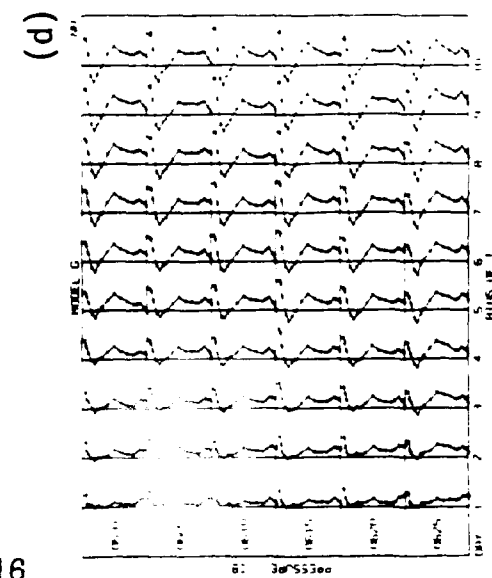
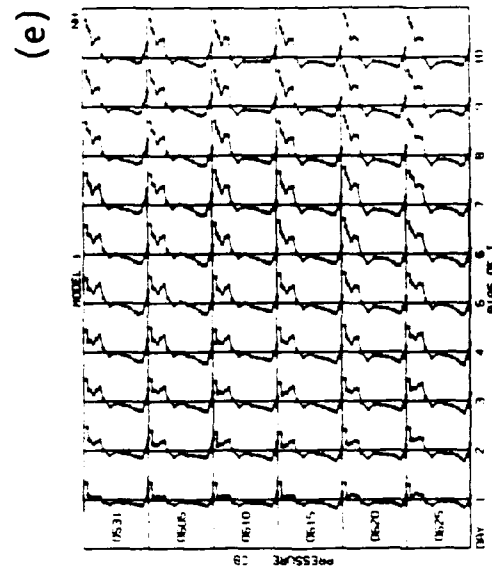
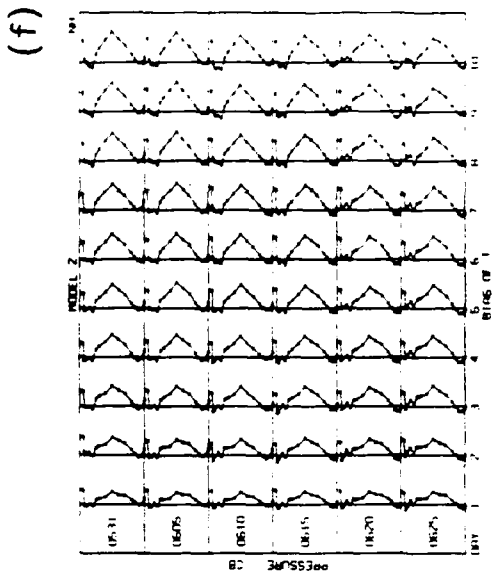
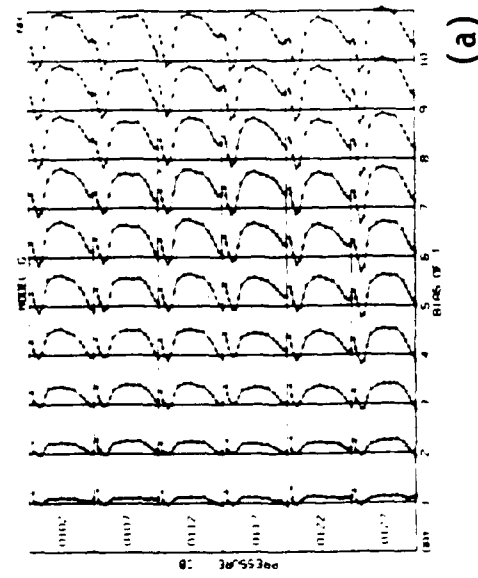
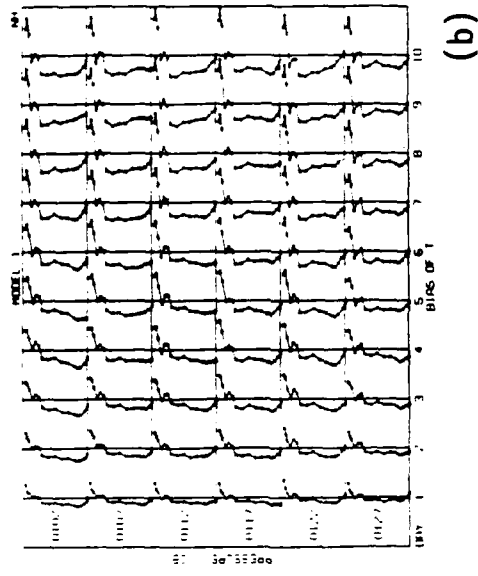
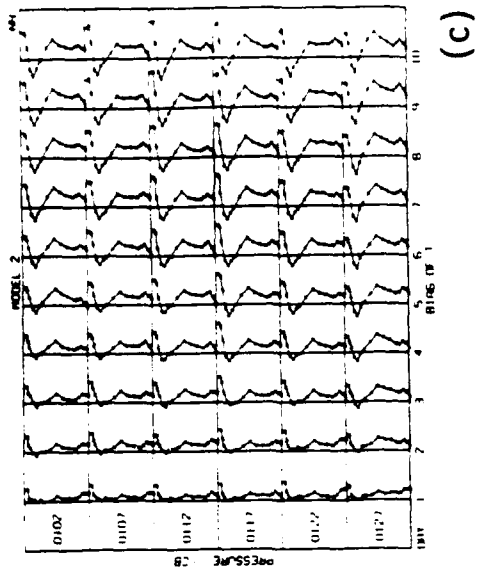


Figure 3. Northern Hemisphere Temperature Bias of (a) GWC84 January, (b) GL-89 January, (c) PL-91 January, (d) GWC84 June, (e) GL-89 June, and (f) PL-91 June.

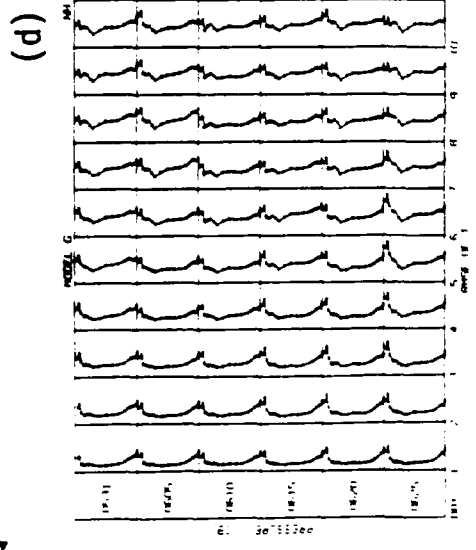
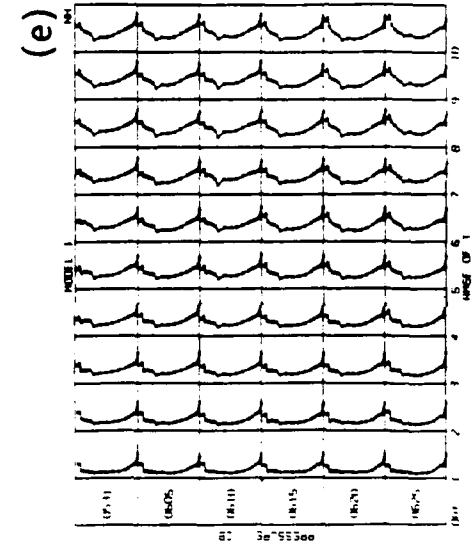
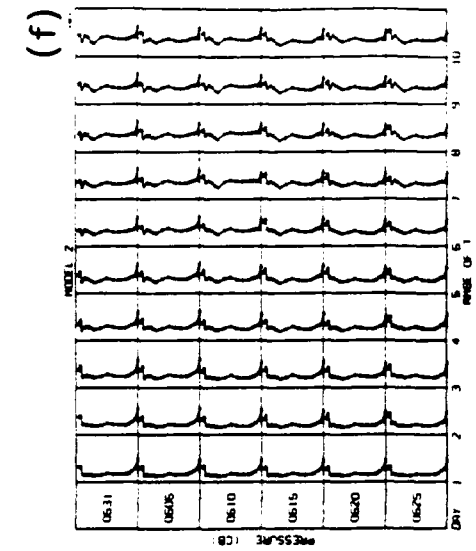
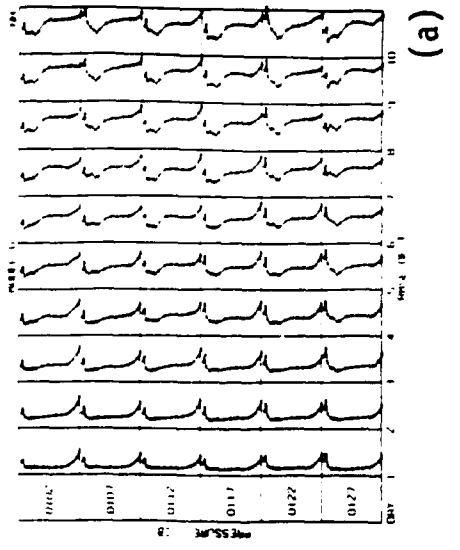
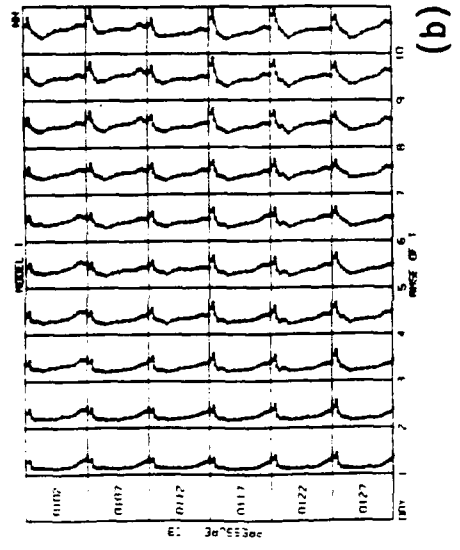
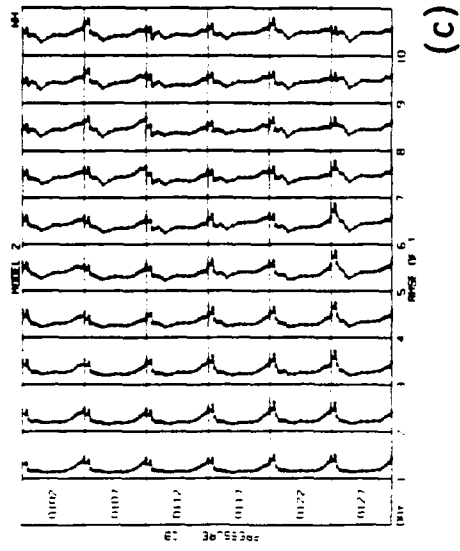


Figure 4. Northern Hemisphere Temperature RMSE of (a) GWC84 January, (b) GL-89 January, (c) PL-91 January, (d) GWC84 June, (e) GL-89 June, and (f) PL-91 June.

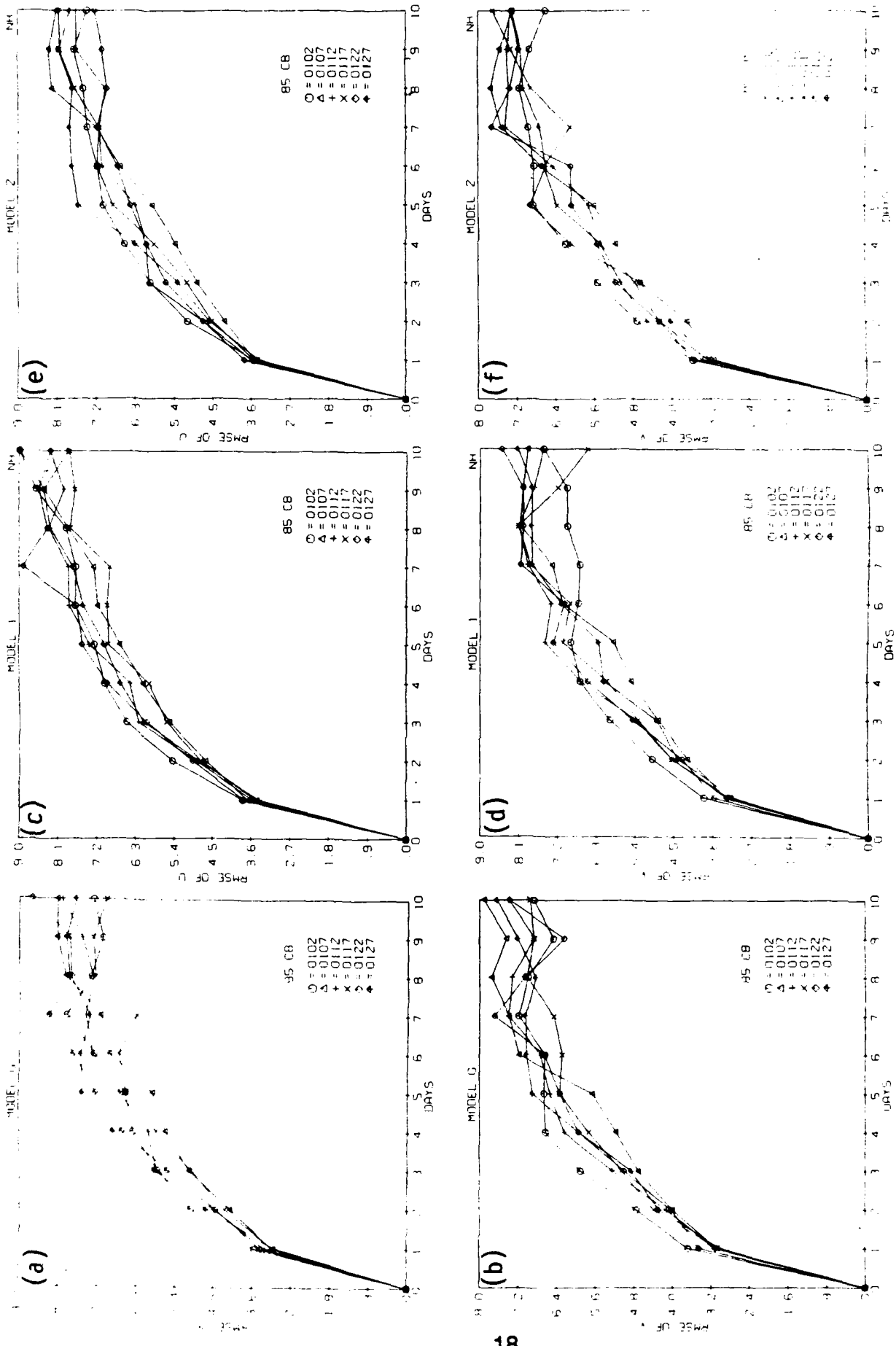


Figure 5. Northern Hemisphere Wind RMSE of 850 mb January Forecasts of (a) GWC84, Zonal Component, (b) GWC84, Meridional Component, (c) GL-89, Zonal Component, (d) GL-89, Meridional Component, (e) PL-91, Zonal Component, (f) PL-91, Meridional Component.

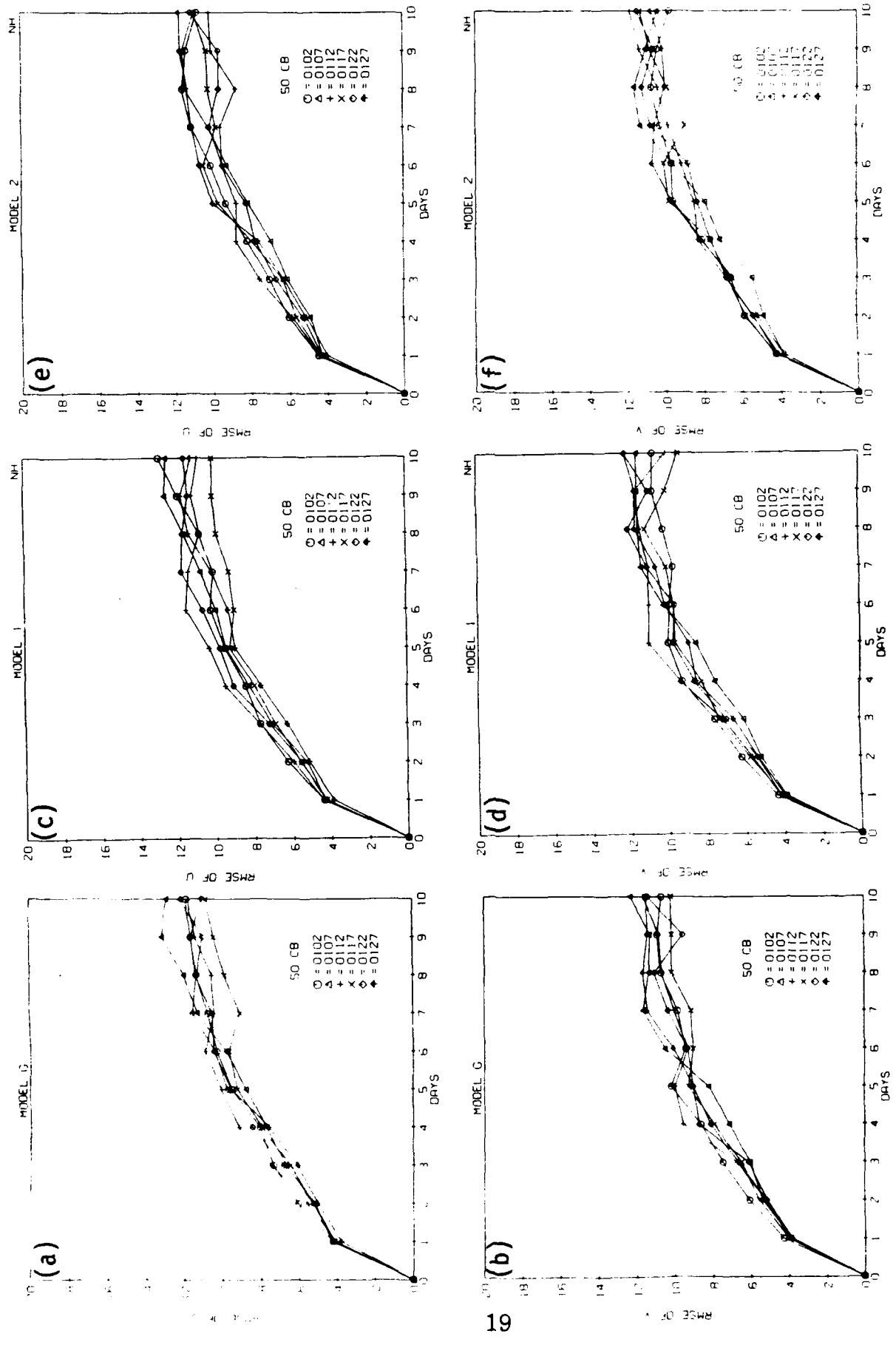


Figure 6. Same as in Figure 5 for 500 mb.

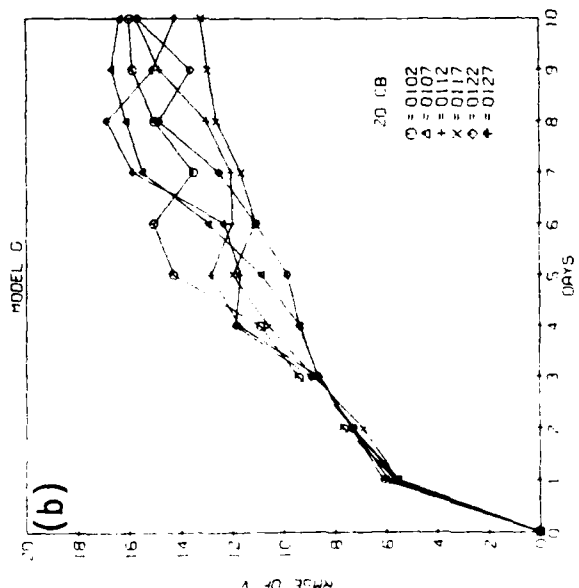
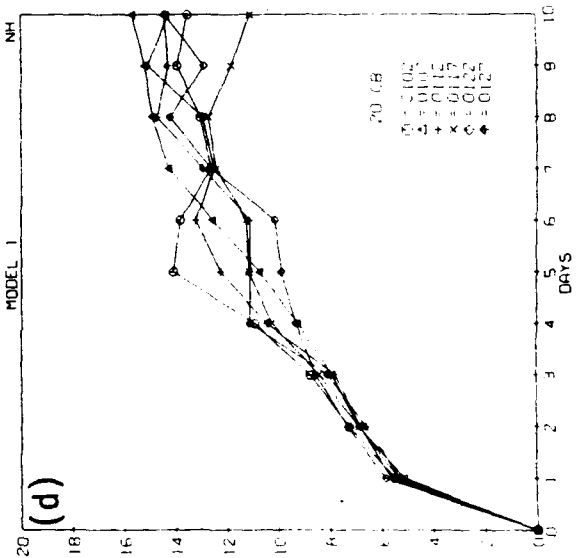
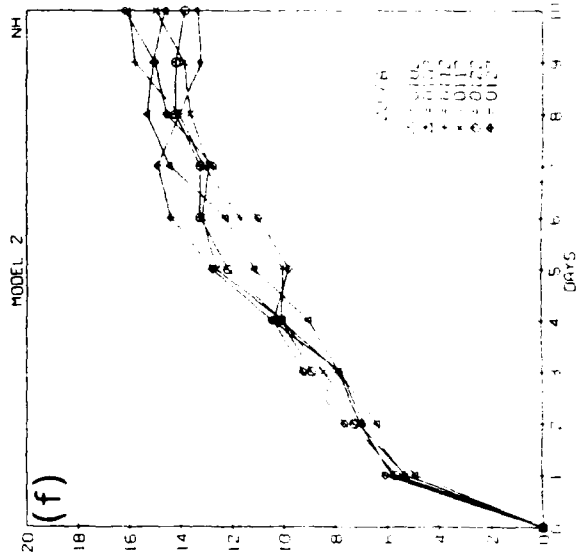
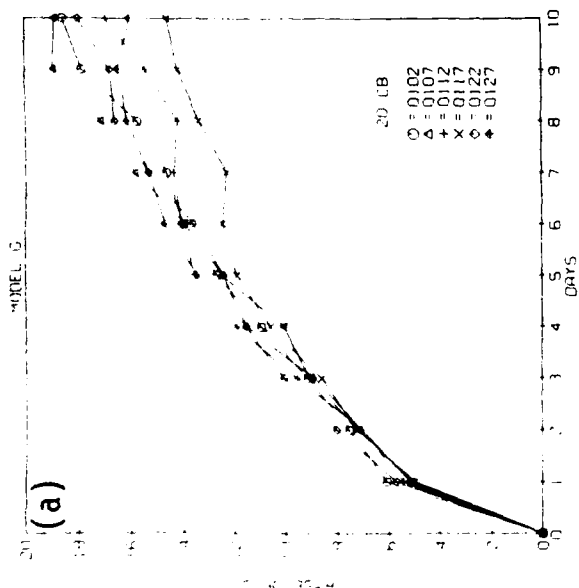
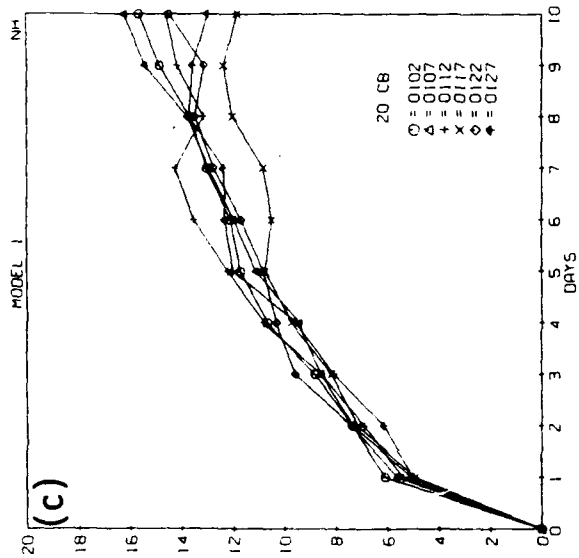
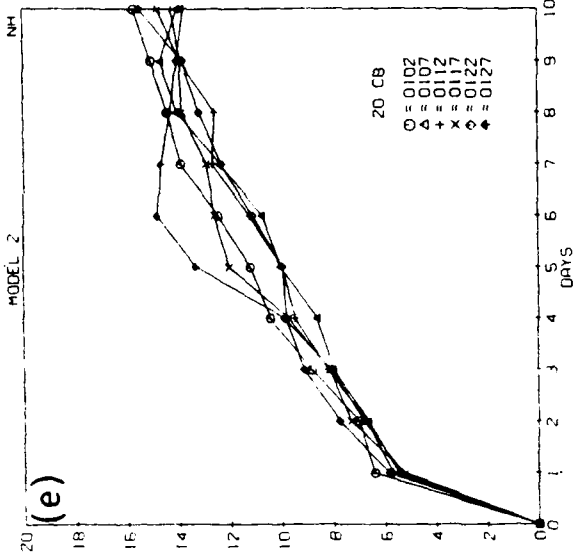


Figure 7. Same as in Figure 5 for 200 mb.

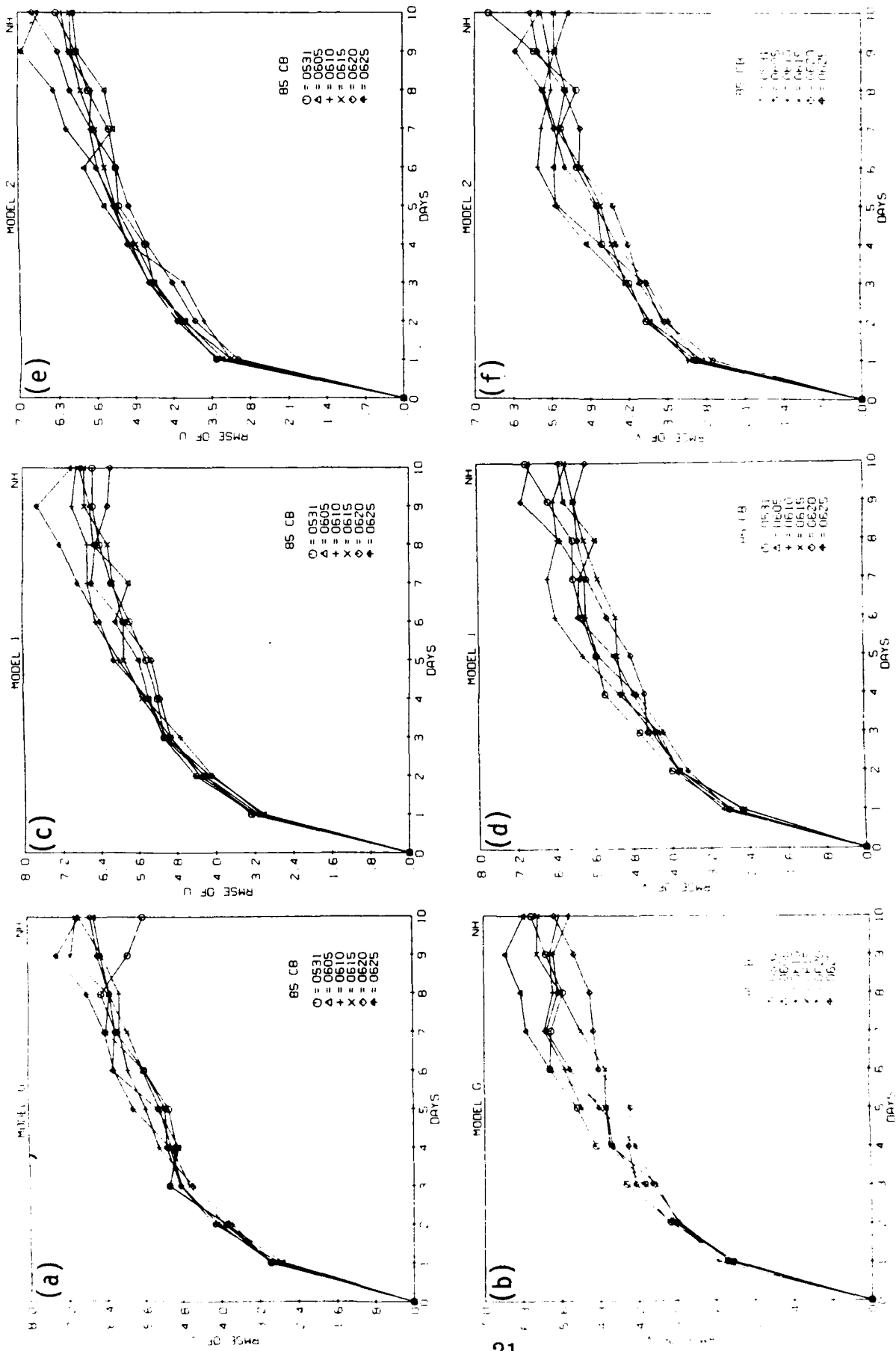


Figure 8. Same as in Figure 5 for June Forecasts.

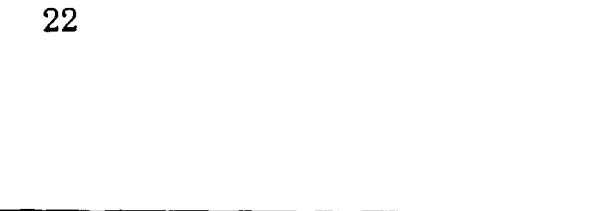
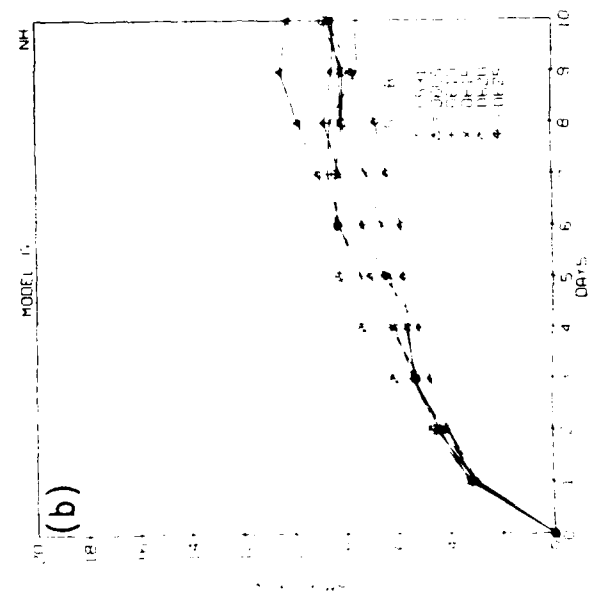
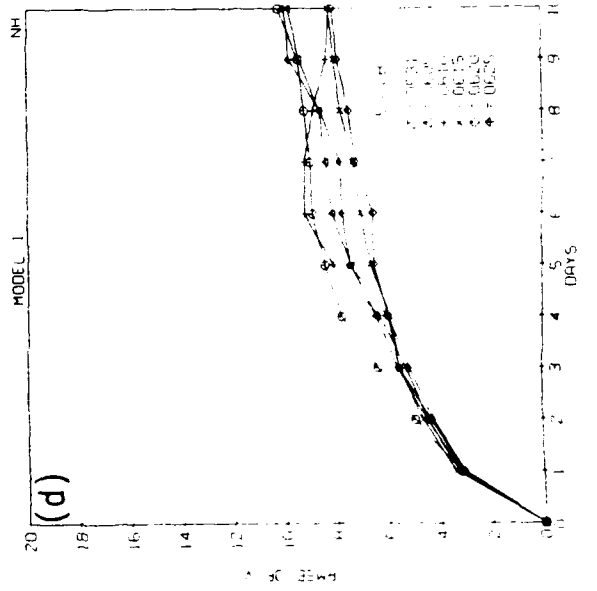
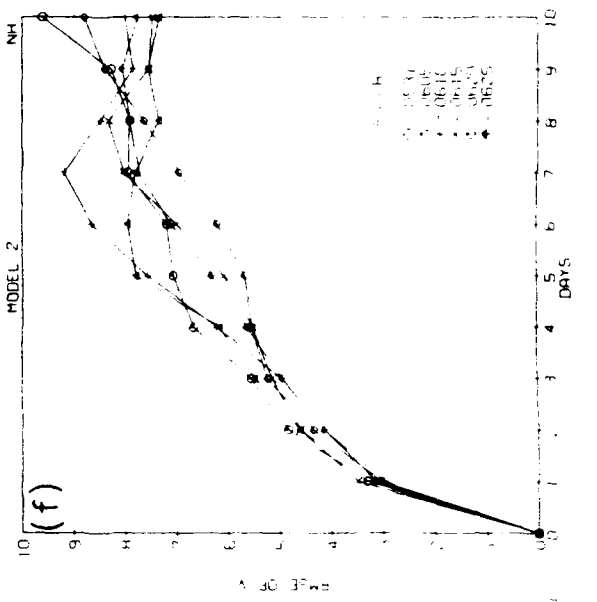
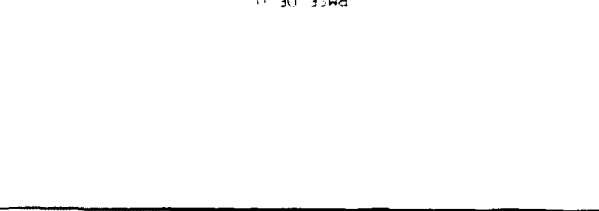
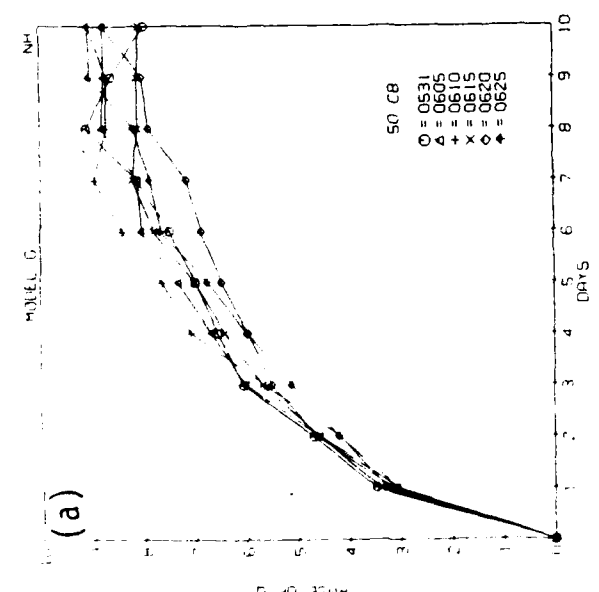
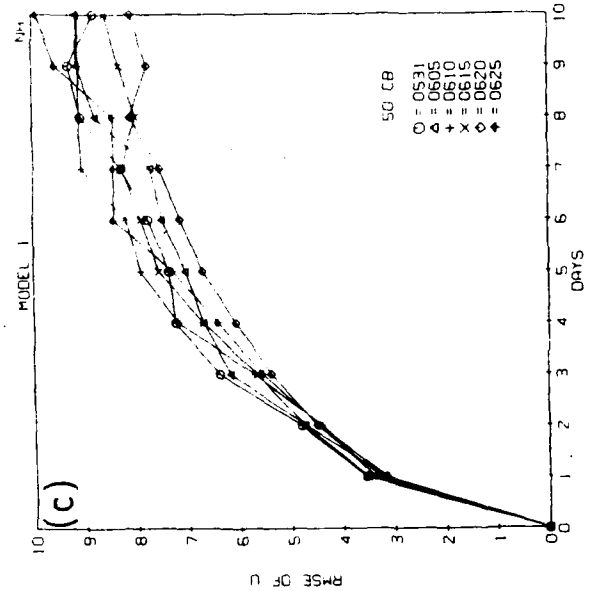
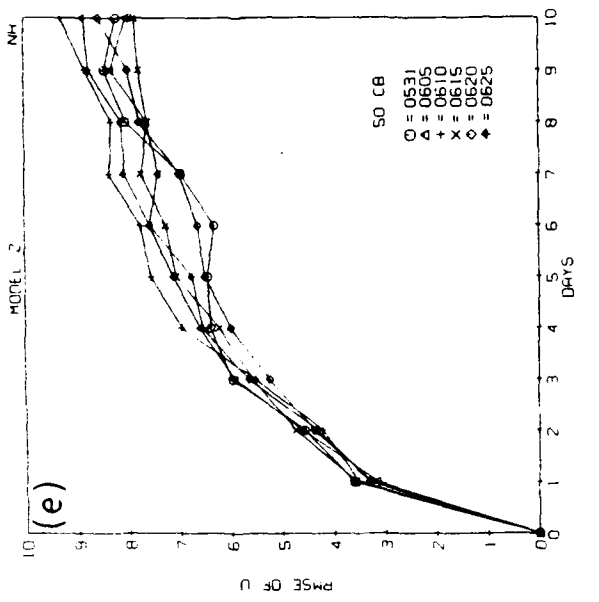


Figure 9. Same as in Figure 6 for June Forecasts.

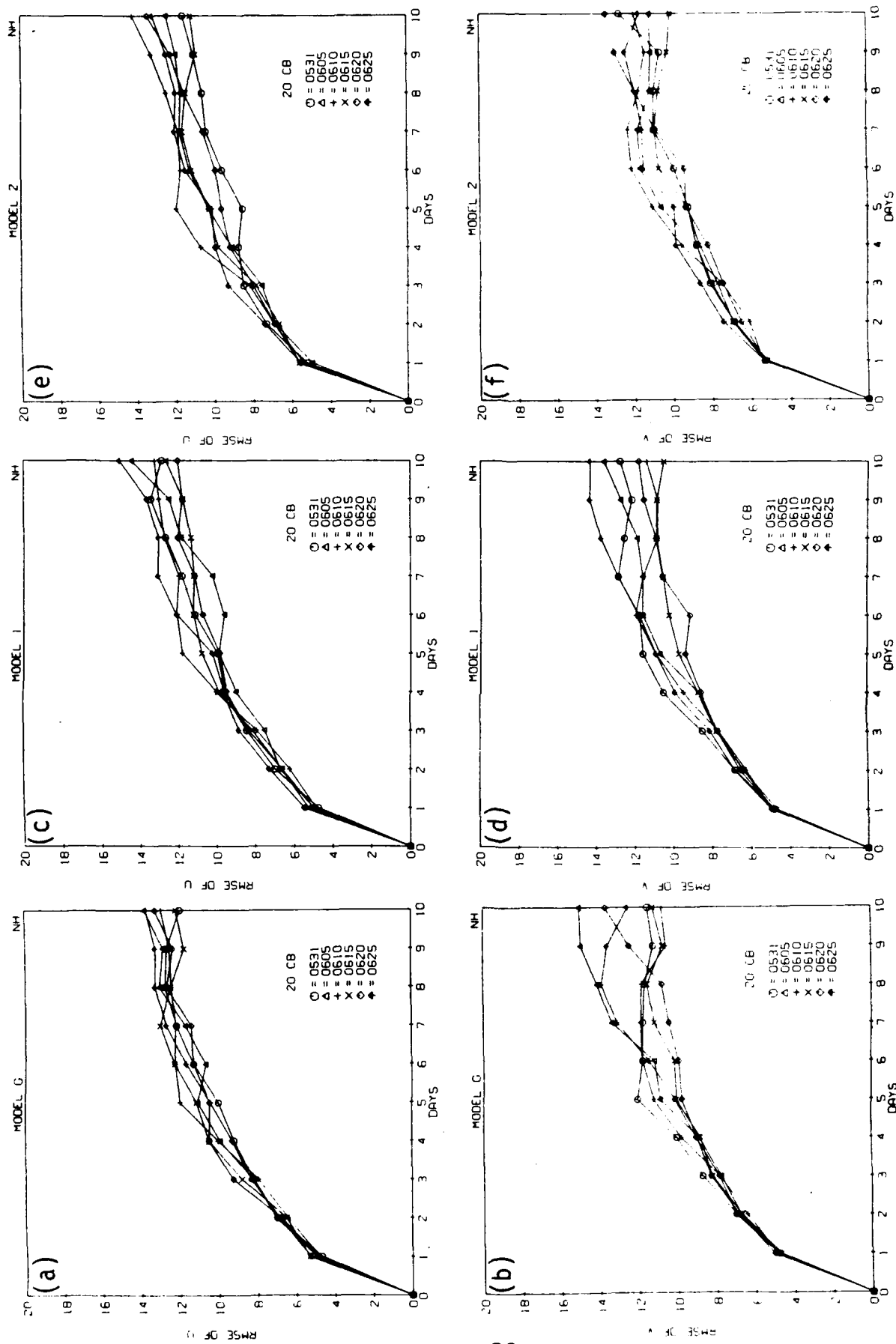


Figure 10. Same as in Figure 7 for June Forecasts.

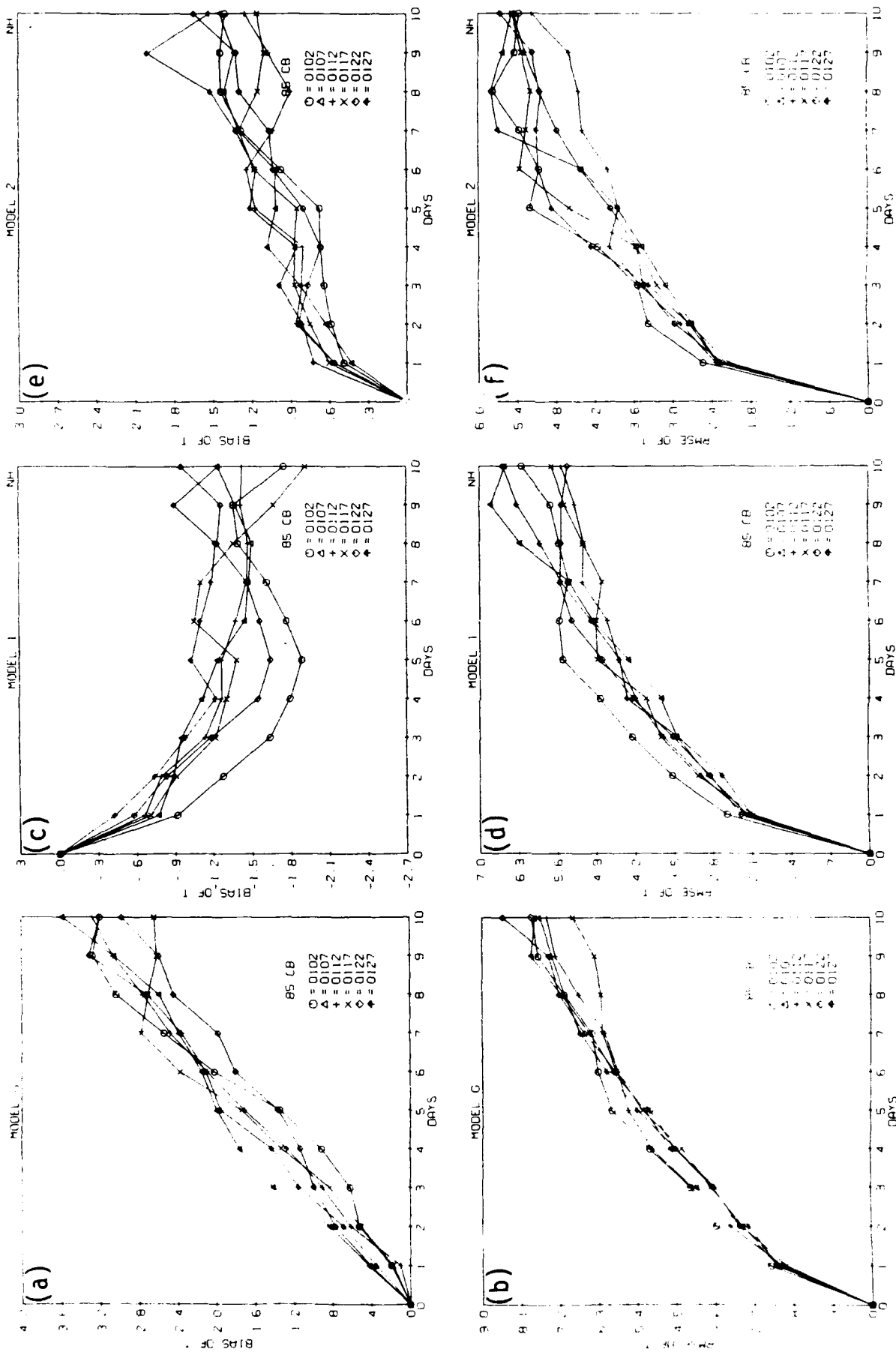


Figure 11. Northern Hemisphere Temperature Bias, RMSE of 850 mb January Forecasts of (a) GWC84, Bias, (b) GWC84, RMSE, (c) GL-89, Bias, (d) GL-89, RMSE, (e) PL-91, Bias, (f) PL-91, RMSE.

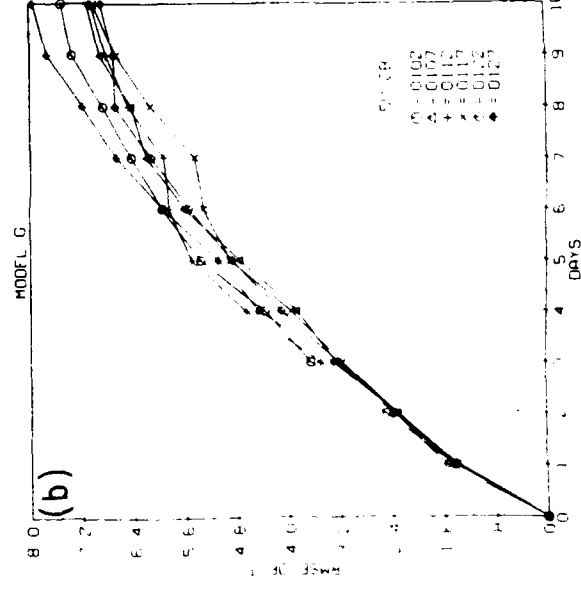
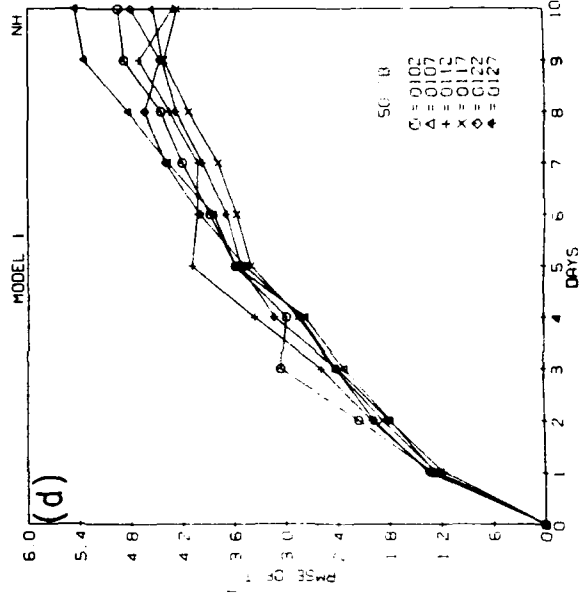
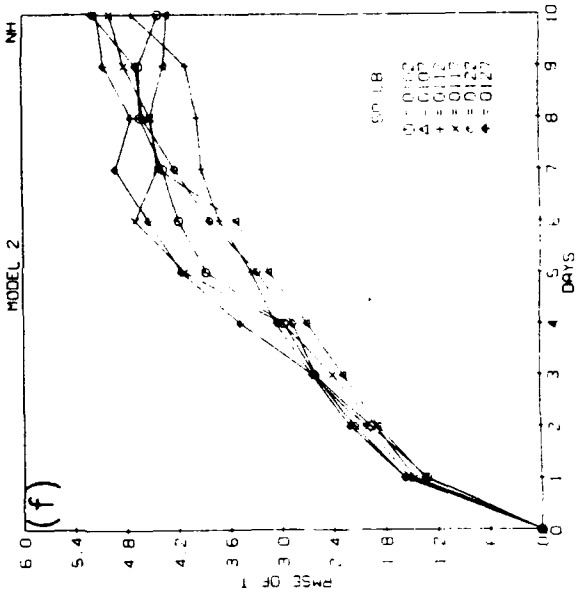
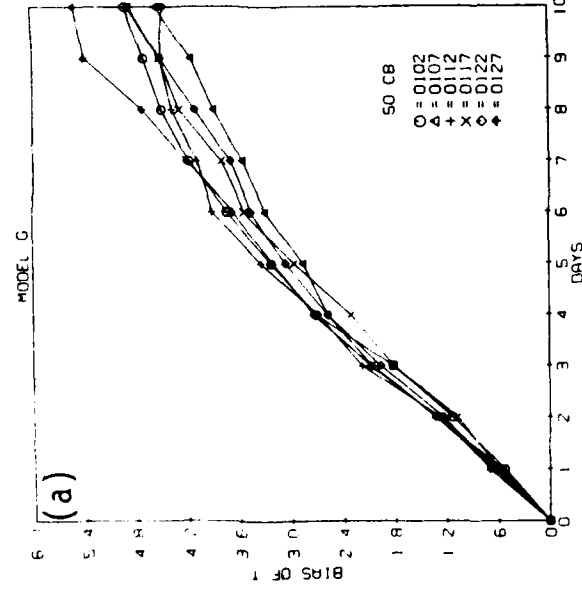
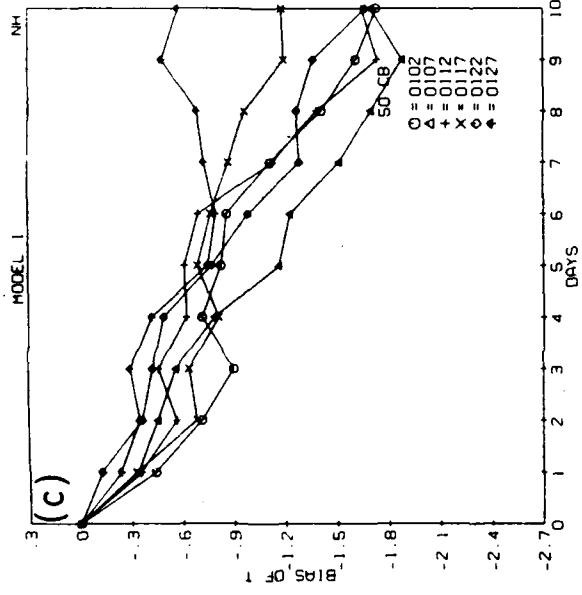
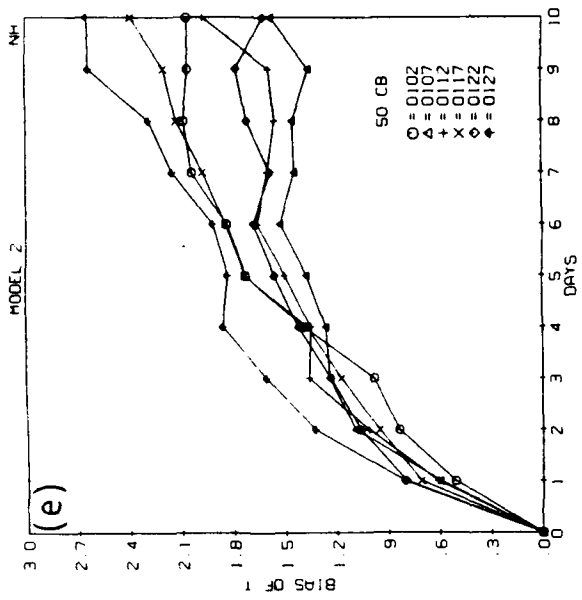


Figure 12. Same as in Figure 11 for 500 mb.

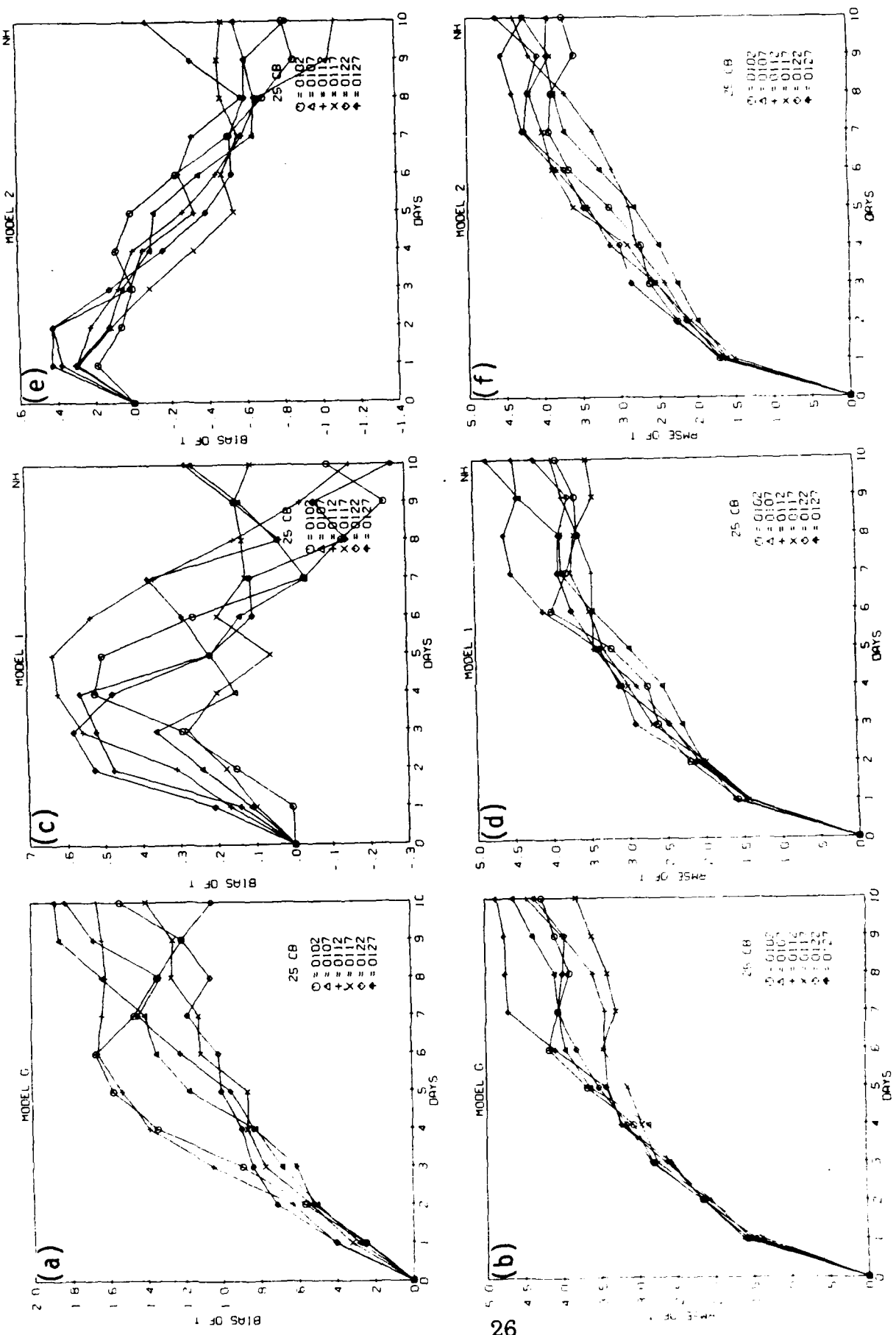


Figure 13. Same as in Figure 11 for 250 mb.

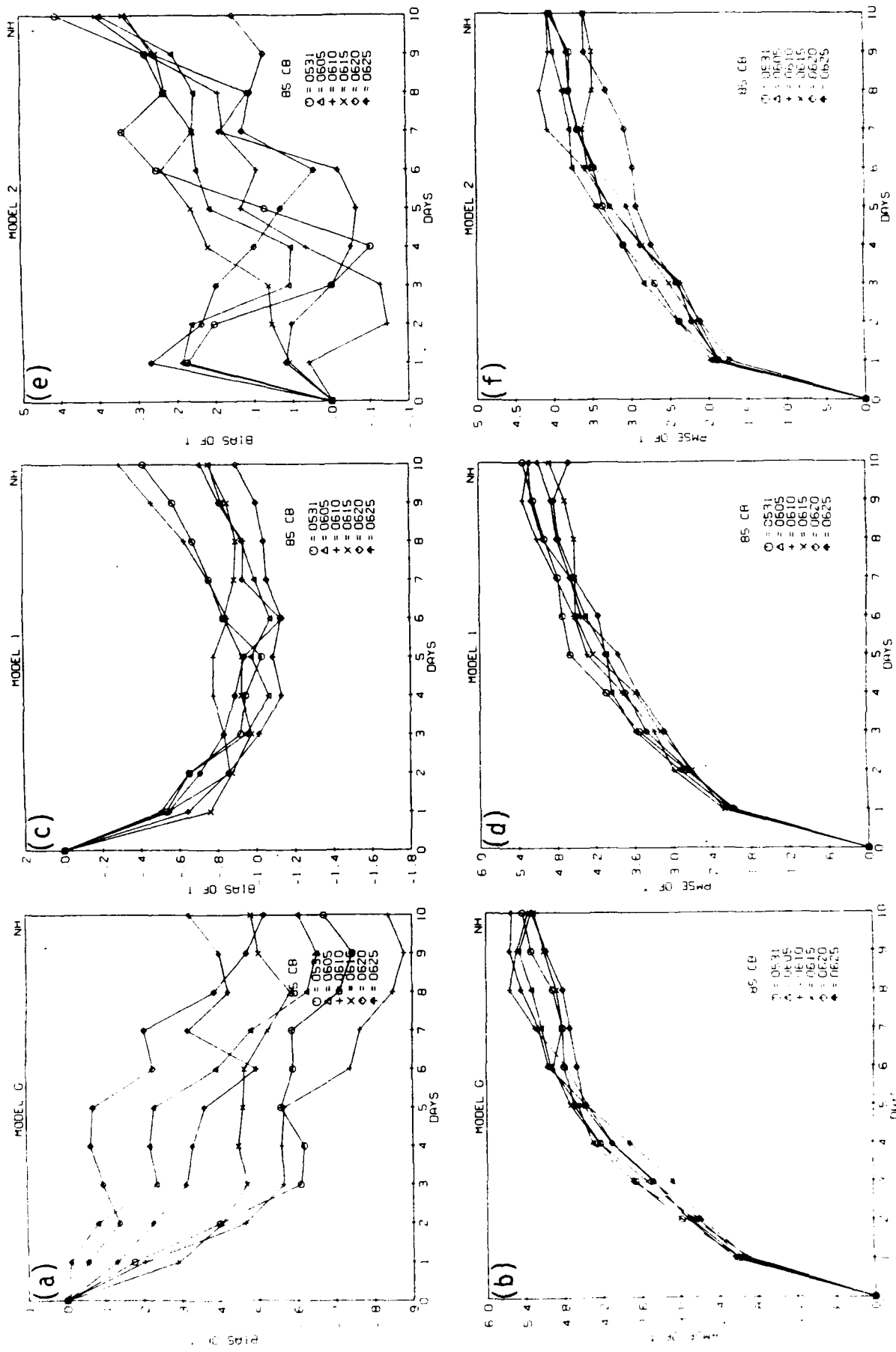


Figure 14. Same as in Figure 11 for June Forecasts.

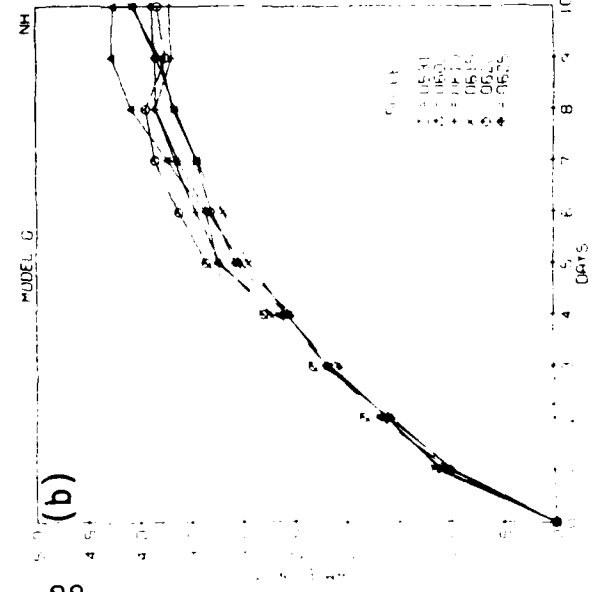
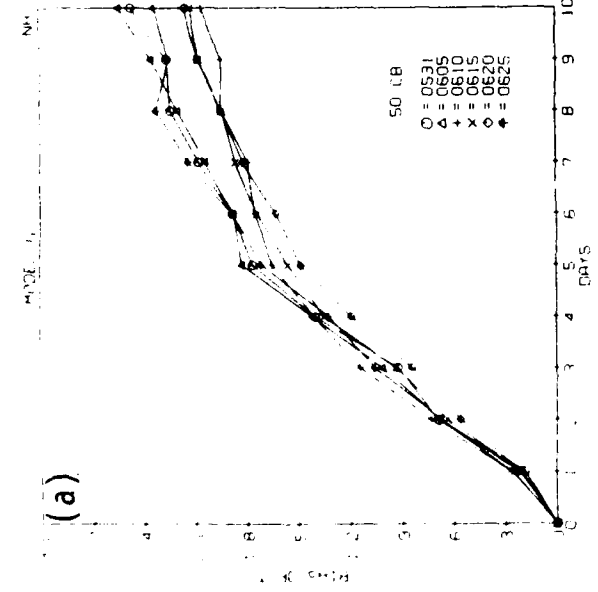
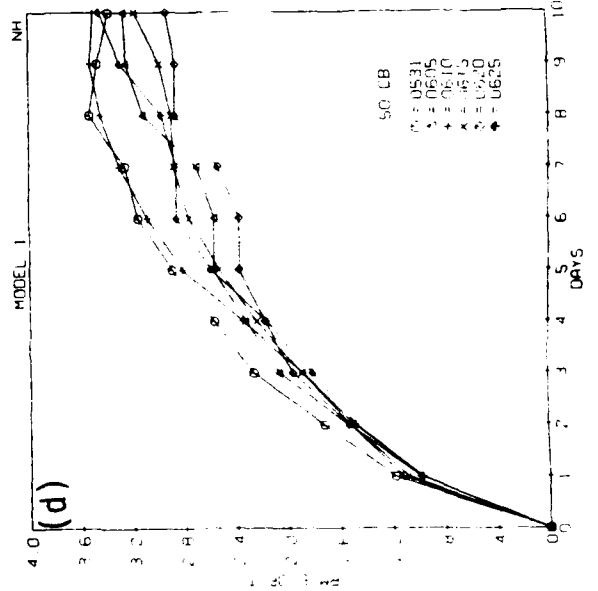
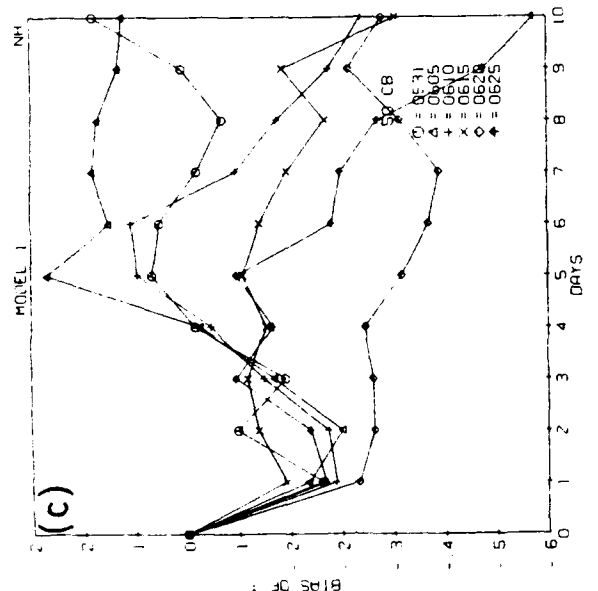
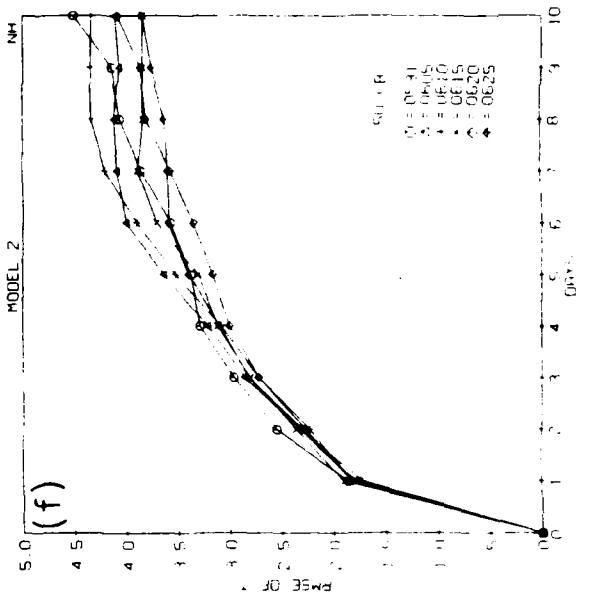
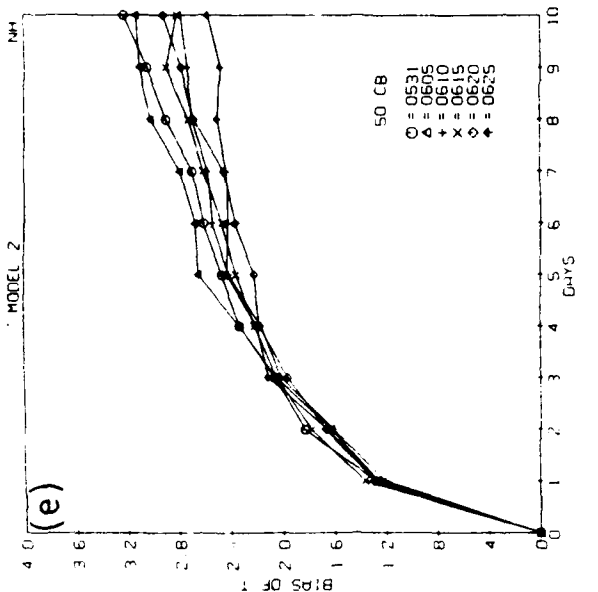


Figure 15. Same as in Figure 12 for June Forecasts.

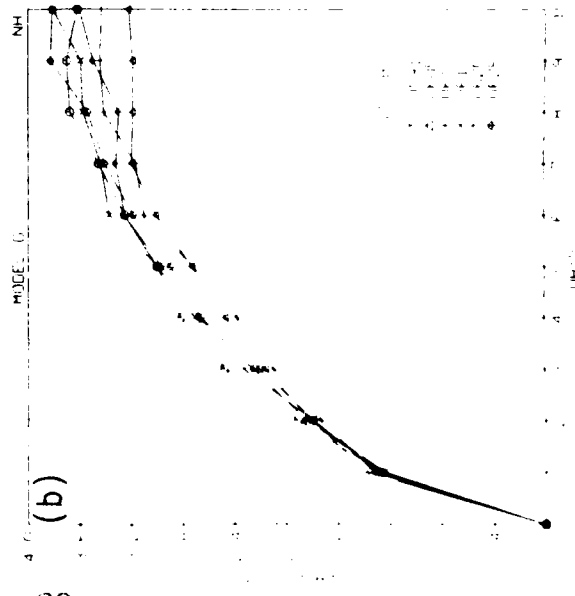
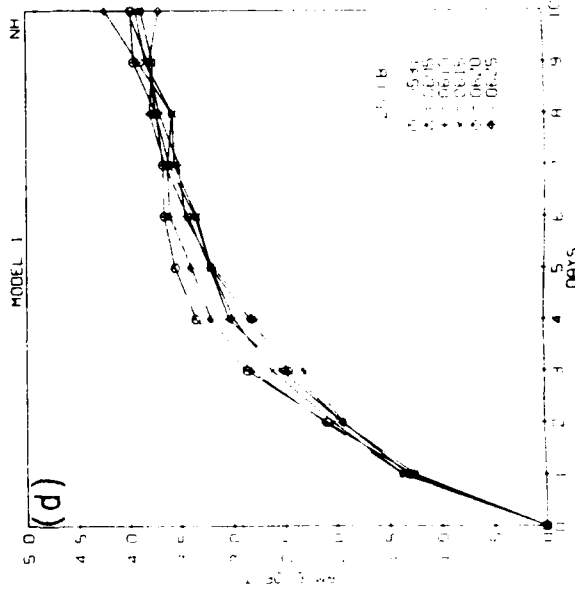
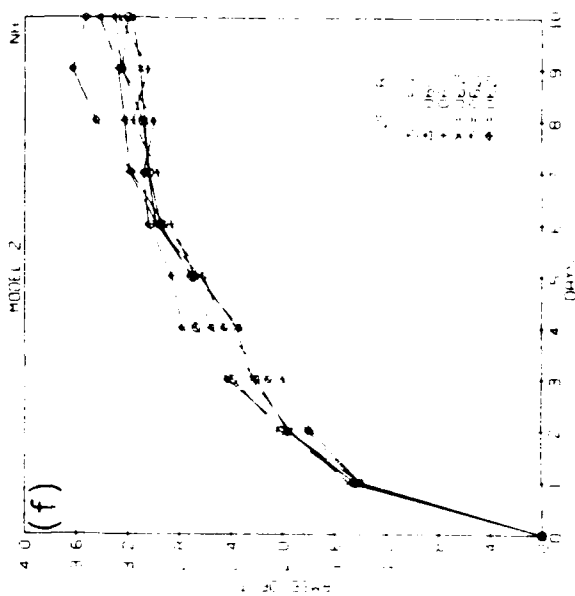
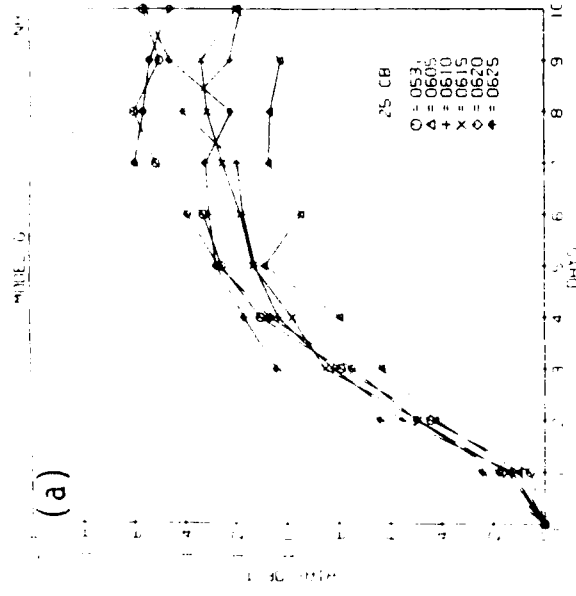
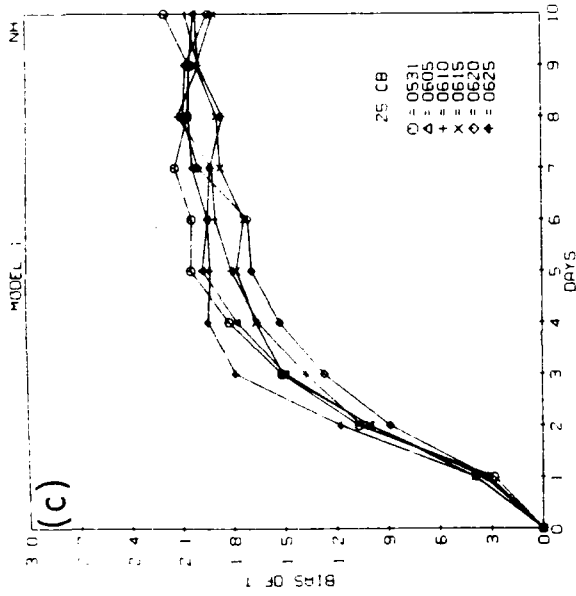
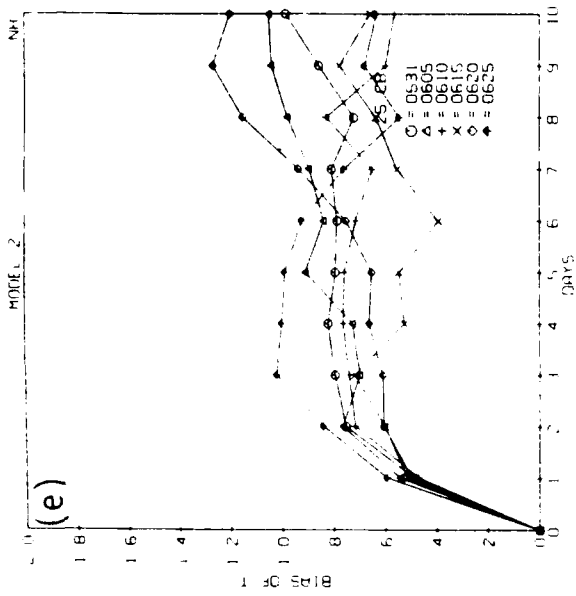


Figure 16. Same as in Figure 13 for June Forecasts.

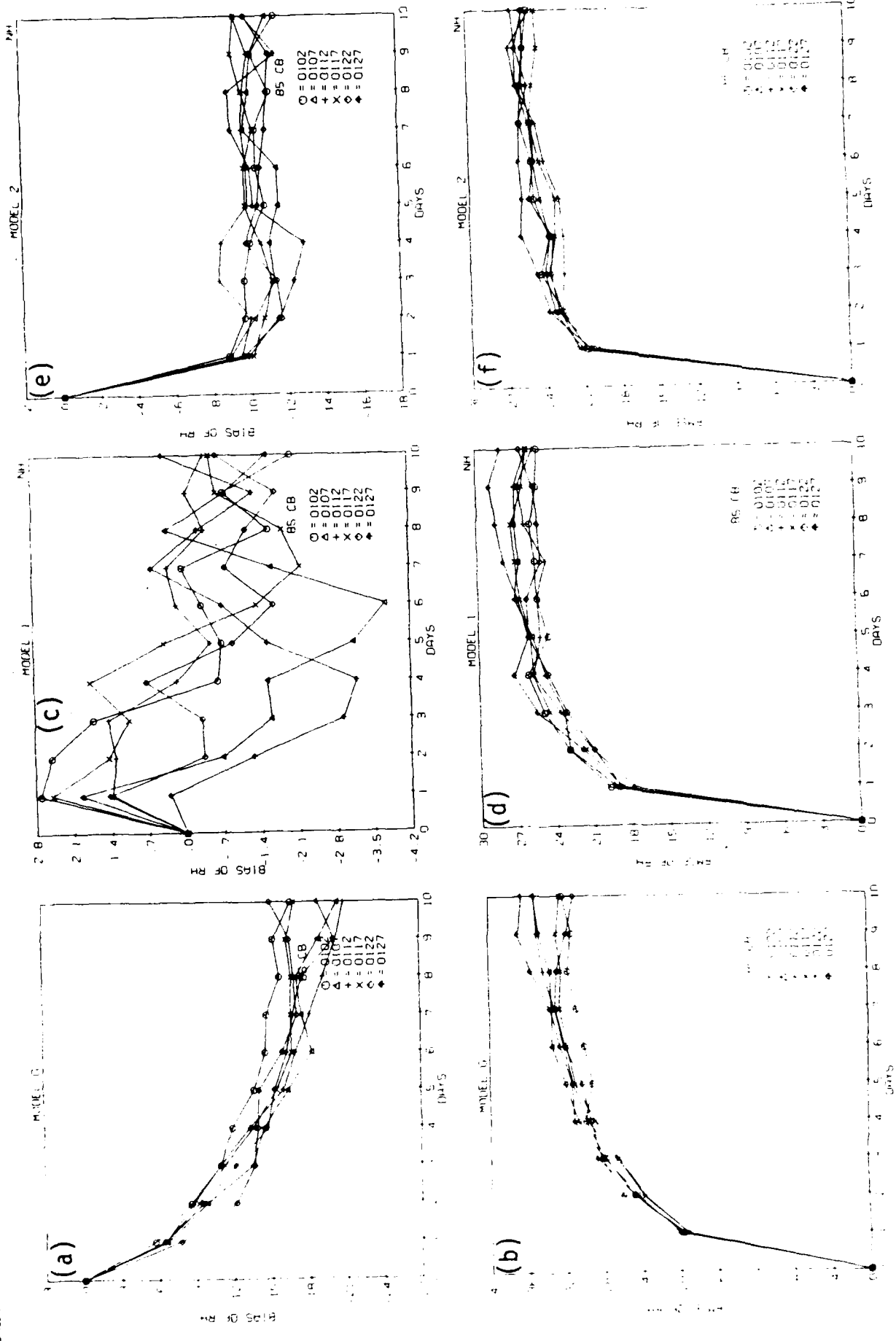


Figure 17. Northern Hemisphere Relative Humidity Bias, RMSE of 850 mb January Forecasts of (a) GWC84 Bias, (b) GWC84, RMSE, (c) GL-89, Bias, (d) GL-89, RMSE, (e) PL-91, Bias, and (f) PL-91 RMSE.

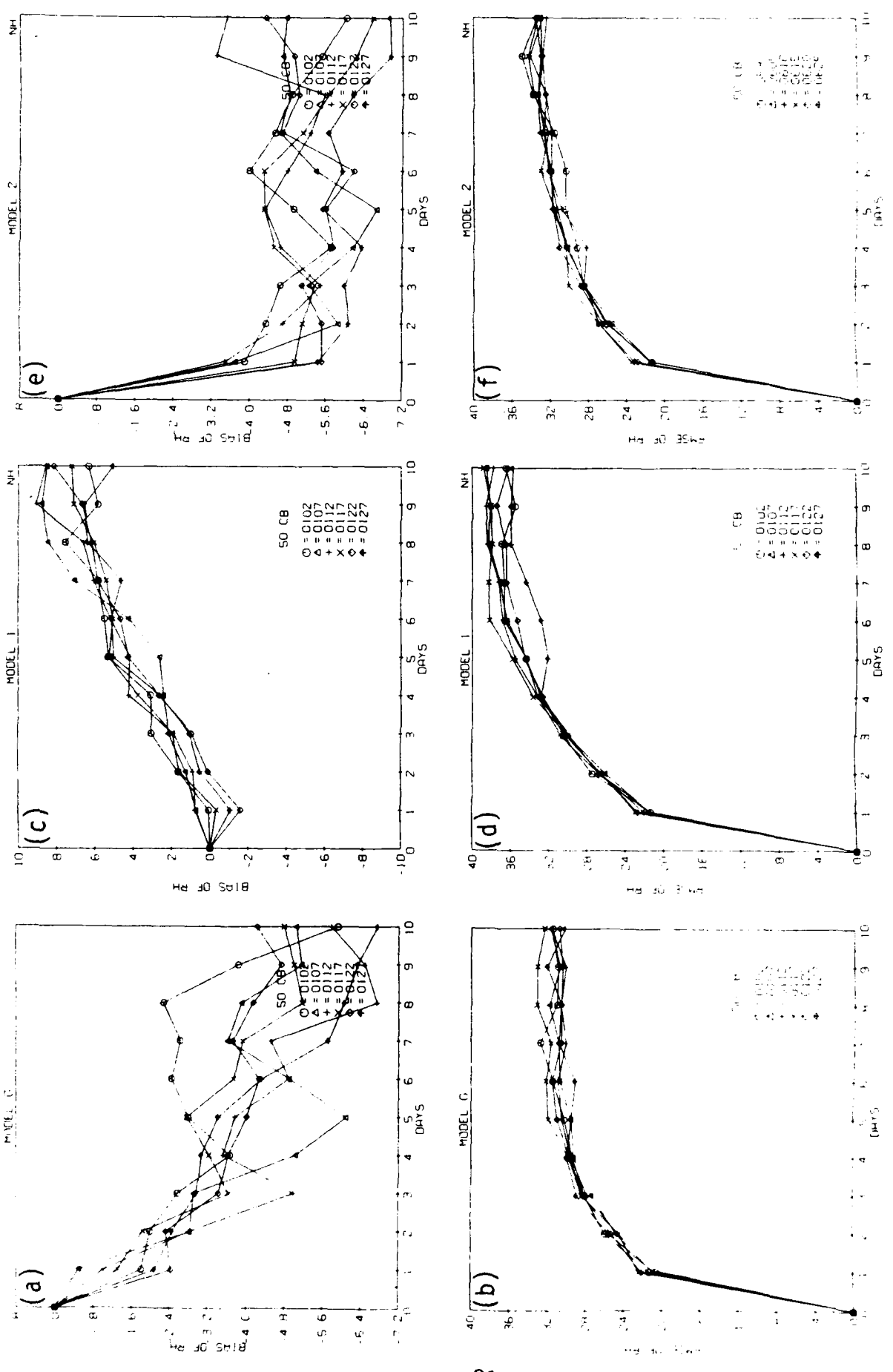


Figure 18. Same as in Figure 17 for 500 mb.

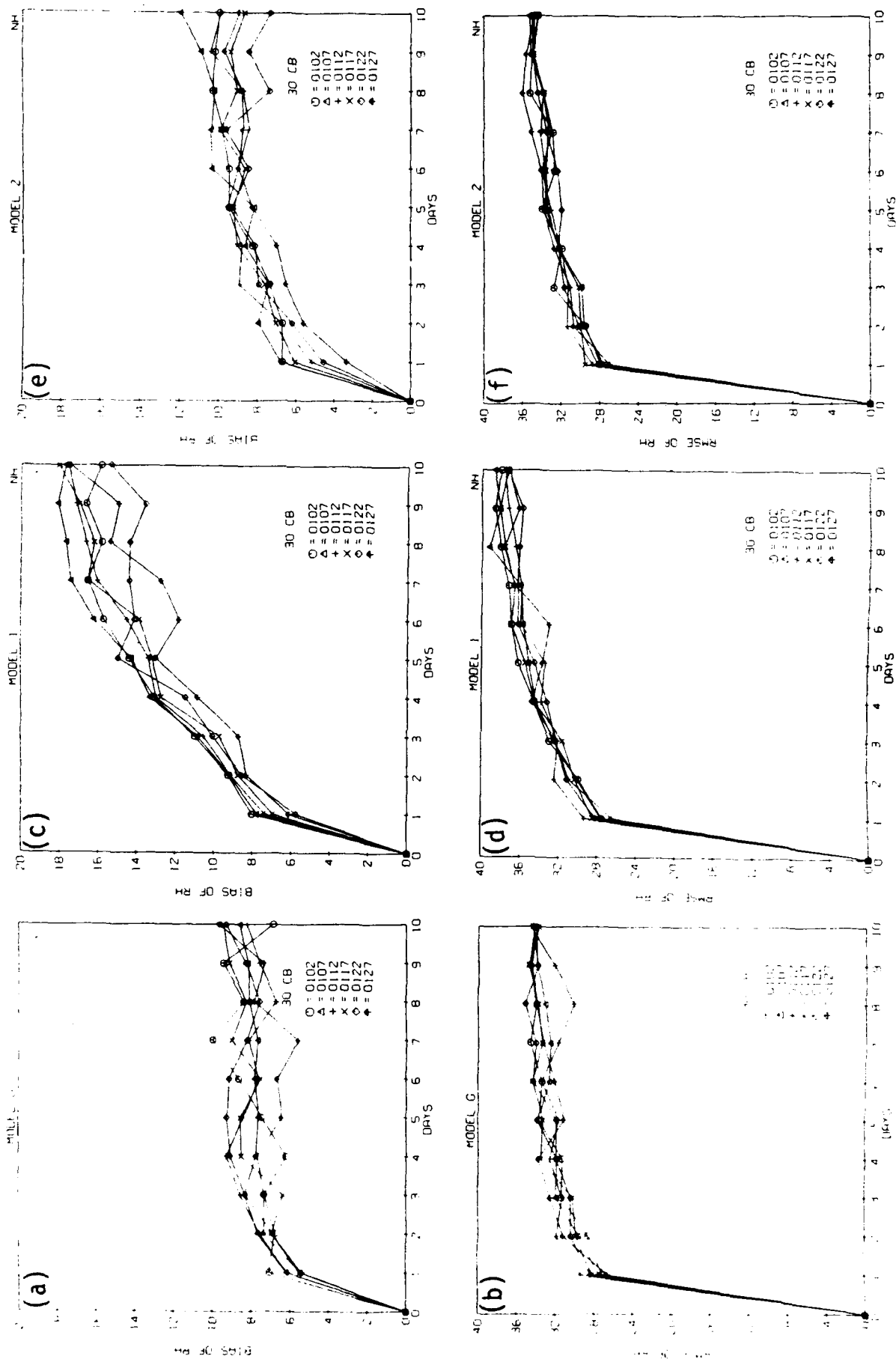


Figure 19. Same as in Figure 17 for 300 mb.

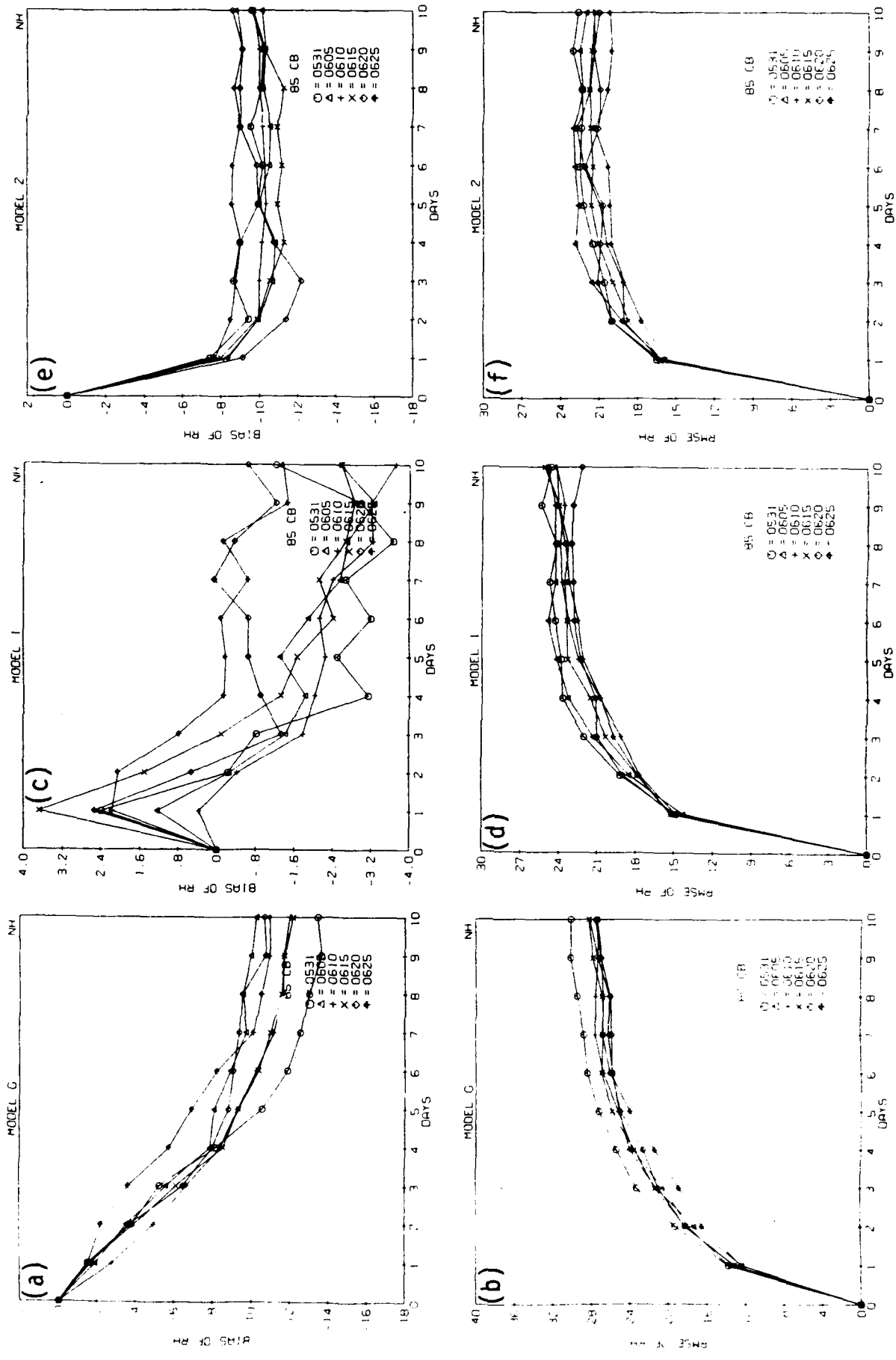


Figure 20. Same as in Figure 17 for June Forecasts.

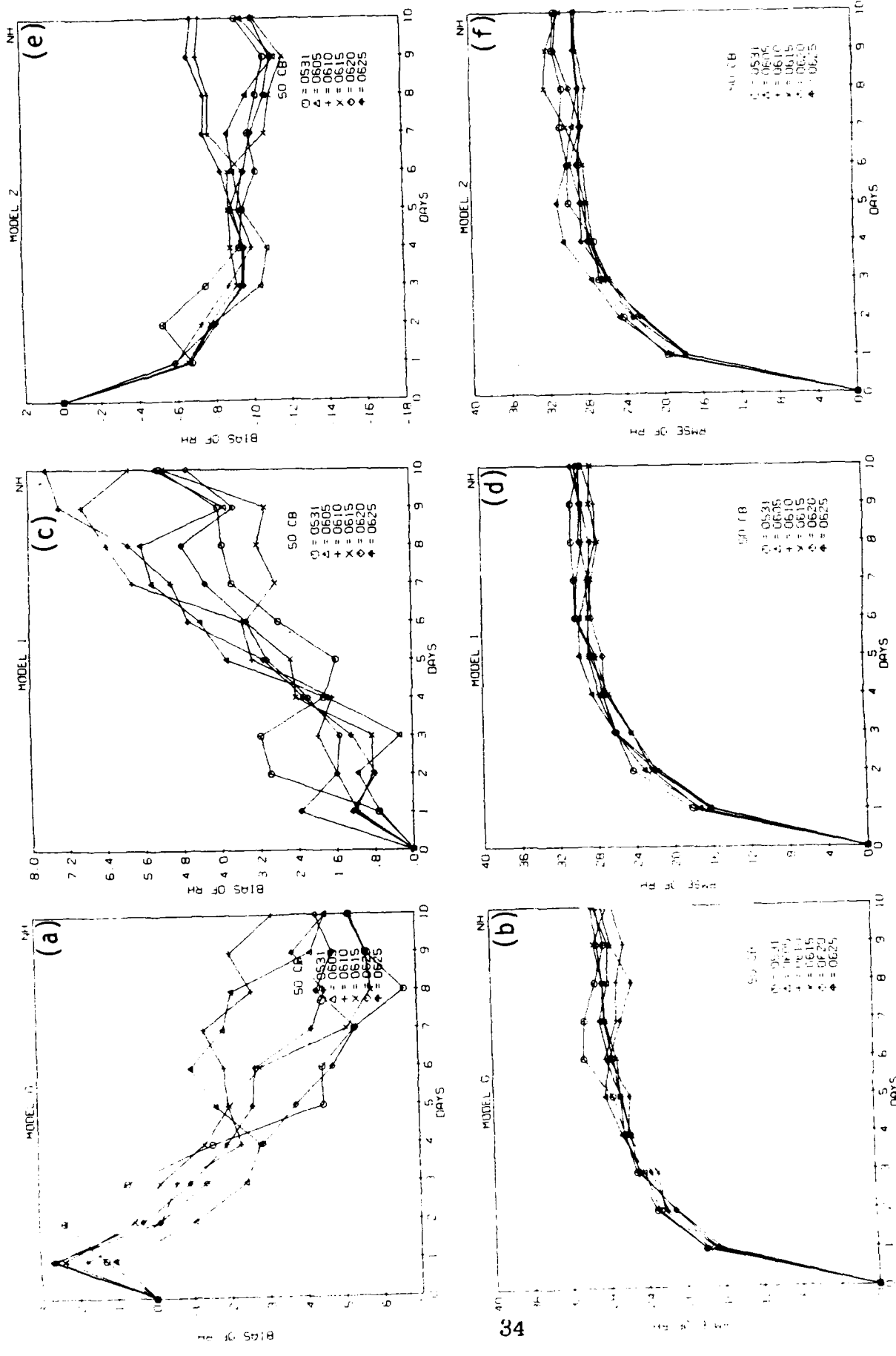


Figure 21. Same as in Figure 18 for June Forecasts.

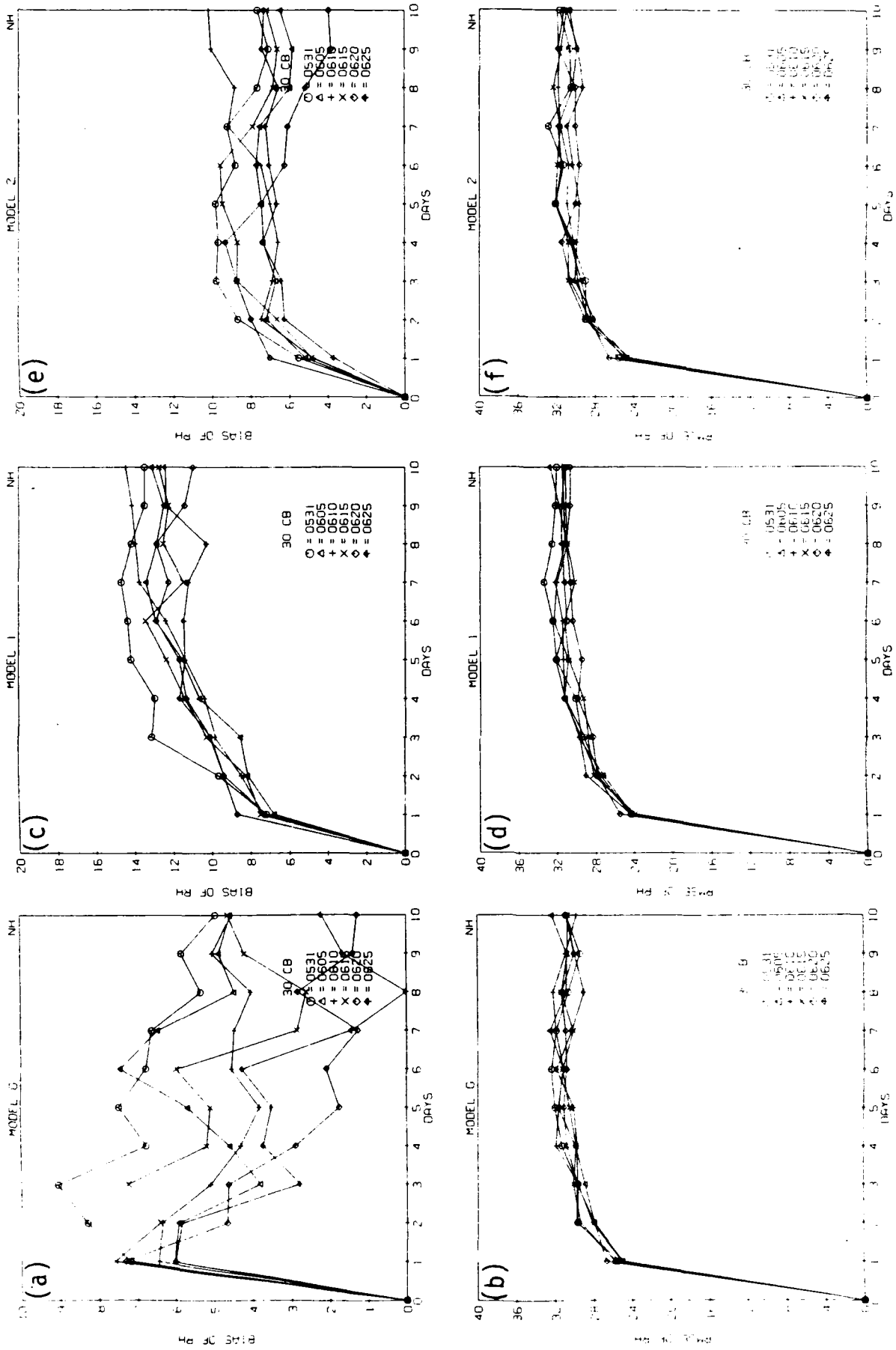


Figure 22. Same as in Figure 19 for June Forecasts.

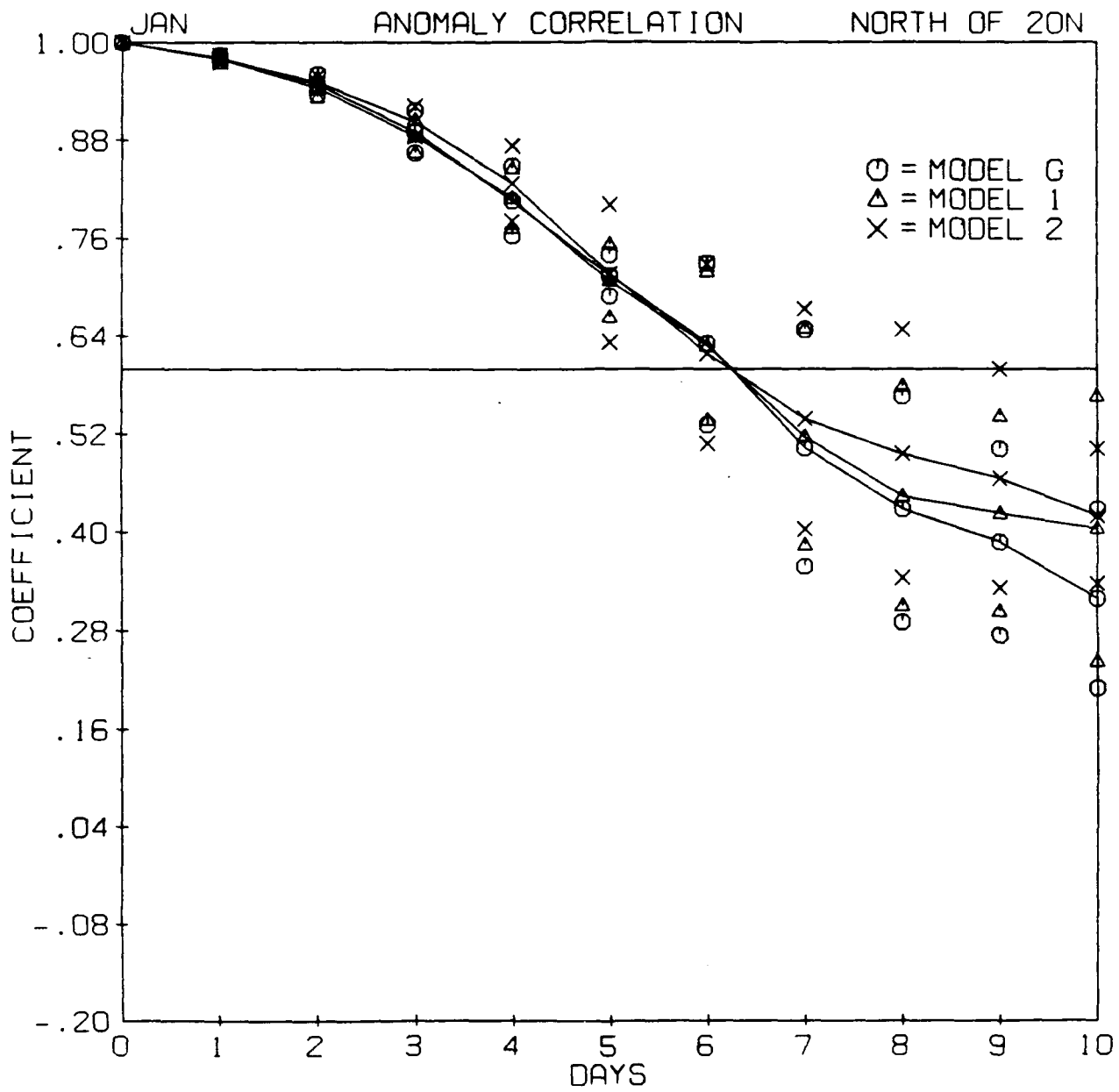


Figure 23. Anomaly Correlation for January 500 mb Geopotential Height Forecasts (Models G, 1, 2 are GWC84, GL-89, PL-91 respectively).

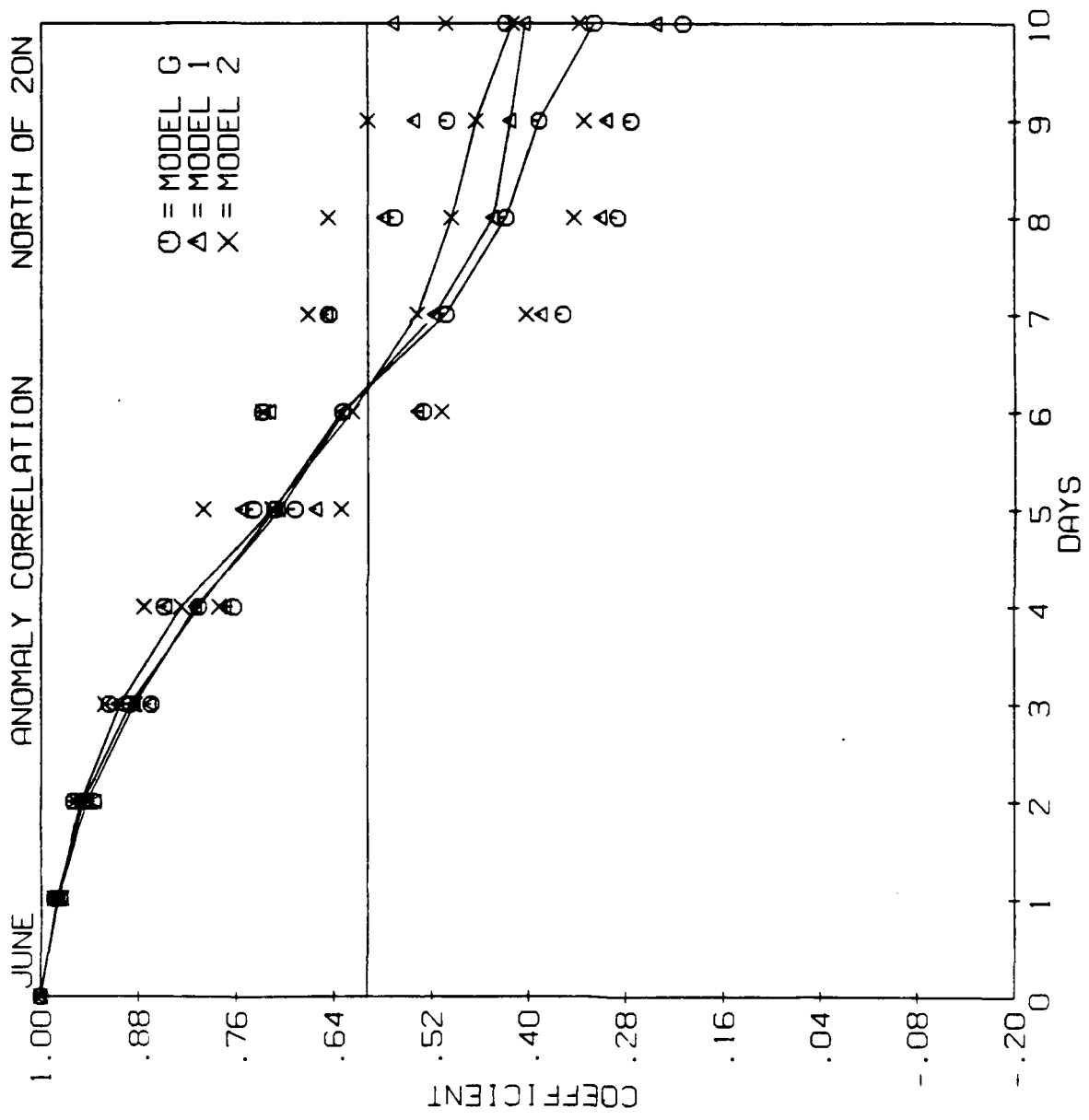


Figure 24. Same as in Figure 23 for June Forecasts.

4.1.2 ZONAL AVERAGE STATISTICS

The composition of the hemispheric error statistics presented in the previous section will now be shown by means of latitude-pressure cross sections of zonally-averaged error statistics for u, T, and RH, in which we regard individual cases as a random sample of the monthly climatology. Zonal statistics were computed for each forecast day over the ensemble of January cases, and over the ensemble of June cases. Forecast cross sections for days 3, 5, and 10 are shown in Figures 25-34. These plots helped us in recognizing the patterns of spatial distribution and trends in temporal evolution of the errors.

The significant warm bias apparent on the zonal mean T cross-sections (Figures 29, 30) and resulting large RMSE (Figures 31, 32) south of about 65S and for pressures greater than 700 mb are an artifact of the post-processing step. Forecast data on sigma layers are extrapolated to pressure surfaces that in actuality are below the ground surface in Antarctica. The typical lapse rate in the region (temperature decreasing with altitude) in the sigma layers would result in an extrapolation which yields temperatures much warmer than those specified in the corresponding analysis. Therefore, comparisons between forecasts should be avoided in this section of the plots.

4.1.3 HEMISPHERIC MAP COMPARISONS

In the preceding section, we presented zonal cross sections depicting the latitude-pressure distribution of errors. In this section, we take this analysis a step further by attempting to assess the three-dimensional spatial distribution of such consistent errors. To do this, we have produced hemispheric maps of the mean and standard deviation of the forecast errors (computed from evaluation against FGGE III-b analyses) for the cases in each month. We computed these statistics over the 60-, 72-, 84-, 96-, 108-, and 120-hour forecasts for all six cases in each month. In all, 36 individual forecasts at each gridpoint contributed to the depicted statistics. This was

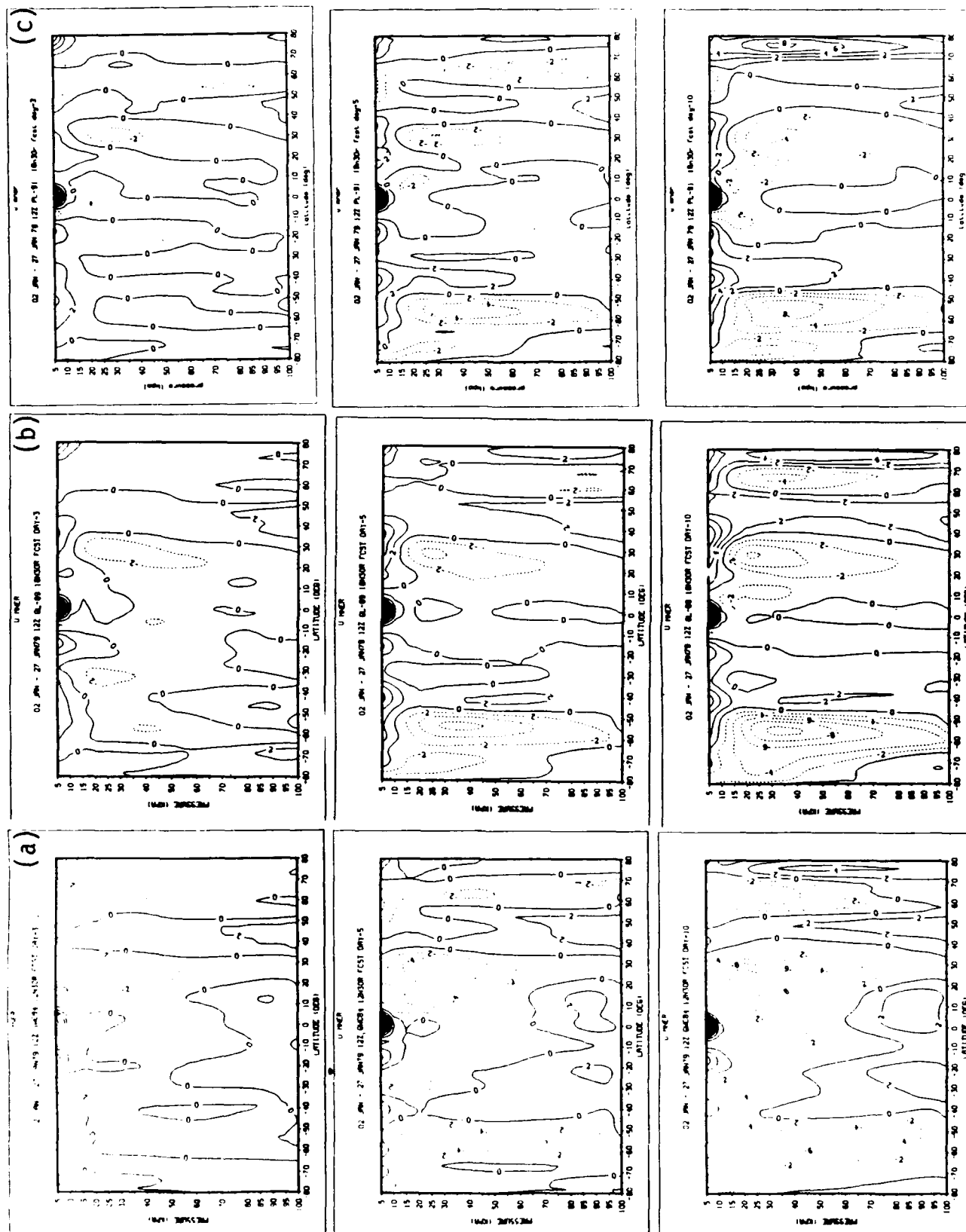


Figure 25. Latitude - Pressure Distributions of Zonal Bias of Zonal Wind Component at Days 3, 5, 10 of the January Forecasts for (a) GWC84, (b) GL-89, (c) PL-91.

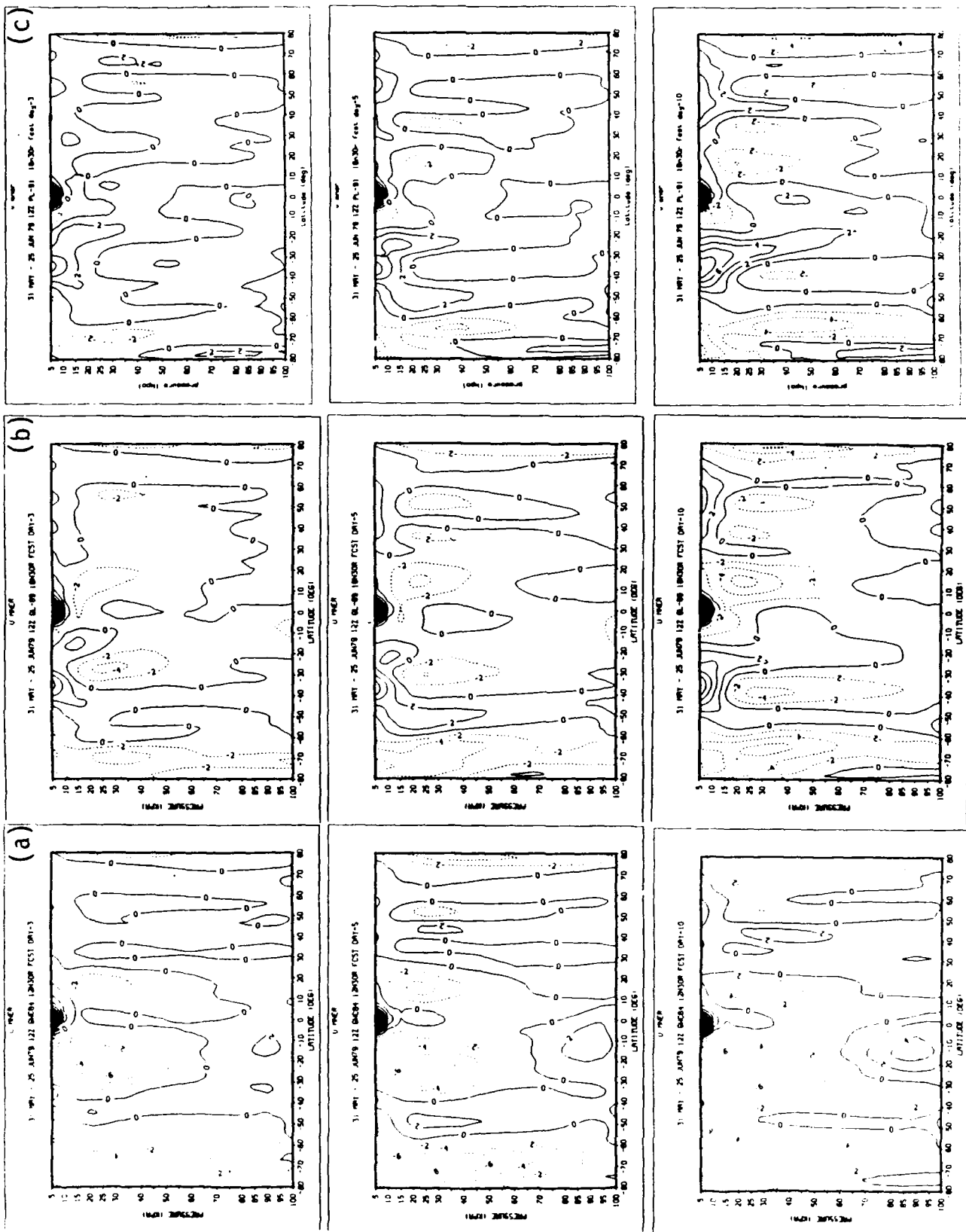


Figure 26. Same as in Figure 25 for June Forecasts.

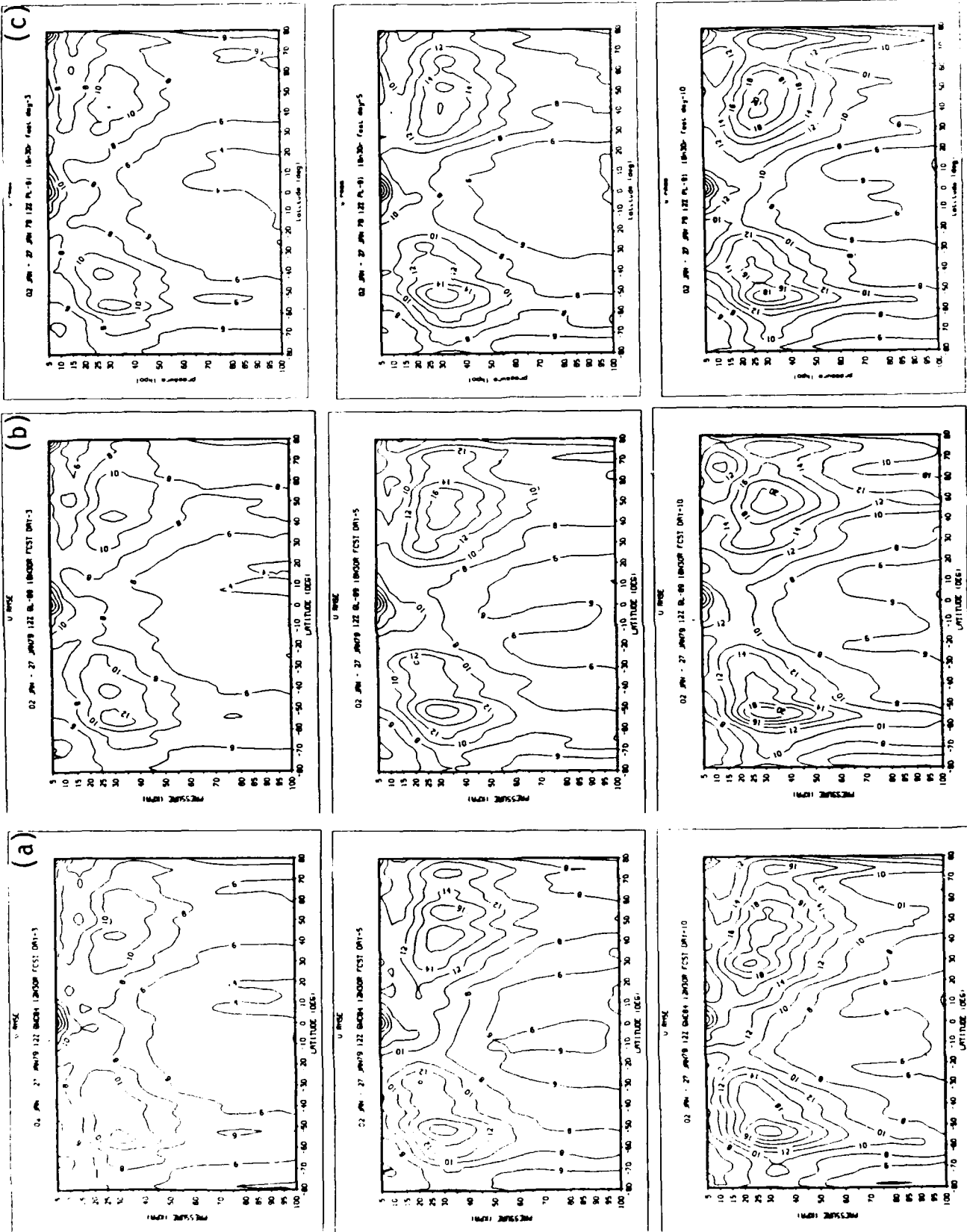


Figure 27. Latitude - Pressure Distributions of Zonal RMSE of Zonal Wind Component at Days 3, 5, 10 of January Forecasts for (a) GWC84, (b) GL-89, and (c) PL-91.

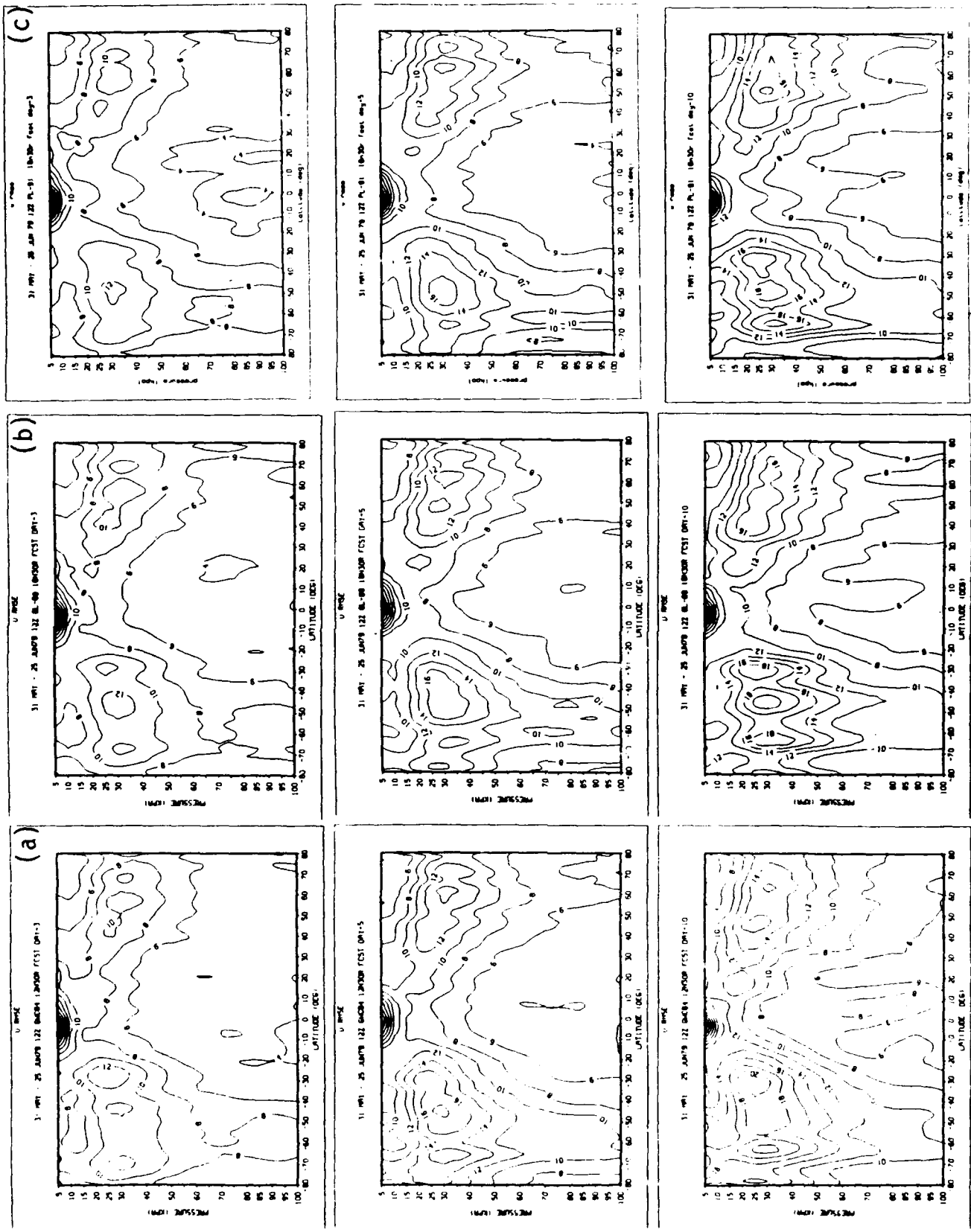


Figure 28. Same as in Figure 27 for June Forecasts.

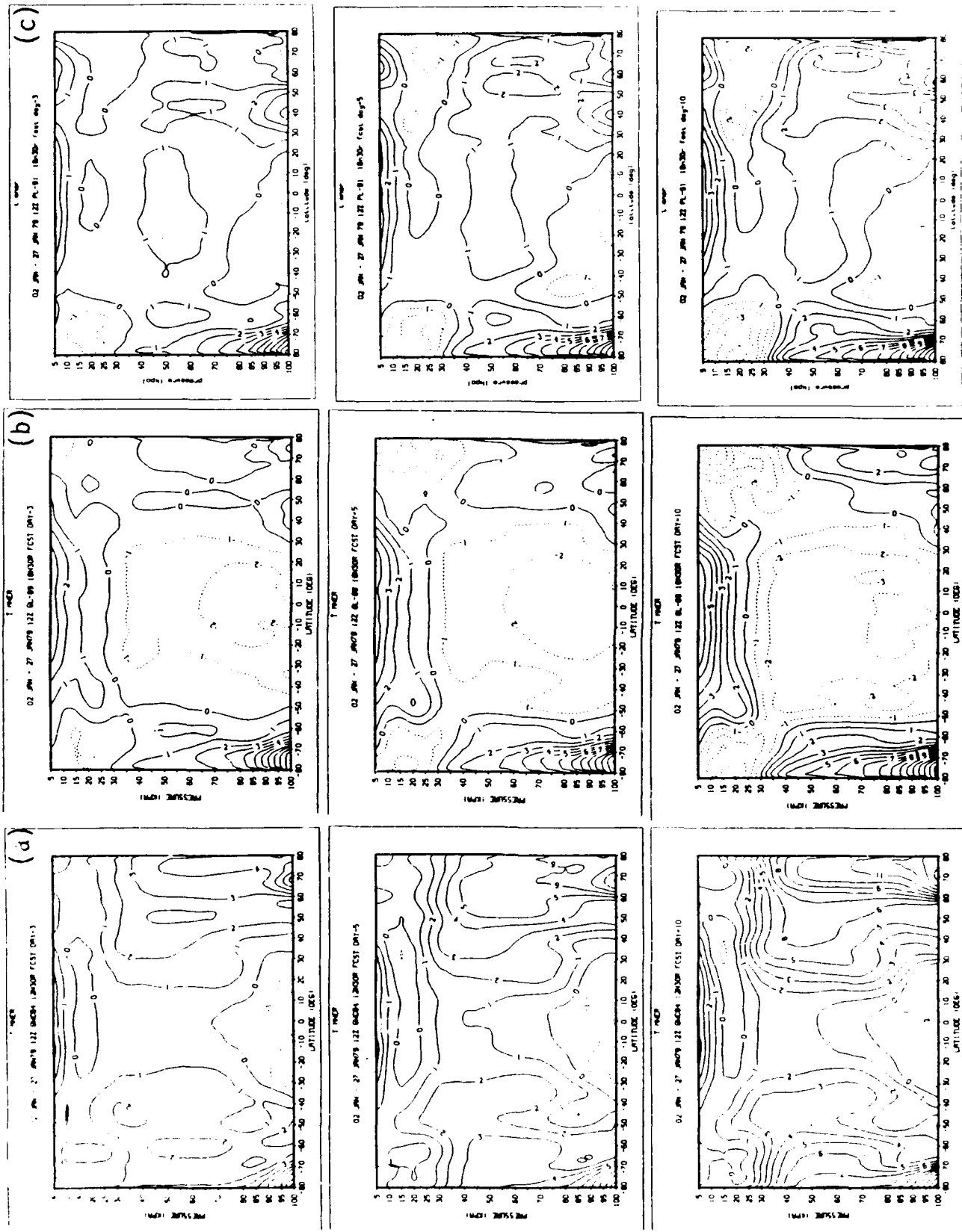


Figure 29. Latitude-Pressure Distributions of Zonal Bias of Temperature at Days 3, 5, 10 of the January Forecasts for (a) GWC84, (b) GL-89, (c) PL-91.

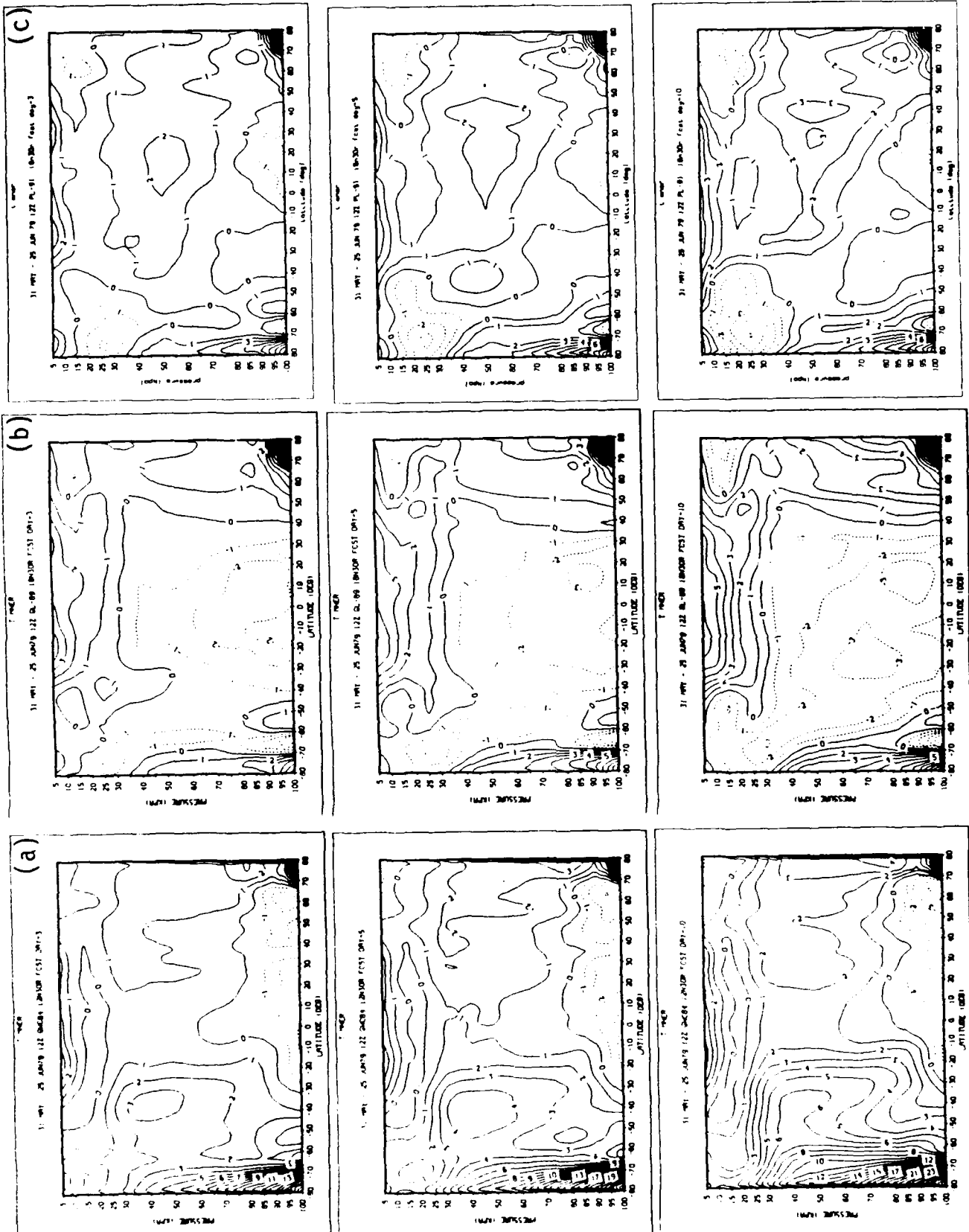


Figure 30. Same as in Figure 29 for June Forecasts.

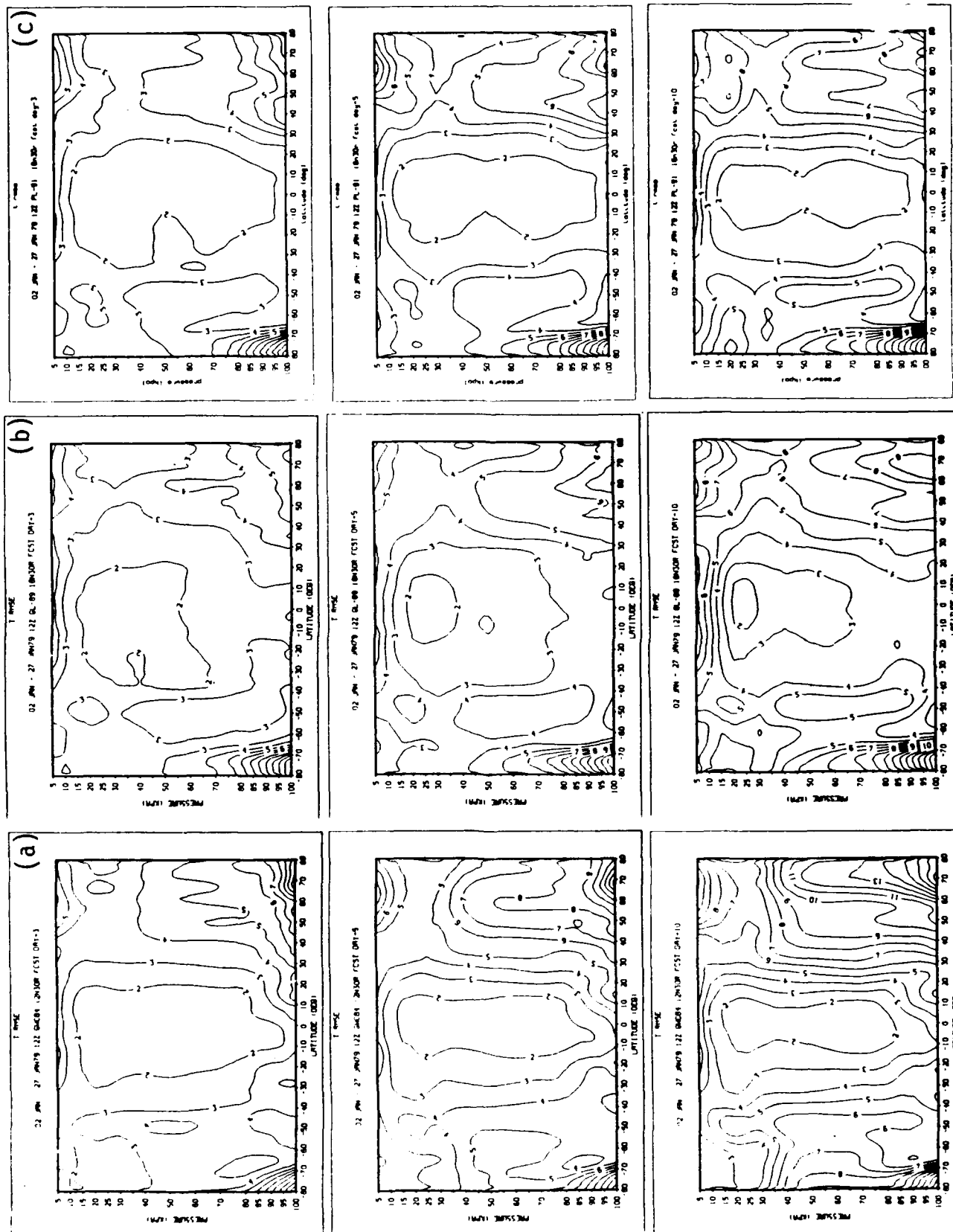


Figure 31. Latitude-Pressure Distributions of Zonal RMSE of Temperature at Days 3, 5, 10 of the January Forecasts for (a) GWC84, (b) GL-89, (c) PL-91.

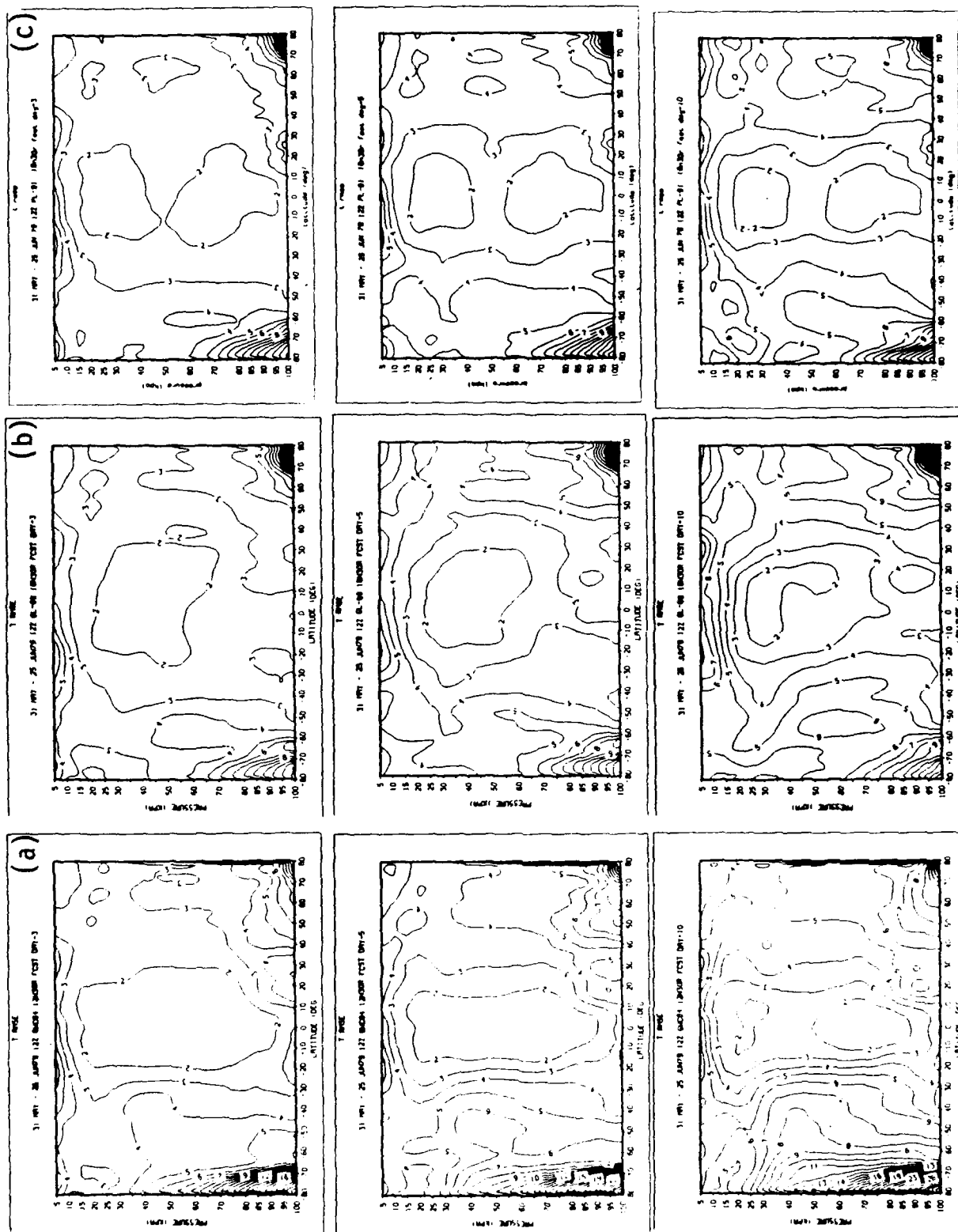


Figure 32. Same as in Figure 31 for June Forecasts.

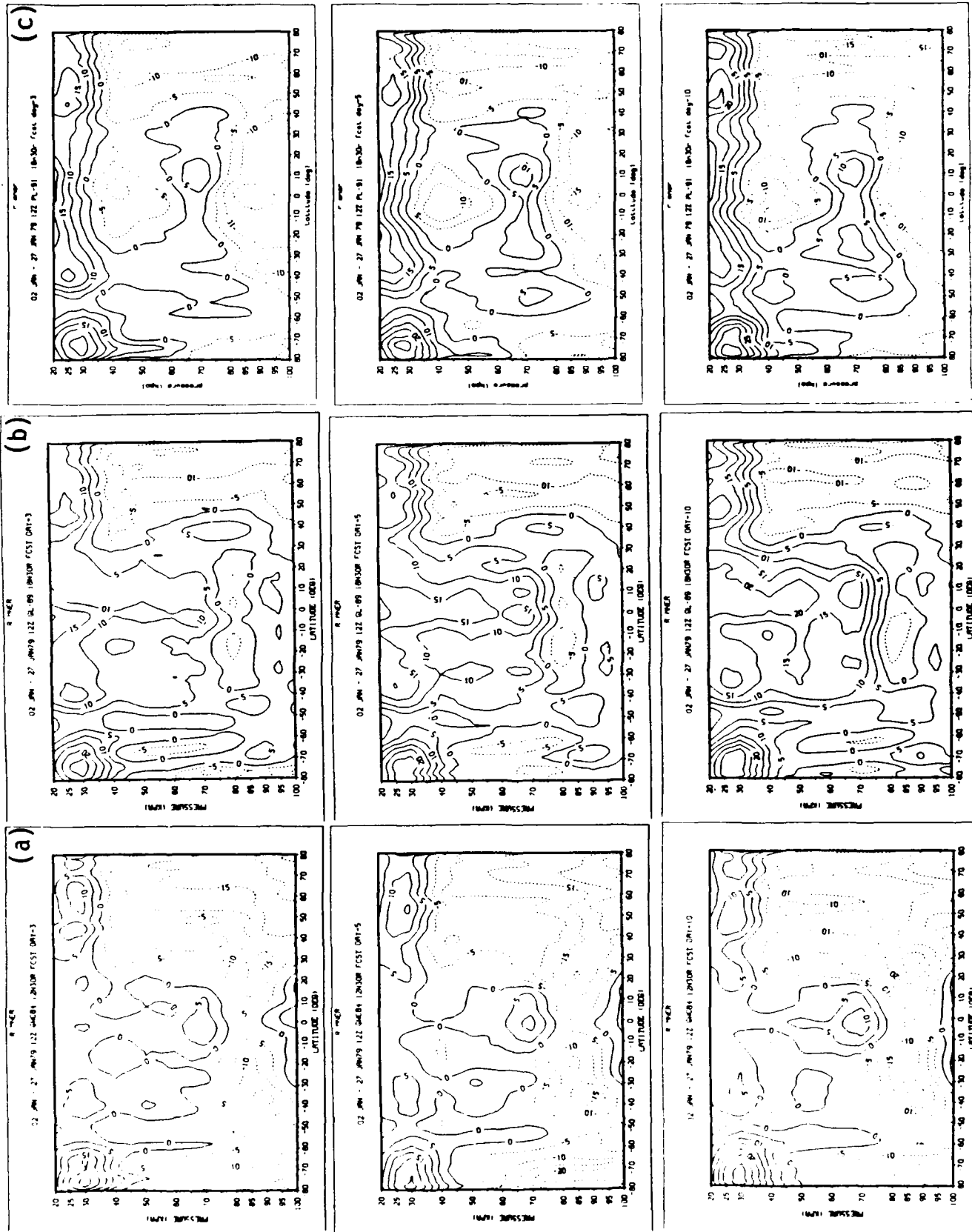


Figure 33. Latitude-Pressure Distributions of Zonal Bias of Relative Humidity at Days 3, 5, 10 of the January Forecasts for (a) GWC84, (b) GL-89, (c) PL-91.

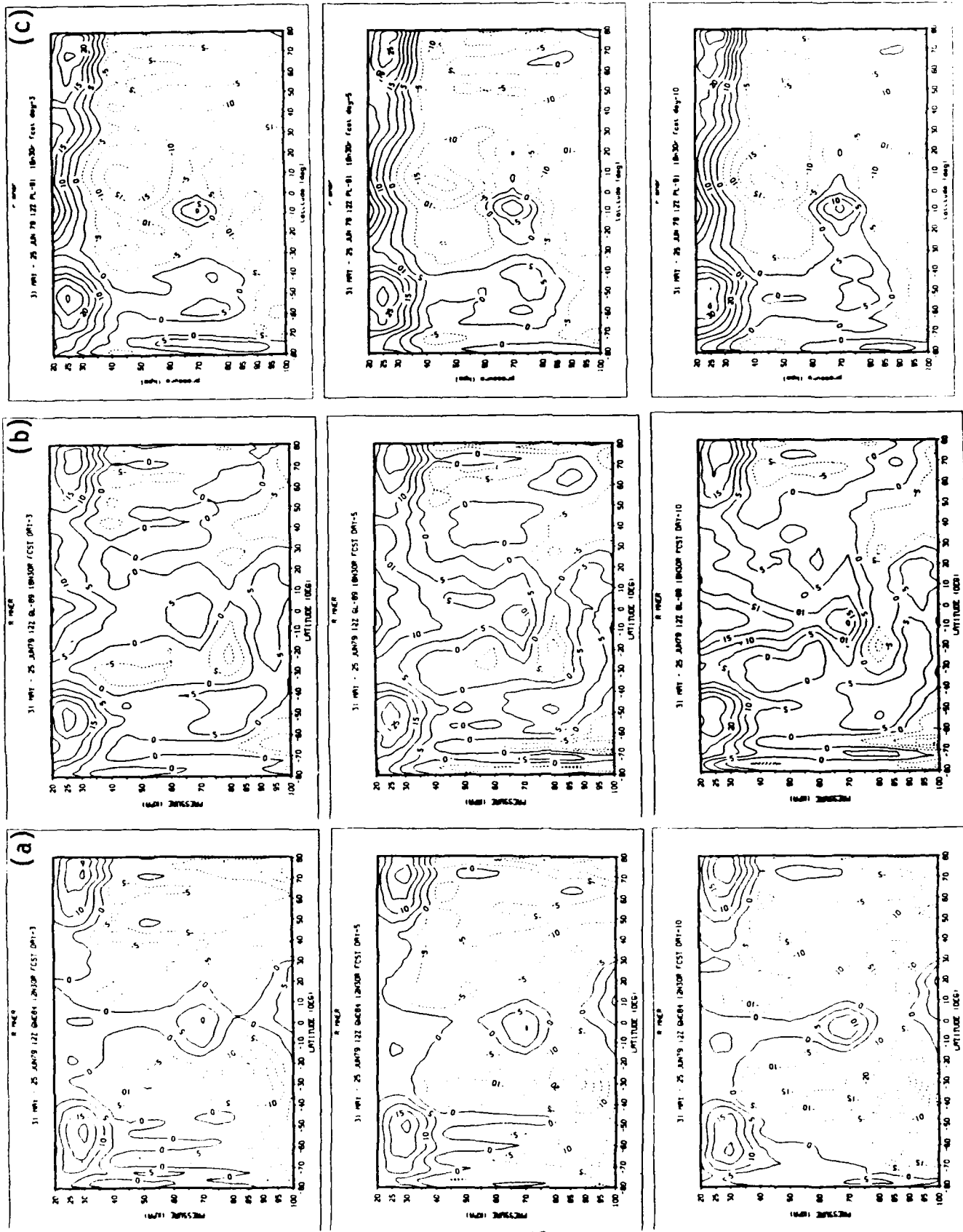


Figure 34. Same as in Figure 33 for June Forecasts.

an attempt to display the short-term forecast error climatology. Thus, these depictions will display the geographic distribution of the errors leading to the three- and five-day zonal mean errors shown in Figures 25-34. As we shall see, these maps are a useful tool in identifying regions of suspected systematic error for more temporally and spatially detailed study.

Because we want to focus on systematic error in this analysis, we will only show error maps where the mean error is of equal or greater magnitude than the standard deviation of the error. Here we present our results of the analysis of the PL-91 version of the PL GSM. In all of the following maps, we have indicated with stippling those areas where the isobaric surface depicted by the map lies at or below the earth's terrain (resulting from a comparison of the mean FGGE III-b geopotential heights with the 1.875° latitude-longitude terrain heights). This helps to identify (and exclude from discussion) those errors that may have resulted from subterranean extrapolation. Indicated latitude and longitude lines are at 30° intervals. To select the maps for the following discussion, we evaluated maps of wind speed, height, temperature, and relative humidity error at 950, 850, 700, 500, and 200 mb. We identified regions of large bias in the mean error maps, then made sure that the standard deviation in the same region was no greater than the indicated bias.

In wind speed in the January maps, we see a region of negative bias off the west coast of South America that appears to be significant at 950 and 850 mb (Figure 35). At 200 mb, we note several regions of systematic positive wind speed bias, notably over Saudi Arabia, between Australia and New Zealand, and over Cuba (Figure 36). In June, we see a region of significant positive wind speed bias at 850 and 700 mb over northwestern South America (Figure 37). A large region of systematic positive bias exists over south central Africa and over Hawaii at 200 mb (Figure 38). In all of the above figures, a strong negative systematic bias is depicted at the extreme high latitudes (near 90°), greatest in the winter hemisphere. Its position and orientation suggest the error is occurring at or very near the pole. Subsequent investigation revealed that the post-processing assigns a zero value to the forecast winds at the poles, as the wind components at the poles are ambiguous. This latter error would

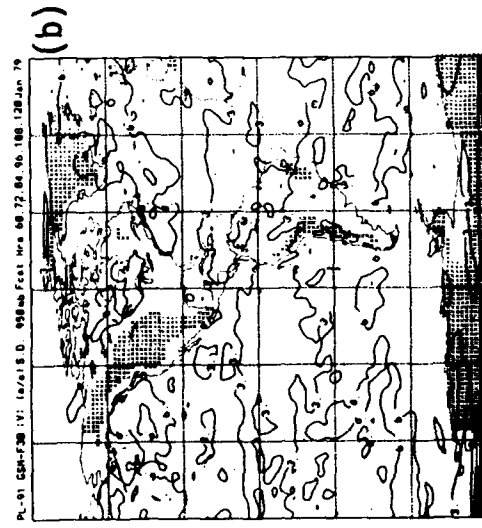
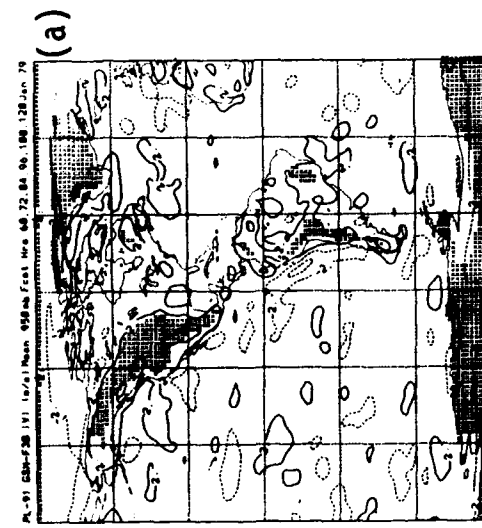
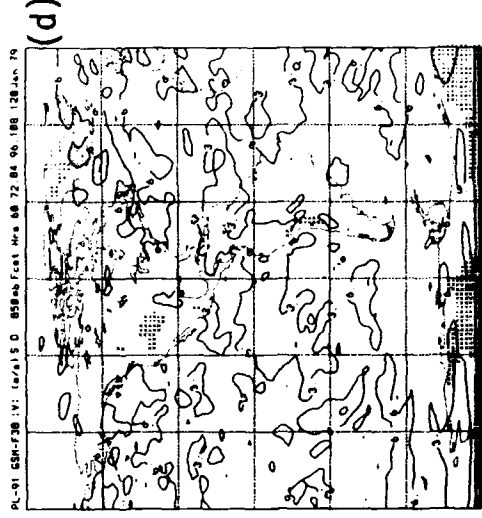
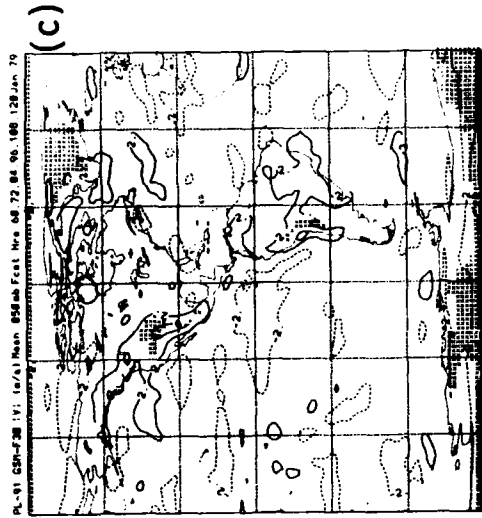


Figure 35. Hemispheric Maps of PL-91 60-120 Hour January Forecast Error of Wind Speed:
 (a) Western Hemisphere (WH), 950 mb Mean Error (ME), (b) WH, 950 mb Standard Deviation of Error (SDE), (c) WH, 850 mb ME, (d) WH, 850 mb SDE.

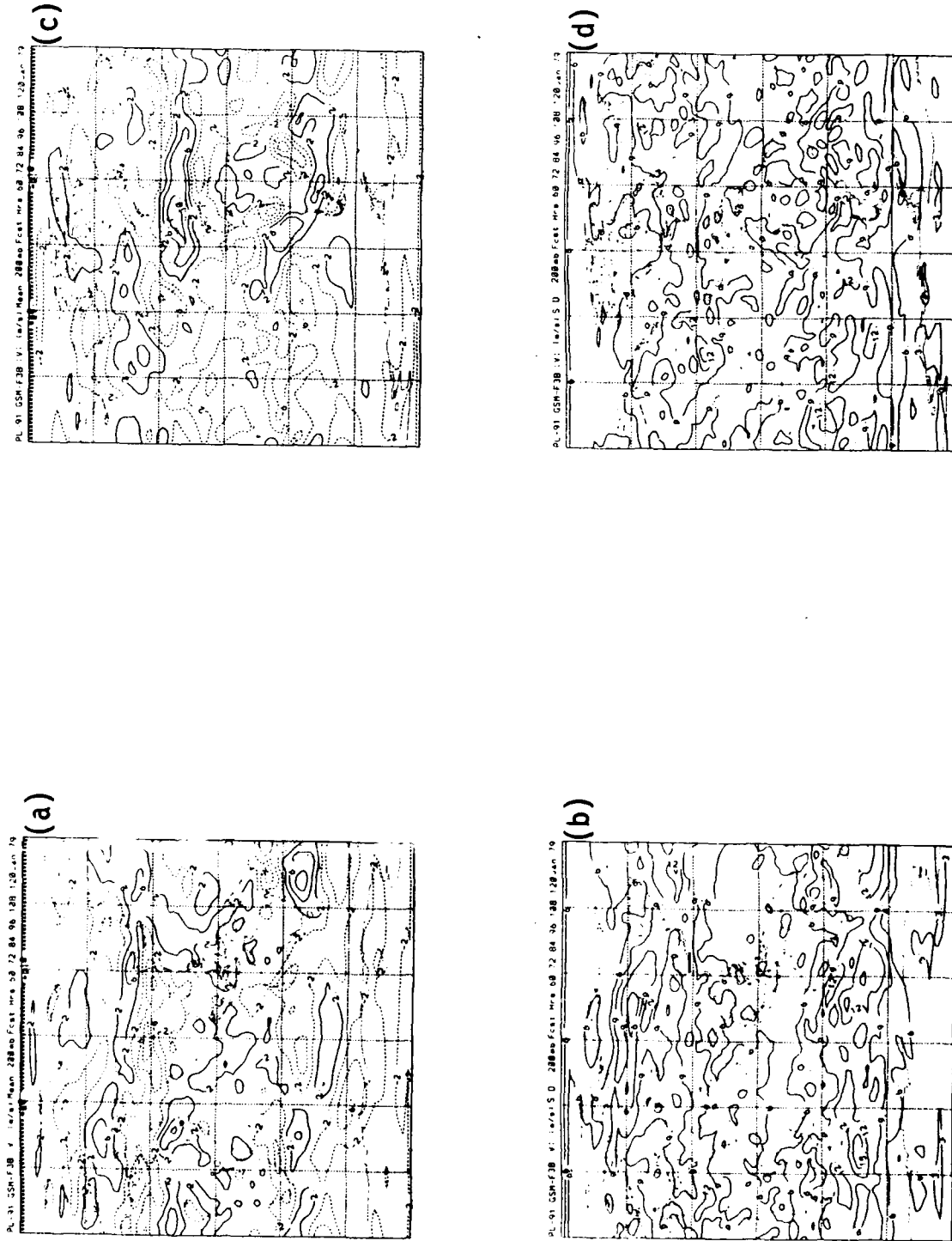


Figure 36. Hemispheric Maps of PL-91 60-120 Hour January Forecast Error of Wind Speed: (a) Eastern Hemisphere (EH), 200 mb ME, (b) EH, 200 mb SDE, (c) WH, 200 mb ME (d) WH, 200 mb SDE.

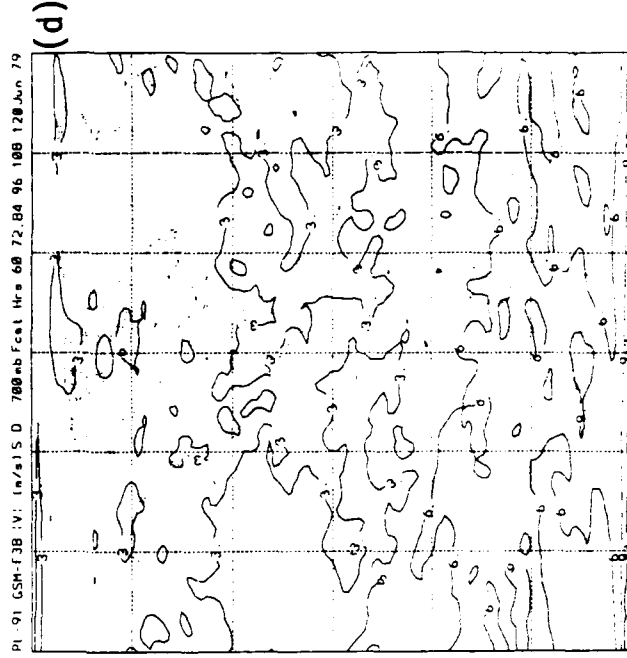
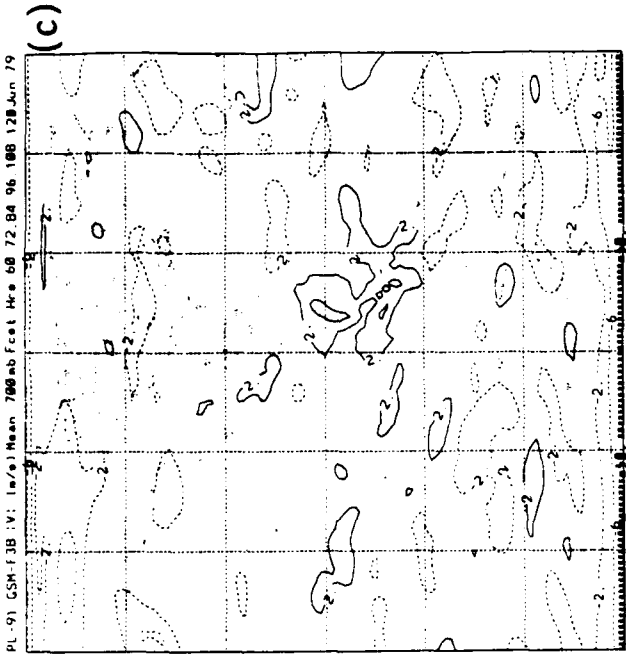
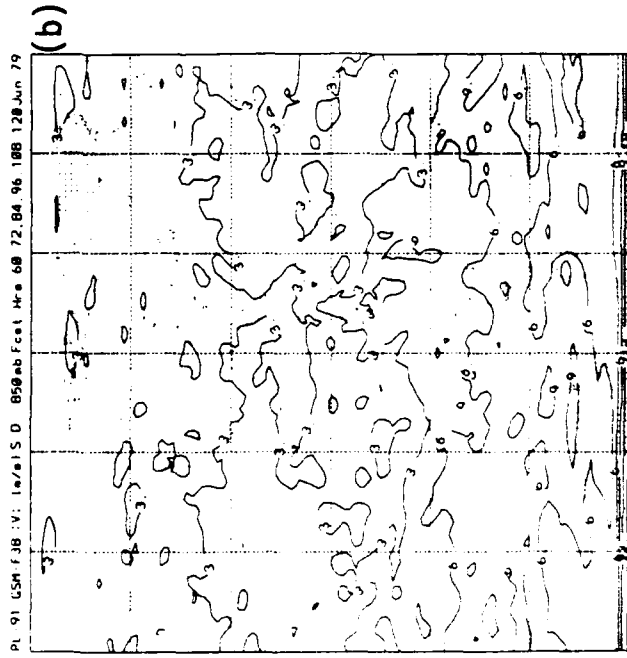
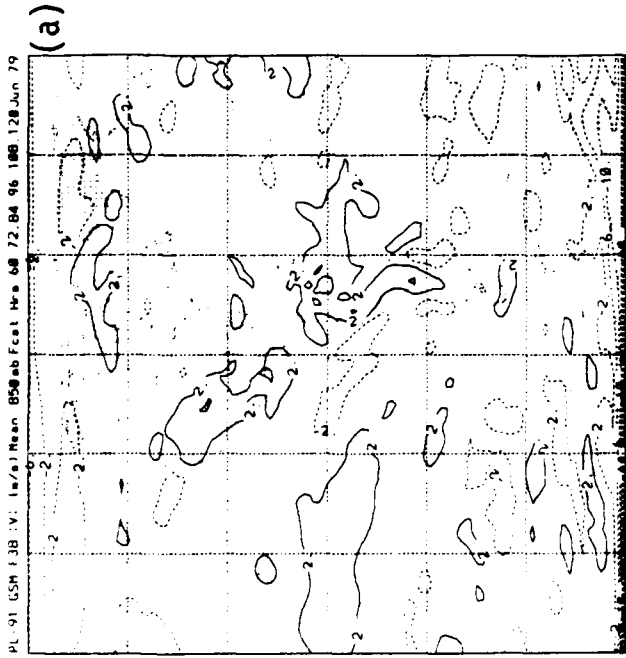


Figure 37. Hemispheric Maps of PL-91 60-120 Hour June Forecast Error of Wind Speed: WH, 850 mb ME, (b) WH, 850 mb SDE, (c) WH, 700 mb ME, (d) WH, 700 mb SDE.

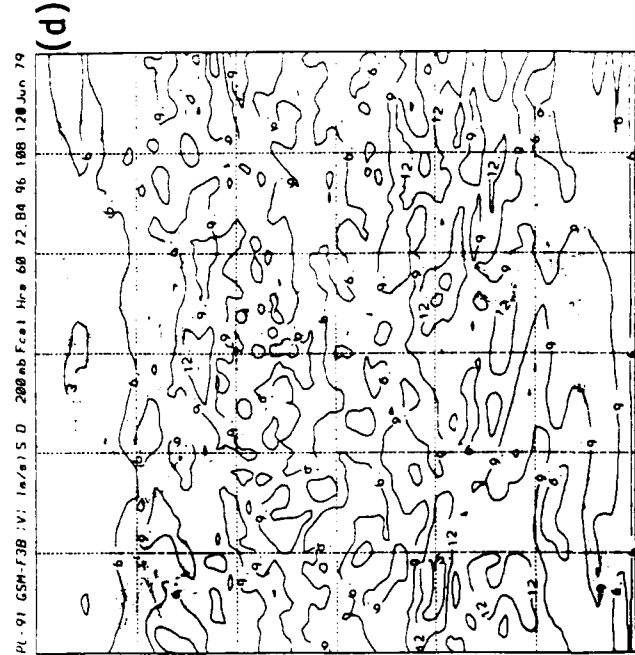
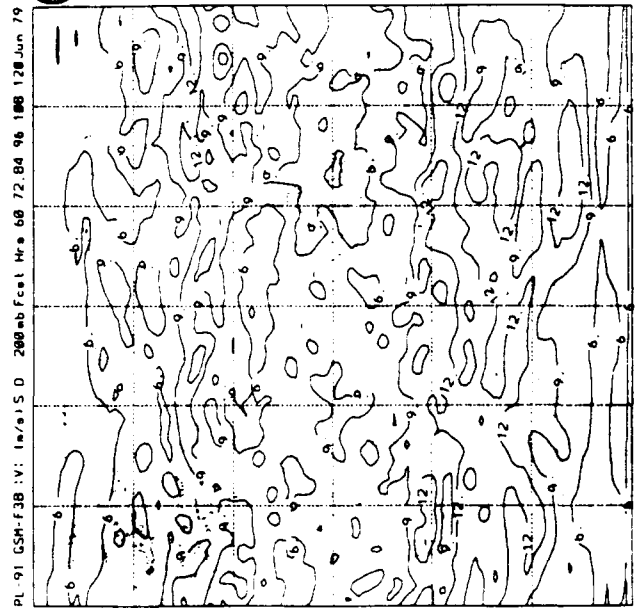
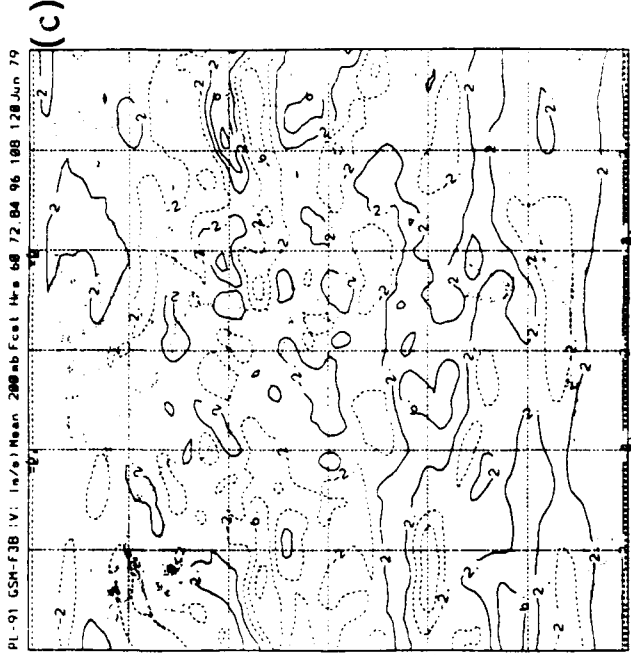
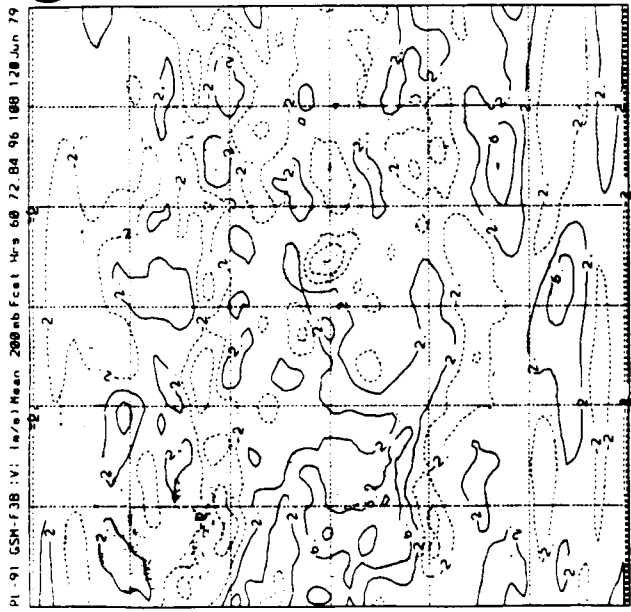


Figure 38. Same as in Figure 36 for June Forecast

not have appeared on the zonal mean cross-sections, which did not include data poleward of 80°.

In view of the hydrostatic relationship, we will show only the temperature errors to represent systematic errors in the predicted mass field. In January, we see systematic positive temperature errors over north-central Siberia, southeastern China, Kamchatka and offshore, south-central Europe, and the Mississippi River basin in the United States at 950 mb (Figure 39). Also at 950 mb, we see a band of significant cold bias extending almost the entire length of South America, much of which appears to lie just east of the Andes Mountains. The warm biases over Europe, Siberia, and Kamchatka and offshore extend up to 850 mb (Figure 40), whereas a strong region of cold bias appears at 850 mb on the Canadian-Alaskan border, while the cold bias persists east of the Andes up to 850 mb. At 200 mb (Figure 41), a large swath of significant warm bias occurs south of Australia, bordered on its south by an equally strong region of cold bias. Another patch of cold systematic bias lies to the west, with a somewhat smaller cold error region off southwestern Alaska. In June, systematic positive temperature forecast errors occur at 950 mb (Figure 42) over northeastern Europe, northwestern Africa, the Amazon basin, and are widespread over northern Canada. Significant negative temperature errors occur over India northward to the Himalayas, the Suez and Persian Gulfs, southeast of the Caspian and Aral Seas, northwestern South America, and along much of the coastline of Antarctica, especially in the region of the International Dateline. At 850 mb, a large systematic positive bias is spread over southern Africa, while at 700 mb, a somewhat lesser positive anomaly lies south of the Caspian Sea (Figure 43). At 500 mb (Figure 44), a significant warm bias (where the mean is $\geq 1K$ greater than the standard deviation) occurs over eastern Siberia, and also overspreads much of the low latitudes, especially over northern Africa, Europe, the Middle East, India, and the equatorial central Pacific. The zonal cross sections for relative humidity mean error (Figures 33, 34) pointed to a tendency of the PL-91 model to develop and sustain a dry bias at low levels (centered at 900 mb and largest in the tropics), a moist bias at 700 mb in the tropics (dry at high latitudes), a dry

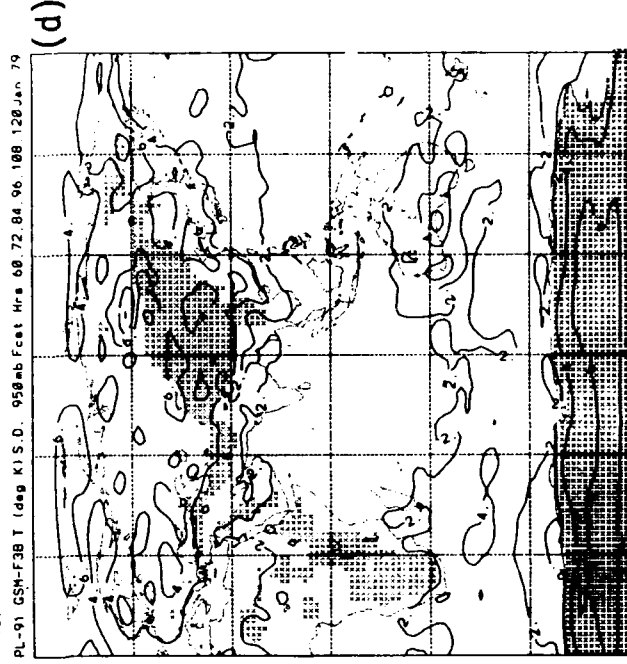
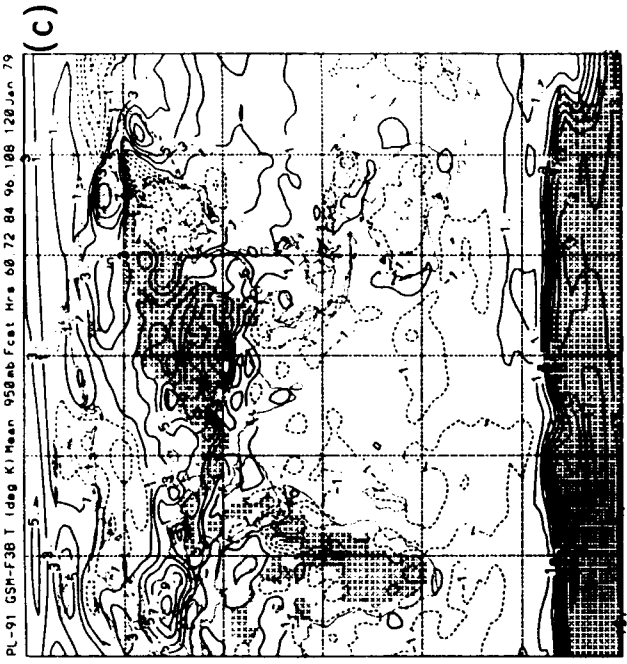
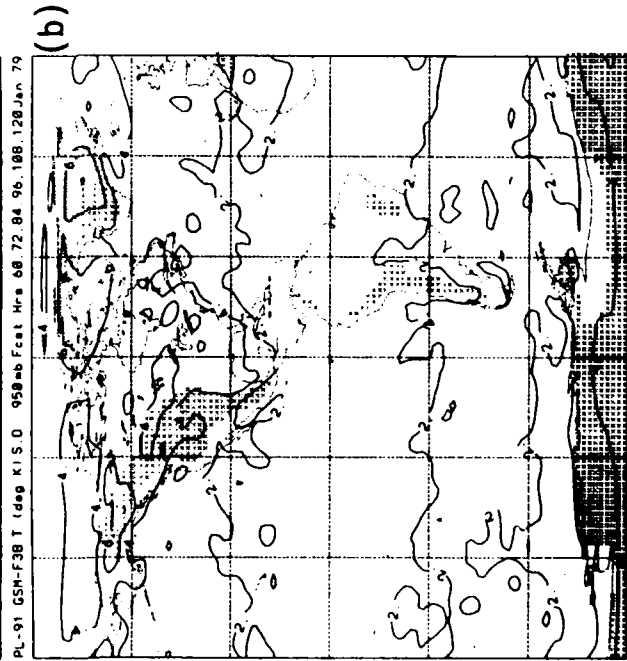
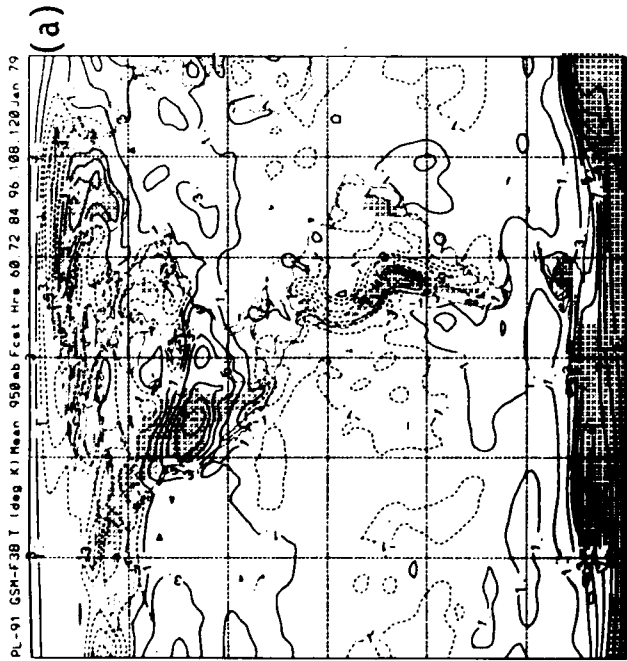


Figure 39. Hemispheric Maps of PL-91 60-120 Hour January Forecast Error of Temperature: (a) WH, 950 mb SDE, (b) WH, 950 mb ME, (c) EH, 950 mb SDE, (d) EH, 950 mb ME.

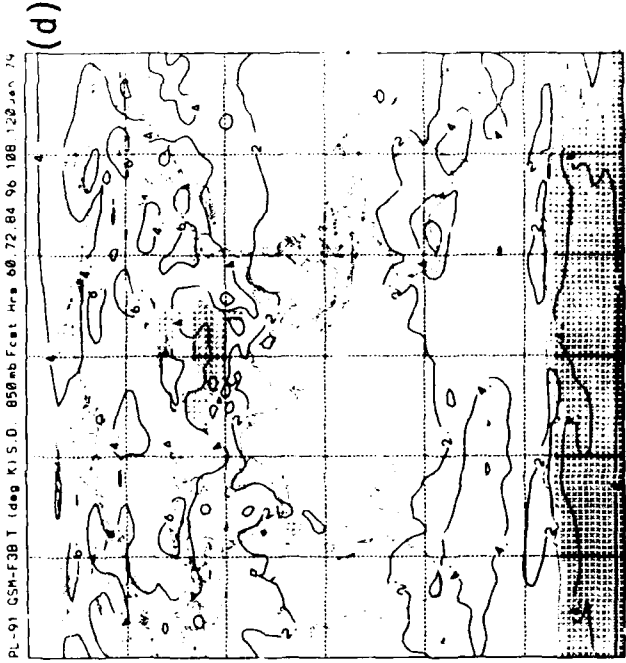
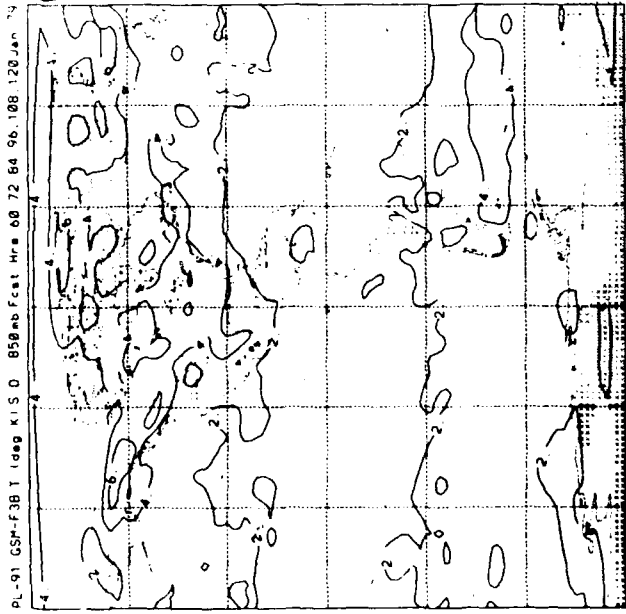
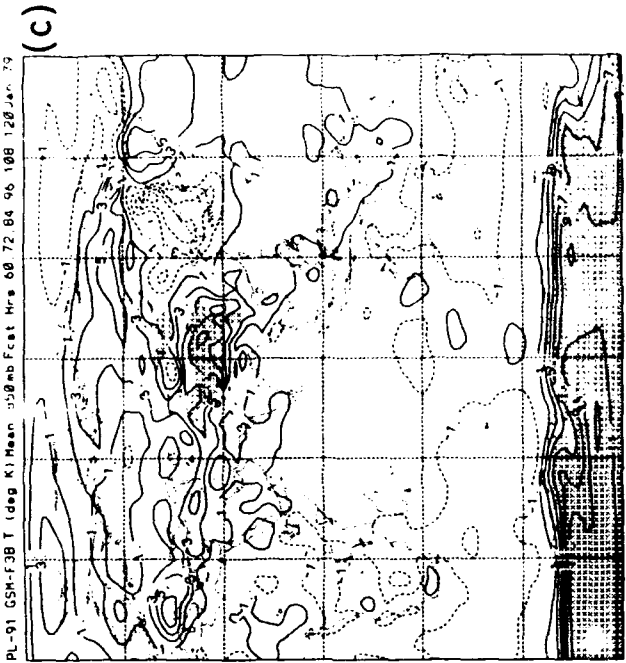
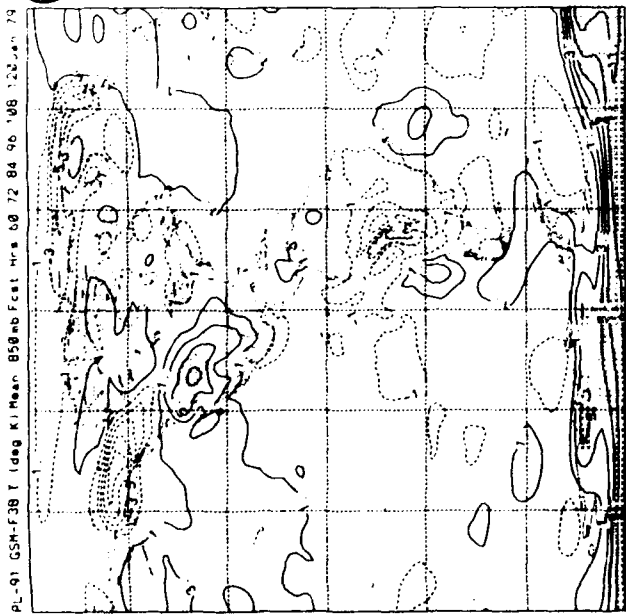


Figure 40. Same as in Figure 39 for 850 mb.

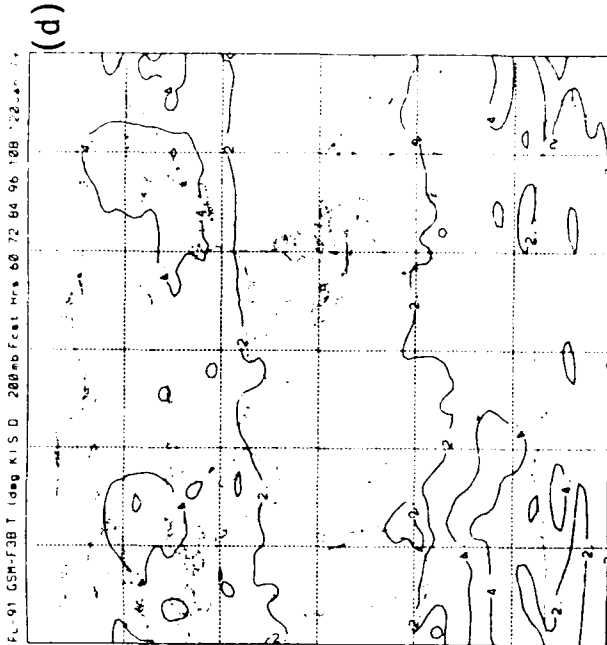
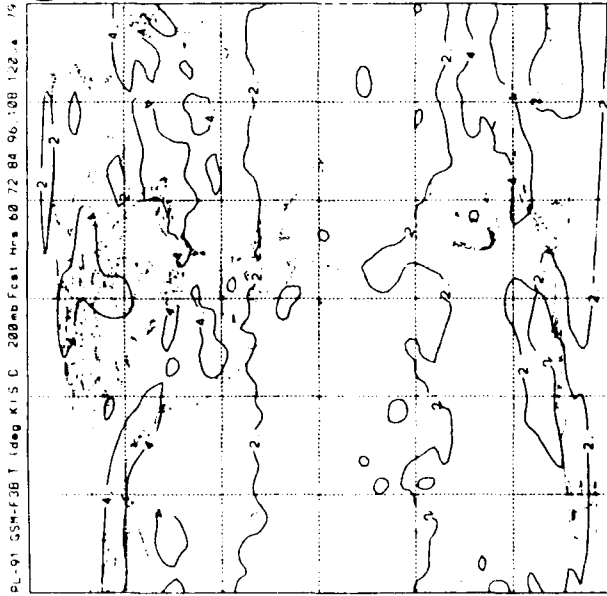
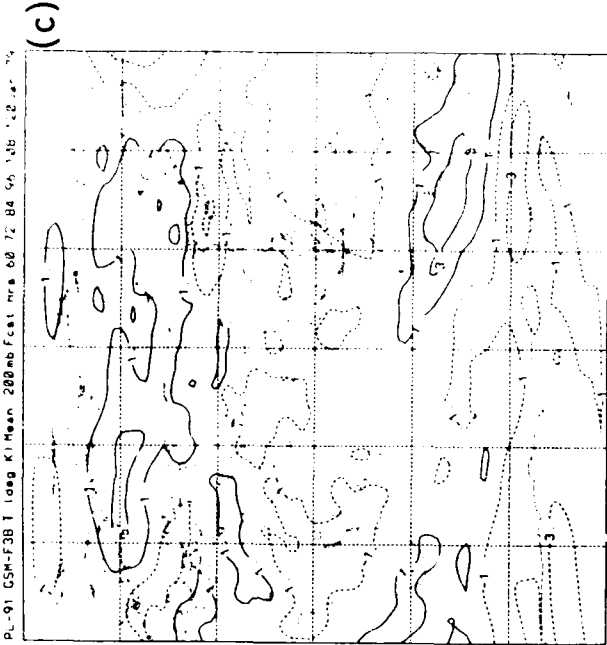
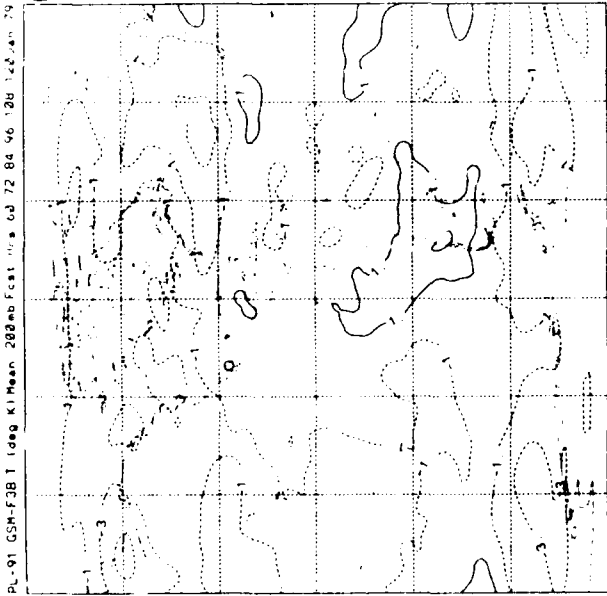


Figure 41. Same as in Figure 39 for 200 mb.

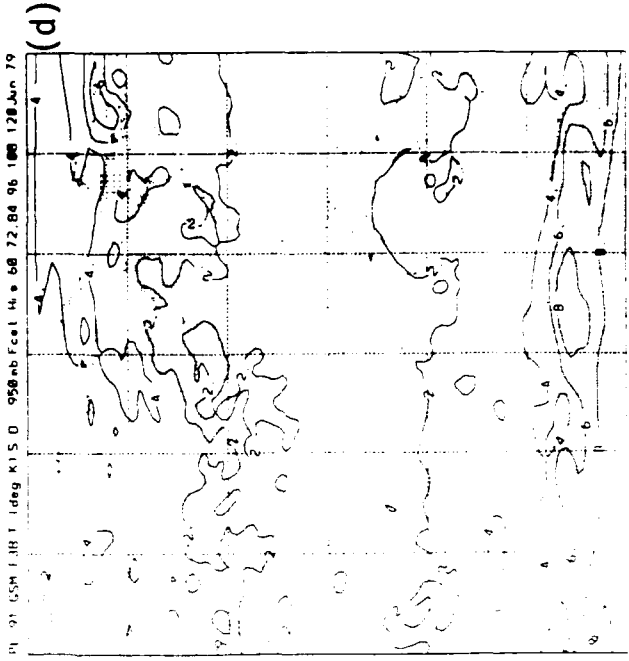
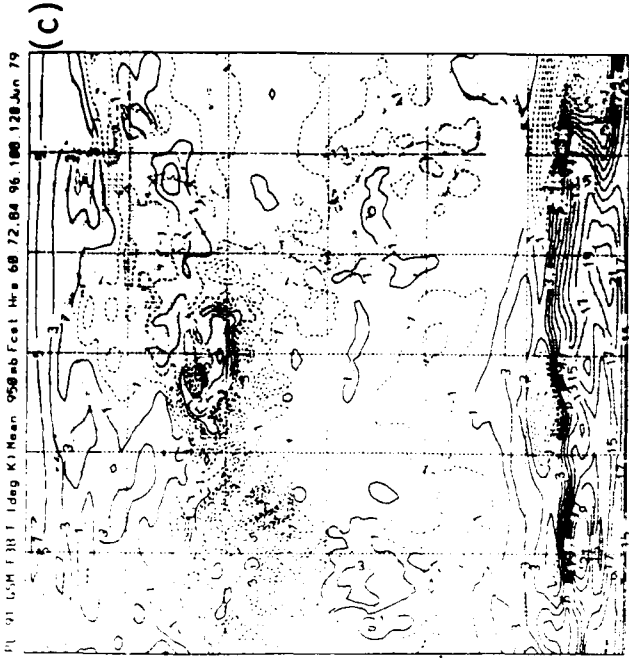
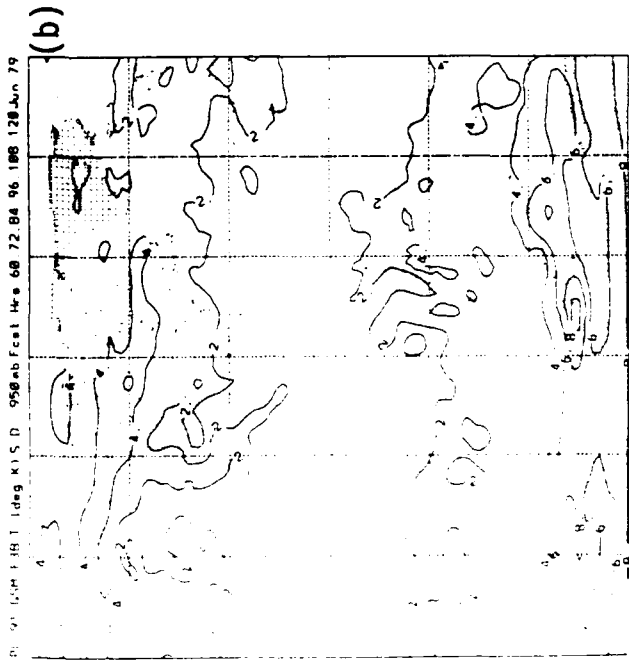
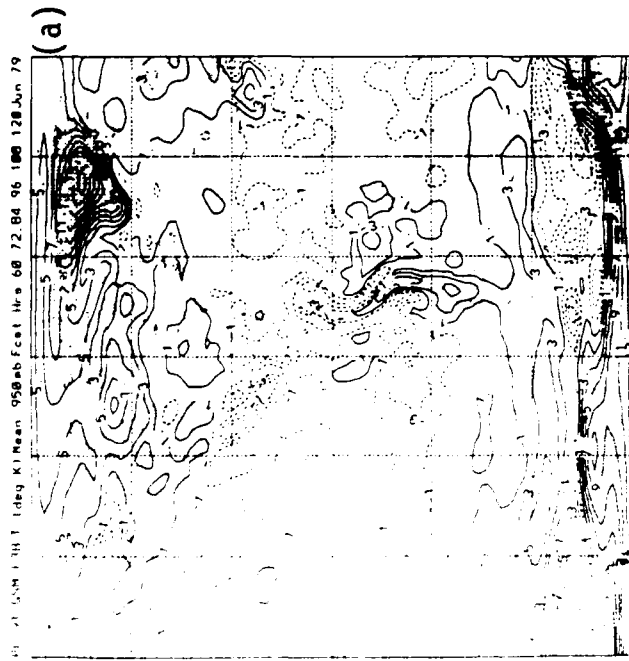


Figure 42. Same as in Figure 39 for June Forecasts.

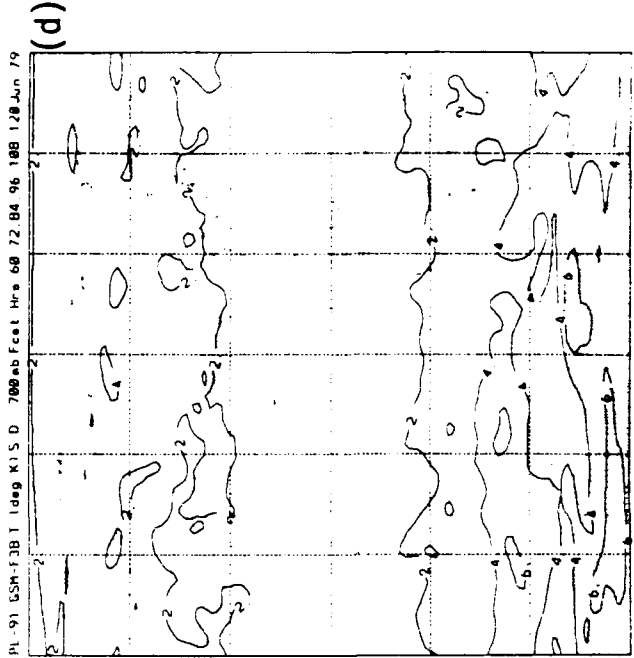
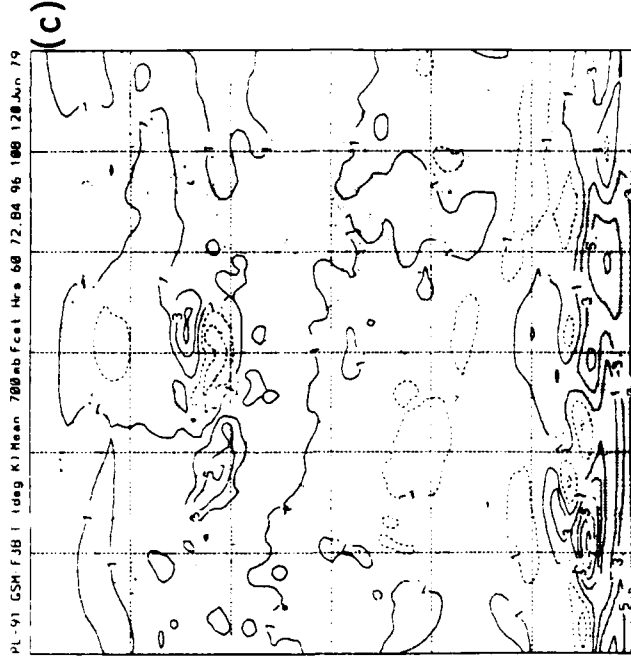
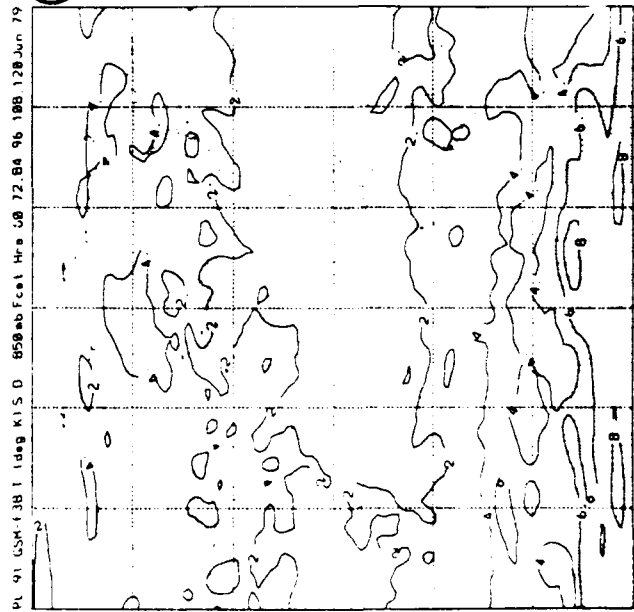
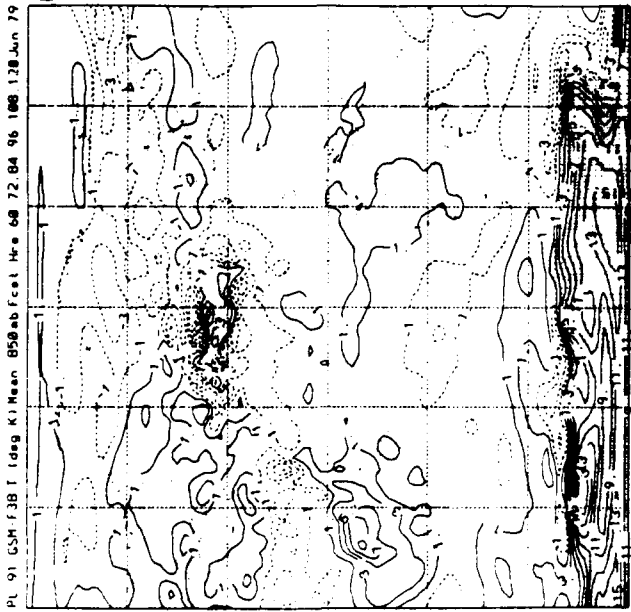


Figure 43. Hemispheric Maps of PL-91 60-120 Hour June Forecast Error of Temperature: (a) EH, 850 mb ME, (b) EH, 850 mb SDE, (c) EH, 700 mb ME, (d) EH, 700 mb SDE.

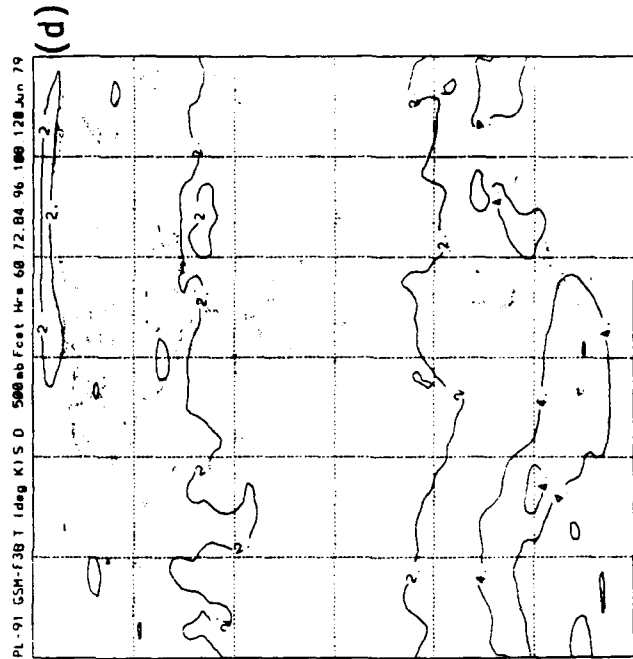
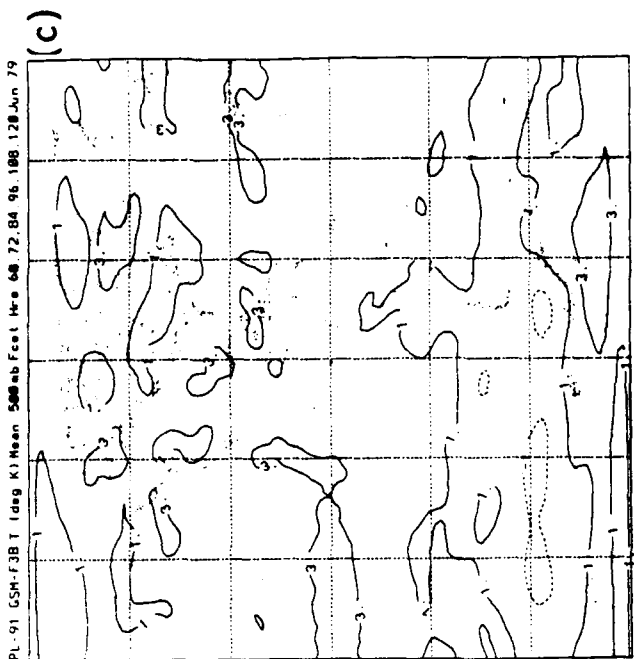
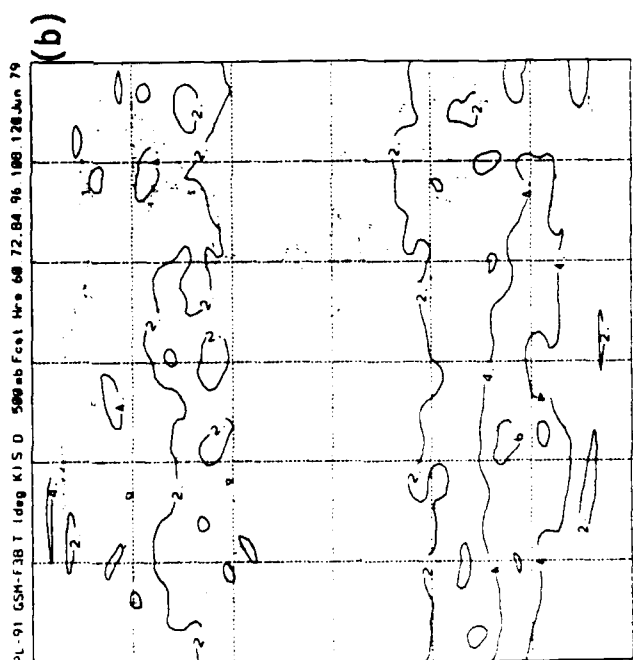
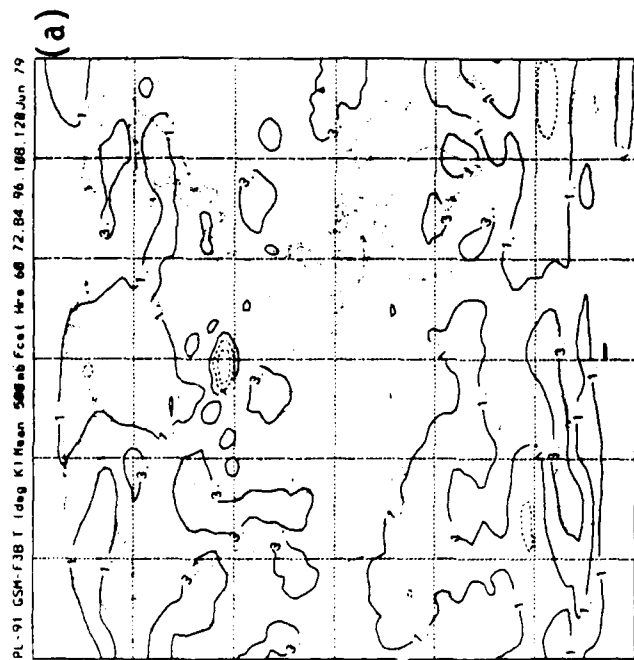


Figure 44. Hemispheric Maps of PL-91 60-120 Hour June Forecast Error of 500 mb Temperature:
 (a) EH ME, (b) EH SDE, (c) WH ME, (d) WH SDE.

bias again at 400 mb, and a moist bias at and above 300 mb. The error maps for relative humidity (not shown) show that these errors are not concentrated in certain locales as are temperature and winds, but are widespread on each isobaric surface. In almost all instances, the standard deviation of the error is greater than the mean.

We also drew maps of mean and standard deviation of the forecast error of mean sea level pressure (not shown). With only two localized exceptions, the mean error was less than the standard deviation in areas away from high terrain. There were no signs of a systematic loss or gain of mass in localized areas. In January, the standard deviation of the error (highest in the midlatitudes) was nearly the same in both Northern and Southern Hemispheres. However, in June the standard deviation of the mean sea level pressure error in the Southern Hemisphere is more than twice that of the Northern Hemisphere, and is somewhat greater than that of the January Northern Hemisphere.

4.1.4 REGIONAL STATISTICS

We now focus our attention on two limited regions. We calculated the error statistics for GWC84, GL-89, and PL-91 over two limited regions, the central Pacific Ocean and North America. The two study "windows" are shown in Figure 45. The regions were chosen for their geographic diversity so that much could be learned about model performance by considering two differing climatic regions.

For the measures of performance on an isobaric surface, we employ mean error (bias) and root-mean-square error (RMSE) over each window. Both the mean errors and RMSEs are the weighted averages of individual gridpoint values. However, in the calculation of the correlation coefficient between a model simulation and the corresponding analysis, all grid points in a window are weighted equally. This was done to better represent the degree of similitude seen on the maps of distribution where no account was given of max factor. The statistics are calculated and displayed separately for each individual case. Figures 46 and 47 depict the bias and RMSE of temperature for the central Pacific window, and Figures 48 and 49 display

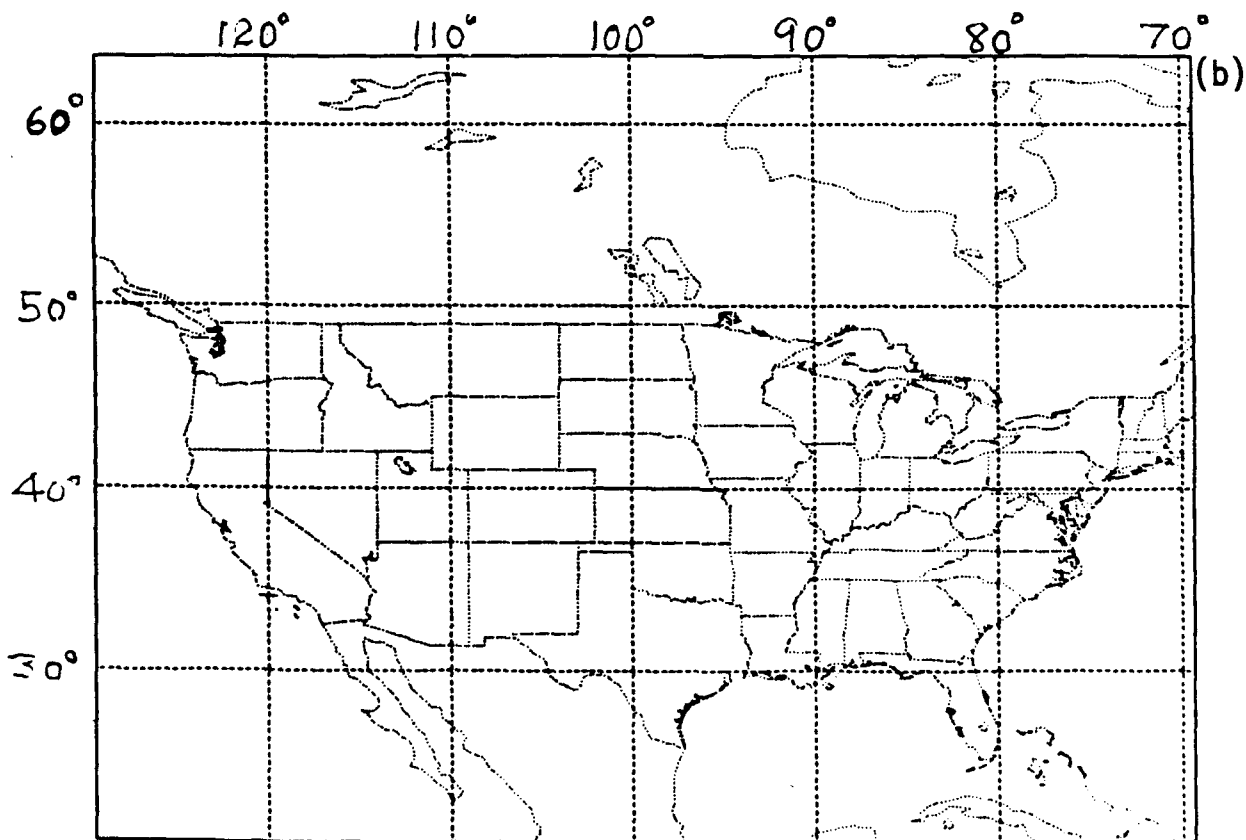
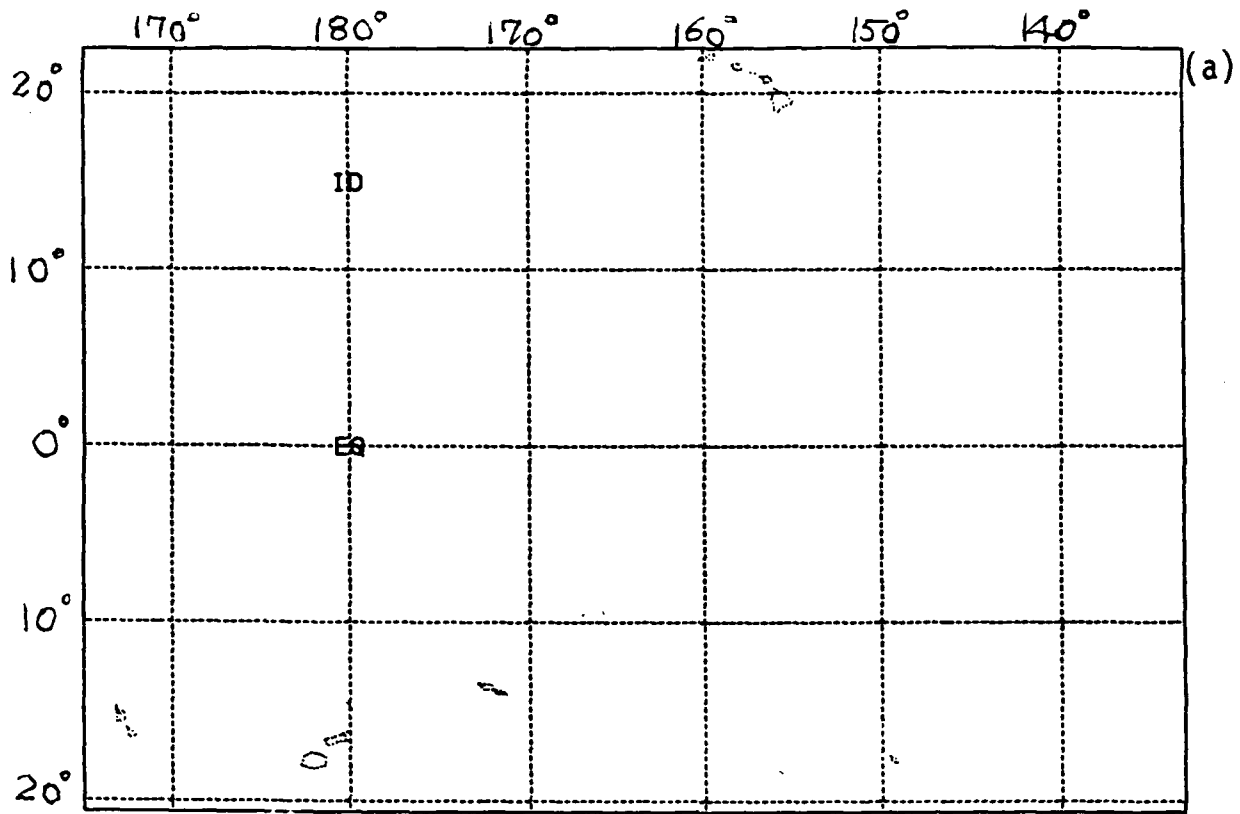


Figure 45. Domain of the (a) Central Pacific Window, and (b) North American Window.

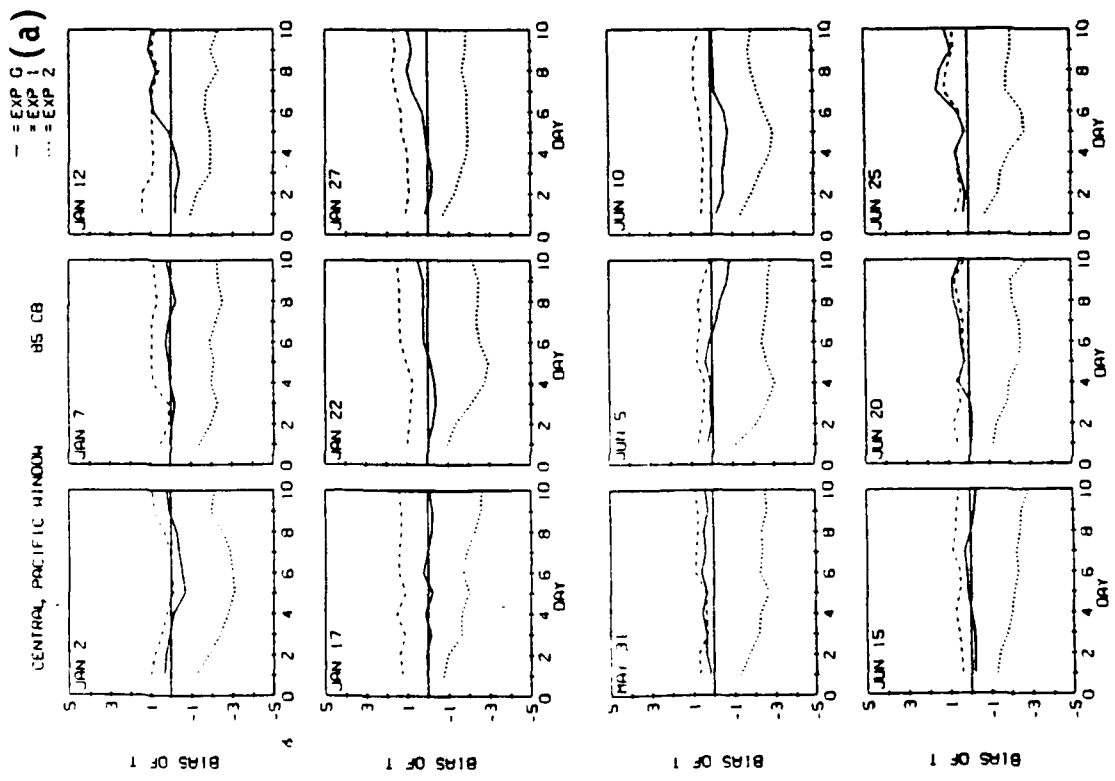
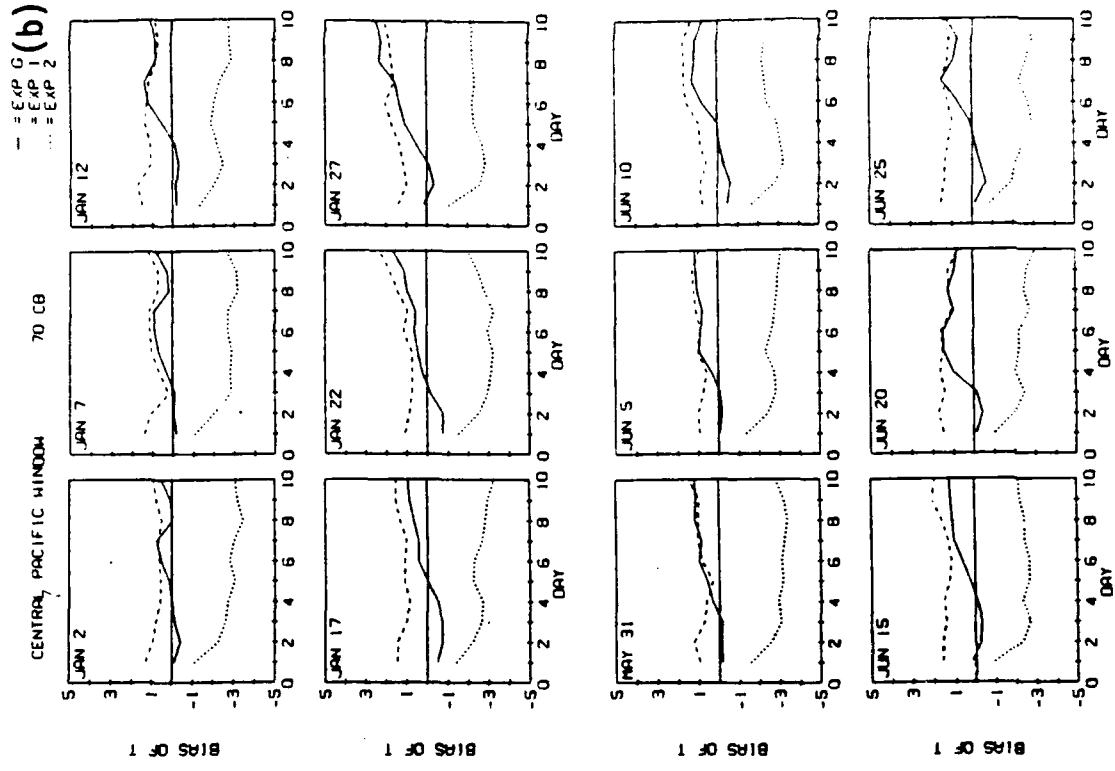


Figure 46. Central Pacific Temperature Bias of January and June Forecasts of (a) 850 mb, (b) 700 mb, (c) 500 mb, and (d) 300 mb.

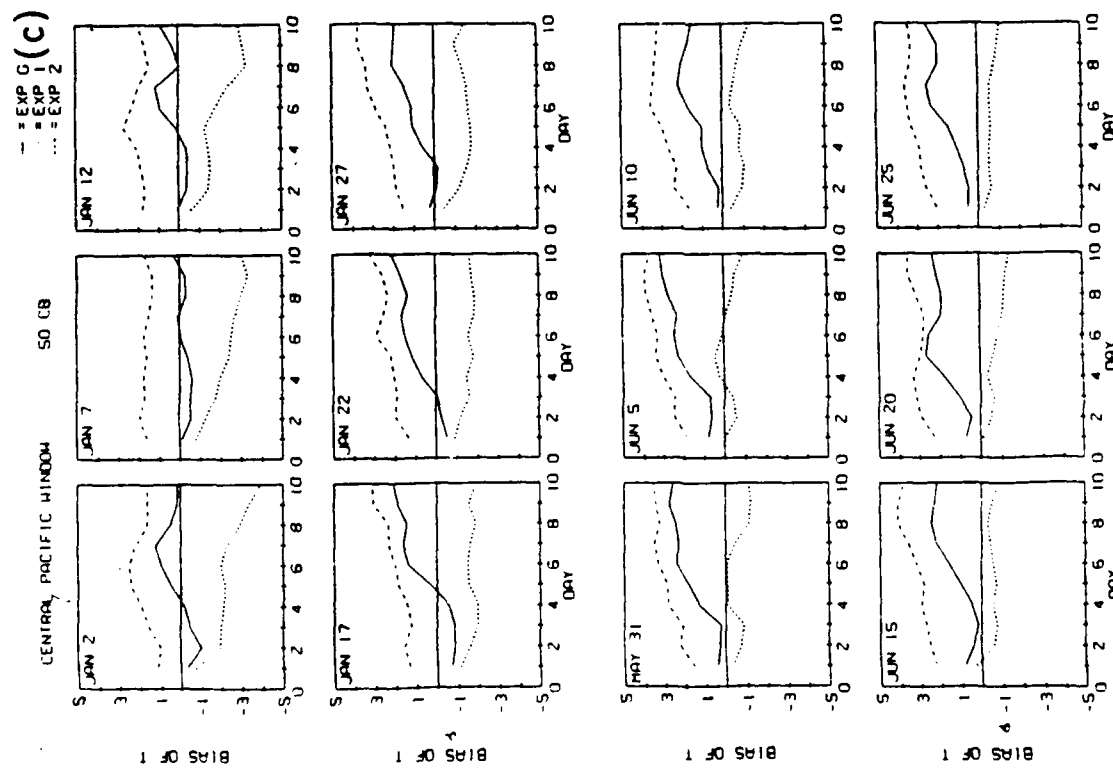
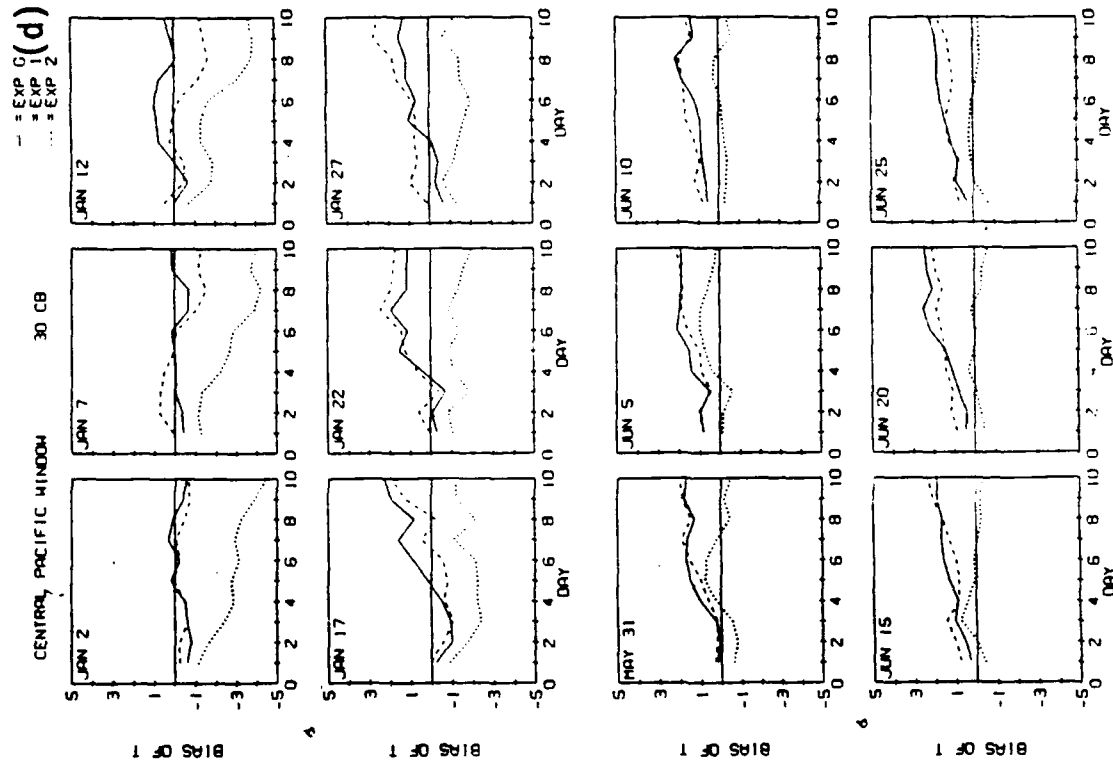


Figure 46. Central Pacific Temperature Bias of January and June Forecasts of (a) 850 mb, (b) 700 mb, (c) 500 mb, and (d) 300 mb.

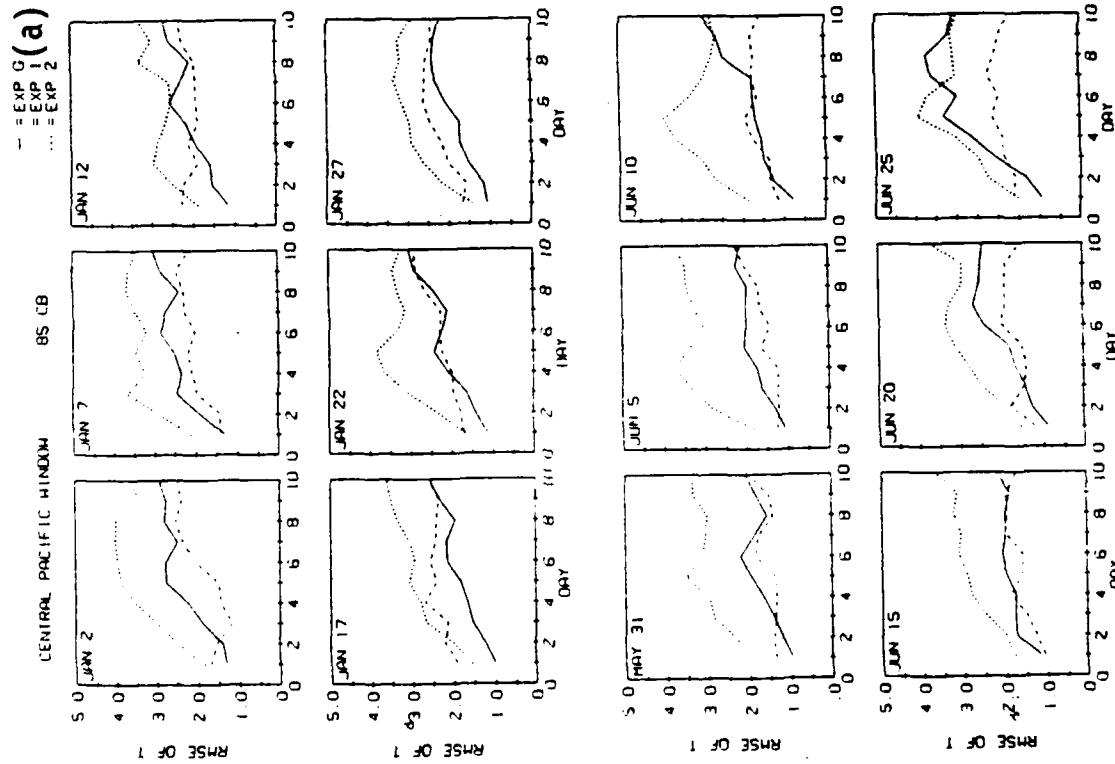
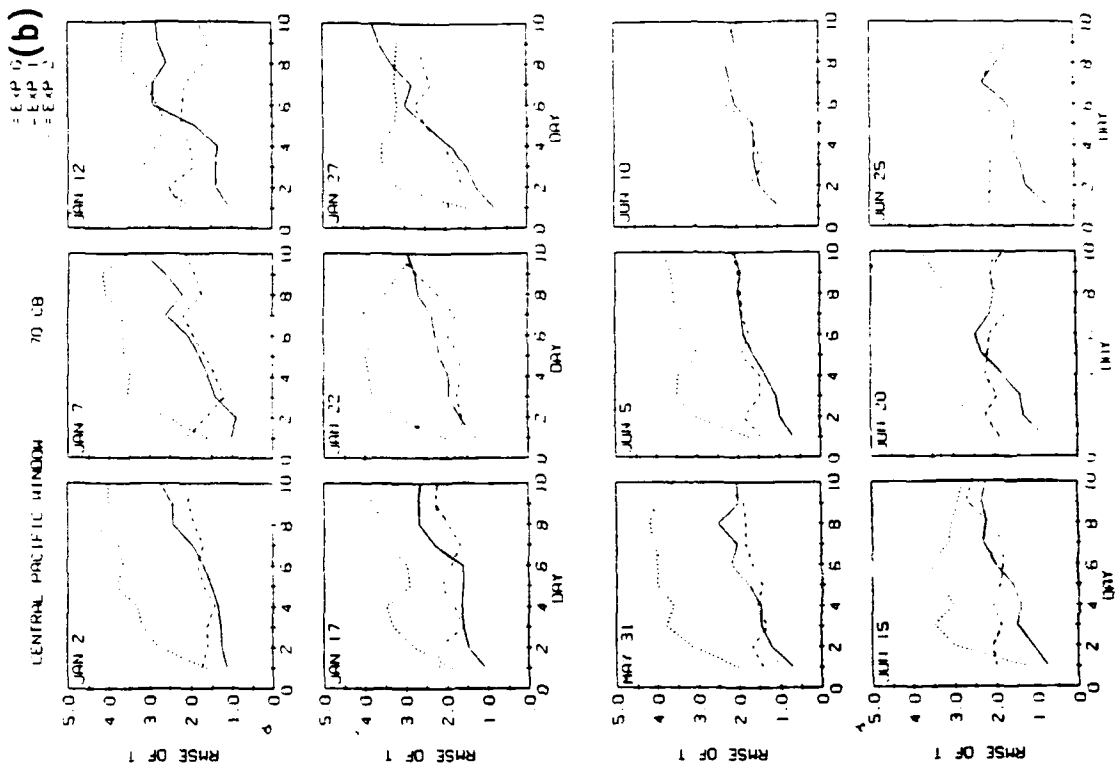


Figure 47. Same as in Figure 46 for RMSE.

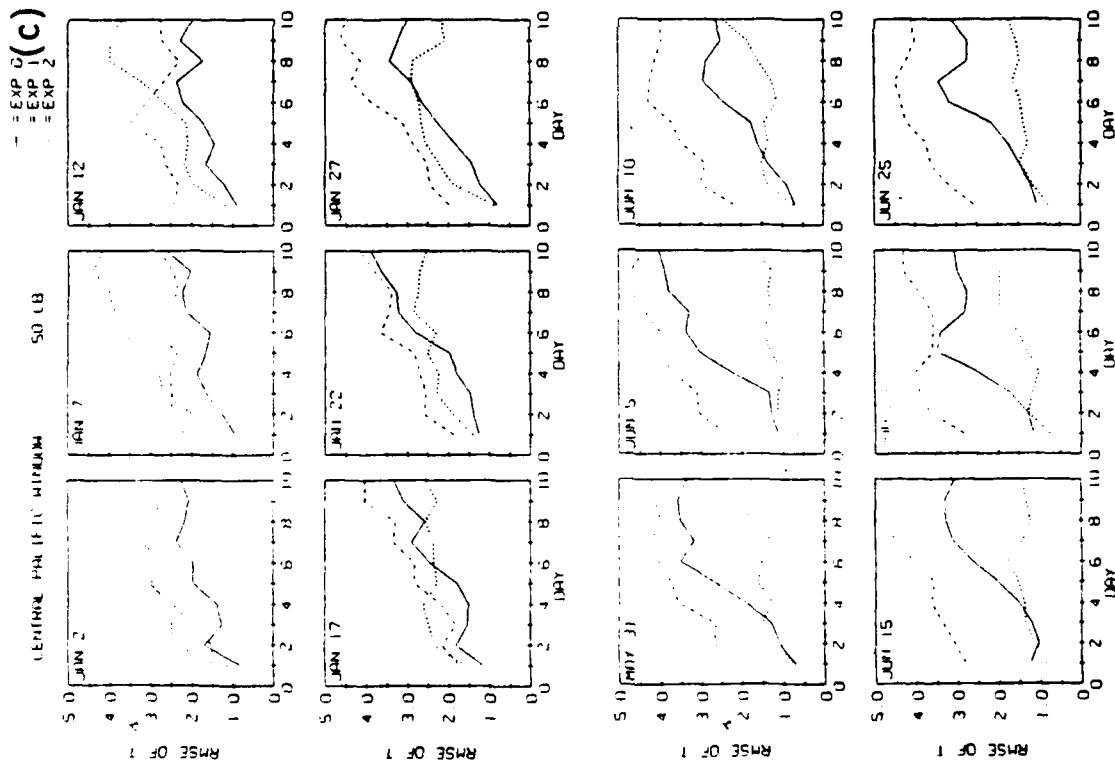
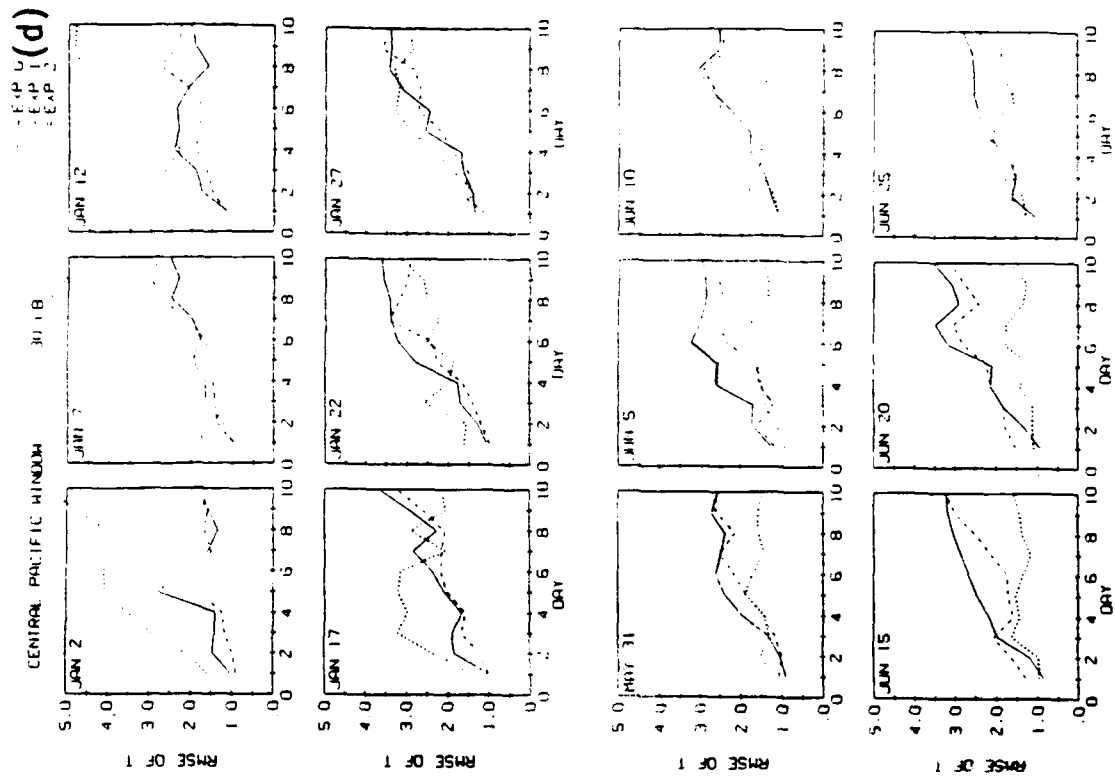


Figure 47. Same as in Figure 46 for RMSE.

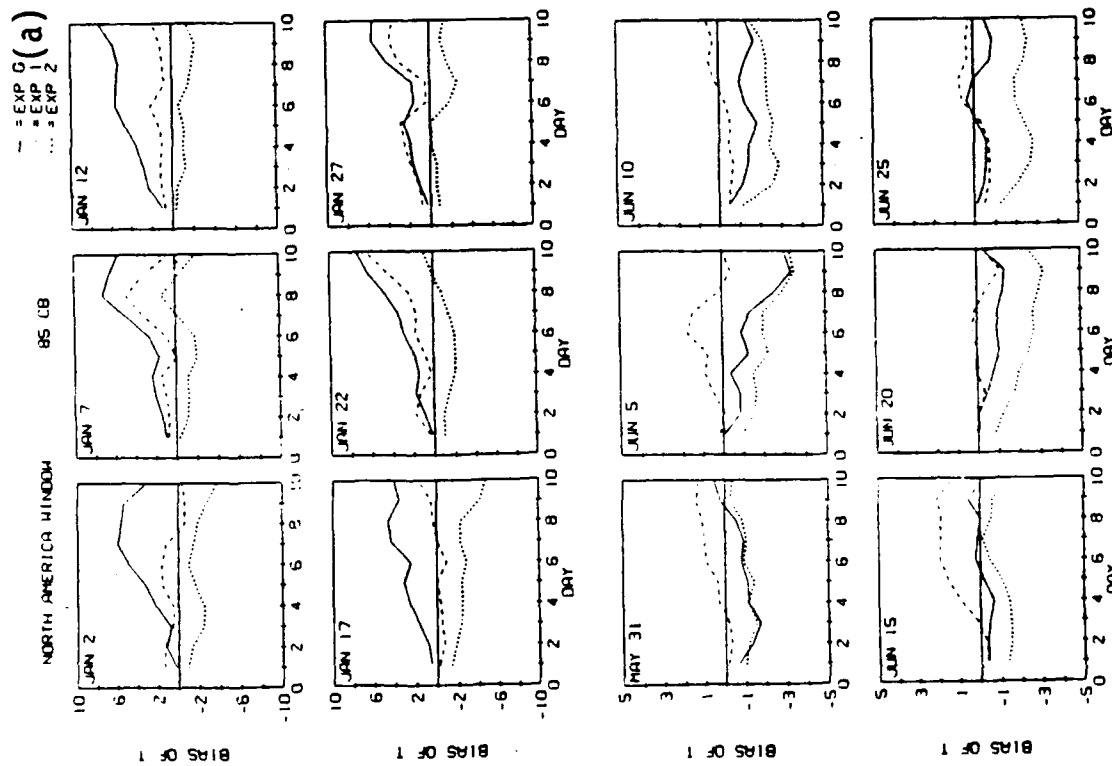
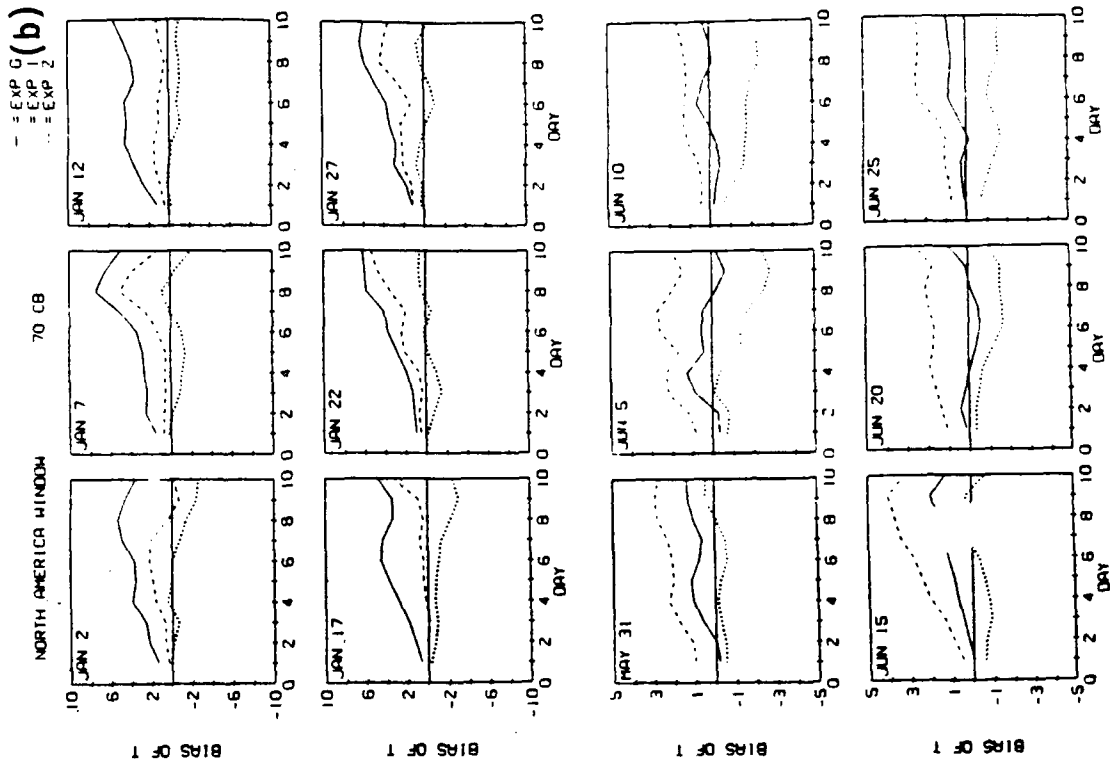


Figure 48. Same as in Figure 46 for North American Window.

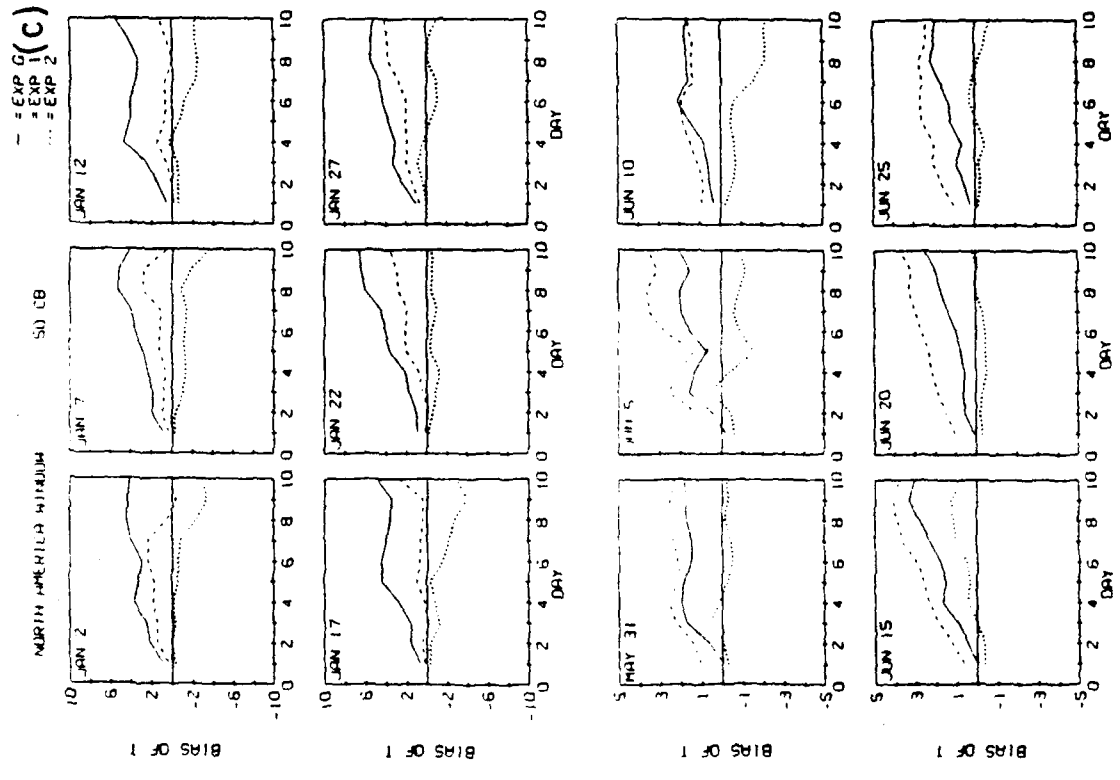
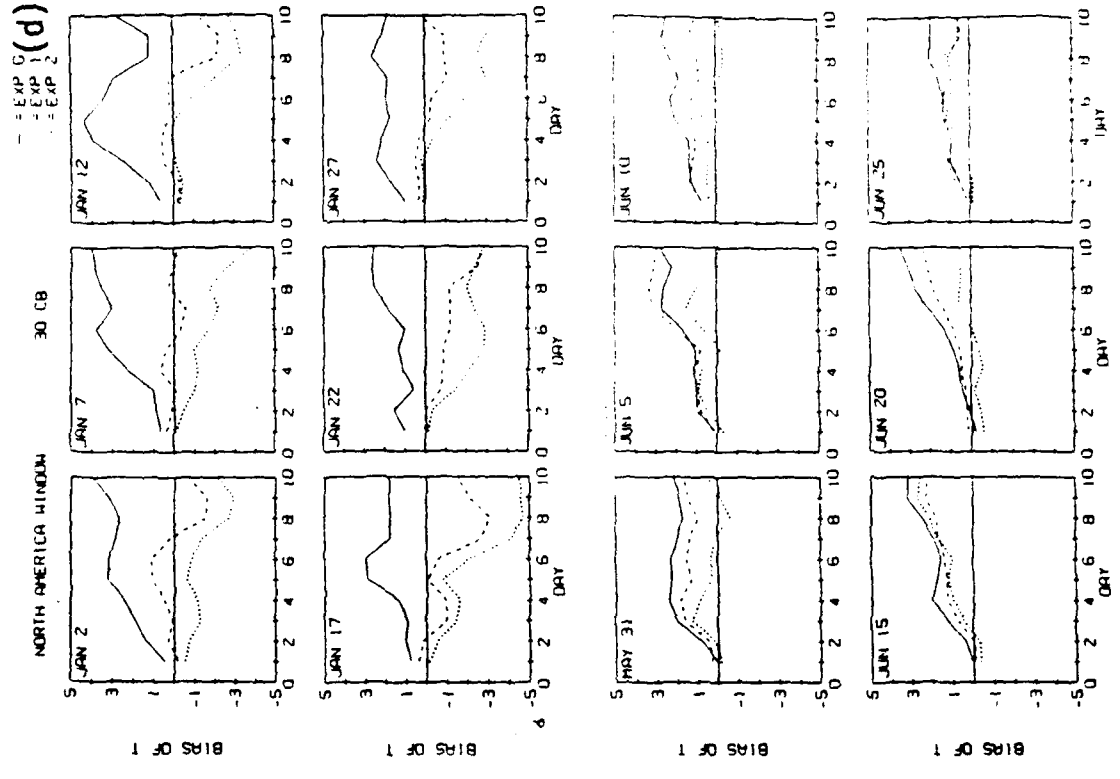


Figure 48. Same as in Figure 46 for North American Window.

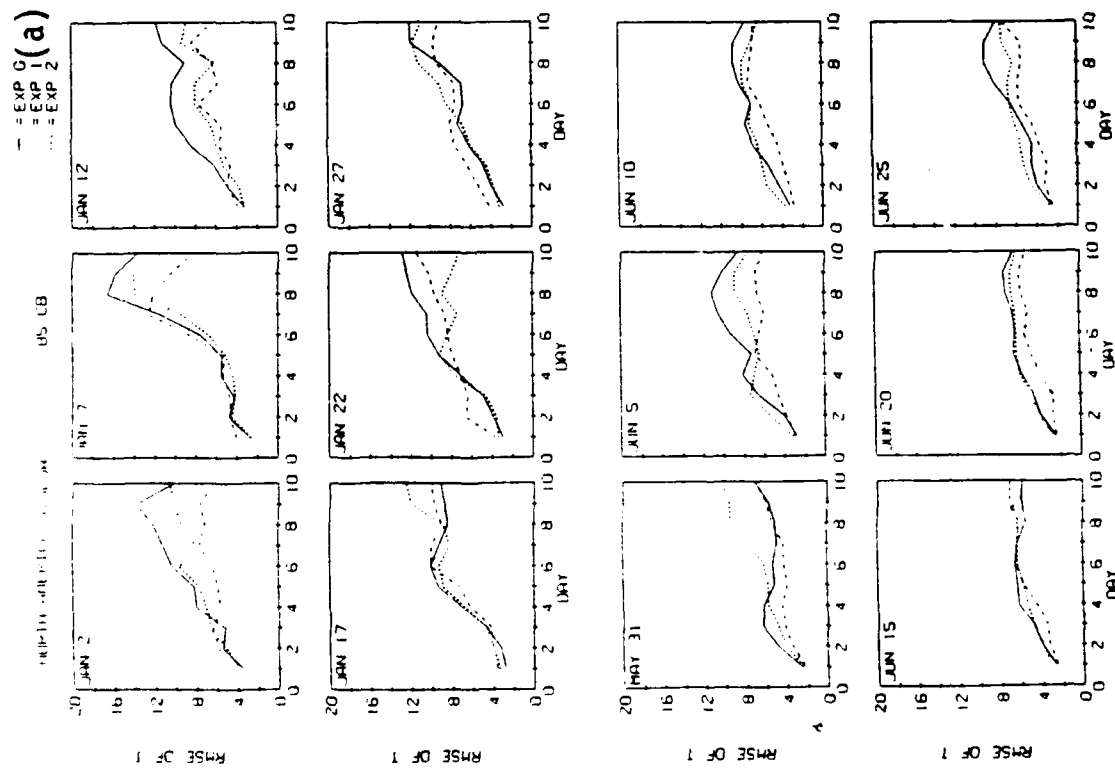
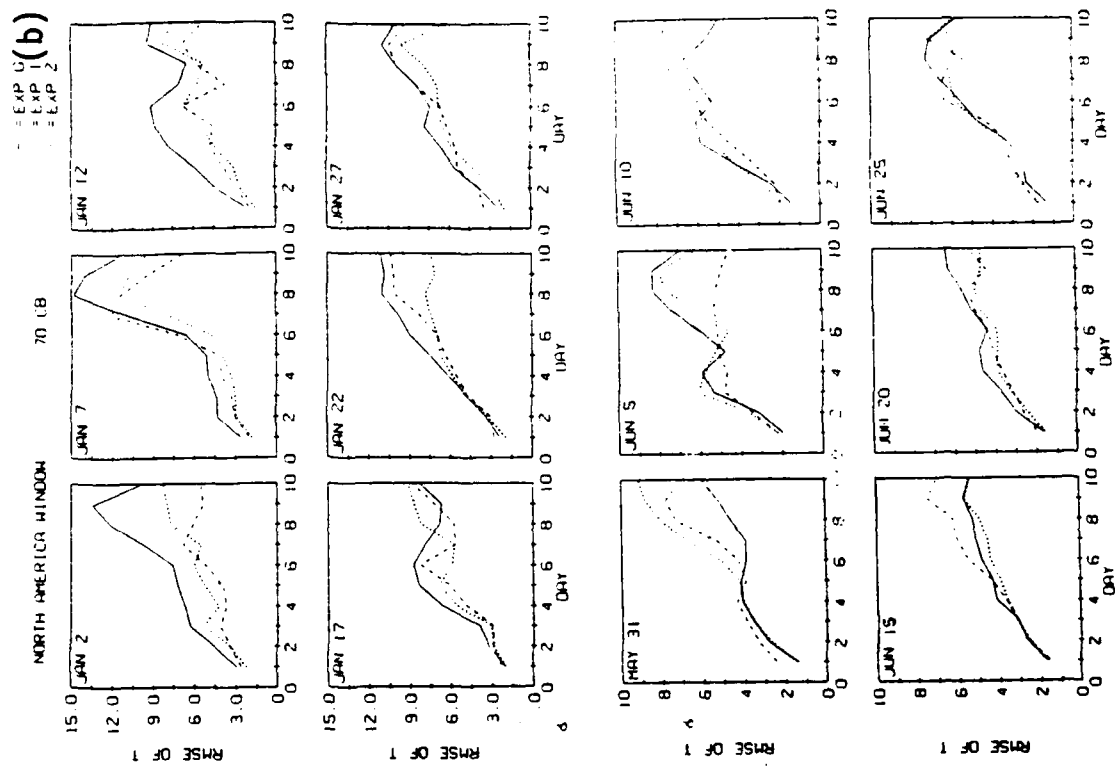


Figure 49. Same as in Figure 48 for RMSE.

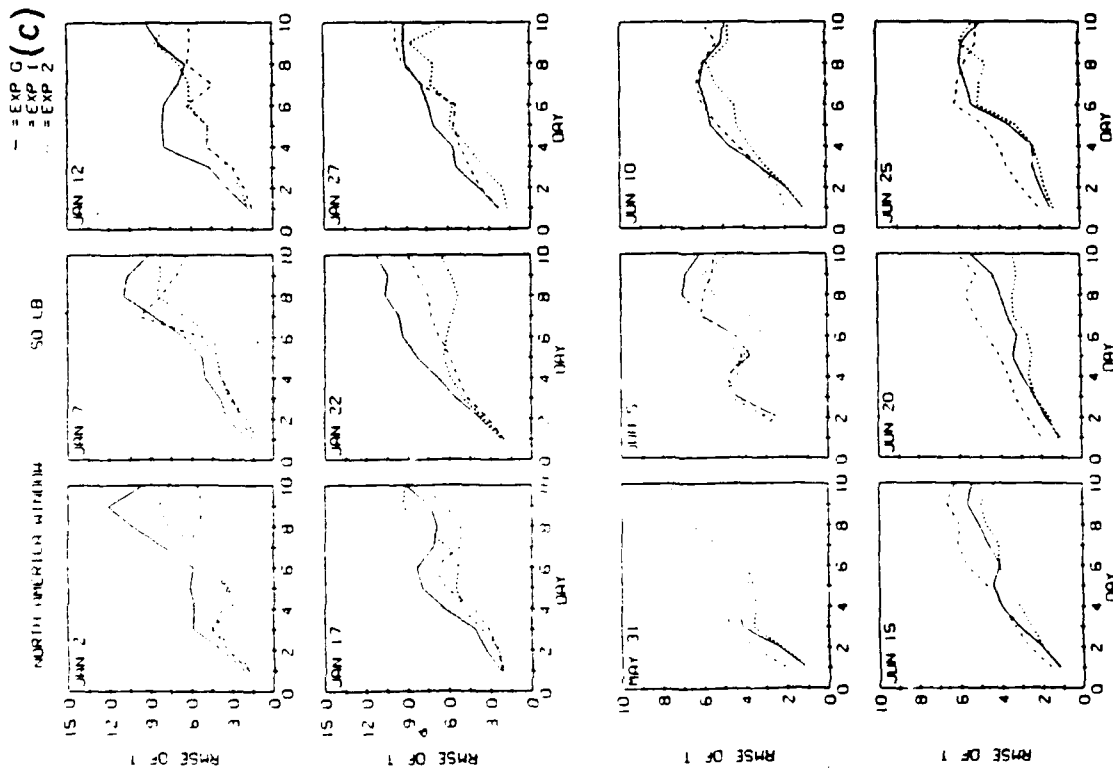
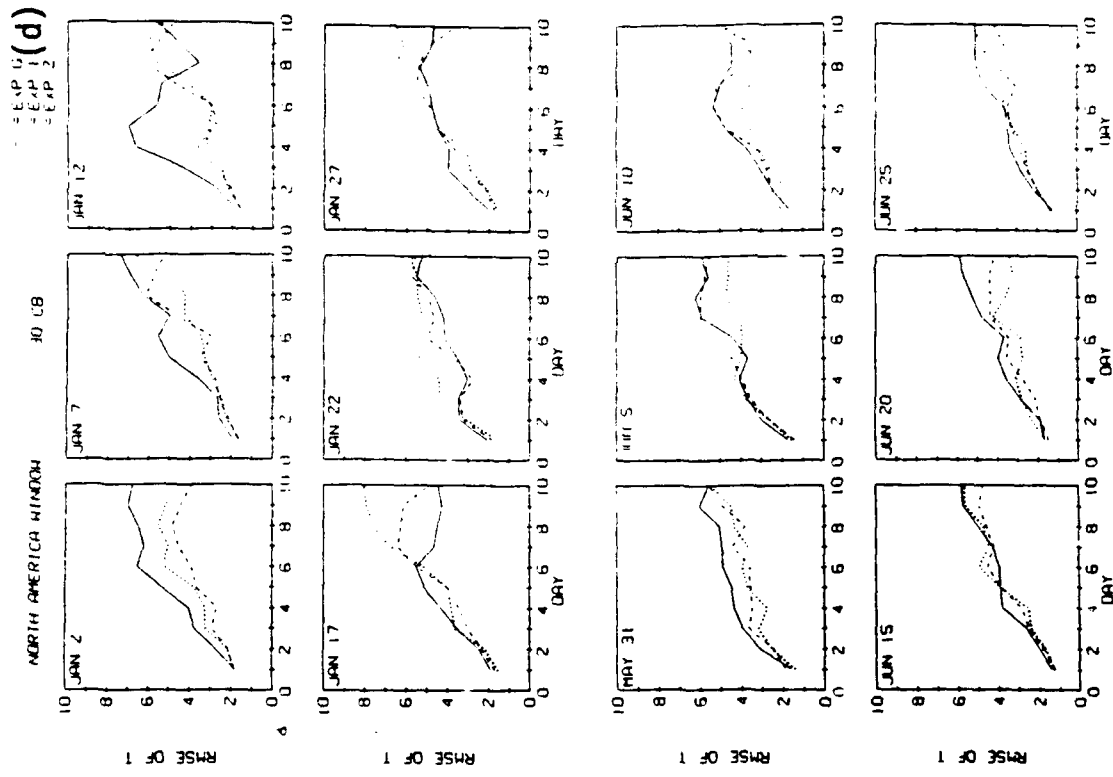


Figure 49. Same as in Figure 48 for RMSE.

the same for the North American window. In these figures, the following associations apply: EXP G = GWC84, EXP 1 = GL-89, and EXP 2 = PL-91. Figure 50 shows values of the correlation coefficients for the temperature forecasts. Plots for the bias of relative humidity are shown in Figures 51 and 52. RMSE for relative humidity quickly degrades to levels greater than 30% for all model versions and are not shown.

4.2 Evaluation of Forecasts in the Planetary Boundary Layer

4.2.1 REGIONAL COMPARISONS WITH FGGE III-b ANALYSES

In this section, we consider the impact of the two most recent enhancements to the planetary boundary layer (PBL) parameterization in the PL GSM. As seen in Table 1, the PL-91 model added spatially varying soil and vegetation type descriptors and a gravity wave drag parameterization. Since these additions are likely to have an impact in the low levels of the model, we focus on the 90 kPa (900 mb) isobaric surface for this discussion. In addition, we compare the impact on the temperature field in two versions of the PL GSM that will isolate the soil-vegetation and gravity wave drag effects. RAD-0 is a model version very much like GL-89 but using only a clear-sky (no clouds) radiation. PBL-2G is RAD-0 but with the new soil-vegetation and gravity wave drag effects included. Figures 53 and 54 show the forecast-analysis temperature difference between these two versions for two days of a single January case over North America.

4.2.2 PERFORMANCE OF THE PBL PREDICTIONS AT MODEL GRIDPOINTS

The PL-91 predictions and the FGGE III-b analyses were processed in such a way as to facilitate comparison on the model's Gaussian grid at several locations. The process was carried out as follows. The analyses for all six January and June PL-91 cases were transformed from 30 rhomboidal spectral form to the model's Gaussian grid (96 equally spaced longitude points at 3.75° longitude, 76 Gaussian latitudes at

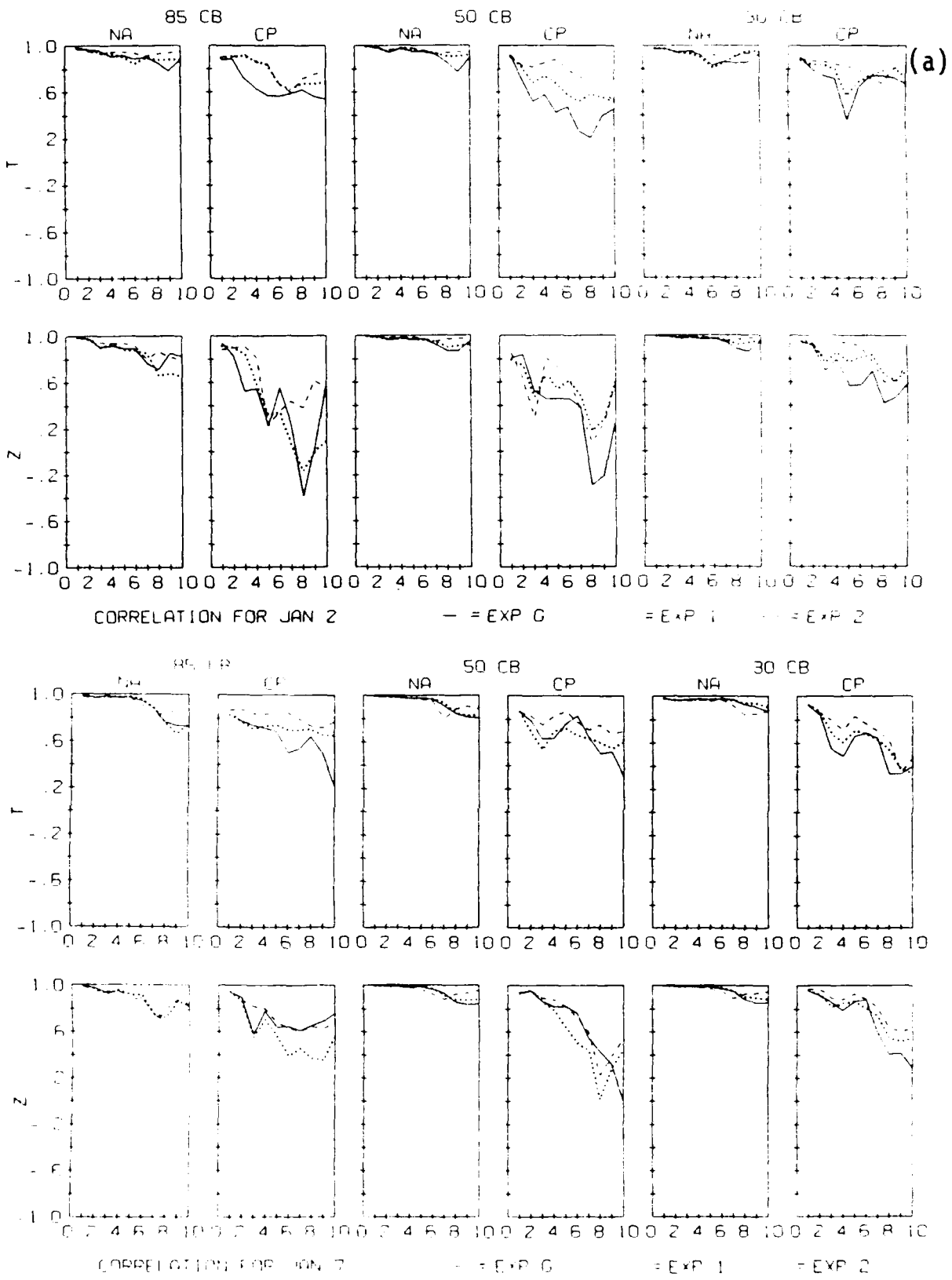


Figure 50. Spatial Correlation of Temperature and Geopotential Height Forecasts with FGGE III-b Analyses for North American (NA) and Central Pacific (CP) Windows at 850, 500, and 300 mb: (a)-(c) January, and (d)-(f) June.

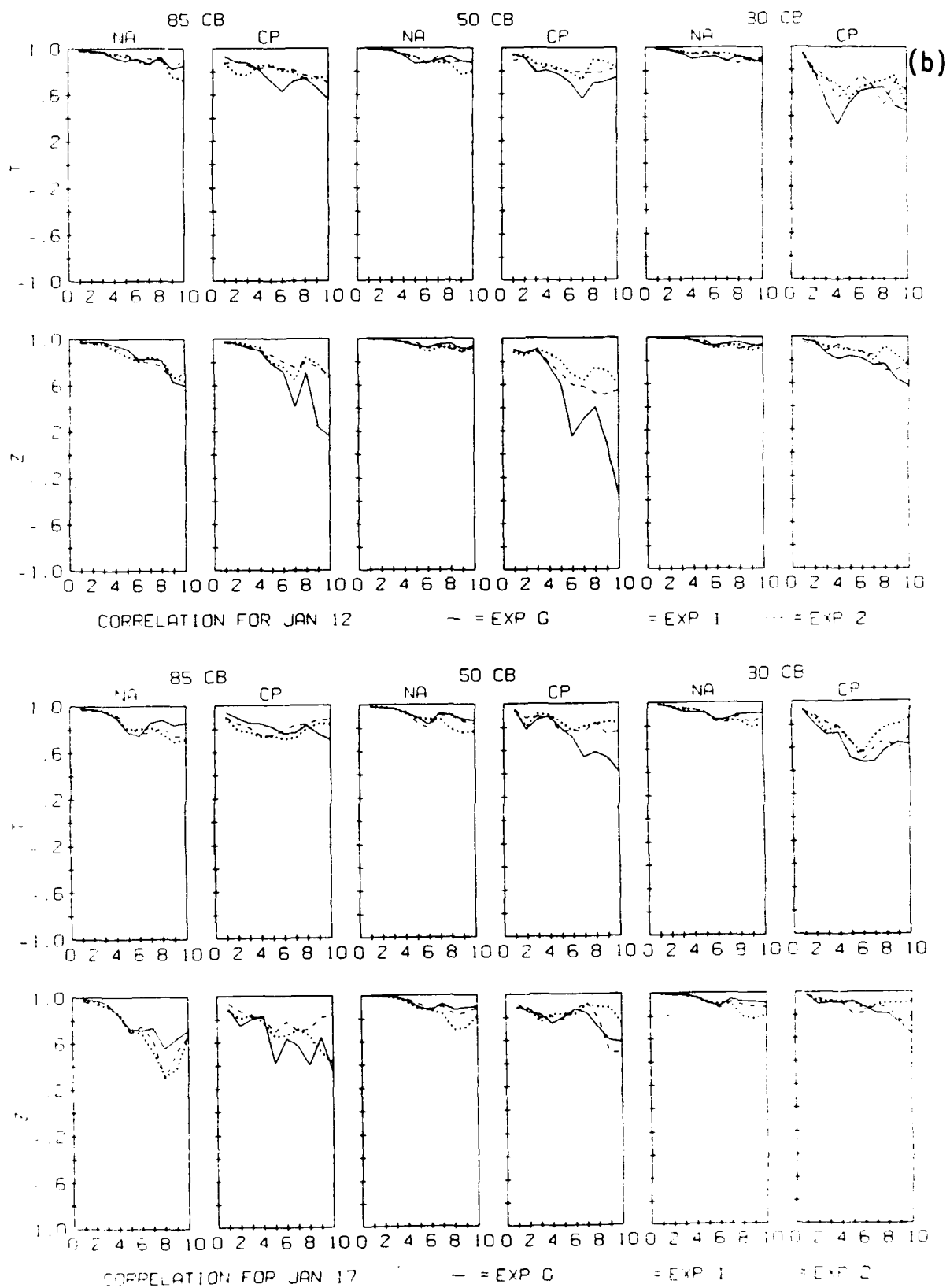


Figure 50. Spatial Correlation of Temperature and Geopotential Height Forecasts with FGGE III-b Analyses for North American (NA) and Central Pacific (CP) Windows at 850, 500, and 300 mb: (a)-(c) January, and (d)-(f) June.

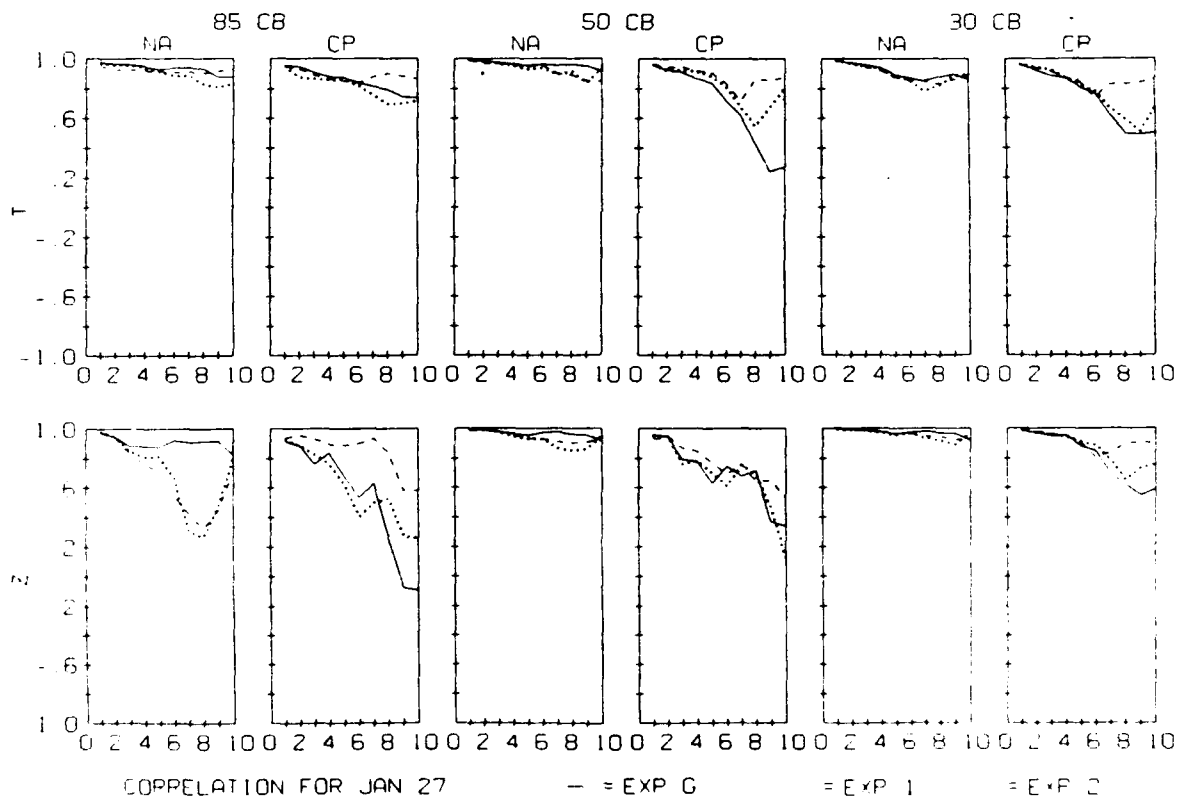
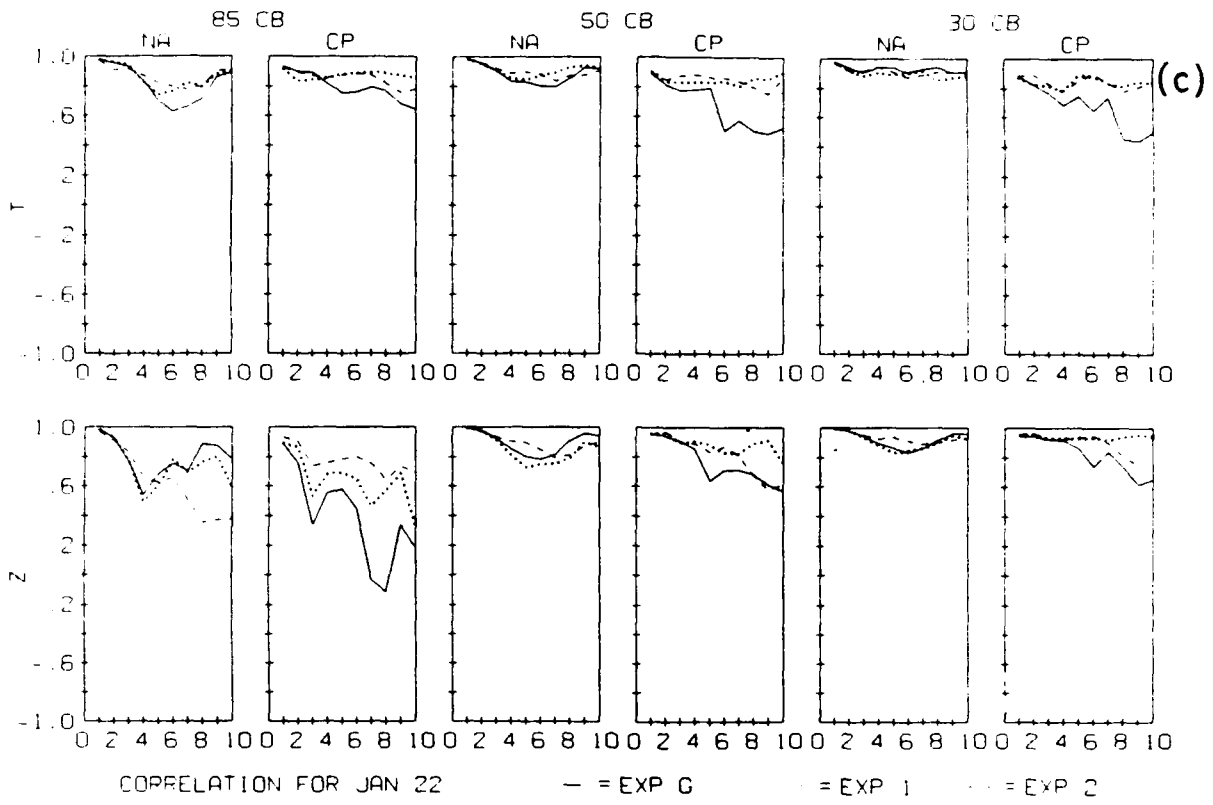


Figure 50. Spatial Correlation of Temperature and Geopotential Height Forecasts with FGGE III-b Analyses for North American (NA) and Central Pacific (CP) Windows at 850, 500, and 300 mb: (a)-(c) January, and (d)-(f) June.

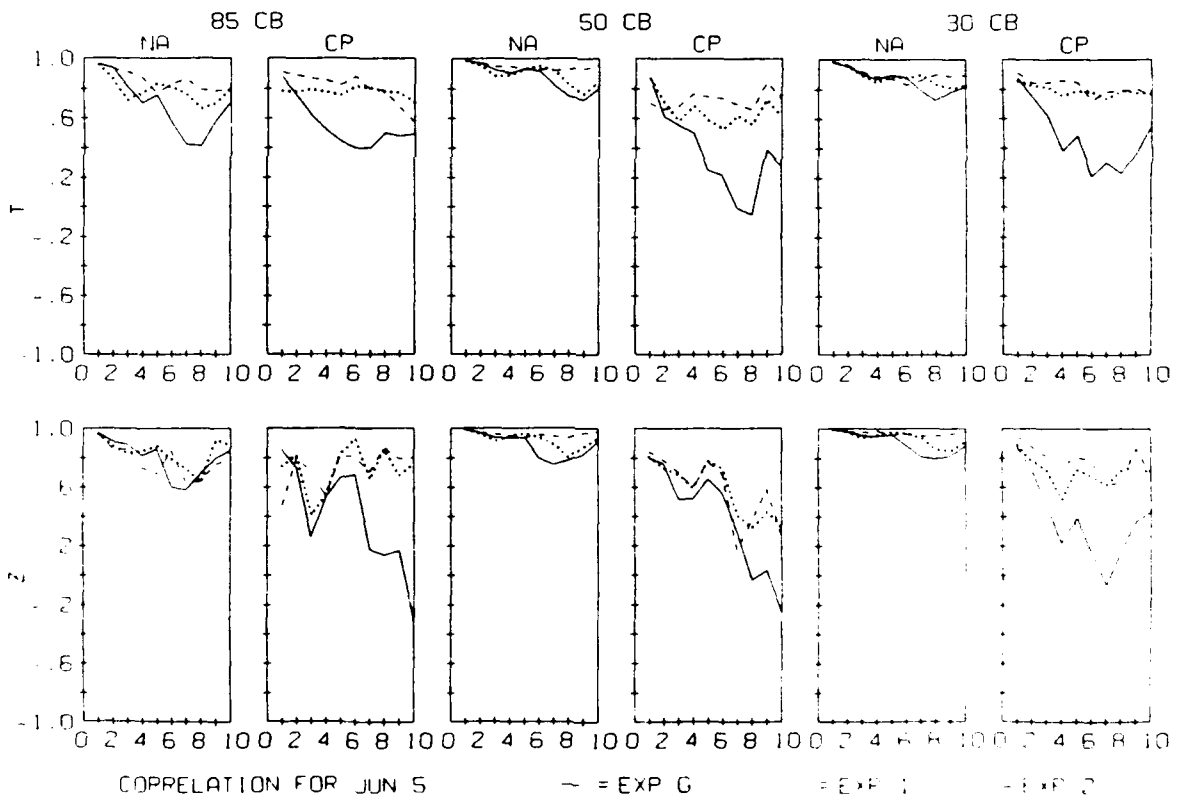
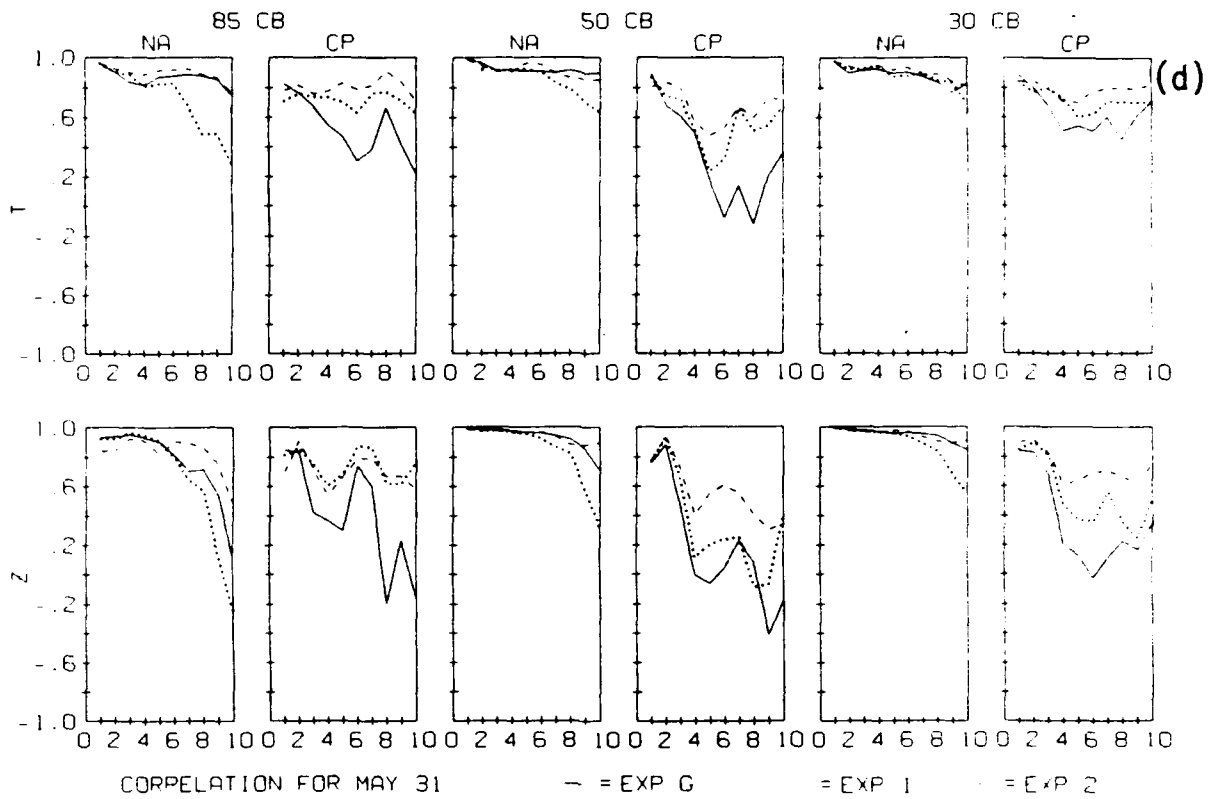


Figure 50. Spatial Correlation of Temperature and Geopotential Height Forecasts with FGGE III-b Analyses for North American (NA) and Central Pacific (CP) Windows at 850, 500, and 300 mb: (a)-(c) January, and (d)-(f) June.

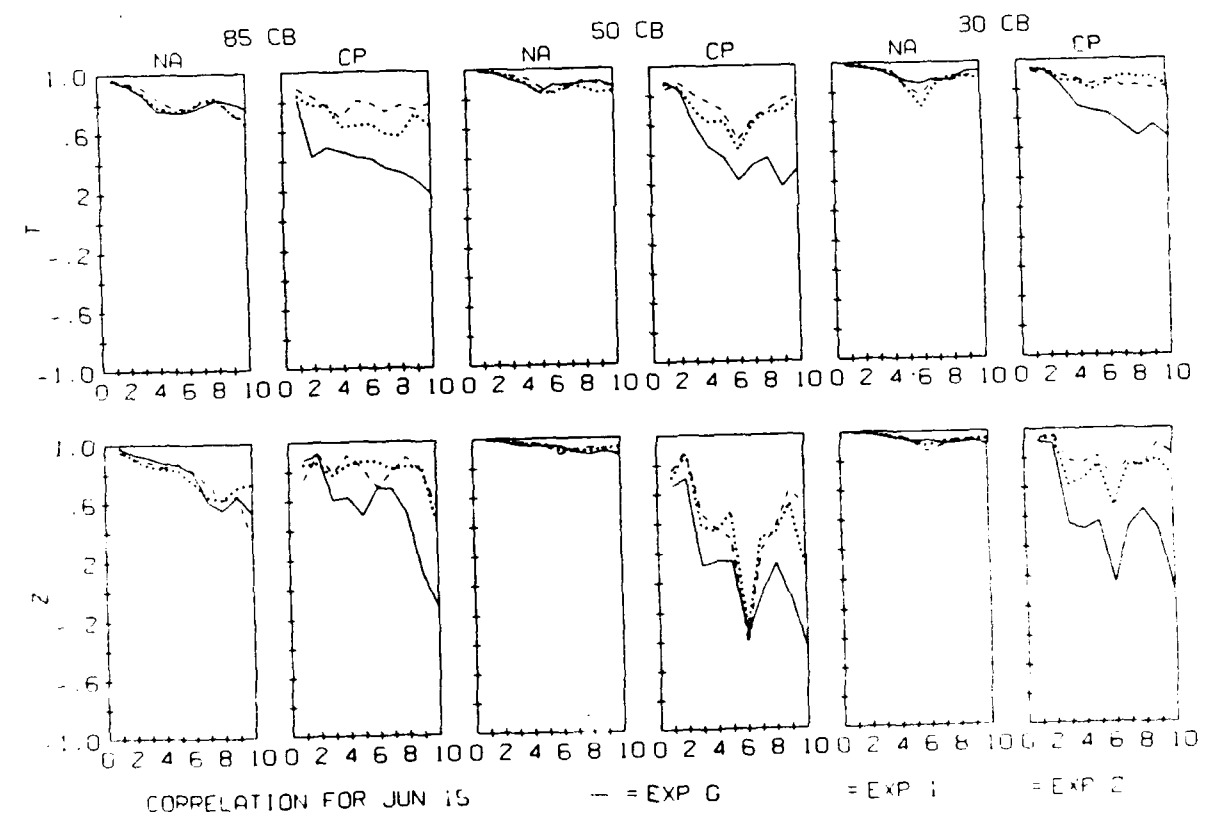
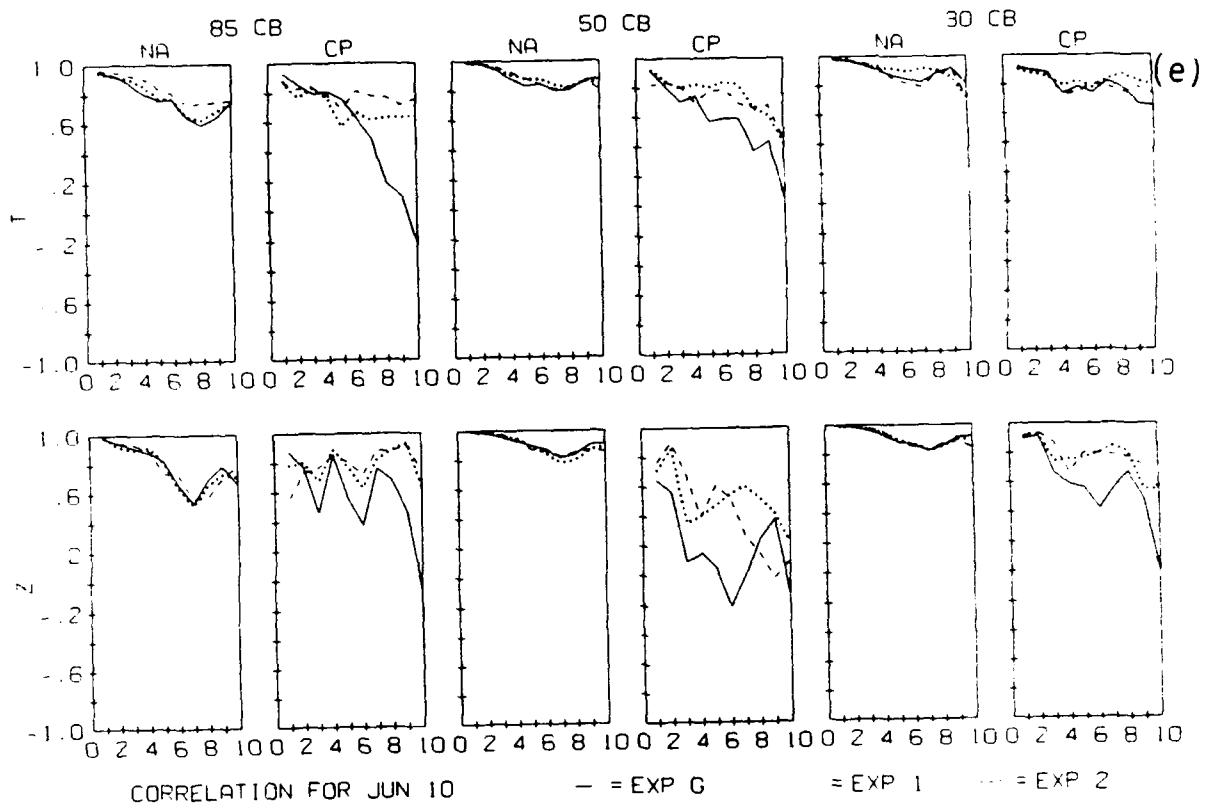


Figure 50. Spatial Correlation of Temperature and Geopotential Height Forecasts with FGGE III-b Analyses for North American (NA) and Central Pacific (CP) Windows at 850, 500, and 300 mb: (a)-(c) January, and (d)-(f) June.

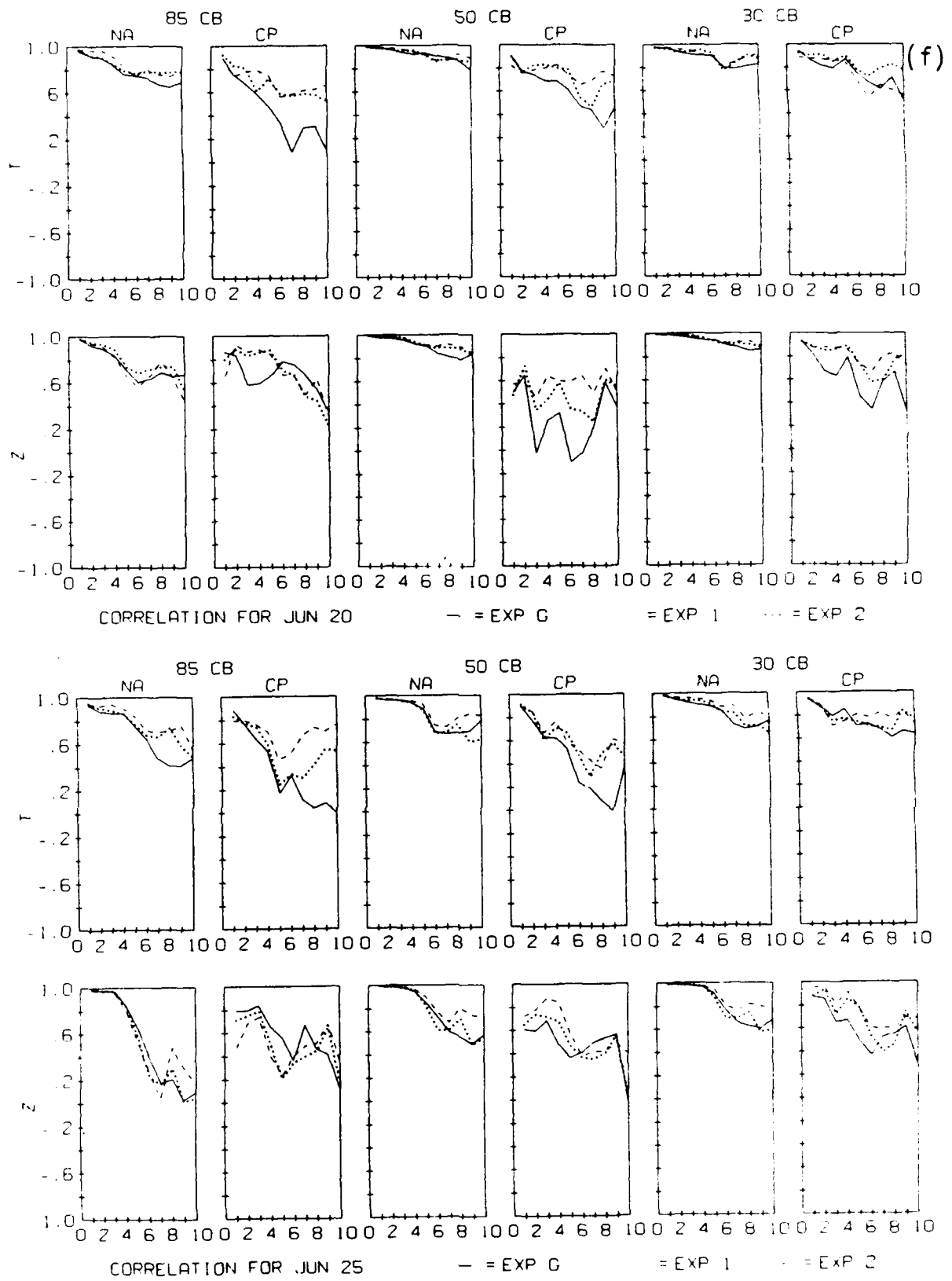


Figure 50. Spatial Correlation of Temperature and Geopotential Height Forecasts with FGGE III-b Analyses for North American (NA) and Central Pacific (CP) Windows at 850, 500, and 300 mb: (a)-(c) January, and (d)-(f) June.

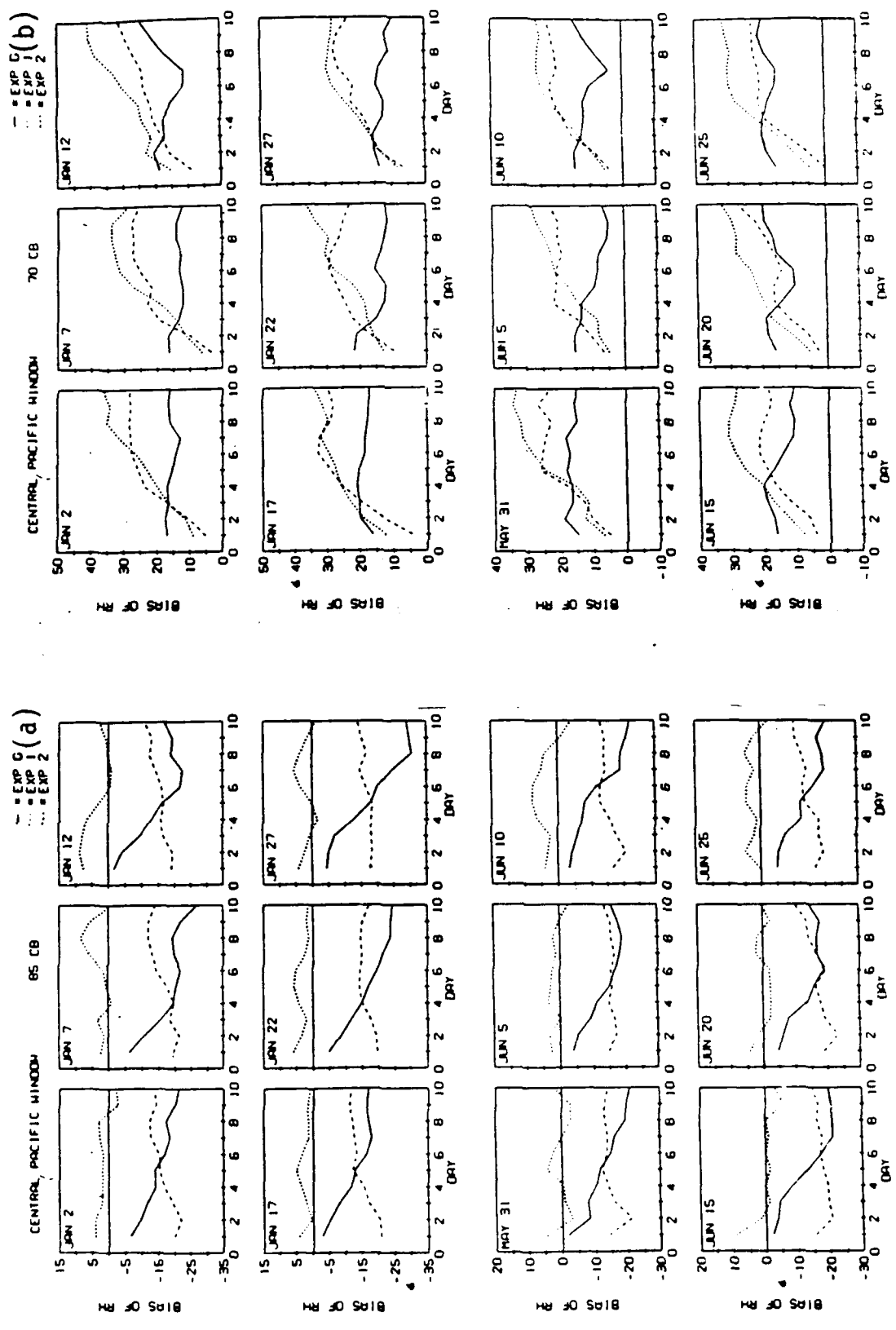


Figure 51. Central Pacific Relative Humidity Bias of January and June Forecasts at (a) 850 mb, (b) 700 mb, (c) 500 mb, and (d) 300 mb.

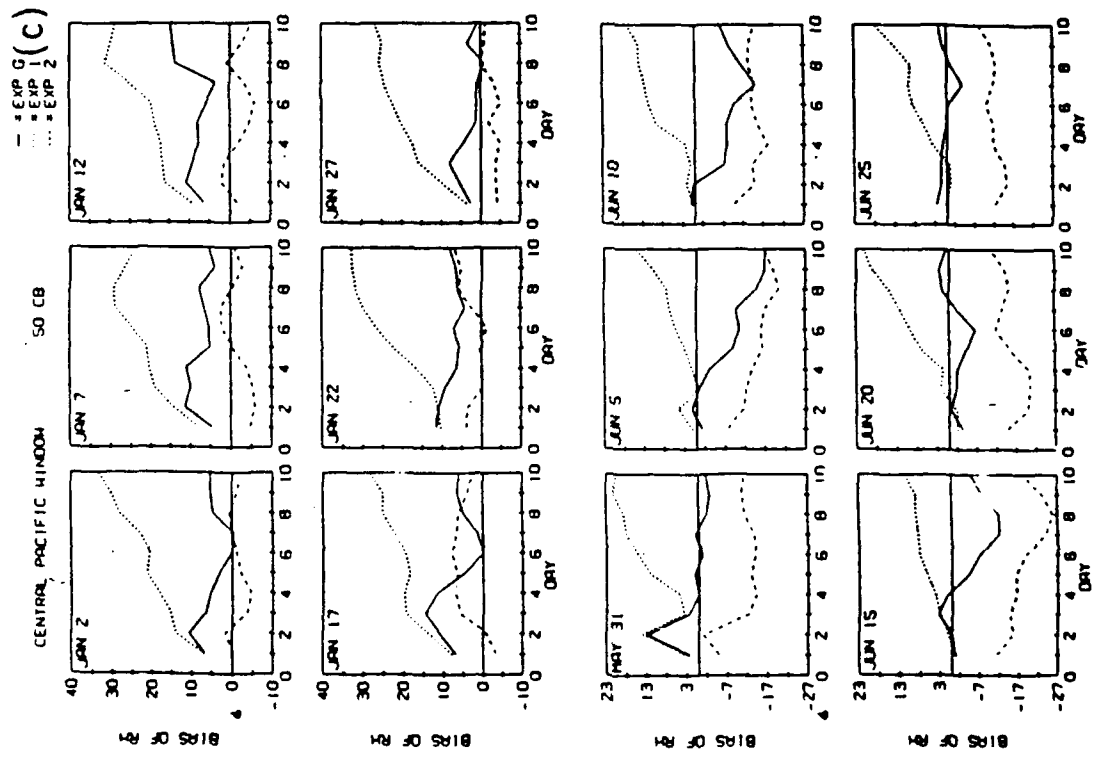
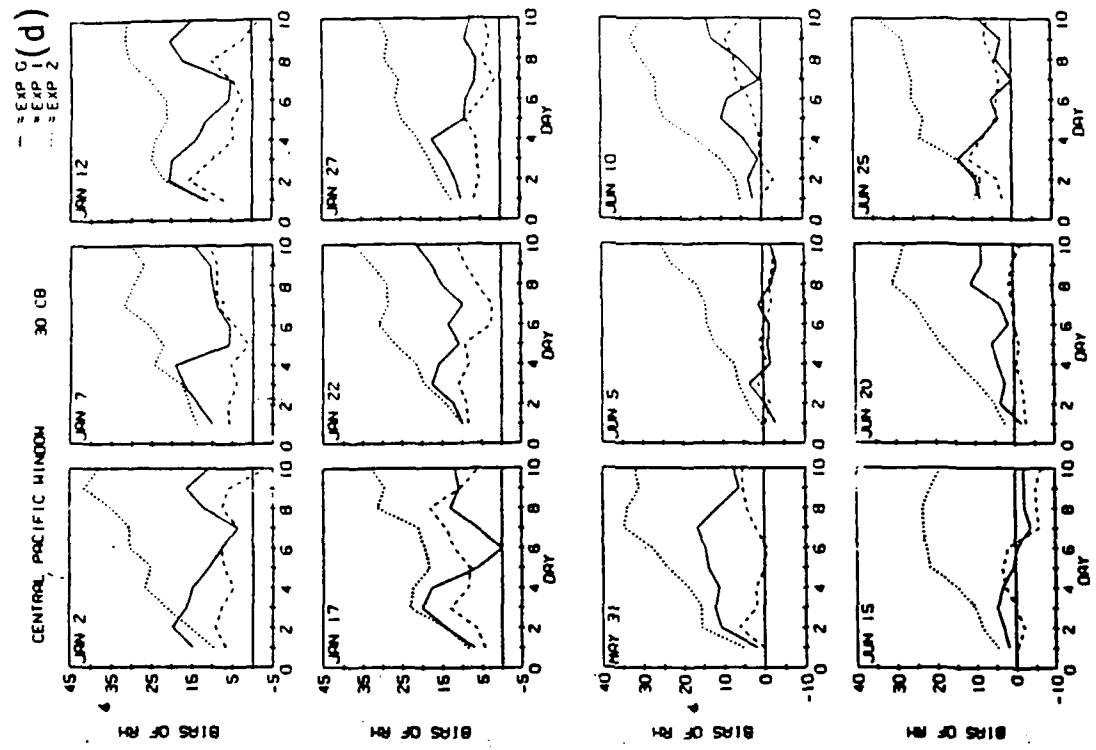


Figure 51. Central Pacific Relative Humidity Bias of January and June Forecasts at (a) 850 mb, (b) 700 mb, (c) 500 mb, and (d) 300 mb.

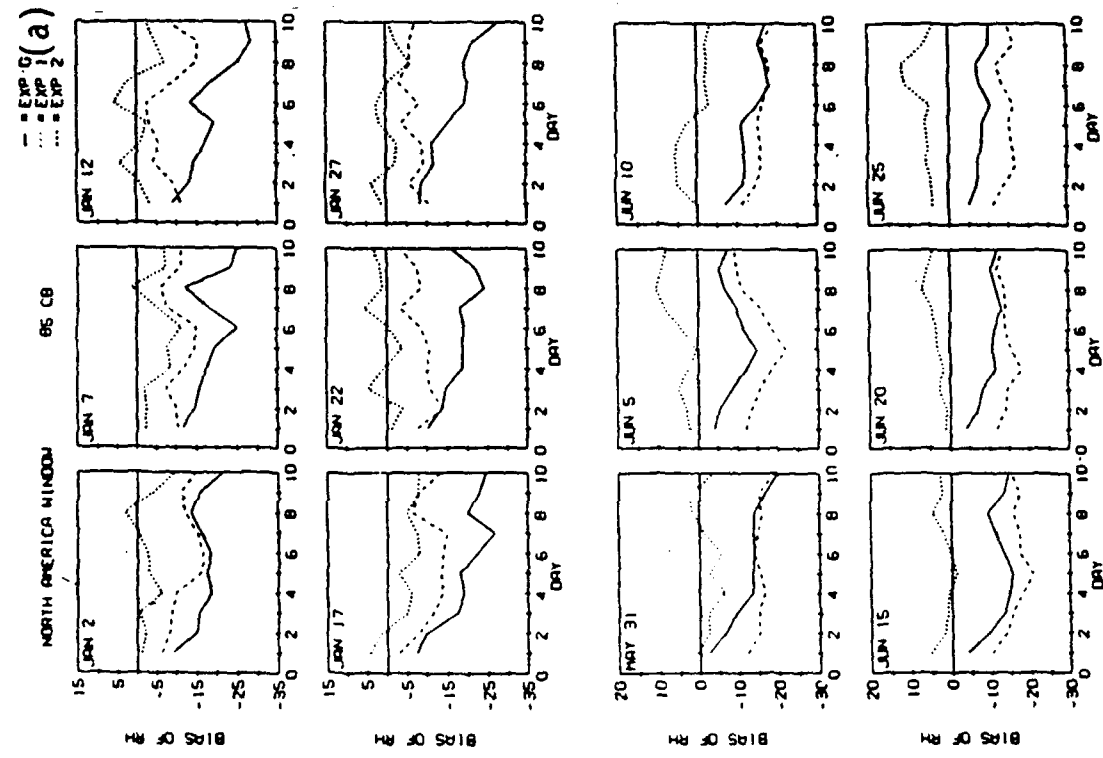
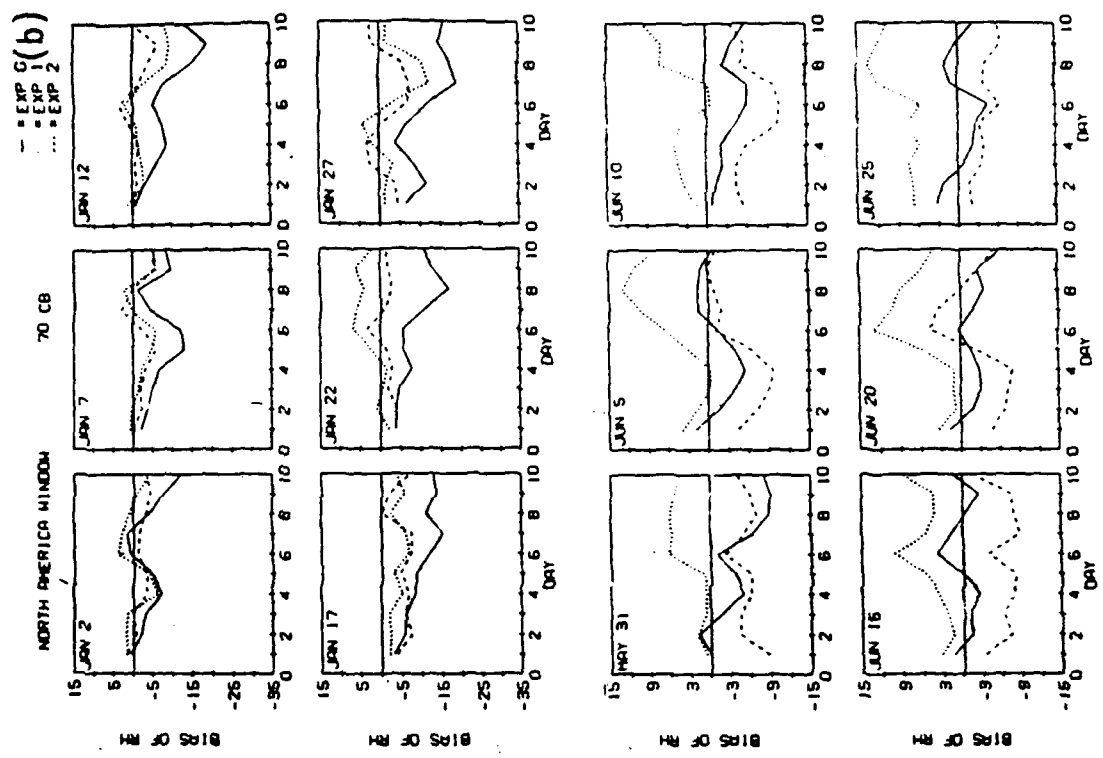


Figure 52. Same as in Figure 51 for North American Window.

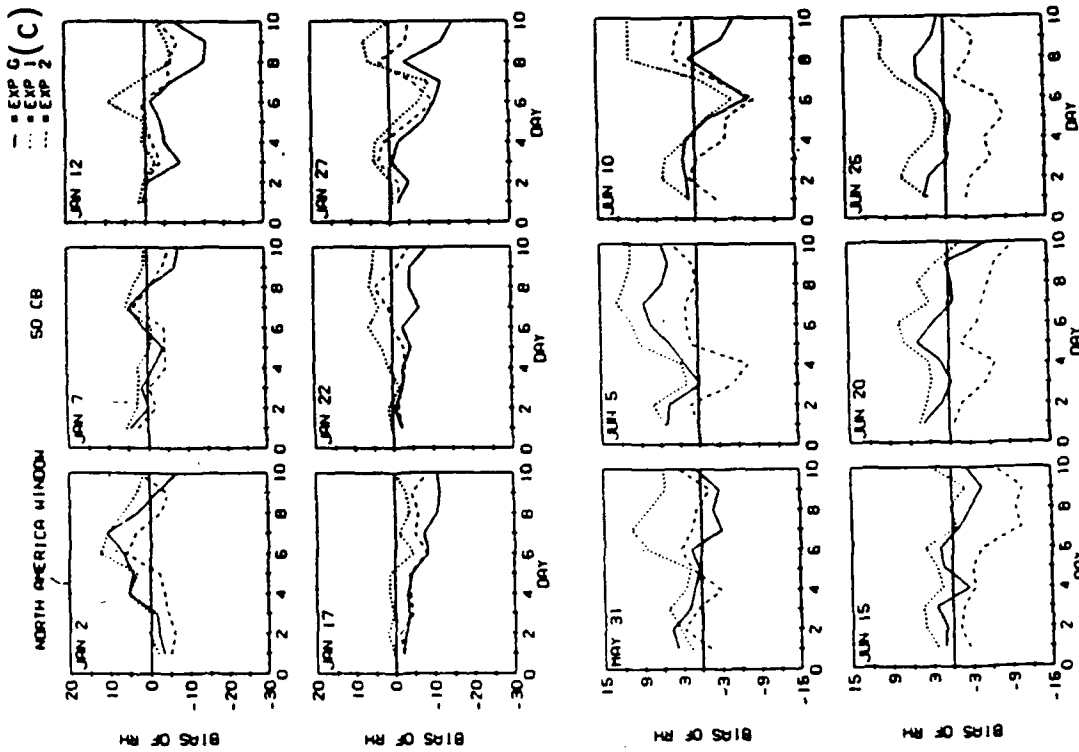
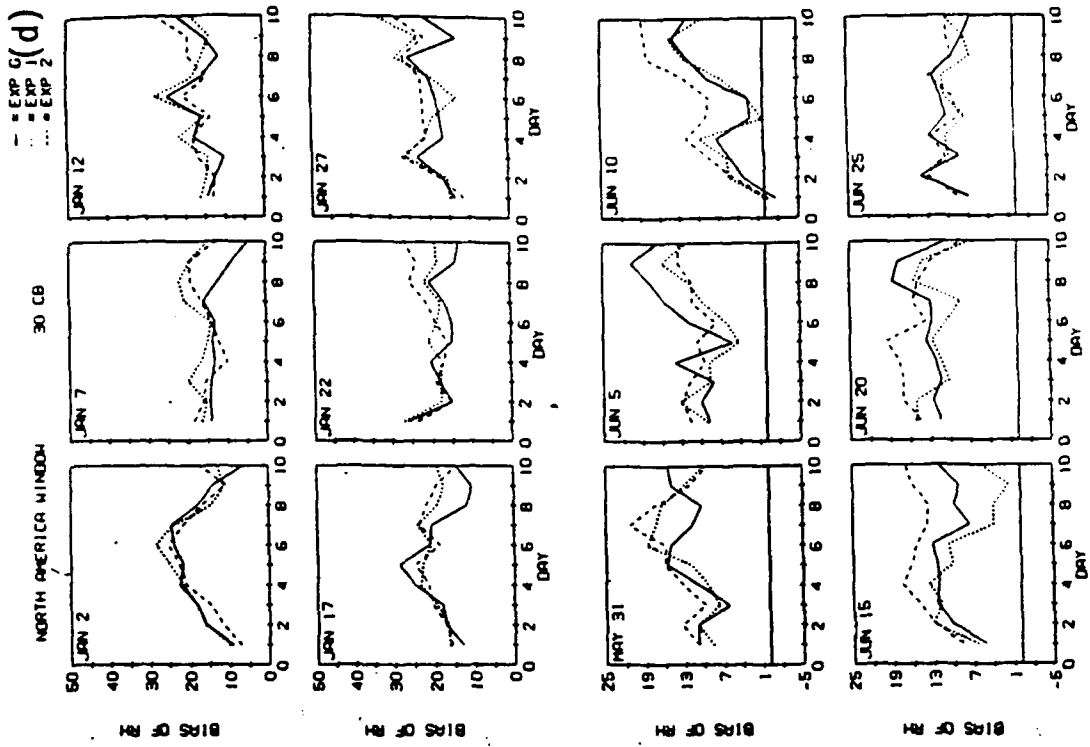
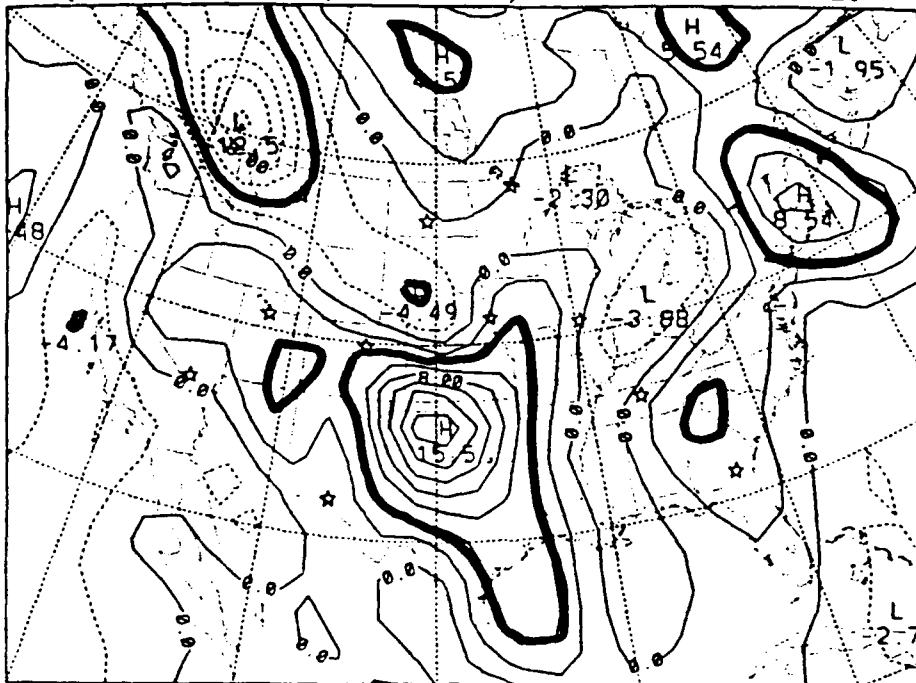


Figure 52. Same as in Figure 51 for North American Window.

(RAD-0 FCST) - (FGGE3B ANAL) 12Z 13JAN79 90 kPa ΔT (a)



(PBL-2G FCST) - (FGGE3B ANAL) 12Z 13JAN79 90 kPa ΔT (b)

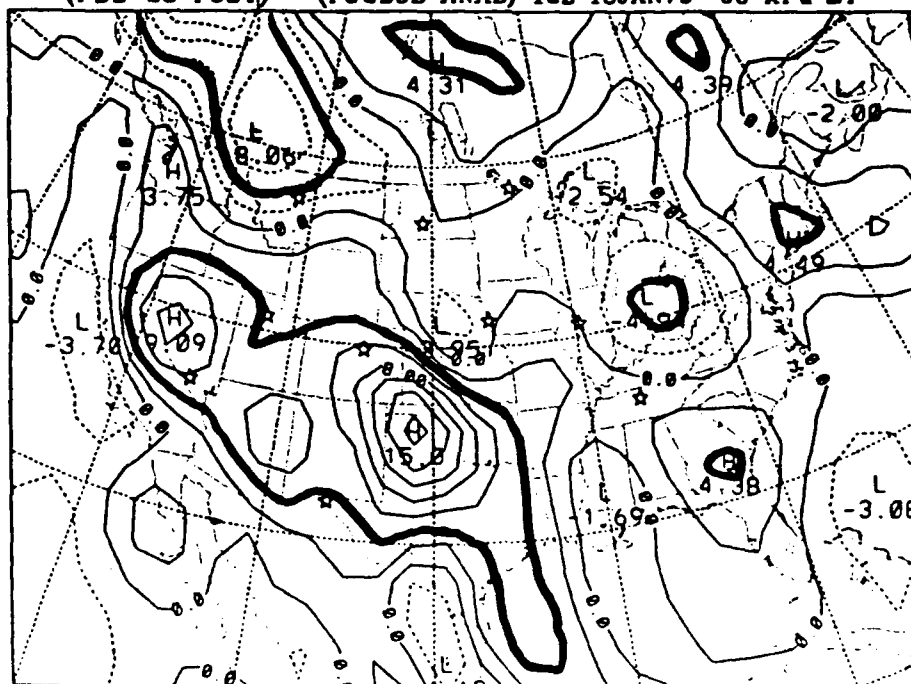
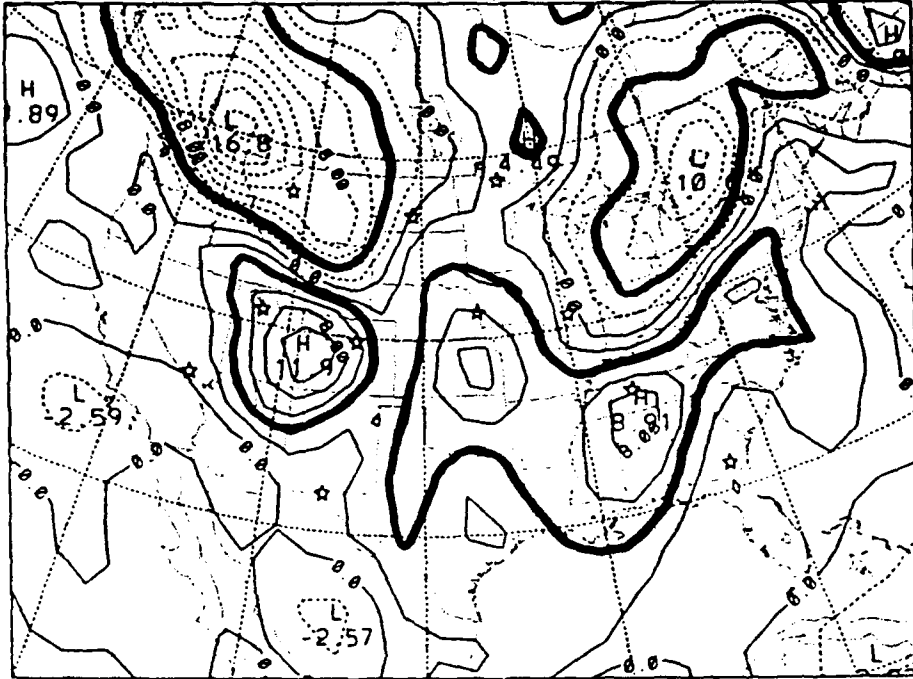


Figure 53. Map of Forecast - Analysis Temperature Differences at 900 mb for 24-Hour Forecasts Valid 1200 UTC 13 January 1979: (a) RAD-0, and (b) PBL-2G.

(RAD-0 FCST) - (FGGE3B ANAL) 12Z 14JAN79 90 kPa ΔT (a)



(PBL-2G FCST) - (FGGE3B ANAL) 12Z 14JAN79 90 kPa ΔT (b)

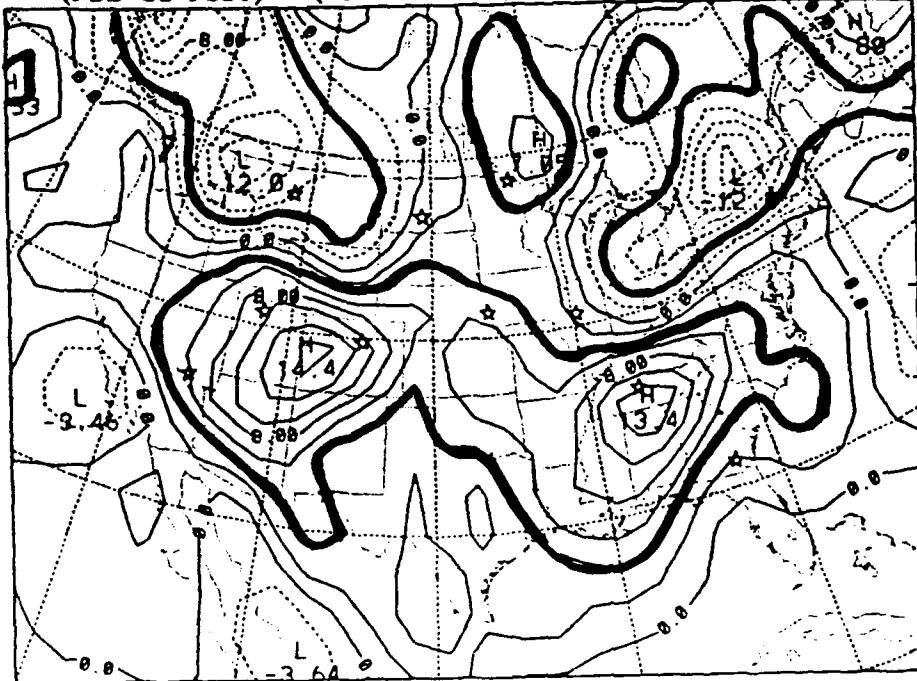


Figure 54. Same as in Figure 53 for 48-Hour Forecast Valid 1200 UTC 14 January 1979.

approximately 2.35° latitude), but were left on the model's sigma layers. The FGGE III-b analysis corresponding to each forecast was pre-processed to the 30 rhomboidal truncation on the model sigma layers, using the same procedure used in constructing the forecast initial conditions (that is, using the PL-91 silhouette orography). Then the analyses were post-processed to the Gaussian grid but left on sigma layers as was done for the forecasts. This process was carried out to ensure that the same spatial scales and same vertical interpolations were applied to both forecast and verification fields. We chose five Gaussian gridpoints, each of which is located near a weather (radiosonde) station to compare PL-91 forecasts with verifying analyses. The five gridpoints were chosen for their geographic diversity and the fact that the analysis at each point is supported by nearby radiosonde data. Table 2 lists the five Gaussian gridpoints chosen for this study, along with their terrain height, and the height of the nearby RAOB station. In all cases, the Gaussian gridpoint closest to the station, whose latitude and longitude are given in Table 2, was chosen as the location of the comparison. Thus, the geographic locations referred to in the following figures actually correspond to the Gaussian gridpoint.

Table 2. Geographical Location of the Five Gridpoints the Evaluation of PBL Prediction.

Gridpoint Number	Latitude	Longitude	Z, m	h (m) The nearest Station	Z. - h m	Local Time at 12UTC
1	38.82N	105.00 W	2698	1625 Denver	1073	5 am
2	41.18N	97.50 W	582	406 Omaha	176	6 am
3	20.00N	153.75 W	223	11 Hawaii	212	2 am
4	83.52N	63.75 W	753	63 Alert	690	8 am
5	88.20S	0.00	2986	2835 Amundsen	151	12 noon

Z. = silhouette topography model surface height; h = nearby RAOB station elevation.

Figures 55-72 show the time series of forecasts and analyses for a single model layer in the boundary layer for all six January and June cases. Temperature, specific humidity, wind speed, and wind direction in the model layer closest in pressure to the nearest radiosonde report level are shown for Denver (Figures 55-60), Hawaii (Figures 61-66), and Alert (Figures 67-72). Choosing this layer for verification ensures that the analysis is supported by nearby (in the vertical) radiosonde data. We show these plots to show the time evolution of the boundary layer forecast performance of PL-91 in a variety of weather conditions and representative geographic locations.

4.3 Patterns of Weather Prediction

This section features a set of maps that compare PL-91 and GWC84 forecasts with verifying FGGE III-b analyses. Software was developed to produce color-filled animations²⁷ of side-by-side forecast and verification maps at 6h intervals out to 10 days. As expected, these animations show a steady phase and amplitude error growth in the forecasts with time. They provide a unique opportunity to look for trends in the way a prediction may systematically depart from the verification. This information may aid in improving the model by suggesting specific areas of investigation of the model design.

Figures 73-81 are black-and-white "snapshots" of the animation sequence for PL-91 and GWC84. In Figures 73-75, we show 72-hour forecasts of mean sea level pressure (pmsl), 500 mb height, 850 mb relative and specific humidities, 300 mb relative humidity, and 200 mb wind speed for the 12 January case over most of the Northern Hemisphere (down to 22.5N). Figures 76-81 show pmsl, wind vectors (alternate gridpoints plotted at 850 mb), specific humidity at 850 mb, and relative

²⁷Norquist, D. (1992) "Everybody talks about the weather, but...", *Vector View*, 5, March-April 1992, 8 pp. [Available from Phillips Laboratory Supercomputer Center, PL/SCI, Kirtland AFB, NM 87117-6008]

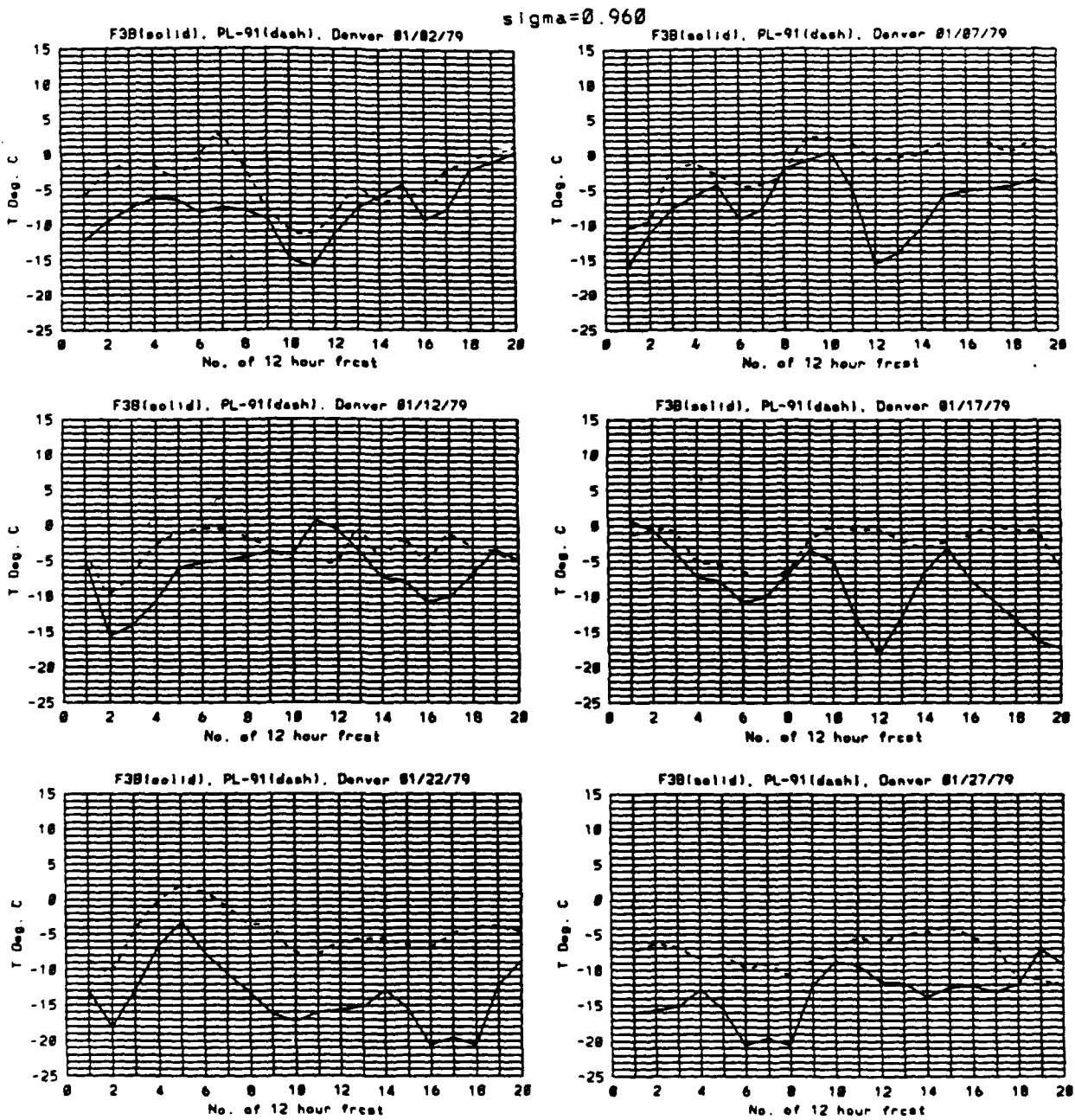


Figure 55. Time Series of $\sigma = 0.960$ FGGE III-b (Solid and PL-91 (Dash) Temperature (C) at Gridpoint Near Denver for Six January Cases (Abcissa is Integer Number of 12-Hour Intervals in 10-Day Forecast).

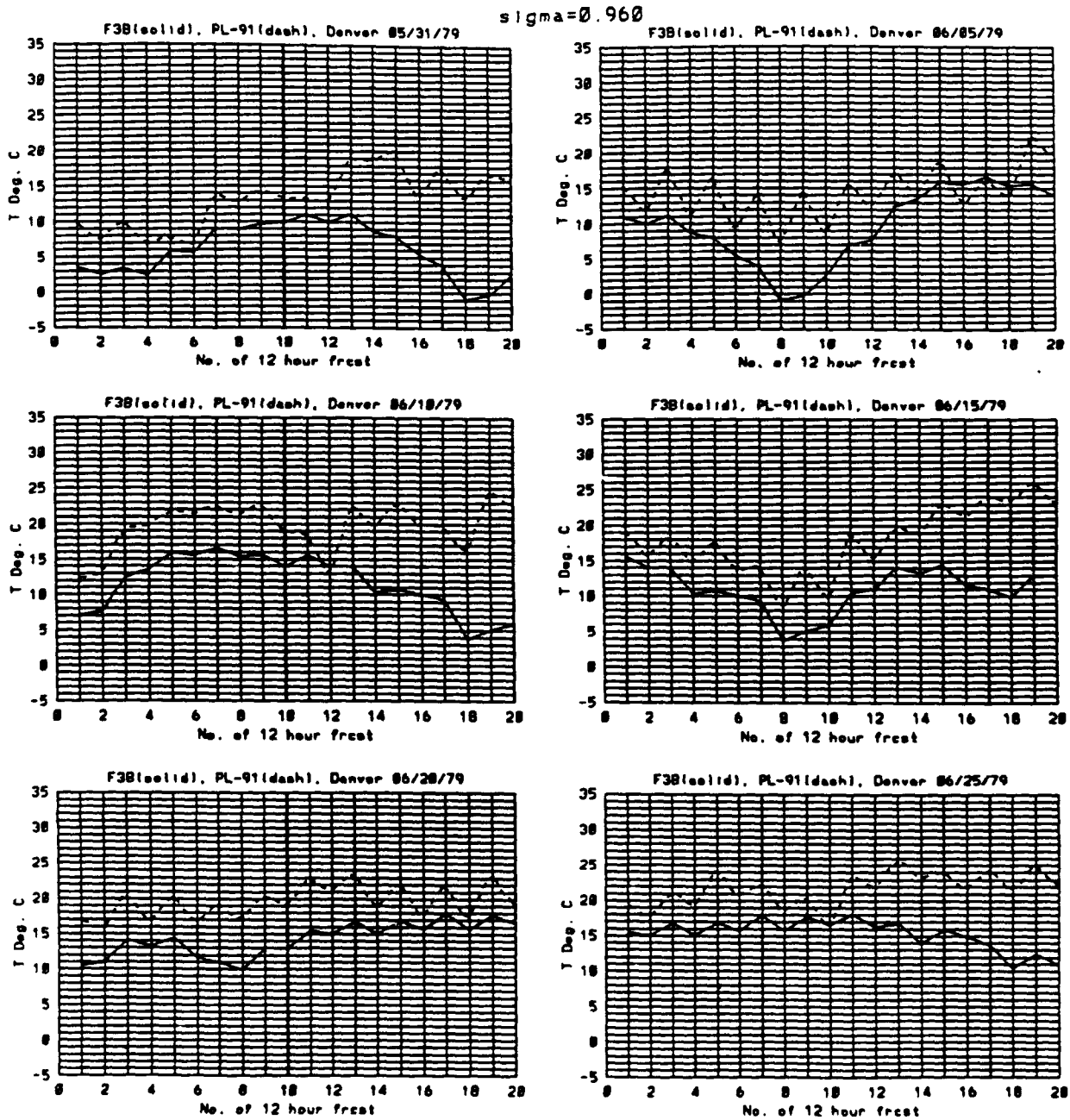


Figure 56. Same as in Figure 55 for June Cases.

sigma=0.960

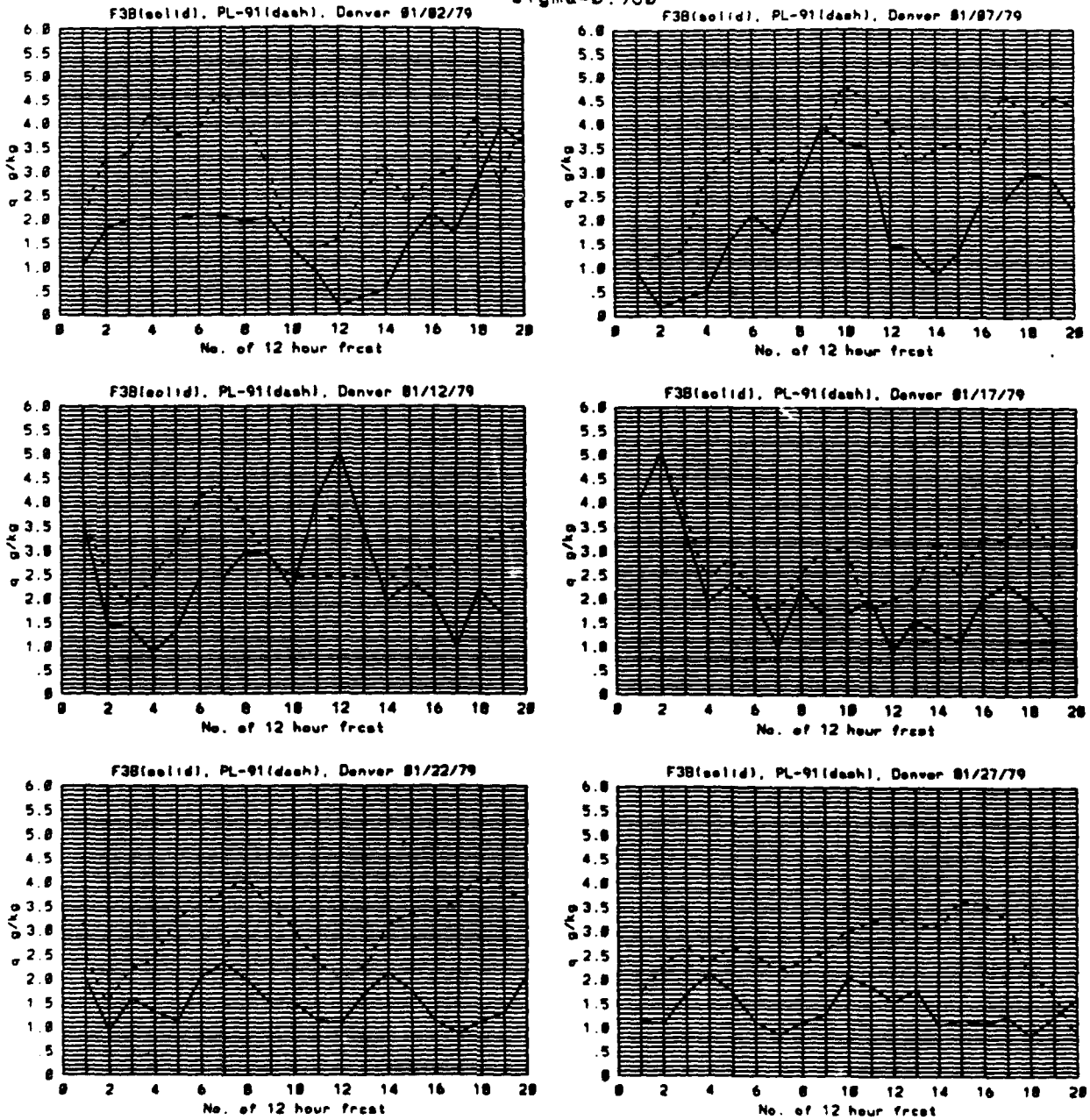


Figure 57. Same as in Figure 55 for Specific Humidity (g/kg).

$\sigma = 0.960$

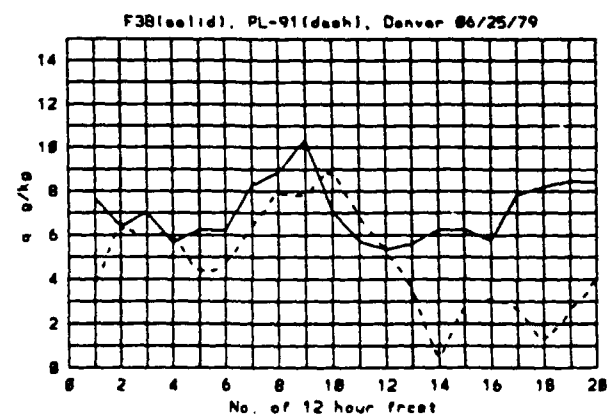
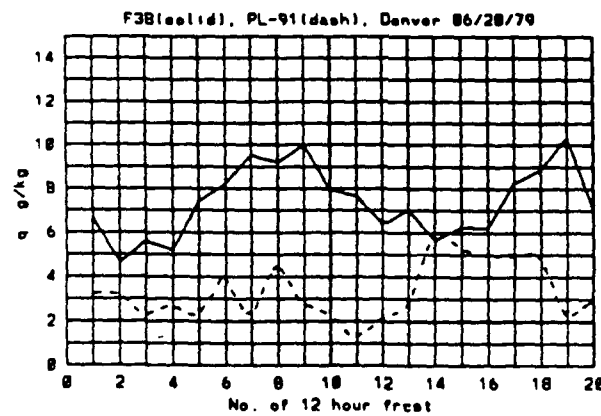
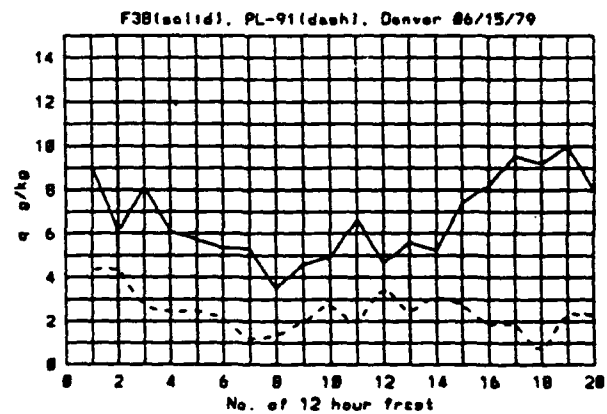
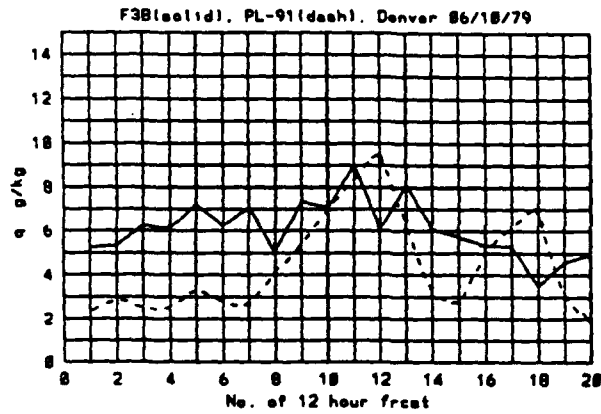
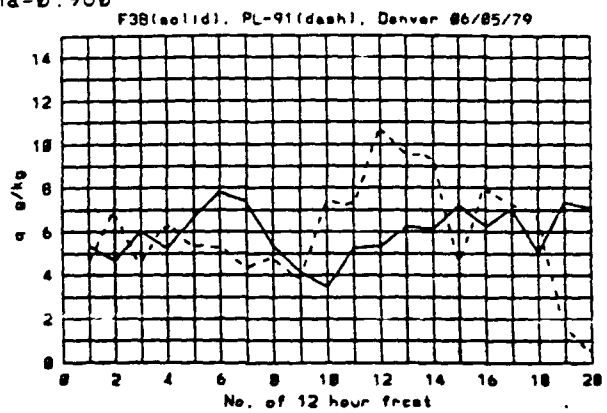
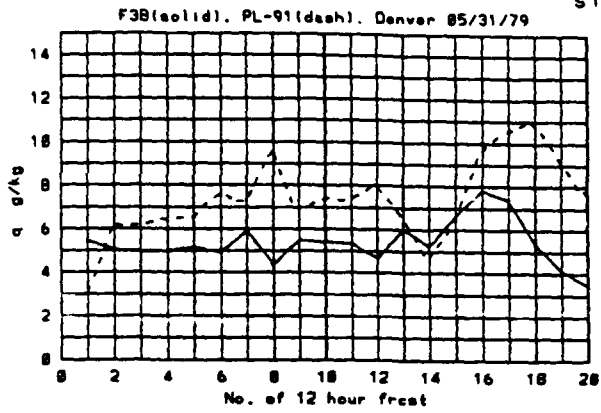


Figure 58. Same as in Figure 57 for June Cases.

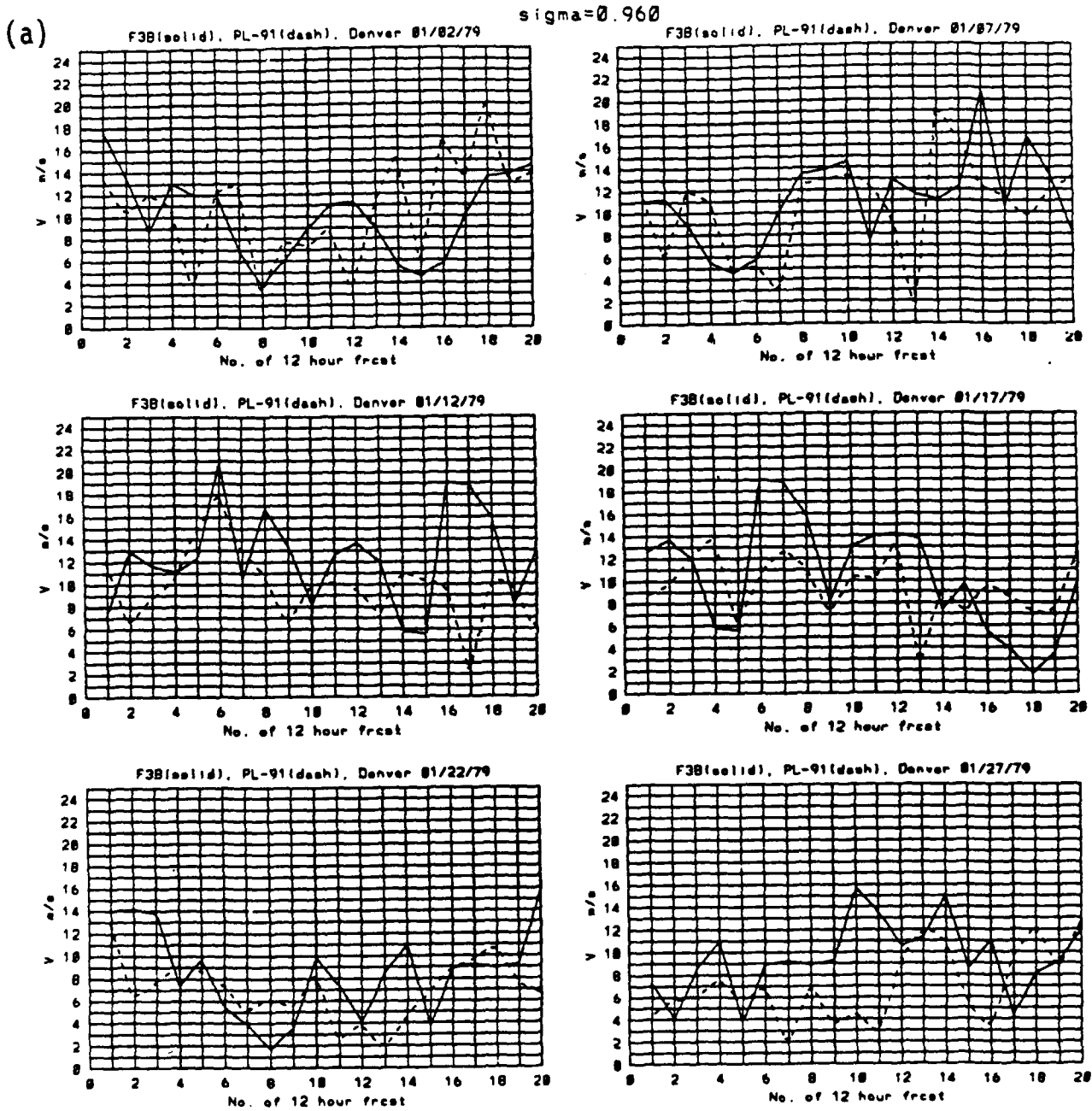


Figure 59. Time Series of $\sigma = 0.960$ FGGE III-b (Solid) and PL-91 (Dash) (a) Wind Speed (m/s) and (b) Wind Direction (degrees) at Gridpoint Near Denver for Six January Cases.

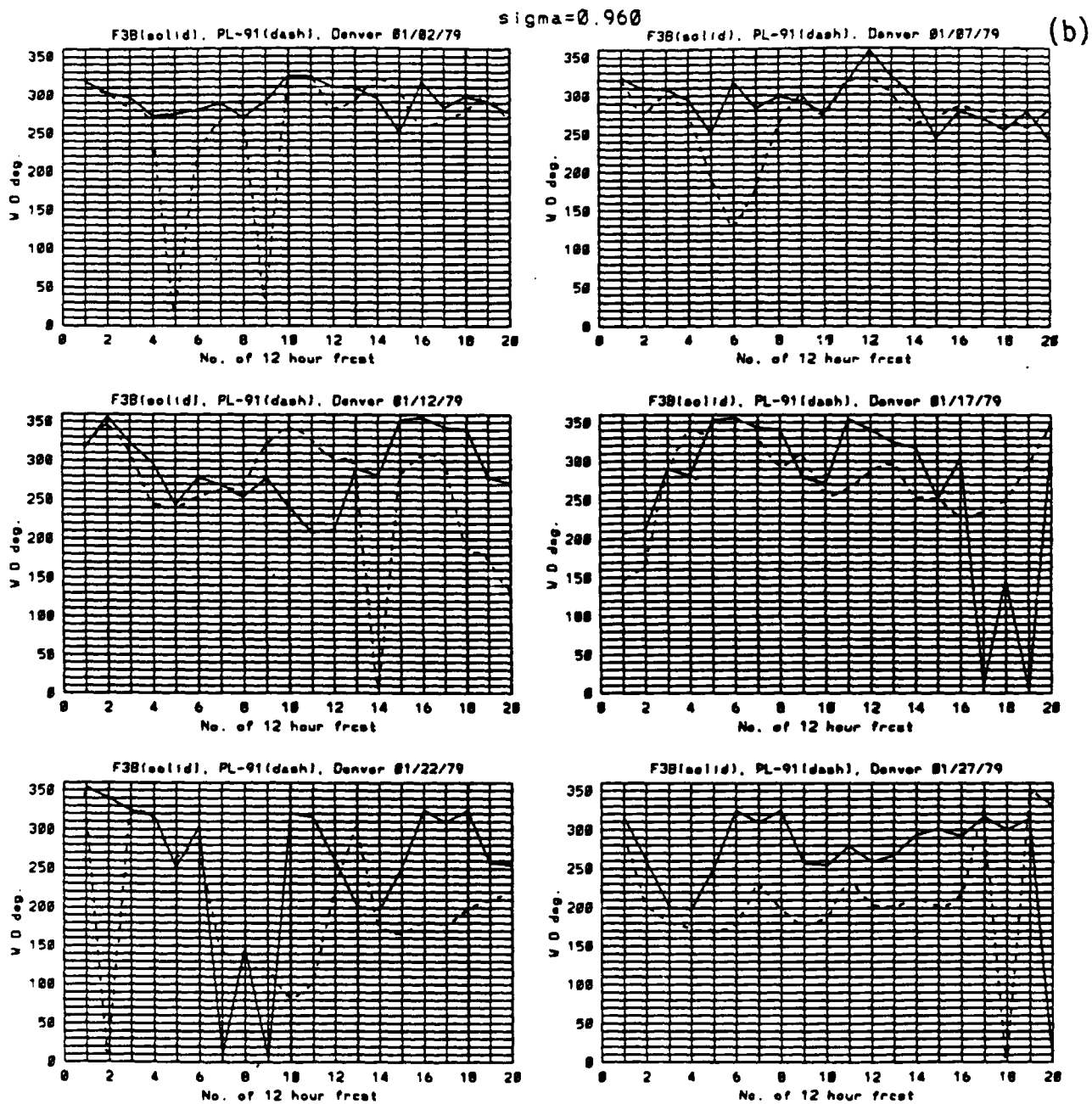


Figure 59. Time Series of $\sigma = 0.960$ FGGE III-b (Solid) and PL-91 (Dash) (a) Wind Speed (m/s) and (b) Wind Direction (degrees) at Gridpoint Near Denver for Six January Cases.

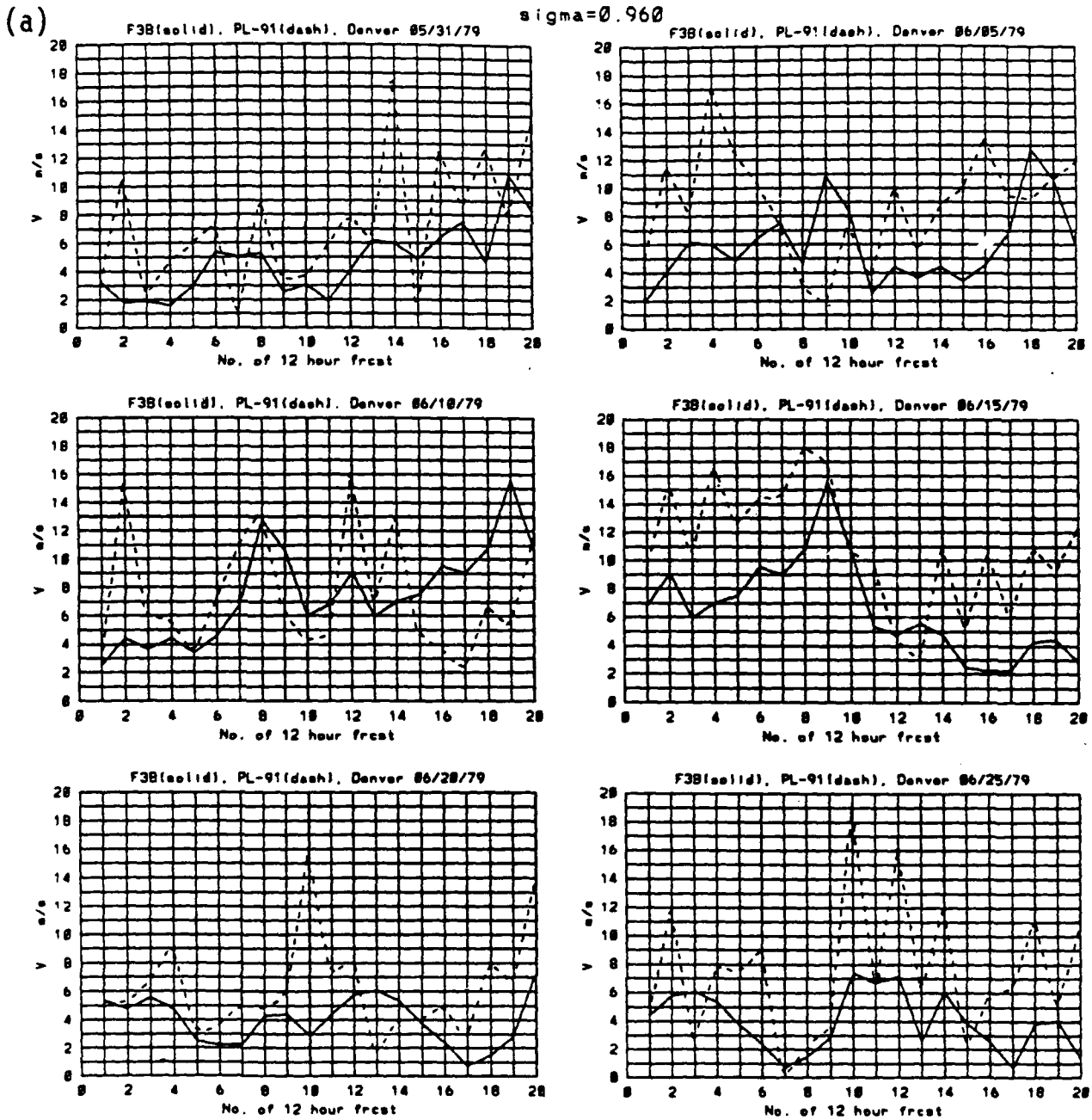


Figure 60. Same as in Figure 59 for June Cases.

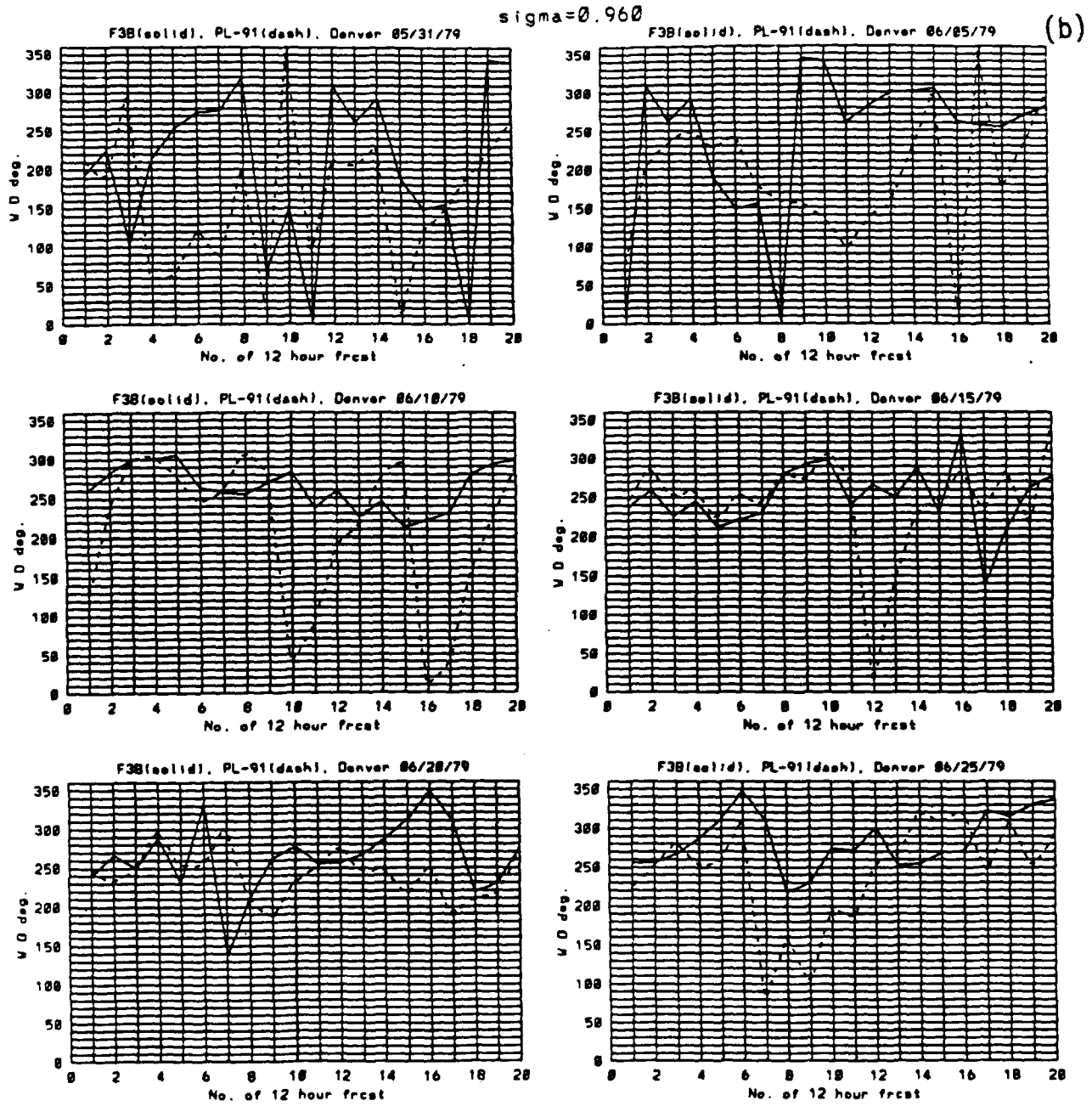


Figure 60. Same as in Figure 59 for June Cases.

sigma=0.995

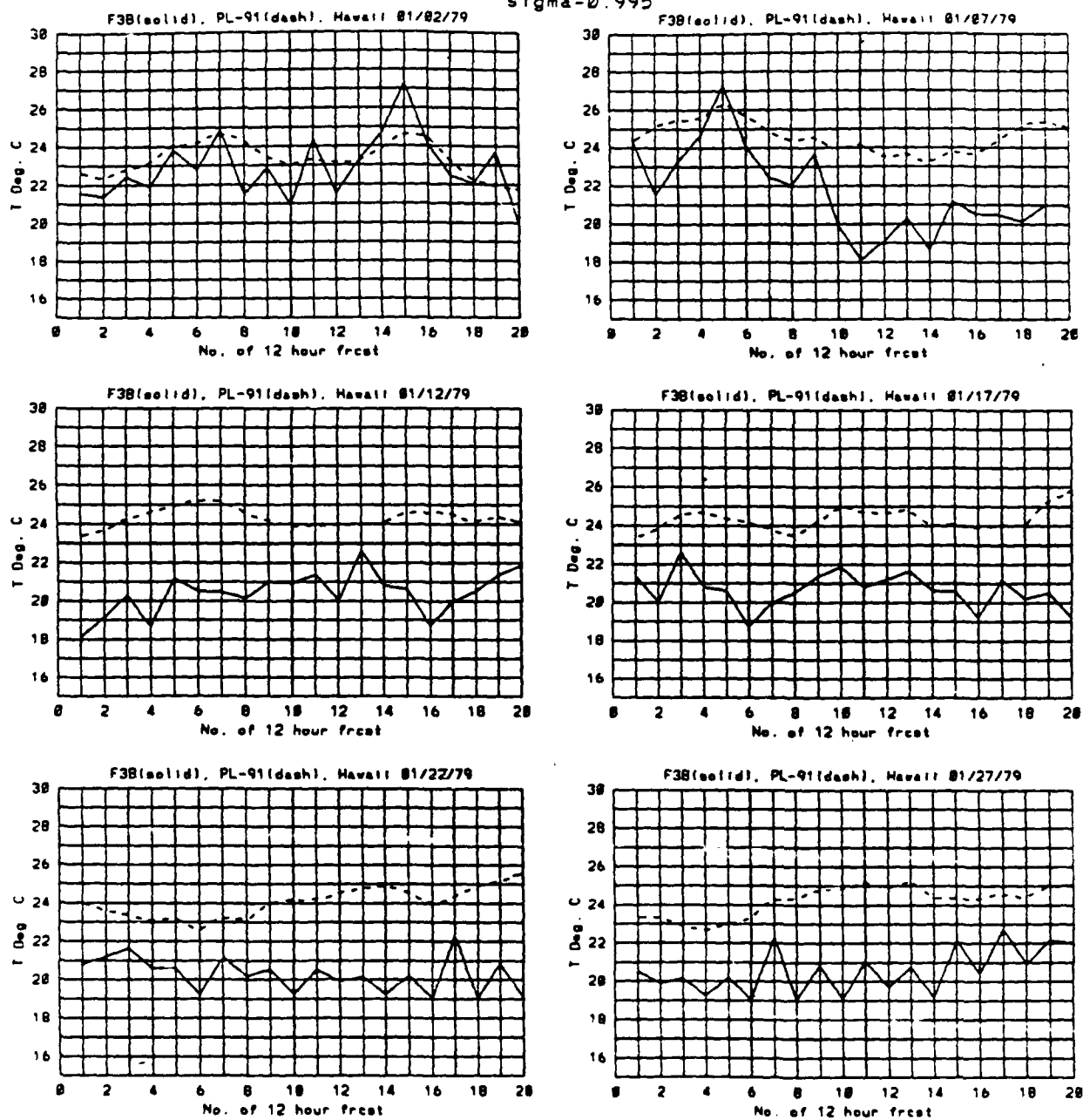


Figure 61. Time Series of $\sigma = 0.995$ FGGE III-b (Solid) and PL-91 (Dash) Temperature (C) at Gridpoint Near Hawaii for Six January Cases.

sigma=0.995

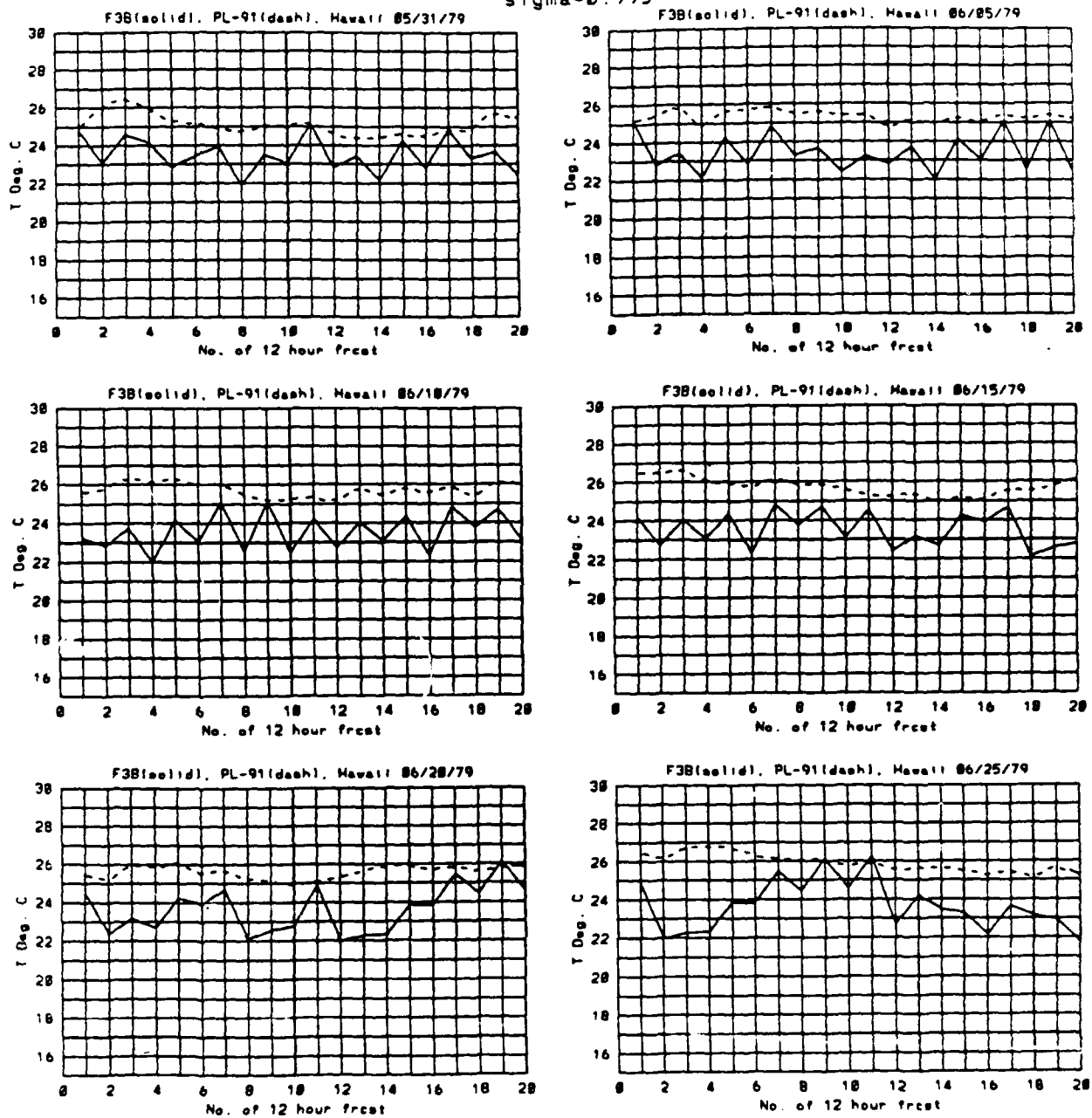


Figure 62. Same as in Figure 61 for June Cases.

sigma=0.995

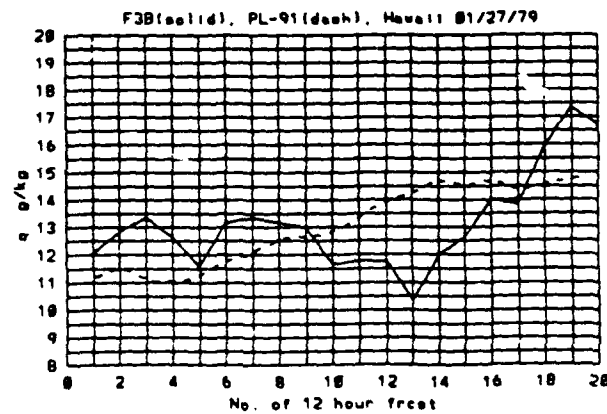
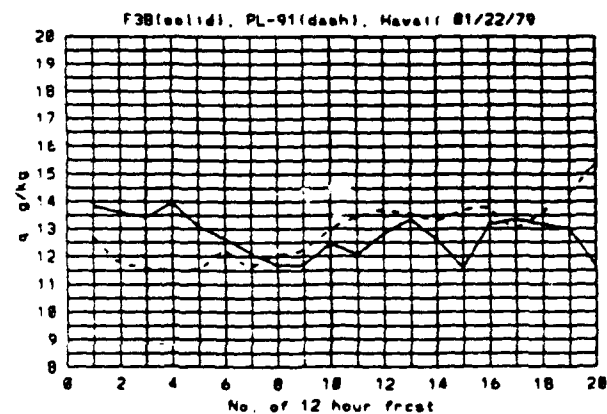
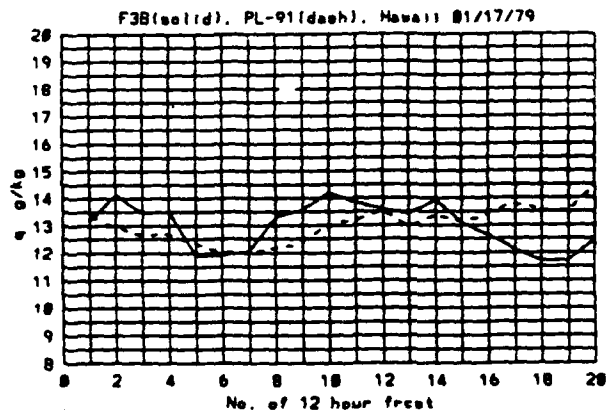
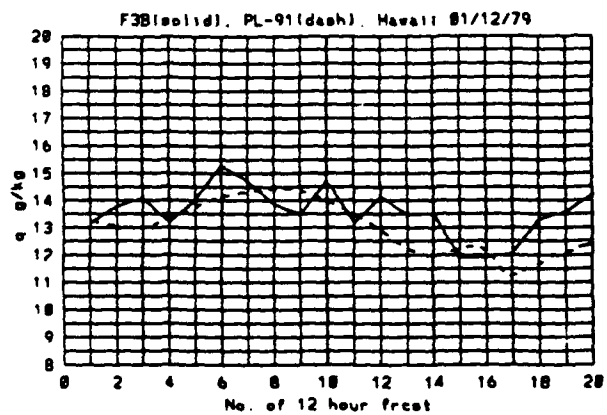
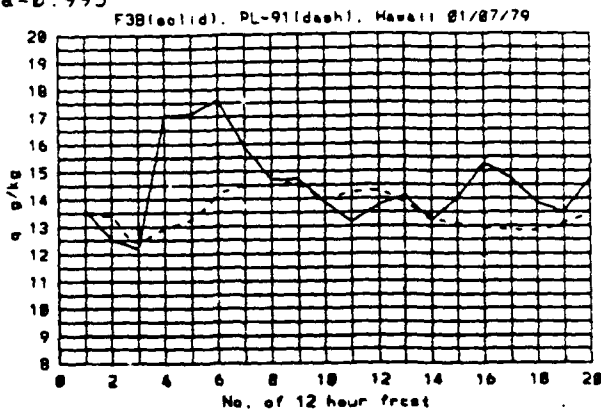
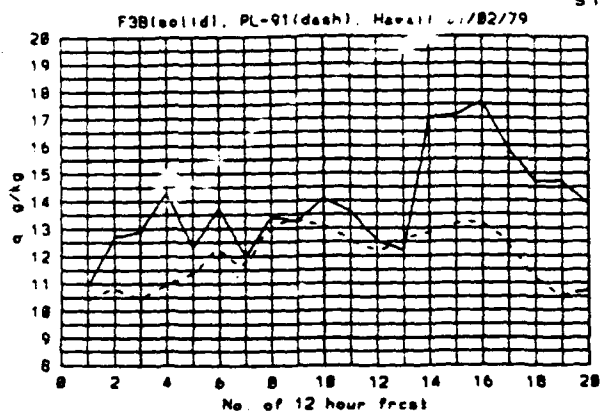


Figure 63. Same as in Figure 61 for Specific Humidity (g/kg).

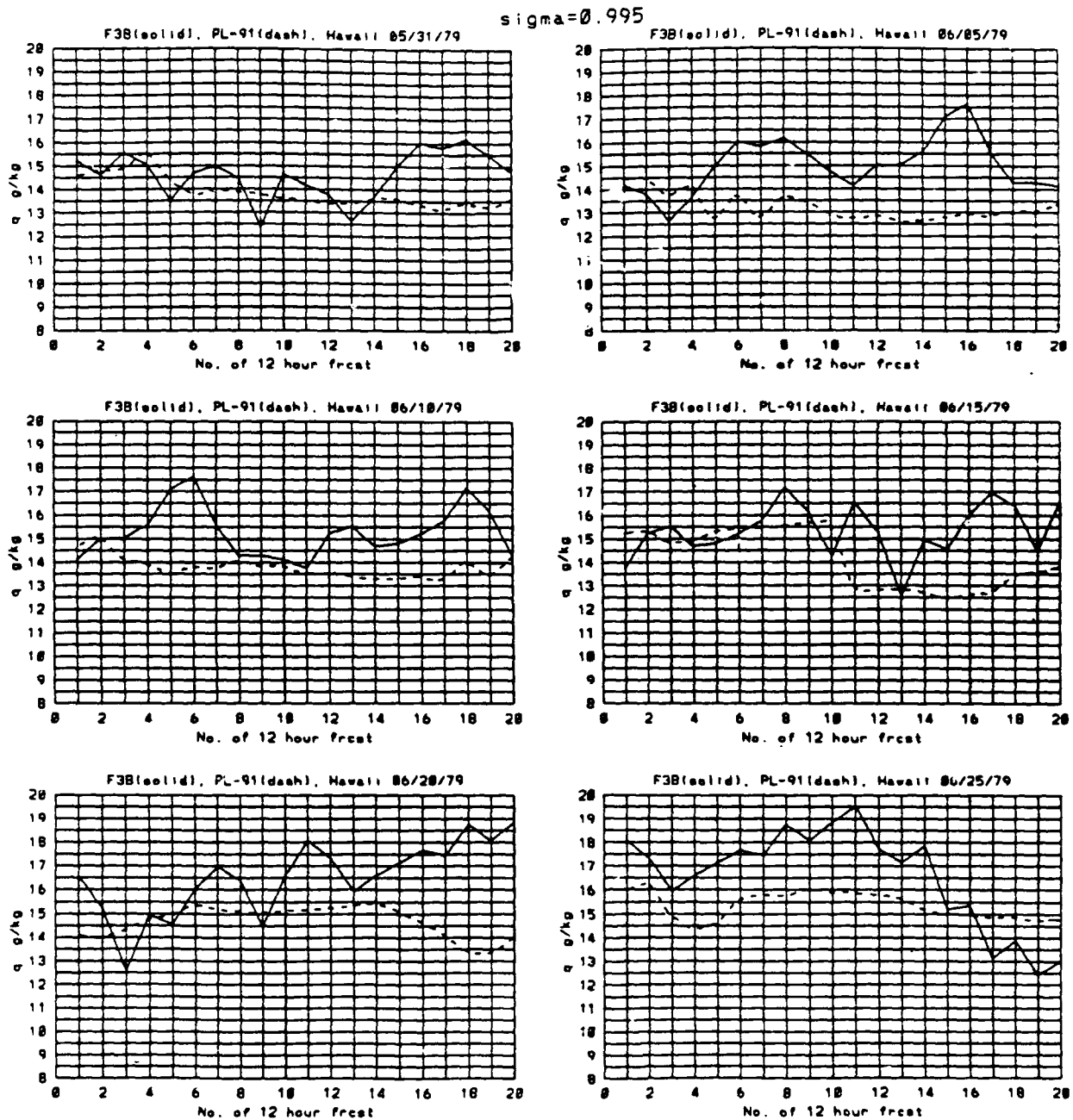


Figure 64. Same as in Figure 63 for June Cases.

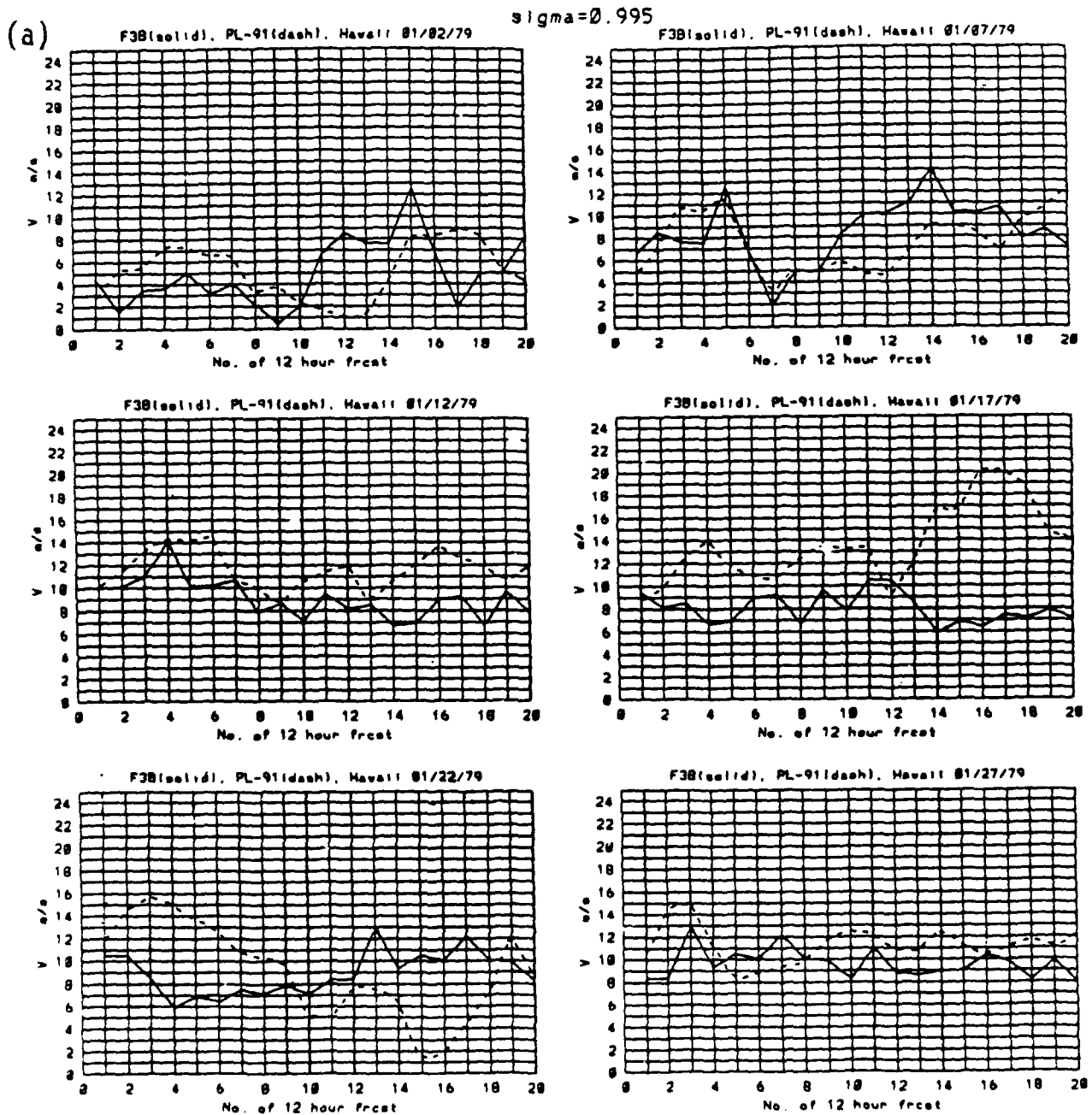


Figure 65. Time Series of $\sigma = 0.995$ FGGE III-b (Solid) and PL-91 (Dash) (a) Wind Speed (m/s), and (b) Wind Direction (Degrees) at Gridpoint Near Hawaii for Six January Cases.

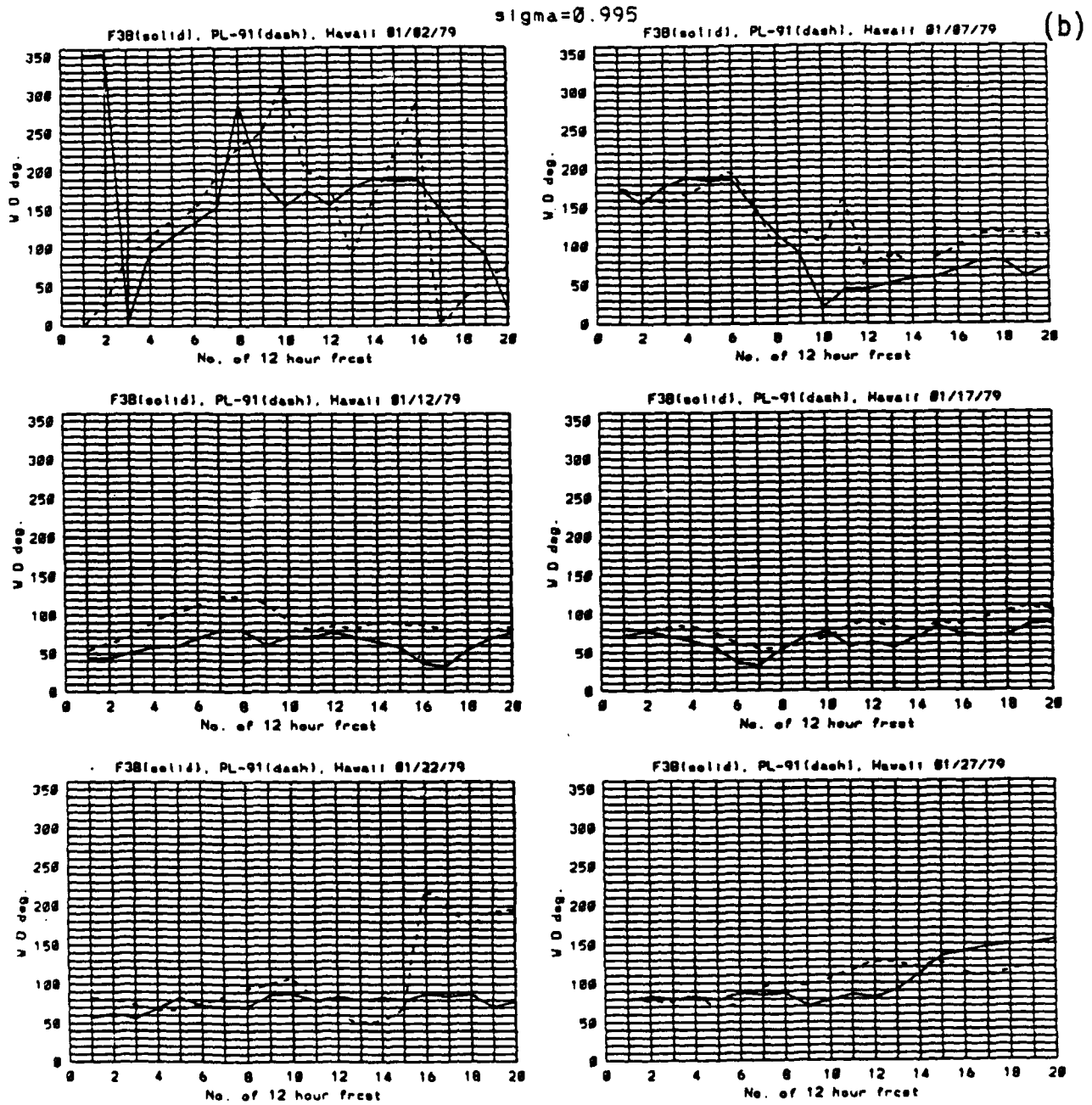


Figure 65. Time Series of $\sigma = 0.995$ FGGE III-b (Solid) and PL-91 (Dash) (a) Wind Speed (m/s), and (b) Wind Direction (Degrees) at Gridpoint Near Hawaii for Six January Cases.

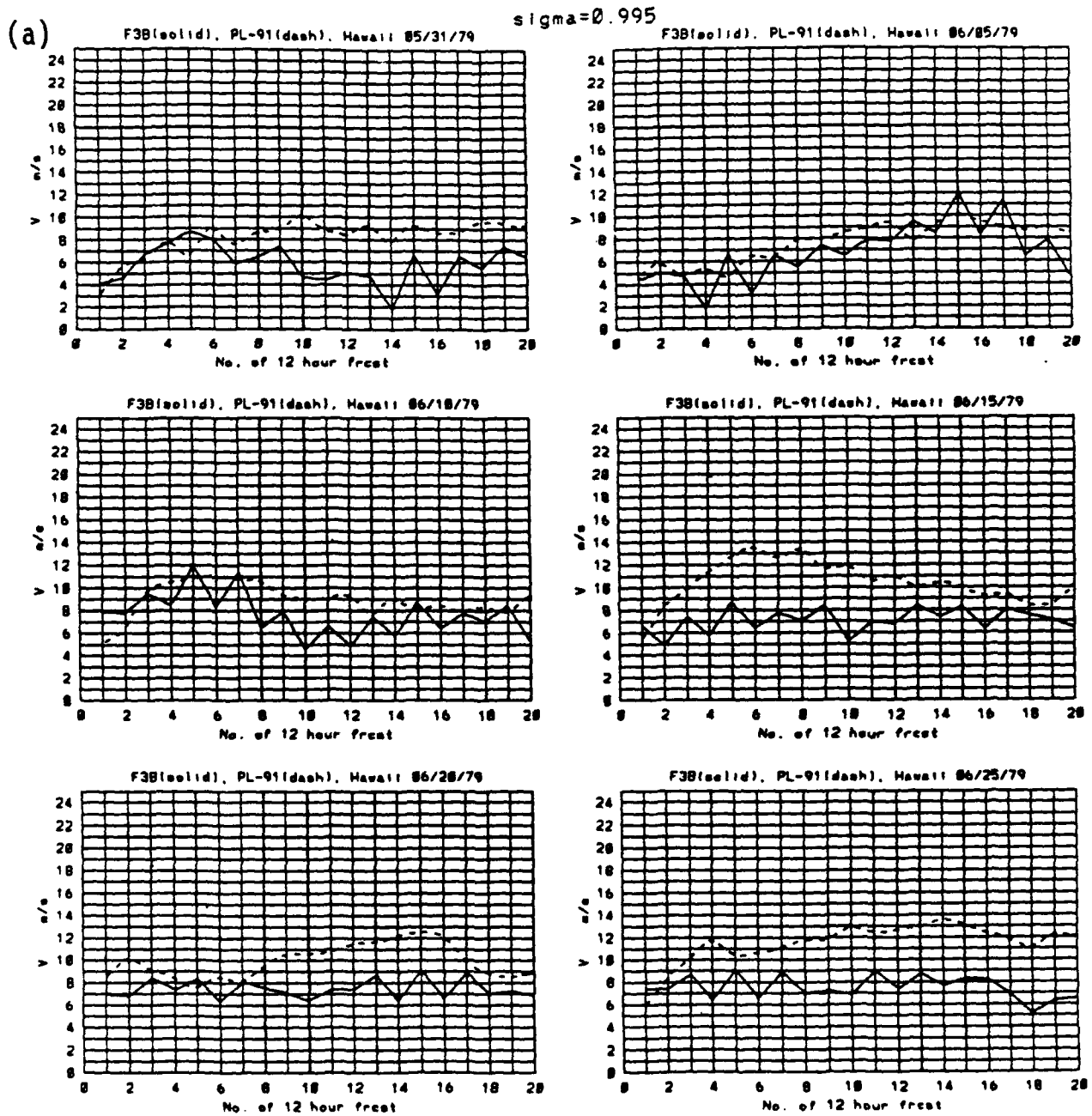


Figure 66. Same as in Figure 65 for June Cases.

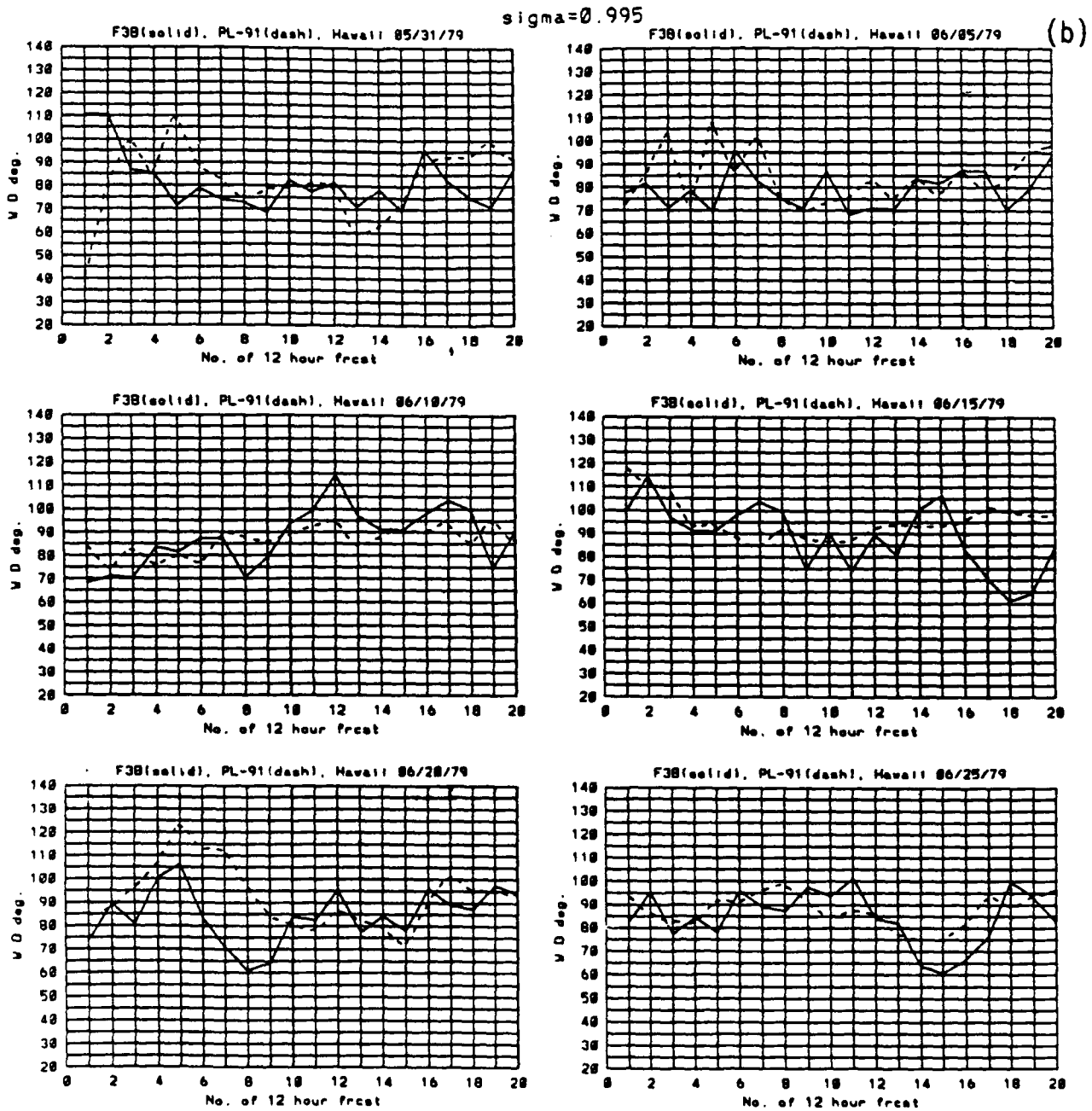


Figure 66. Same as in Figure 65 for June Cases.

sigma=0.960

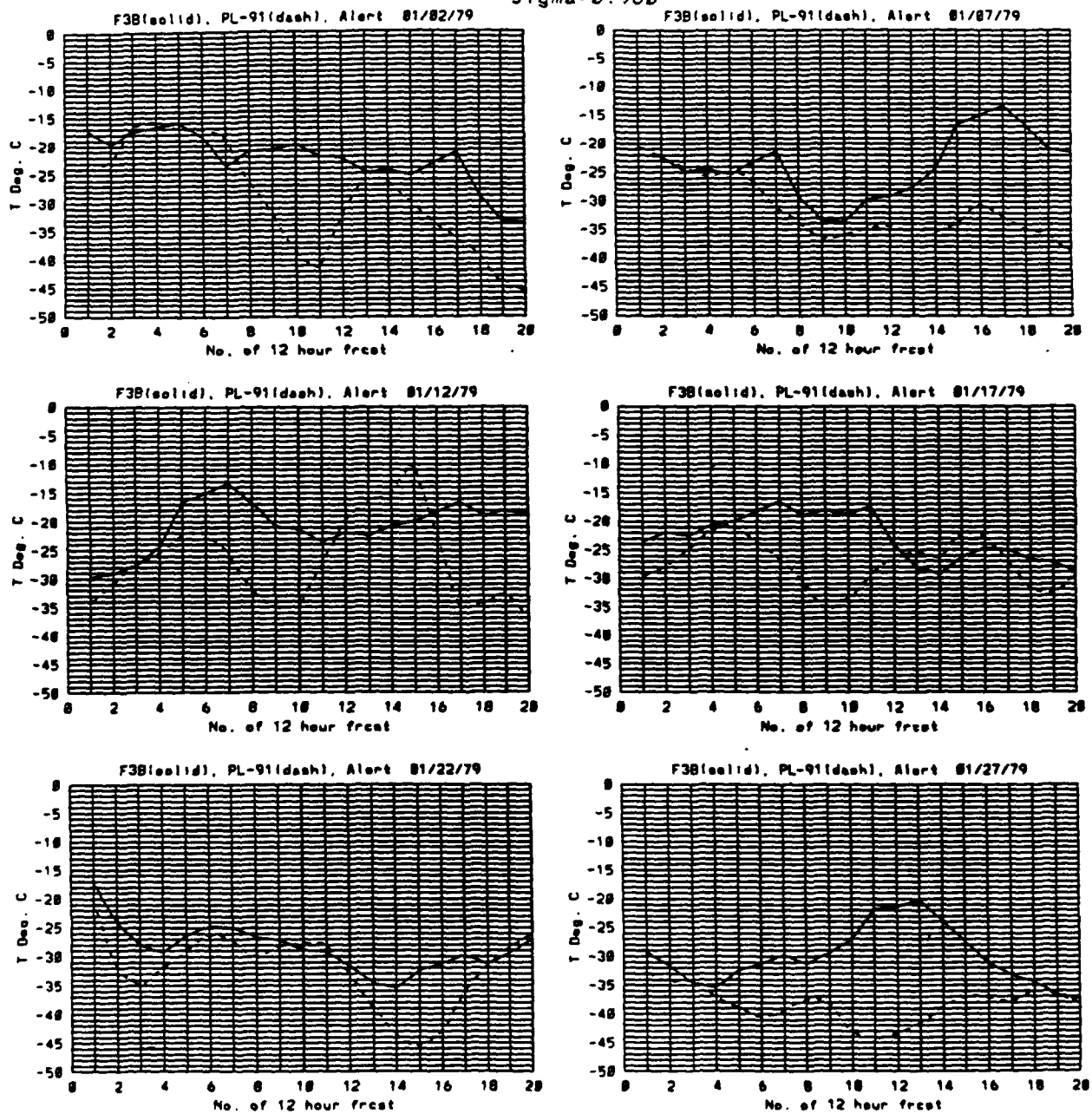


Figure 67. Time Series of $\sigma = 0.960$ FGGE III-b (Solid) and PL-91 (Dash) Temperature (C) at Gridpoint Near Alert for Six January Cases.

sigma=0.960

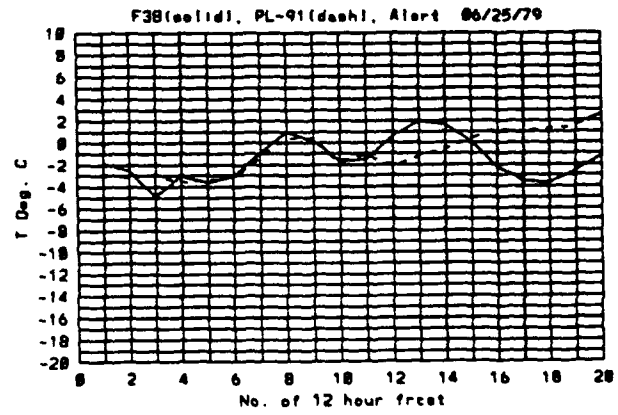
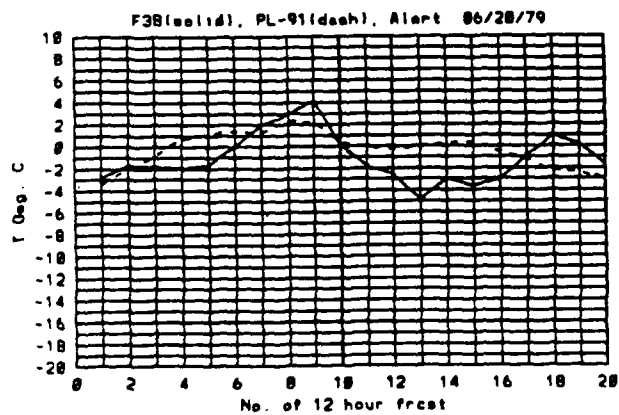
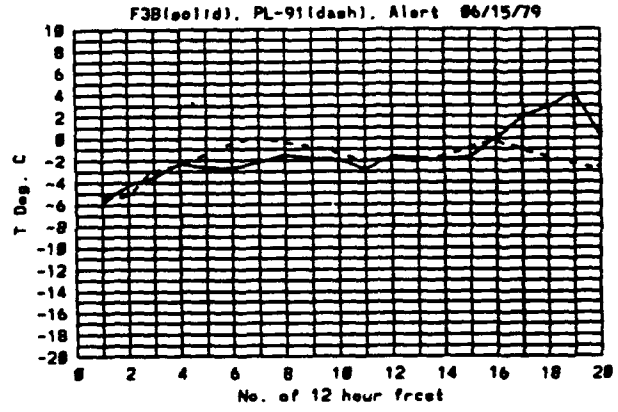
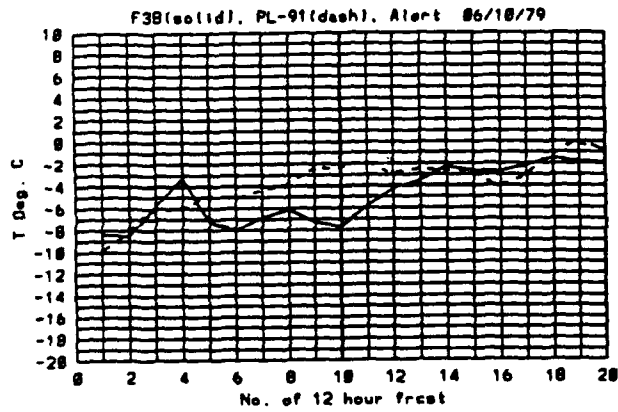
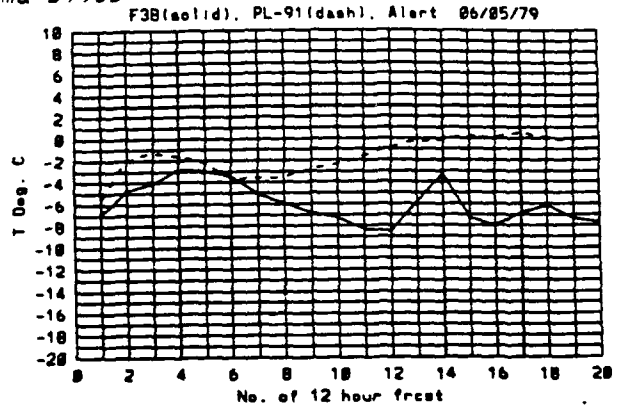
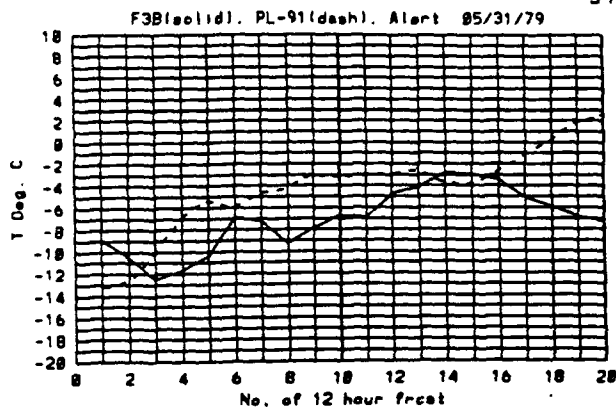


Figure 68. Same as in Figure 67 for June Cases.

sigma=0.960

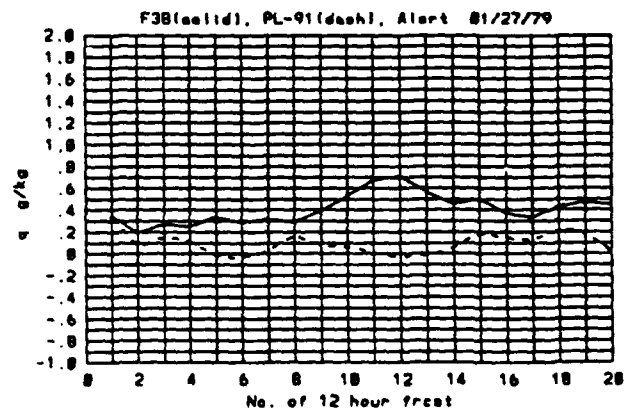
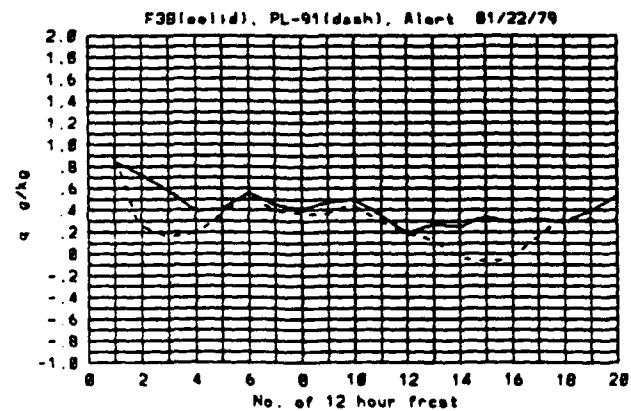
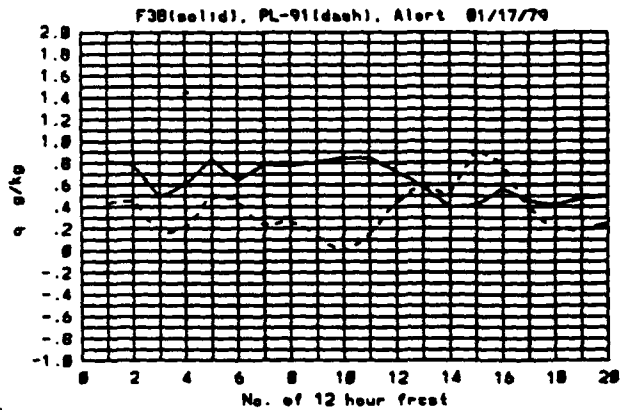
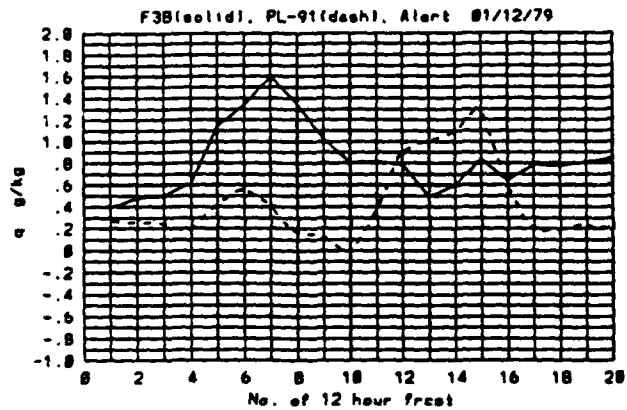
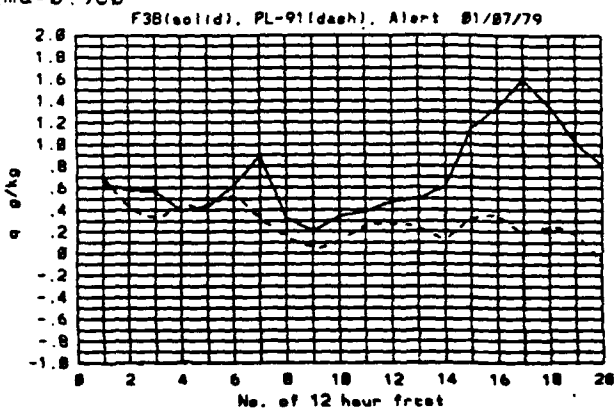
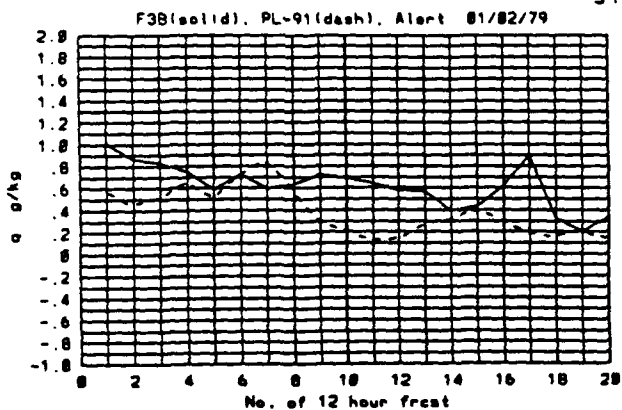


Figure 69. Same as in Figure 67 for Specific Humidity (g/kg).

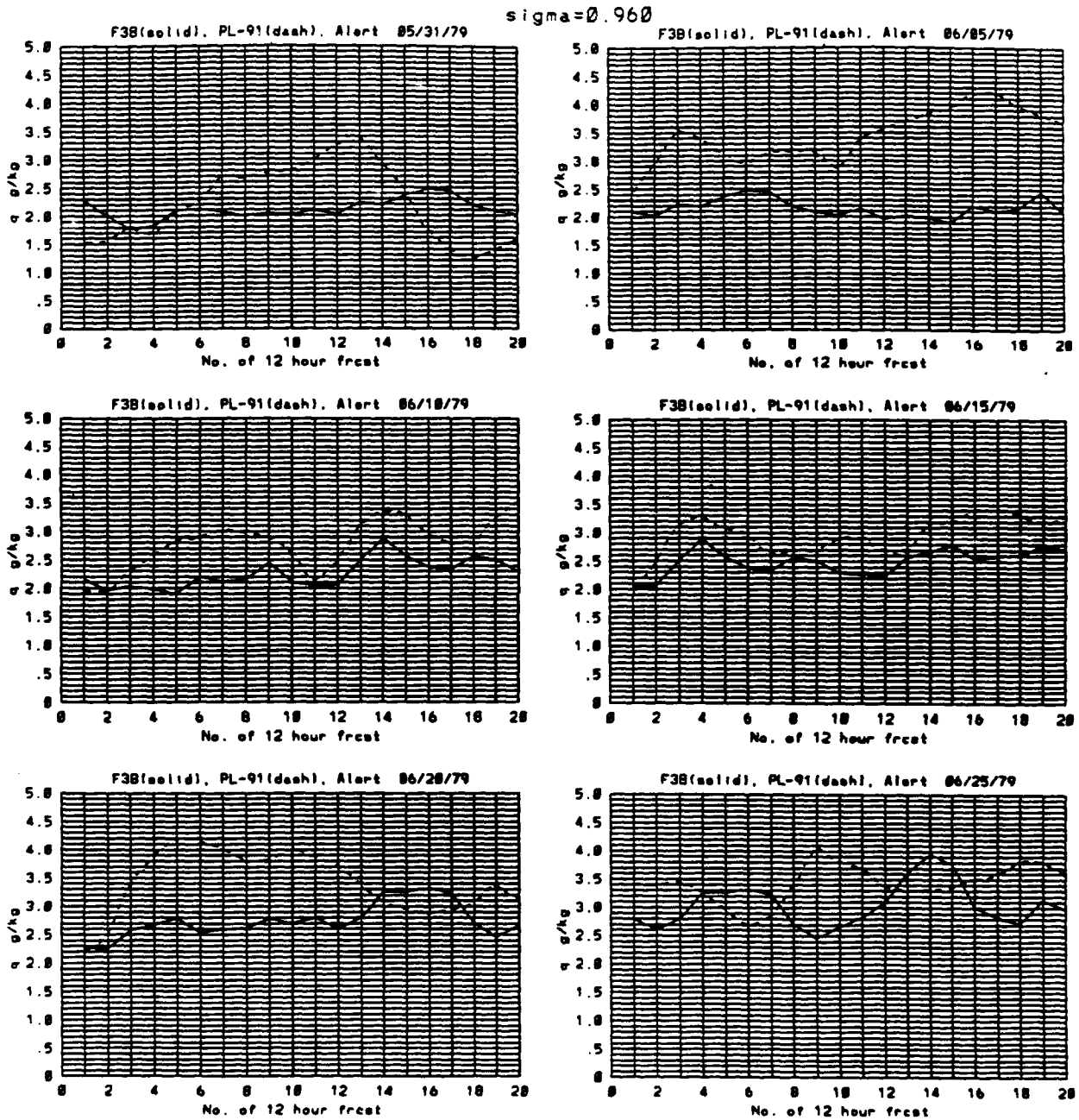


Figure 70. Same as in Figure 69 for June Cases.

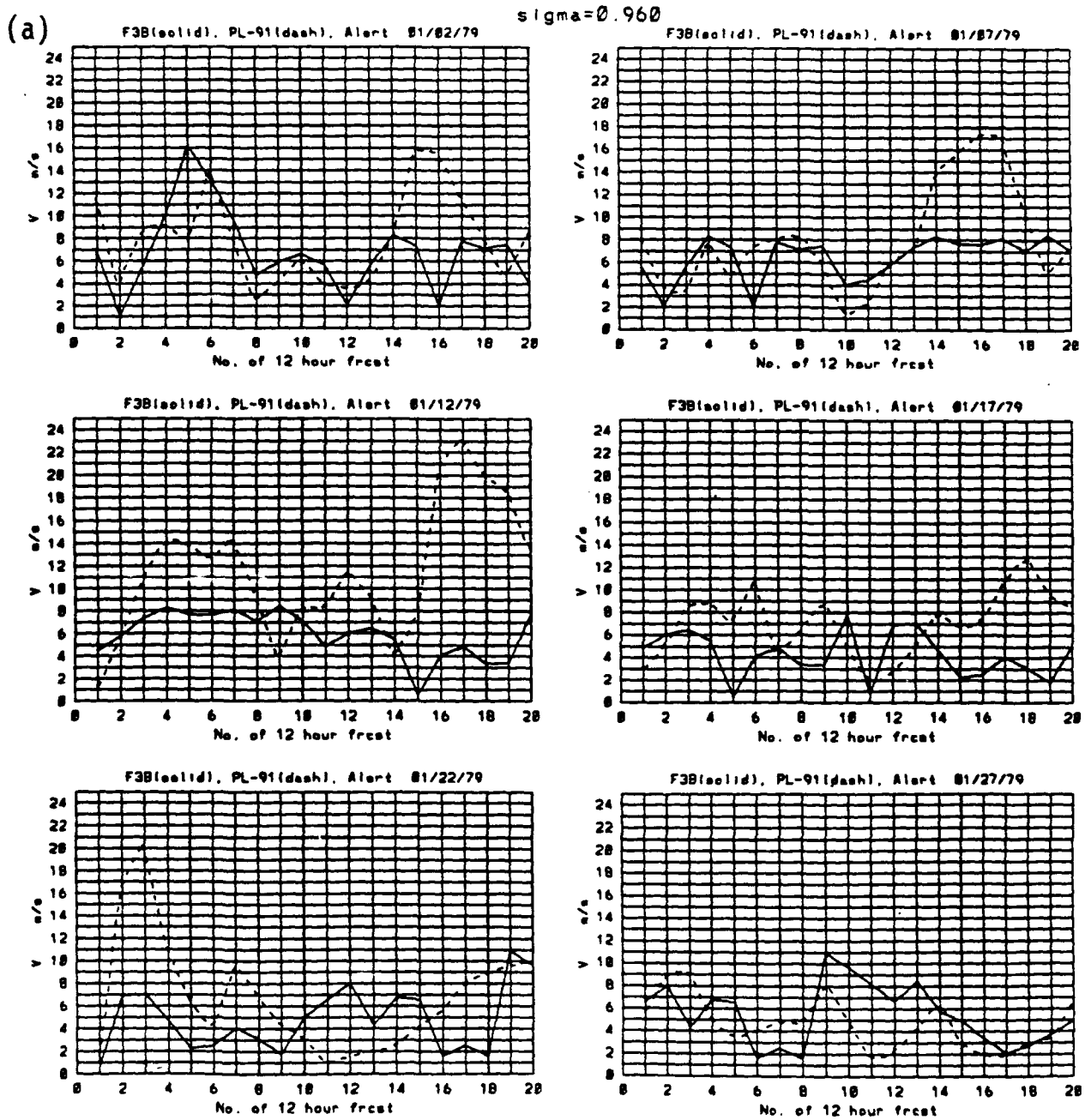


Figure 71. Time Series of $\sigma = 0.960$ FGGE III-b (Solid) and PL-91 (Dash) (a) Wind Speed (m/s), and (b) Wind Direction (degrees) at Gridpoint Near Alert for Six January Cases.

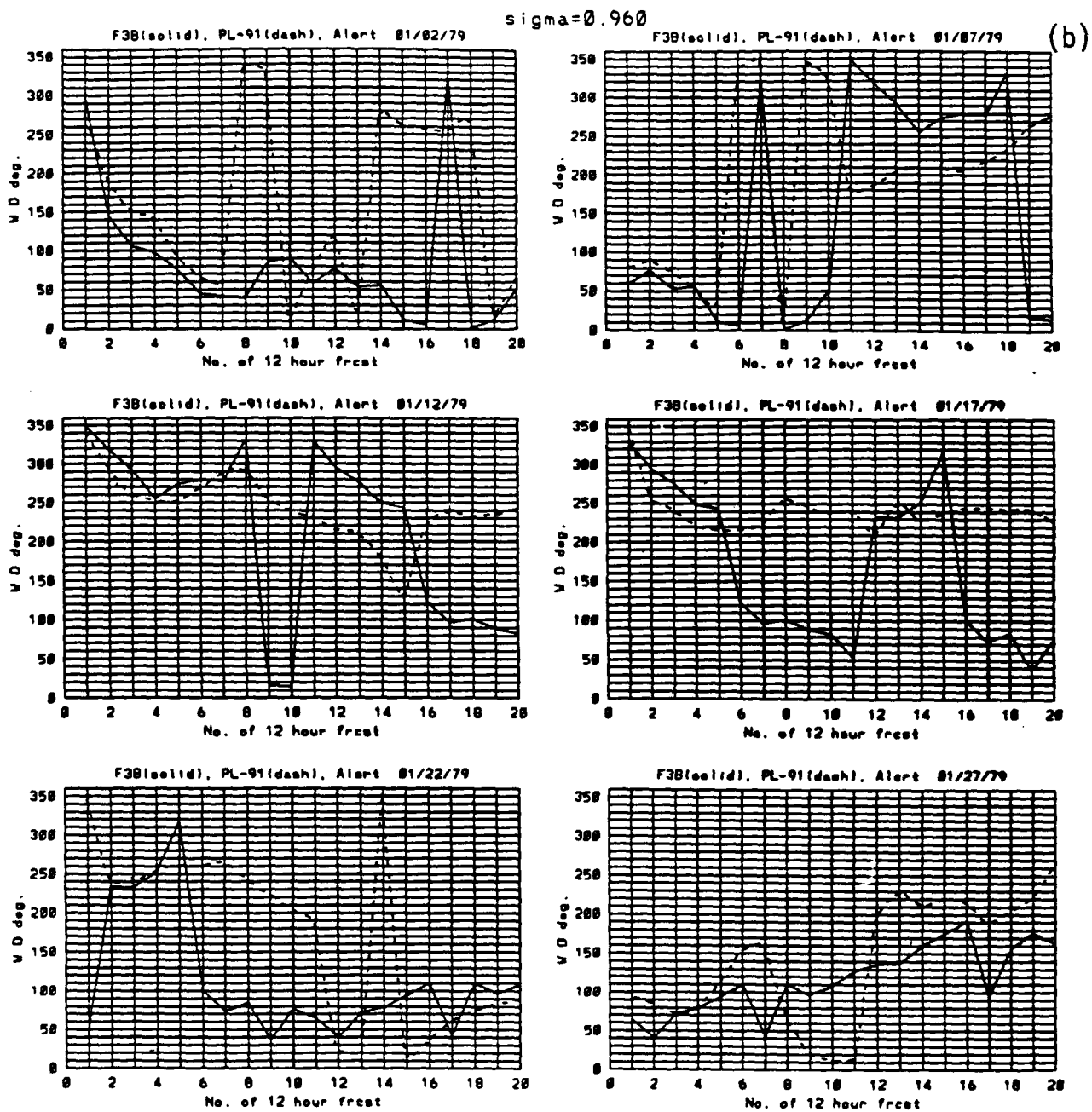


Figure 71. Time Series of $\sigma = 0.960$ FGGE III-b (Solid) and PL-91 (Dash) (a) Wind Speed (m/s), and (b) Wind Direction (degrees) at Gridpoint Near Alert for Six January Cases.

(a)

$\sigma = 0.960$

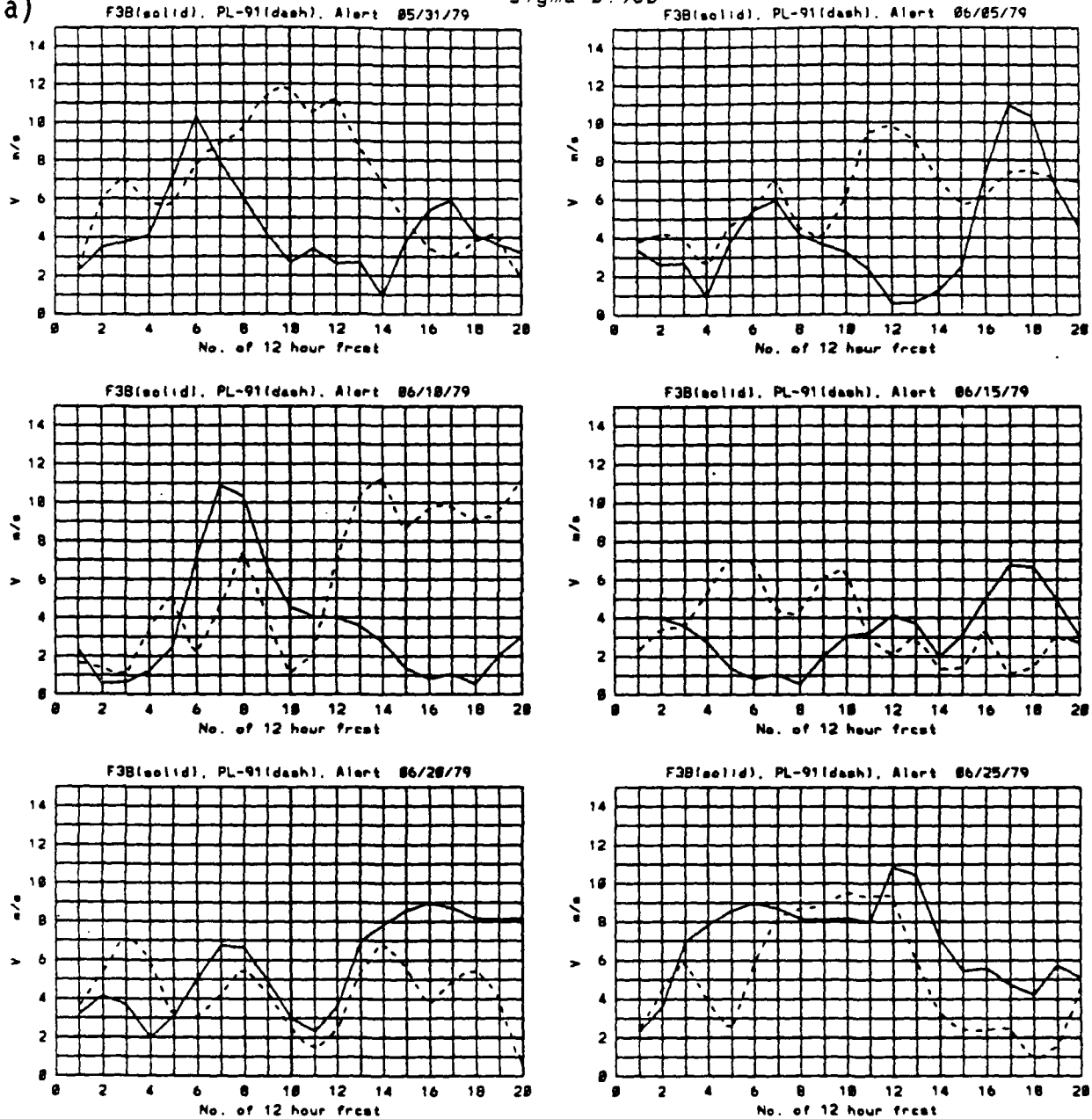


Figure 72. Same as in Figure 71 for June Cases.

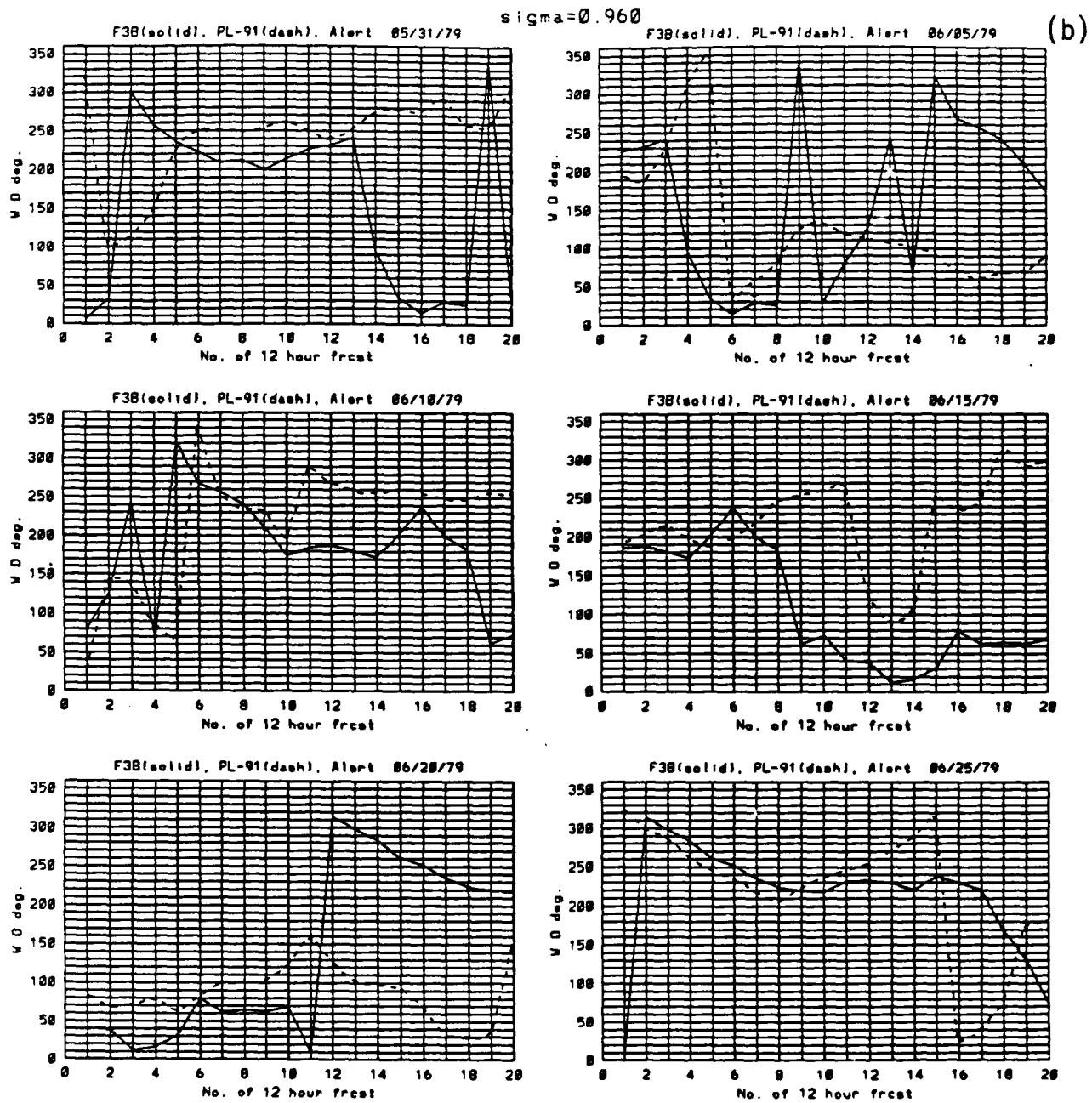


Figure 72. Same as in Figure 71 for June Cases.

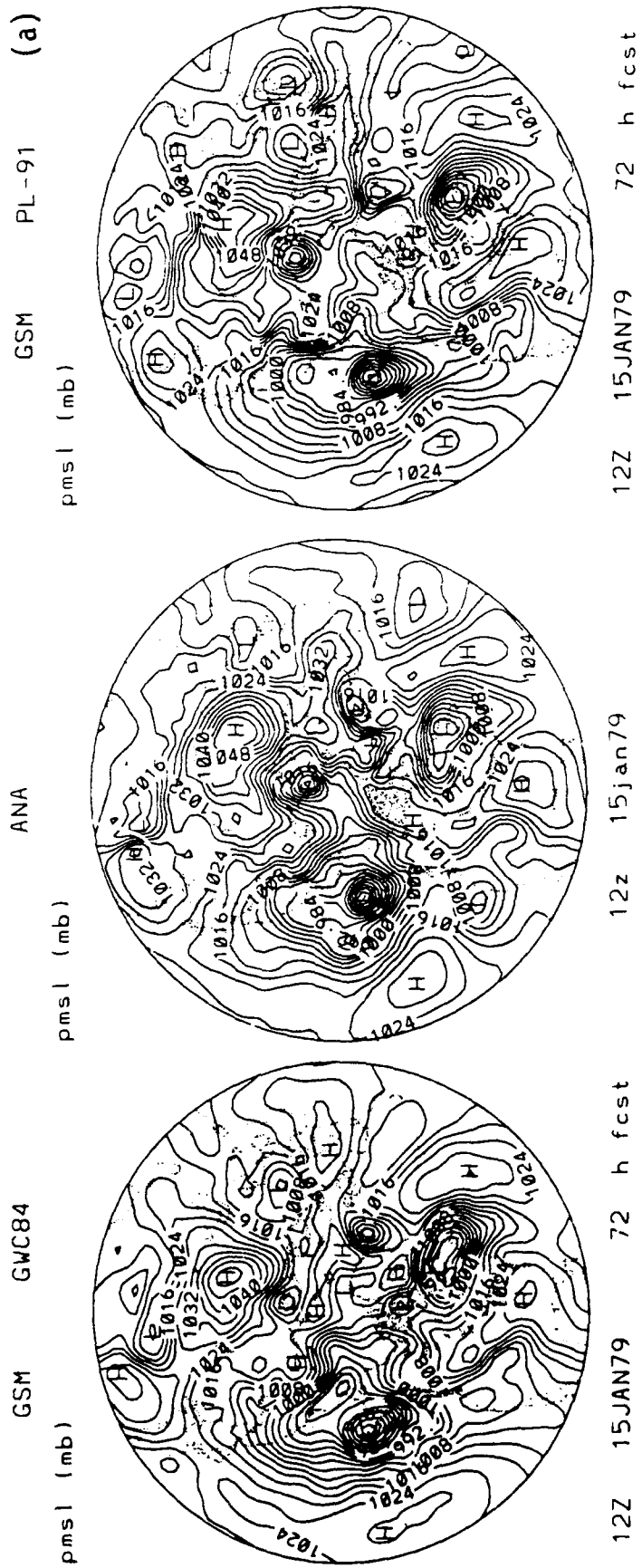


Figure 73. Northern Hemisphere (a) Mean Sea Level Pressure (Contour Interval - 4 mb) and (b) 500 mb Geopotential Height (Contour Interval - 6 decameters) for 72 Hour GWC84 and PL-91 1200 UTC 12 January 1979 Forecasts, and Verifying FGGE III-b Analysis.

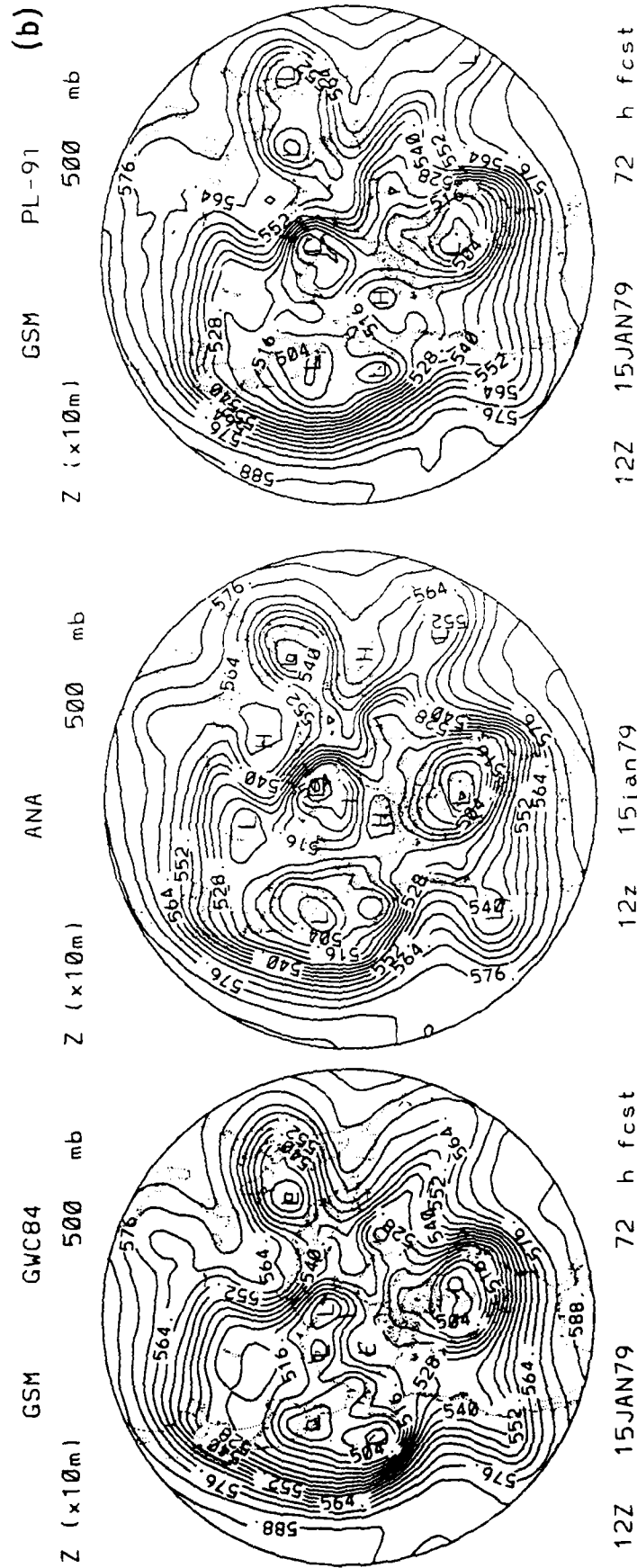


Figure 73. Northern Hemisphere (a) Mean Sea Level Pressure (Contour Interval - 4 mb) and (b) 500 mb Geopotential Height (Contour Interval - 6 decameters) for 72 Hour GWC84 and PL-91 1200 UTC 12 January 1979 Forecasts, and Verifying FGGE III-b Analysis.

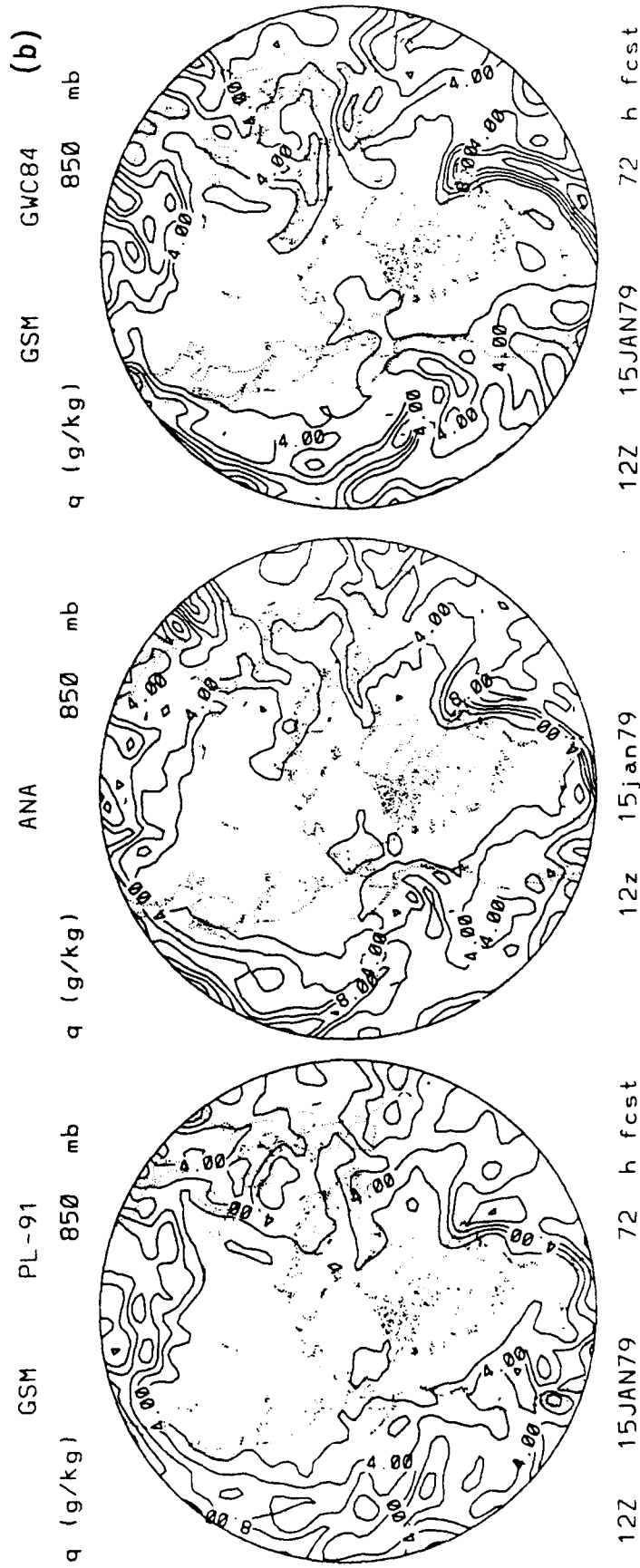


Figure 74. Northern Hemisphere (a) 850 mb Relative Humidity (Contour Interval = 20%) and (b) 850 mb Specific Humidity (Contour Interval = 2 g/kg) for 72 Hour GWC84 and PL-91 1200 UTC 12 January 1979 Forecasts, and Verifying FGGE III-b Analysis.

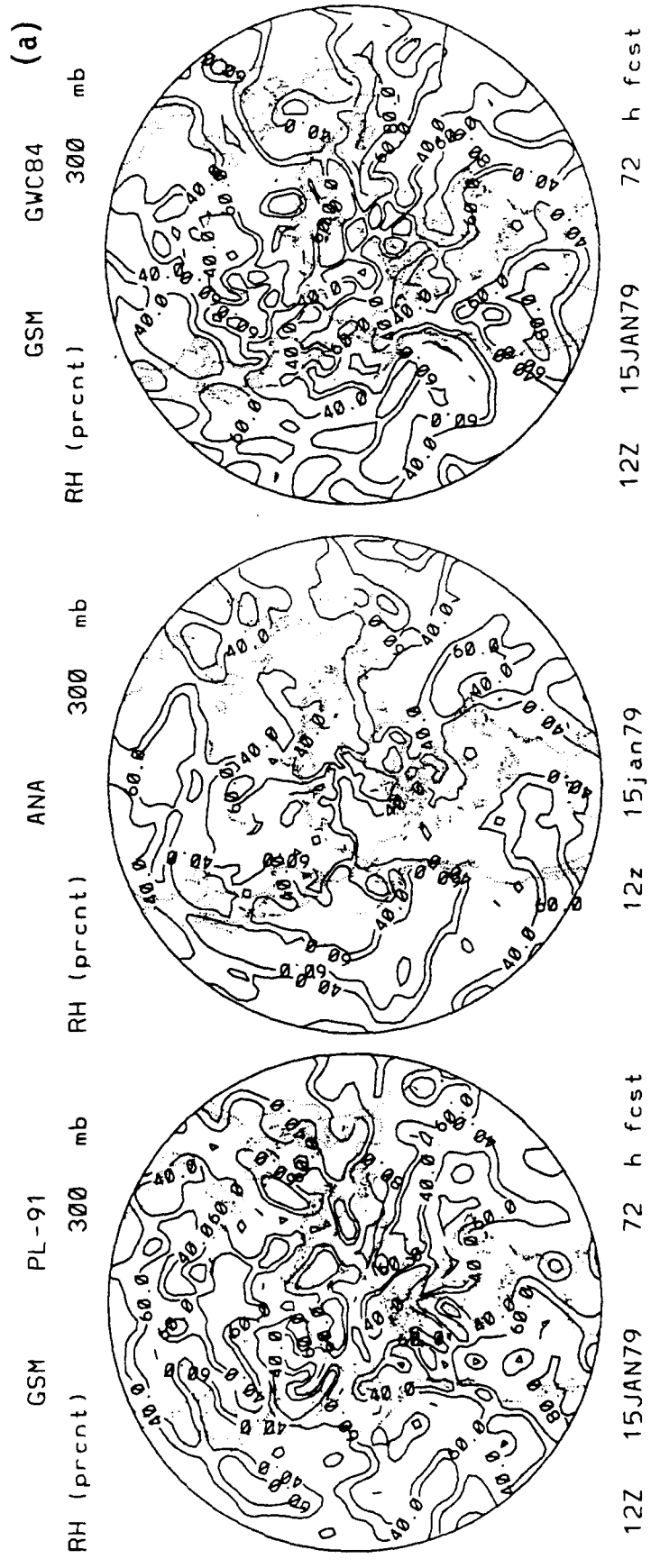


Figure 75. Northern Hemisphere (a) 300 mb Relative Humidity (Contour Interval = 20%) and (b) 200 mb Wind Speed (Contour Interval = 10 m/s) for 72 Hour GWC84 and PL-91 1200 UTC 12 January 1979 Forecasts, and Verifying FGGE III-b Analysis.

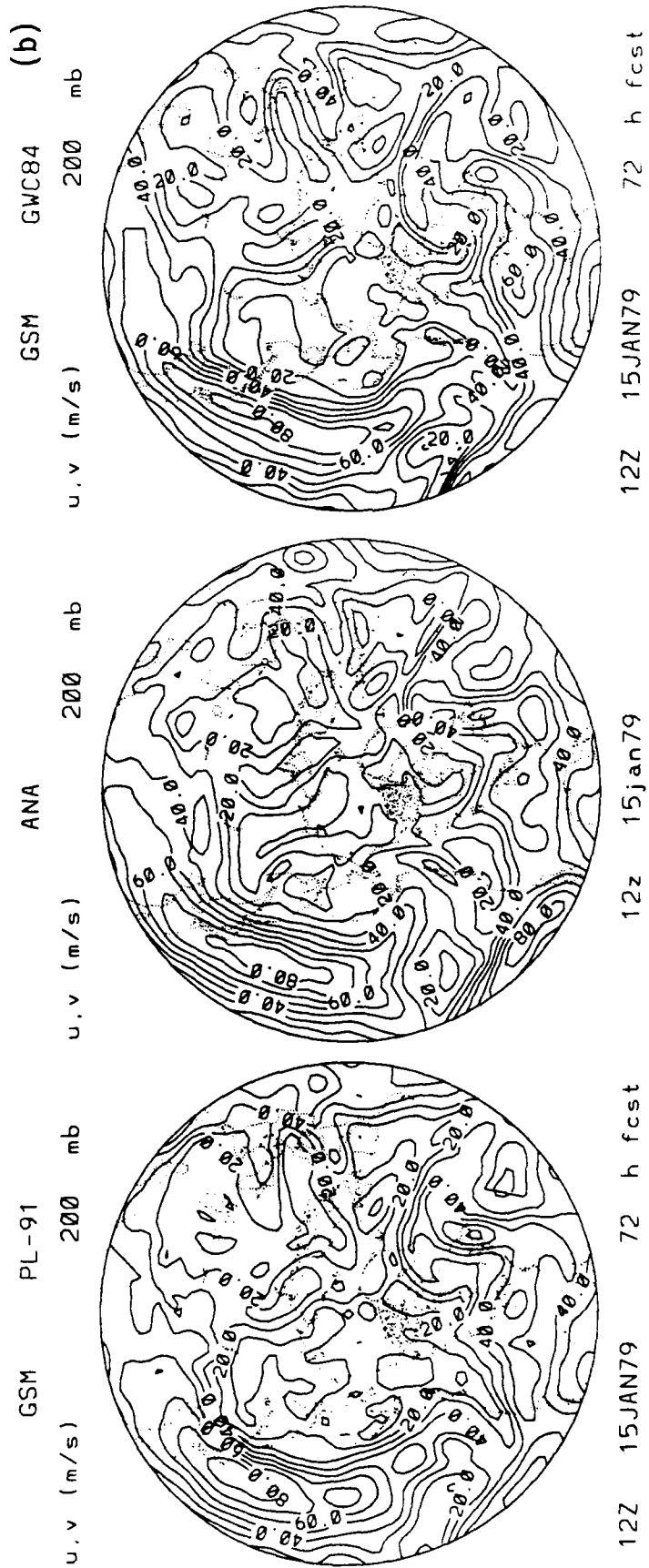
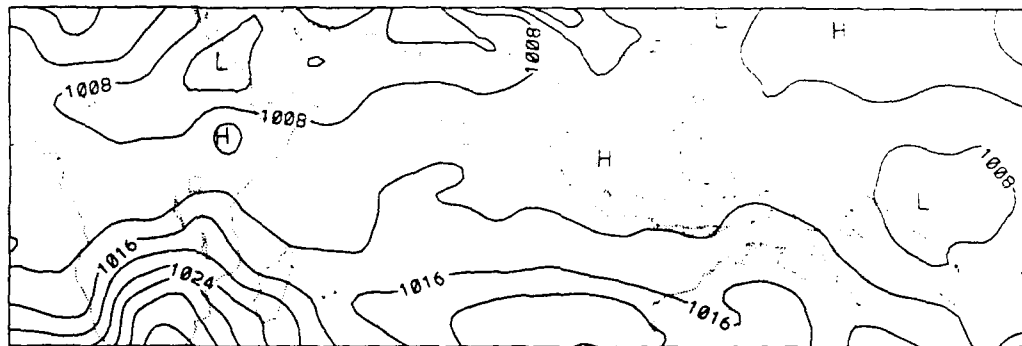


Figure 75. Northern Hemisphere (a) 300 mb Relative Humidity (Contour Interval = 20%) and (b) 200 mb Wind Speed (Contour Interval = 10 m/s for 72 Hour GWC84 and PL-91 1200 UTC 12 January 1979 Forecasts, and Verifying FGGE III-b Analysis.

GSM GWC84

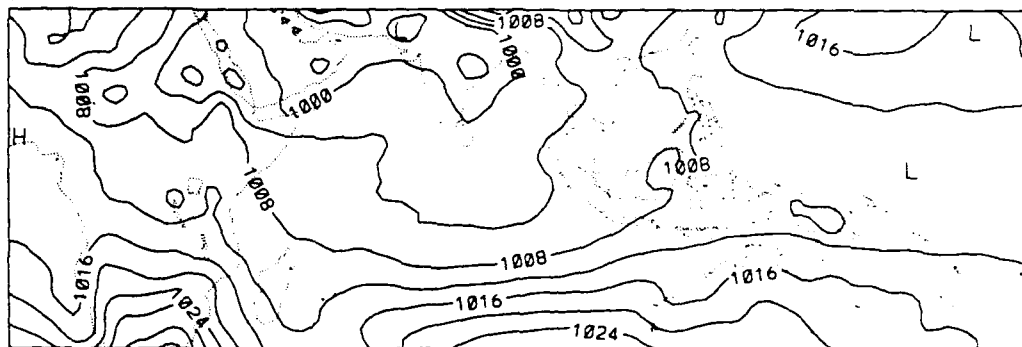
pmsl (mb)



12Z 13JUN79 72 h fcst

ANA

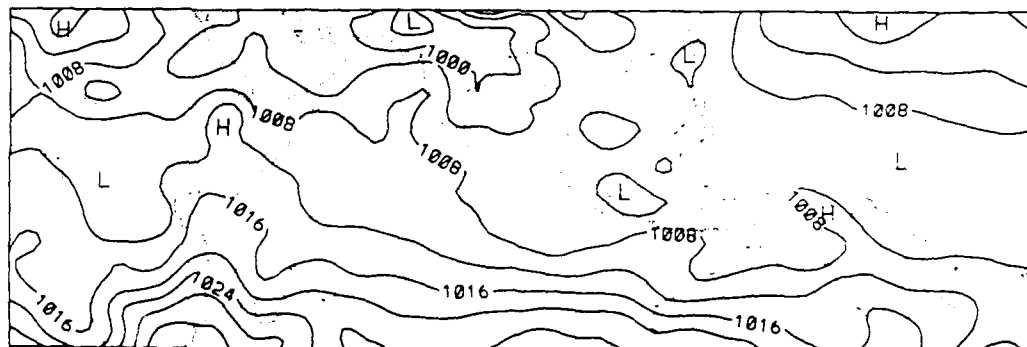
pmsl (mb)



12z 13jun79

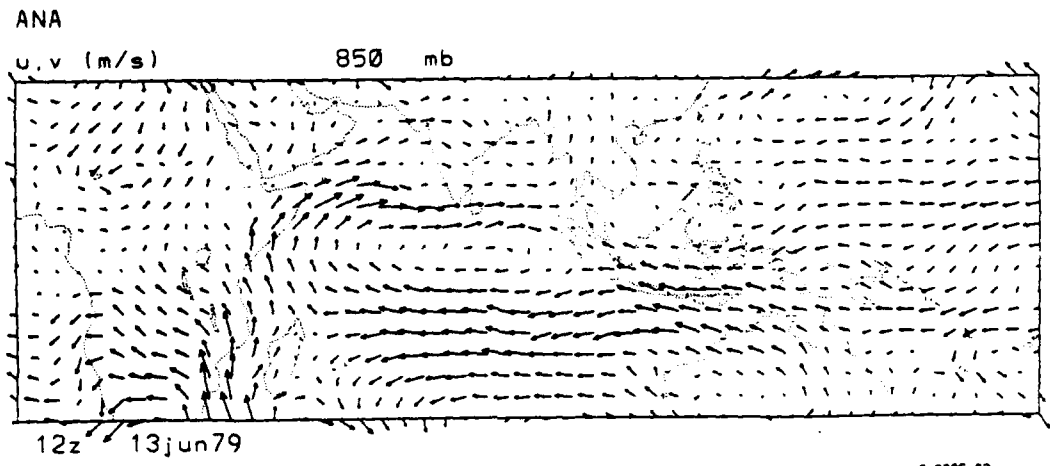
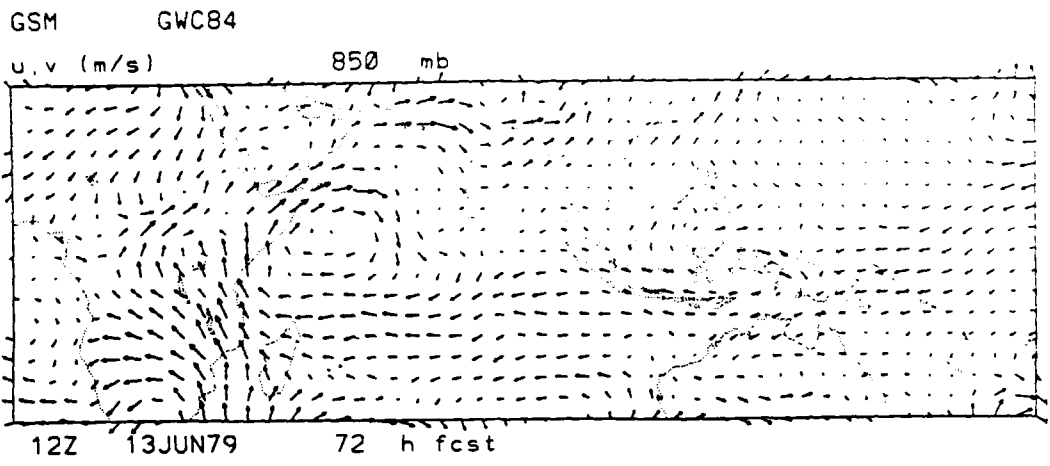
GSM PL-91

pmsl (mb)



12Z 13JUN79 72 h fcst

Figure 76. Eastern Hemisphere Tropical (30S to 30N) Mean Sea Level Pressure (Contour Interval = 4 mb) for 72-Hour GWC84 and PL-91 1200 UTC 10 June 1979 Forecasts and Verifying FGGE III-b Analysis.



0.338E+02
 MAXIMUM VECTOR

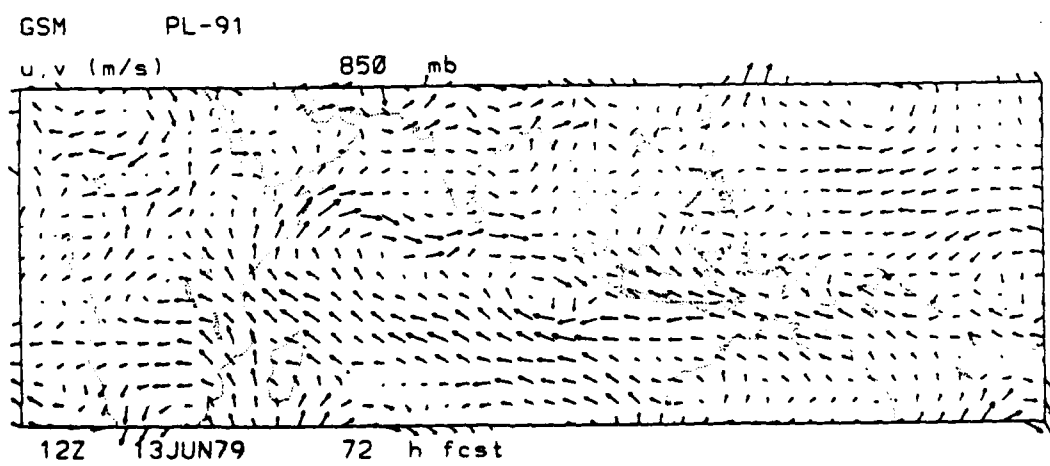


Figure 77. Same as in Figure 76 for 850 mb Wind.

GSM GWC84

q (g/kg) 850 mb



12Z 13JUN79 72 h fcst

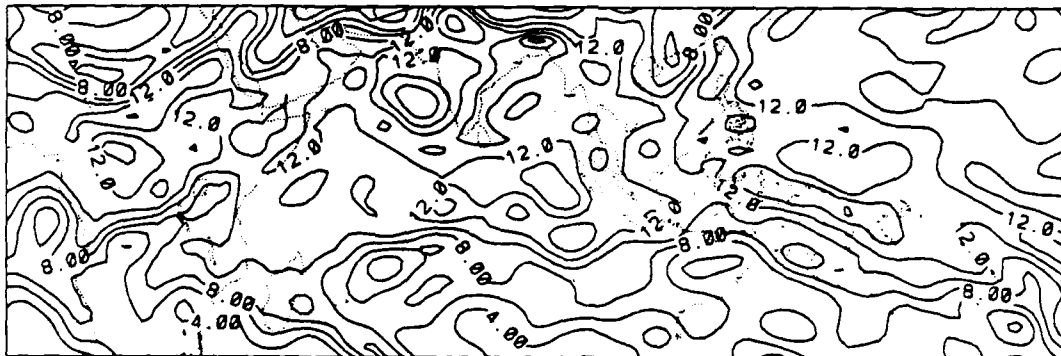
ANA

q (g/kg) 850 mb



12z 13jun79

q (g/kg) 850 mb

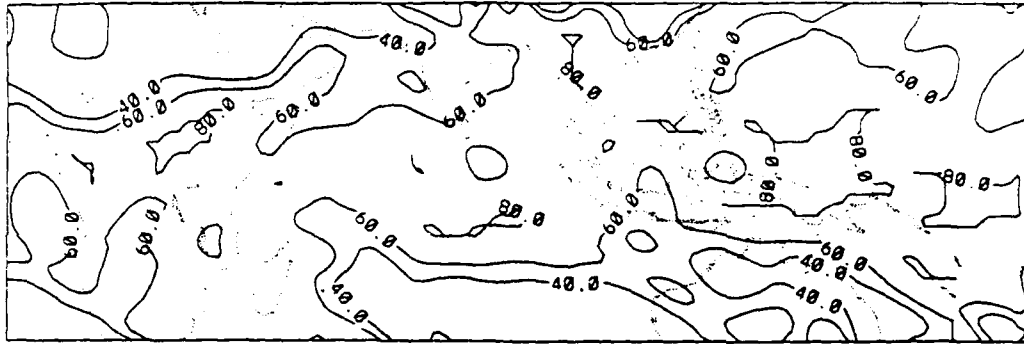


12Z 13JUN79 72 h fcst

Figure 78. Same as in Figure 76 for 850 mb Specific Humidity (Contour Interval = 2 g/kg).

GSM GWC84

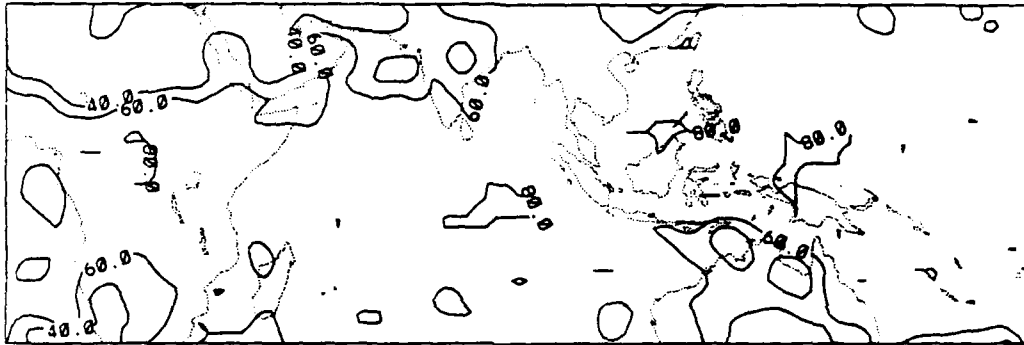
RH (prcnt) 850 mb



12Z 13JUN79 72 h fcst

ANA

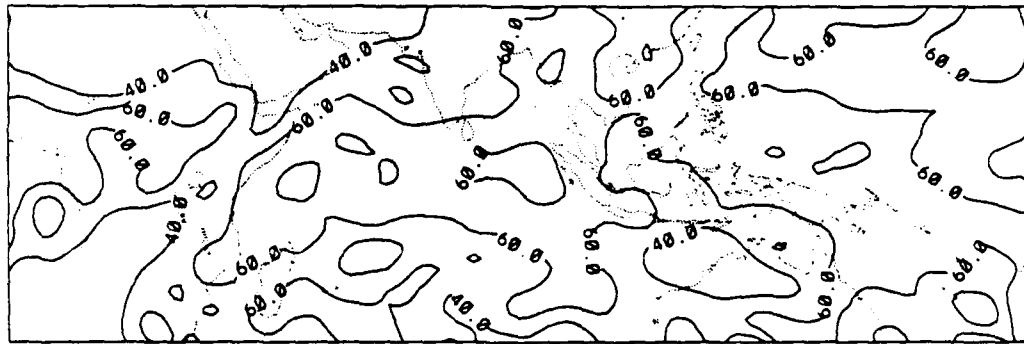
RH (prcnt) 850 mb



12z 13jun79

GSM PL-91

RH (prcnt) 850 mb

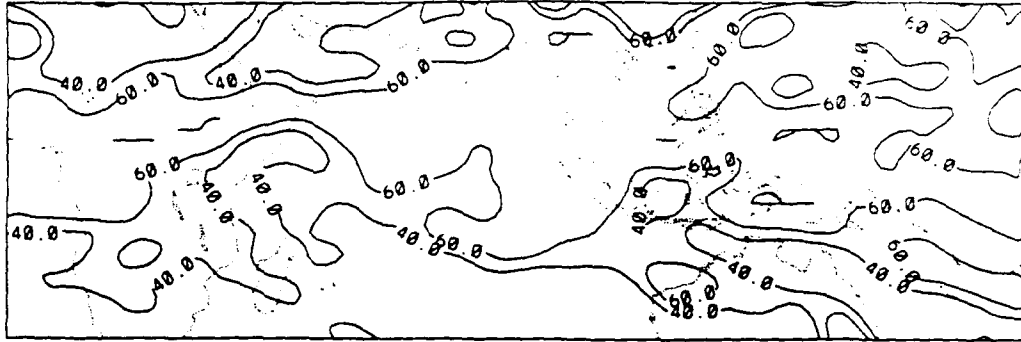


12Z 13JUN79 72 h fcst

Figure 79. Same as in Figure 76 for 850 mb Relative Humidity (Contour Interval = 20%).

GSM GWC84

RH (prcnt) 700 mb



12Z 13JUN79 72 h fcst

ANA

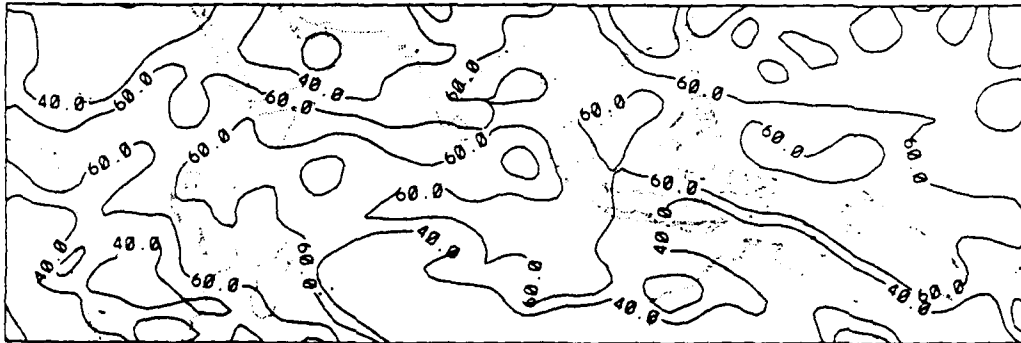
RH (prcnt) 700 mb



12z 13jun79

GSM PL-91

RH (prcnt) 700 mb

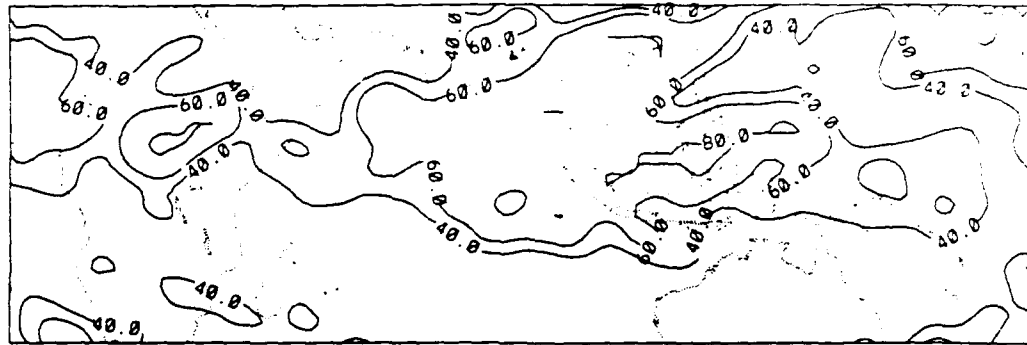


12Z 13JUN79 72 h fcst

Figure 80. Same as in Figure 79 for 700 mb.

GSM GWC84

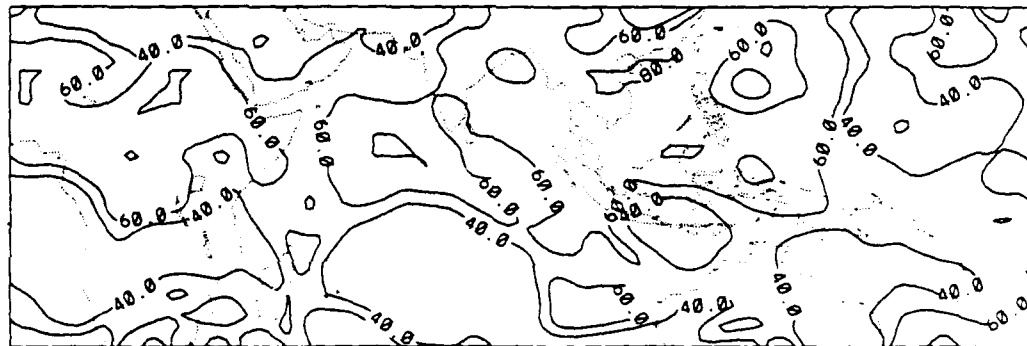
RH (prcnt) 400 mb



12Z 13JUN79 72 h fcst

ANA

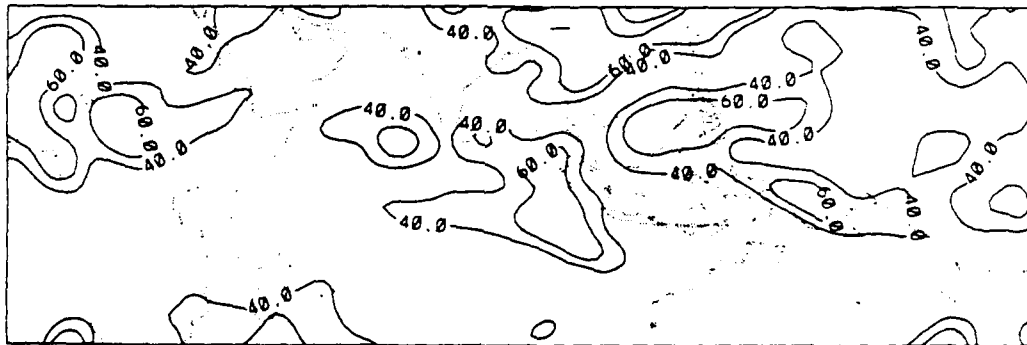
RH (prcnt) 400 mb



12z 13jun79

GSM PL-91

RH (prcnt) 400 mb



12Z 13JUN79 72 h fcst

Figure 81. Same as in Figure 79 for 400 mb.

humidity at 850, 700, and 400 mb over the tropical (30N-30S) Eastern Hemisphere. The relative humidity fields (both forecast and analysis) were smoothed before they were plotted.

An advantage of the color-filled version of the figures is that they allow quantitative comparisons to be made much more readily than the black-and-white contours. This is especially true of fields like mean sea level pressure, where one must count the contour lines to compare amplitudes of the features. Even so, the referenced black-and-white figures show clearly that by 72 hours of forecast time, both versions of the PL GSM have departed from the analyzed fields in both phase and amplitude. We have not yet conducted an exhaustive study of the animations to determine forecast error trends for the PL GSM versions; however, a brief discussion of what we have noticed from the 12 January 1979 1200 UTC forecasts is included in Section 5.

4.4 Forecast Precipitation, Evaporation, and Cloud Results

The three versions of the PL GSM (GWC84, GL-89, PL-91) simulate precipitation and evaporation of water from the surface (GWC84 evaporates over oceans only). All three versions share the same large-scale (stratiform) precipitation parameterization scheme; however, as shown in Table 1, they have quite different convective parameterization schemes. As we shall see, different convective parameterizations can have differing impacts on the performance of the stratiform parameterization scheme (as well as on other parameterizations in the model).

The results discussed below were developed in the following manner. The global average precipitation and evaporation rates for all of the six cases were averaged to produce the January and June ensemble means. For the accumulated precipitation amounts, we summed Days 2-6 accumulations over the six cases to arrive at the monthly accumulation for each model Gaussian gridpoint. Day 1 precipitation was not used in order to allow the model to adjust to the initial state. The six five-day accumulations represent all of the precipitation the model produced for the periods

3 January 1979 1200 UTC - 2 February 1979 1200 UTC (January accumulation) and 1 June 1979 1200 UTC - 1 July 1979 1200 UTC (June accumulation).

Table 3 displays the global average precipitation and evaporation rates (in mm/day) during Days 2-6 of the January and June cases. The evaporation rates for GWC84 were not saved, but should be much lower than the corresponding rates for GL-89 and PL-91 since GWC84 considered evaporation only over the oceans.

Table 3. Global Average Precipitation and Evaporation Rates (mm/day)

	January			June		
	GWC84	GL-89	PL-91	GWC84	GL-89	PL-91
Total Precipitation	1.07	2.88	3.15	1.08	3.14	3.36
Convective Precipitation	0.10	1.17	2.05	0.10	1.46	2.30
Evaporation		2.98	3.33		3.08	3.43

The global average total (stratiform plus convective) precipitation rates may be compared with the climatological values computed by Jaeger²⁸ of 2.56 mm/day for January and 2.97 mm/day for June. Averaged over the two seasons, the stratiform precipitation accounts for 90, 55, and 33 percent of the total for GWC84, GL-89, and PL-91, respectively. Evaporation rates are in approximate balance with precipitation rates over the five-day forecast periods in January and June for both GL-89 and PL-91. Figure 82 shows the global average total precipitation and evaporation rates for the January and June cases as a function of forecast time. The diurnal signal in the GL-89 and PL-91 curves result from the bulk of the precipitation being concentrated at certain longitudes in the tropics. A "spin-up" of precipitation is apparent in GWC84 and GL-89, while a "spin-down" occurs in the PL-91 experiments. The approximate precipitation-evaporation balance in GL-89 and PL-91 occurs by the end of Day 2.

²⁸Jaeger, L. (1983) Monthly and areal patterns of mean global precipitation, in *Variations in the Global Water Budget*, A. Street-Perrott, M. Beran, R. Ratcliffe, Eds., D. Reidel, Dordrecht.

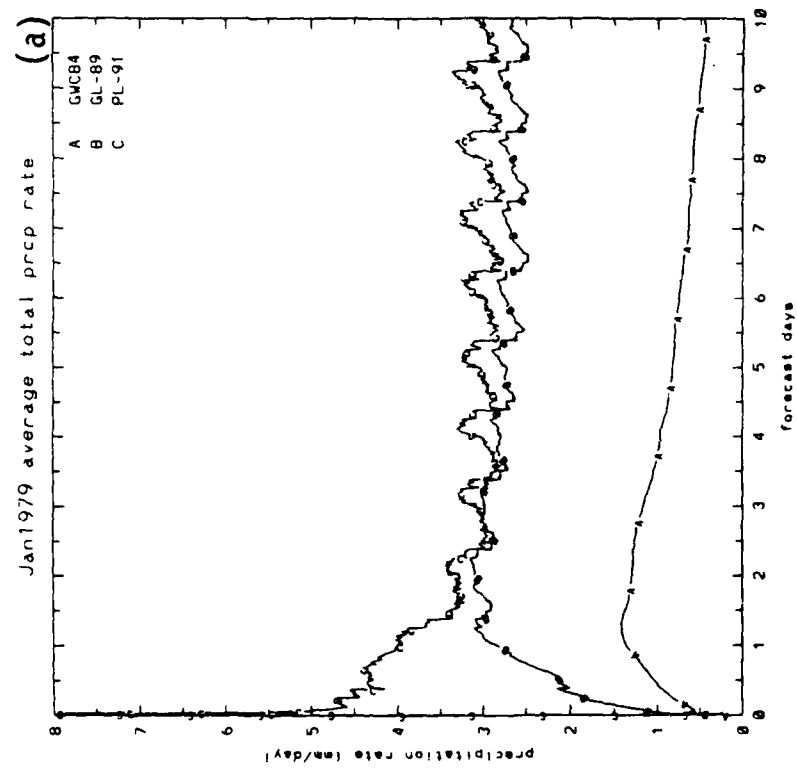
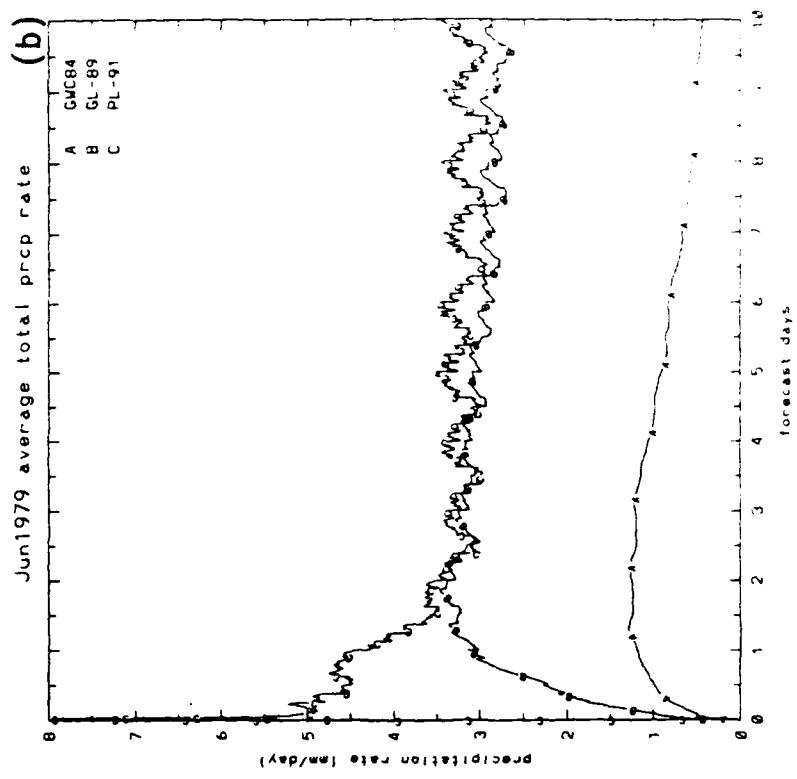


Figure 82. Global Average (a) and (b) Precipitation Rate (mm/day) and (c) and (d) Evaporation Rate (mm/day) Averaged over Six January [(a) and (c)] and June [(b) and (d)] Forecasts.

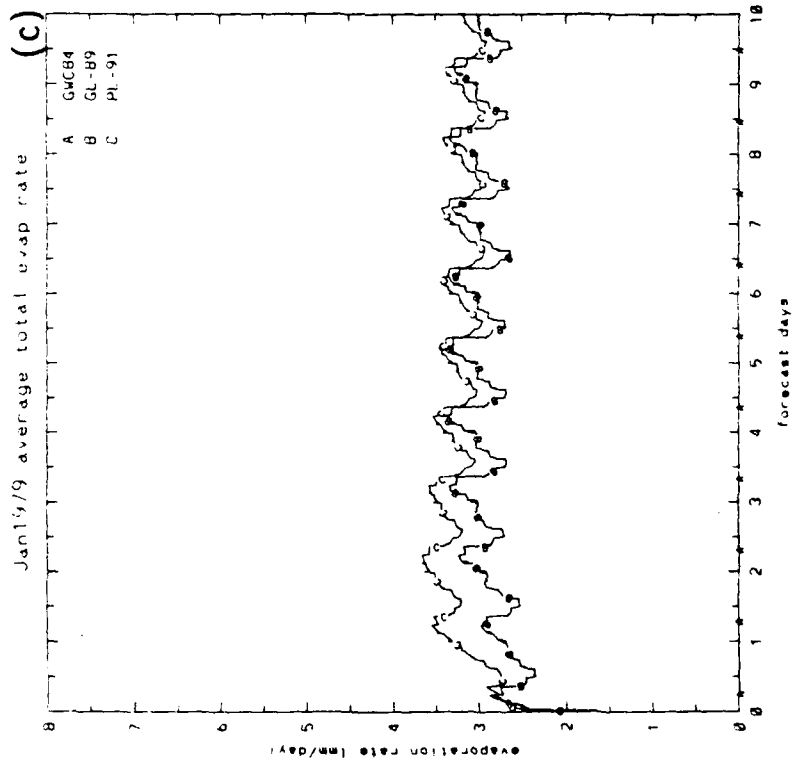
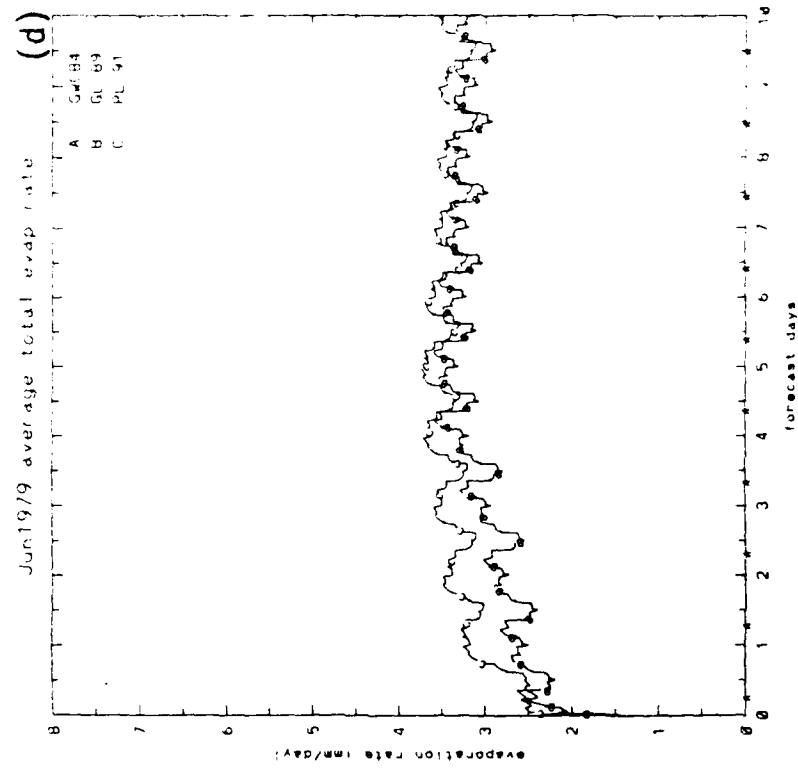


Figure 82. Global Average (a) and (b) Precipitation Rate (mm/day) and (c) and (d) Evaporation Rate (mm/day) Averaged over Six January [(a) and (c)] and June [(b) and (d)] Forecasts.

Figure 83 depicts the meridional cross-sections of the monthly accumulation in January and June for the three versions of the model. For reference, the climatological values from Jaeger²⁹ are also plotted. Figures 84 and 85 show the geographic distributions of the accumulated precipitation for all three model versions in January and June, respectively. As was shown in Norquist and Yang,¹² the GL-89 version produces the tropical maxima in the locations indicated by precipitation climatology and outgoing longwave radiation (OLR) observations. PL-91 produces maxima in approximately the same locations but with somewhat greater amounts. PL-91 also produces what appears to be excessive maxima in certain regions of the winter hemisphere side of the equator (which are also apparent in the zonal means in Figure 83).

The PL-91 version of PL GSM includes a cloud parameterization scheme based on that of Slingo²⁹. Schattel¹⁶ has described its formulation and its performance based on the January experiments. The Slingo scheme was modified to yield more realistic cloud amounts in PL-91. In particular, the original Slingo scheme with its cirrus anvil formulation was generating too much high cloud. This feature was removed, and the critical relative humidity (the threshold above which cloudiness is inferred) was made to increase linearly from 80 to 100 percent with decreasing σ through the high cloud deck. We made this modification to reduce the excessive high cloudiness found in PL-91 resulting from the version's tendency to be overly moist in the high cloud deck. We also set the top of the high clouds to $\sigma = 0.2$ in the tropics to help alleviate this problem, as we noted many instances of saturation or near-saturation above $\sigma = 0.2$ due to this same moisture build-up. However, this limitation probably imposed a cap too low in altitude on tropical convection as suggested by OLR results presented by Schattel.¹⁶ As can be seen in Figure 86, PL-91 still produces an abundance of high cloud at most latitudes when compared to the

²⁹Slingo, J. (1987) The Development and Verification of a Cloud Prediction Scheme for the ECMWF Model, *Quart. J. Roy. Meteor. Soc.*, 113:899-927.

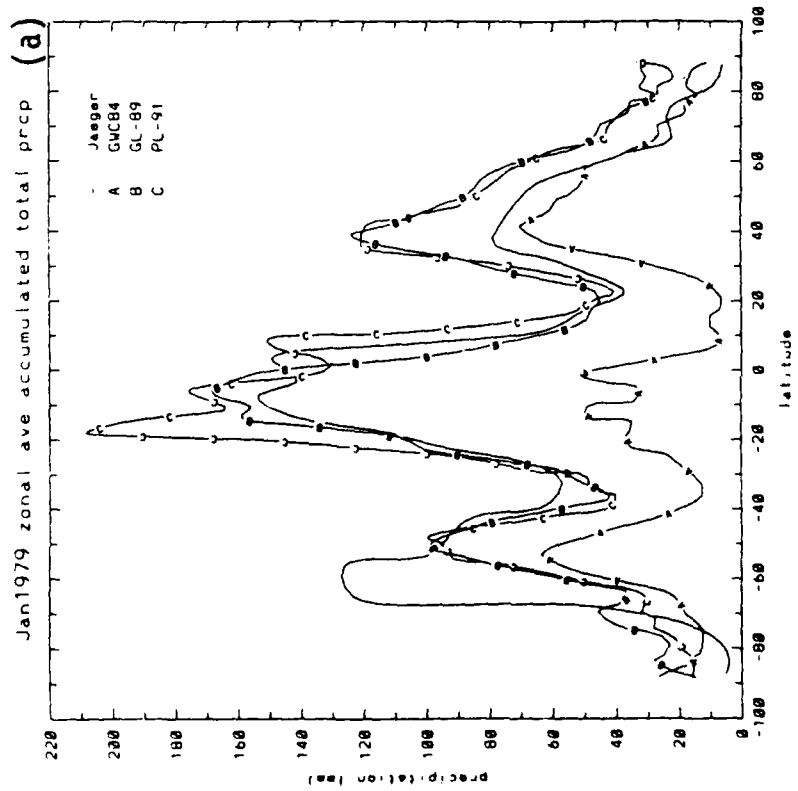
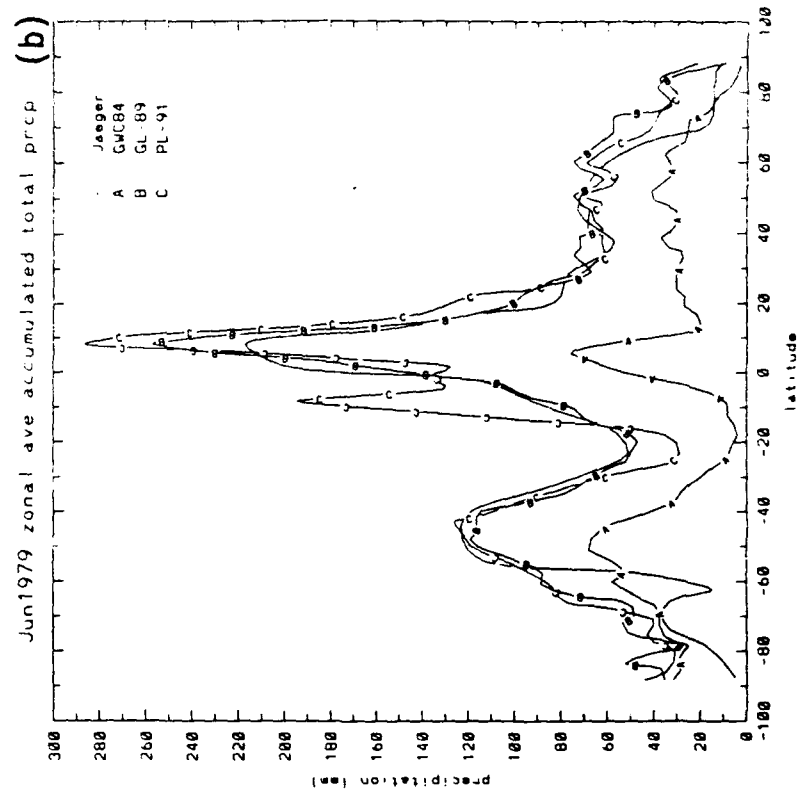
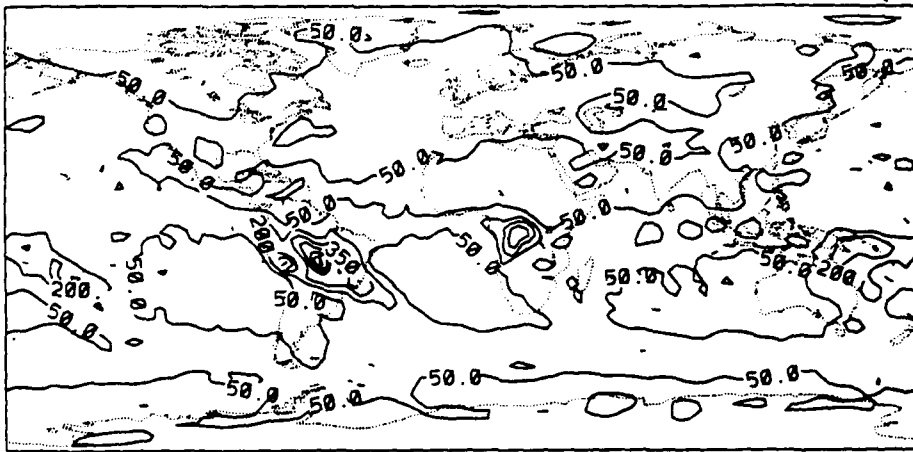


Figure 83. Zonal Average of Accumulated Total Precipitation (mm) Over Days 2-6 of Six (a) January and (b) June Forecasts, Compared with Climatology.

(a)



(b)



(c)

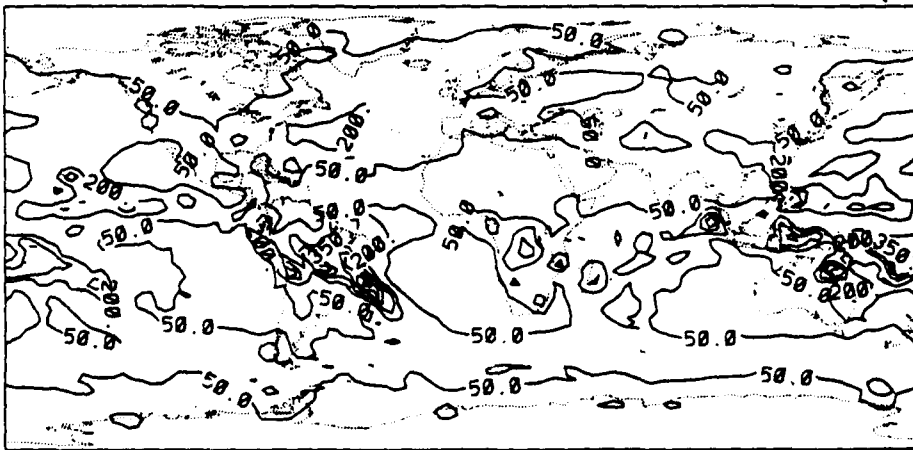
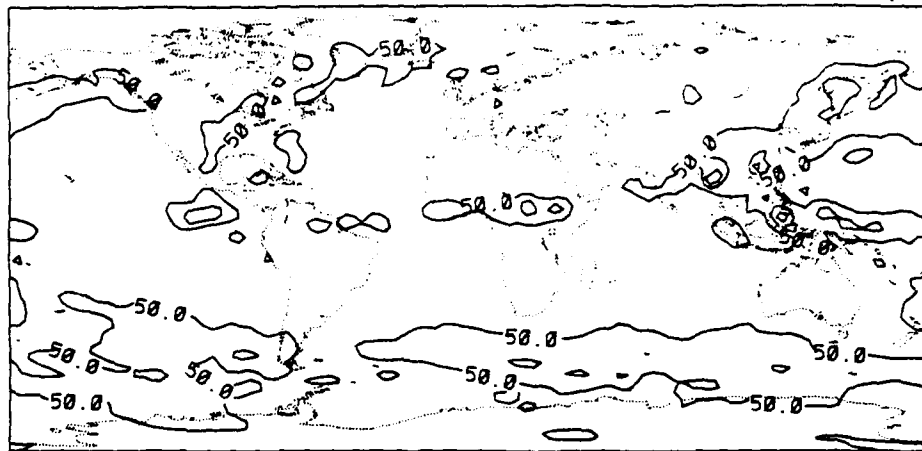


Figure 84. Global Maps of Accumulated Total Precipitation (mm) Over Days 2-6 of Six January Forecasts for (a) GWC84, (b) GL-89, and (c) PL-91 (Contour Interval = 150 mm).

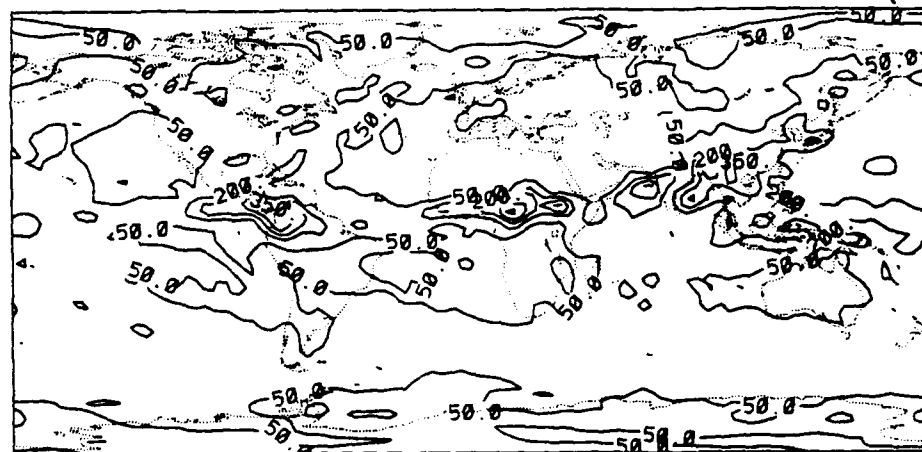
GWC84 prcp (mm) 30d total Jun1979

(a)



GL-89 prcp (mm) 30d total Jun1979

(b)



PL-91 prcp (mm) 30d total Jun1979

(c)

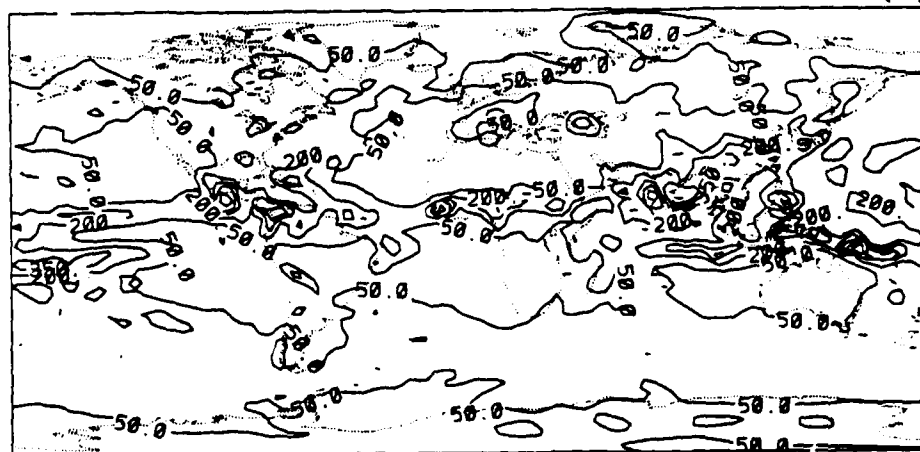


Figure 85. Same as in Figure 84 for Six June Forecasts.

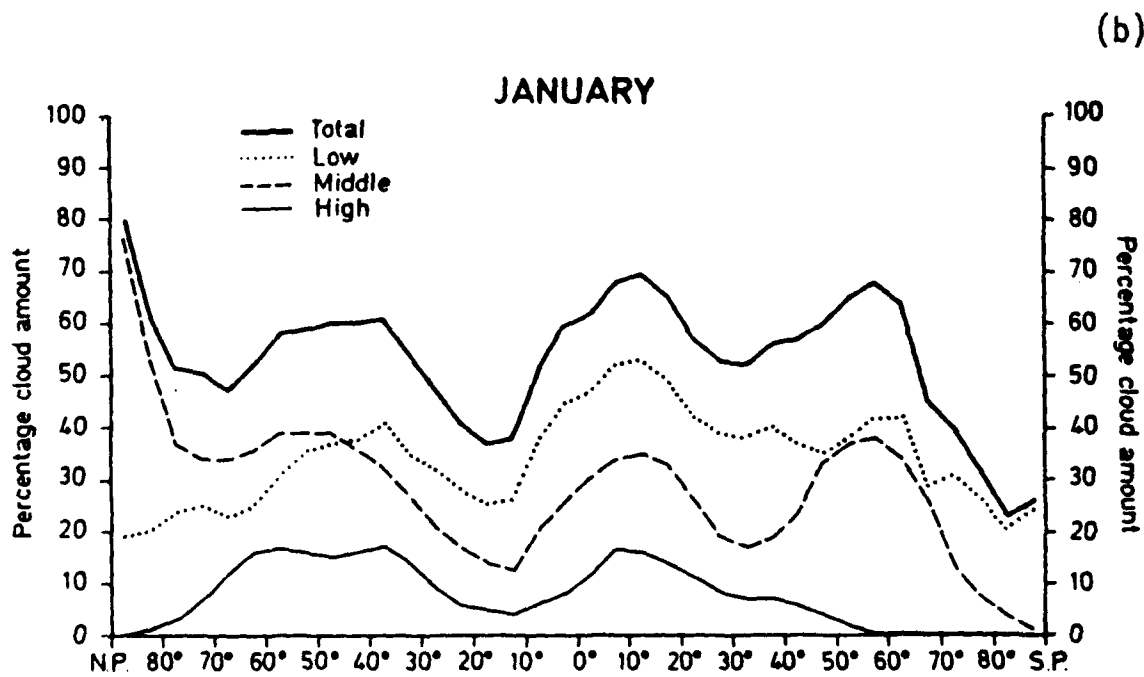
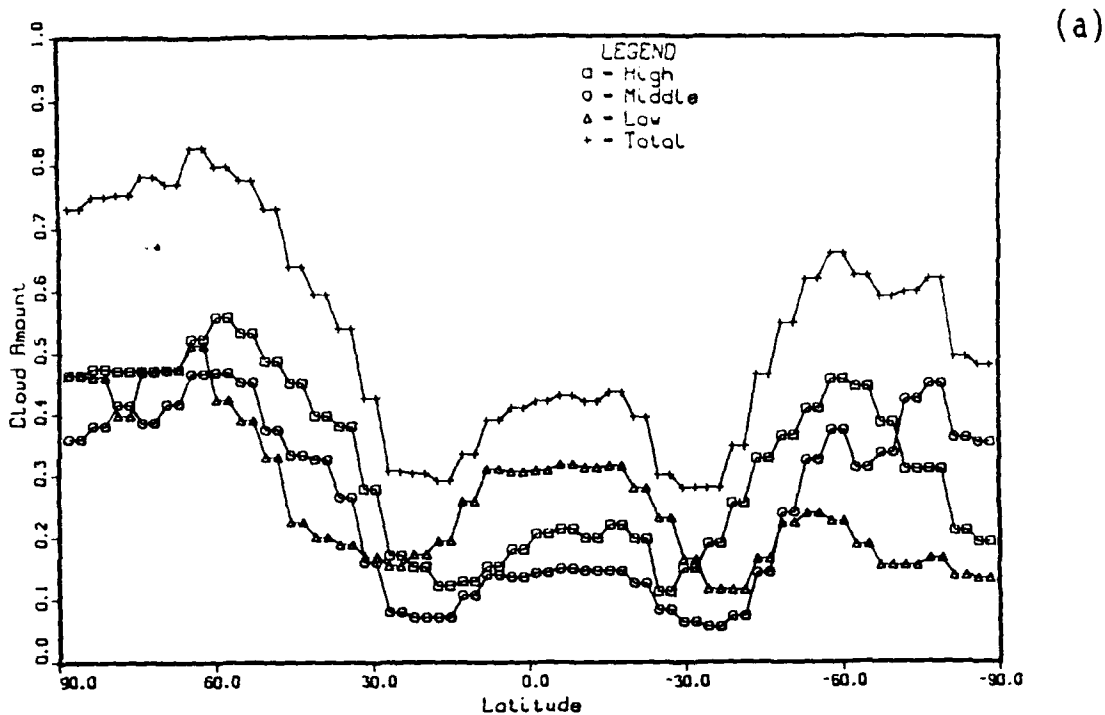


Figure 86. Zonal Time Average of Cloud Amounts From (a) Three 10-Day January 1979 PL-91 Forecasts, and (b) Climatology Based on January 1979 3DNEPH Data [from Schattel¹⁵].

cloud climatology. Furthermore, the model appears to produce too little low cloud, particularly in the tropics. Since the stratiform cloud formulation is based primarily on relative humidity, these results are seen to agree with the results presented in Figure 33.

5. ANALYSIS AND CONCLUSIONS

In this section, we present our analysis of and the resulting conclusions from the experimental results presented in Section 4. In view of the limited number of samples we have dealt with, the conclusions should be taken as preliminary. In some cases, we choose to speculate as to the cause of a certain error characteristic of some version of the PL GSM. These speculations should be considered only as suggested causes.

Figures 3 and 4 were selected for illustration for a number of reasons. First of all, we consider temperature to be the single most important and the best predicted prognostic variable. Secondly, bias and root-mean-square-error (RMSE) are the direct global measures of the two most important attributes of a forecast model, namely, the systematic error and the collective accuracy of forecast.

It also turned out that the error statistics of temperature were more coherent spatially and more consistent not only from case to case but also from one hemisphere to the other and from January to June, than other prognostic variables studied, as we saw in later figures. This convinced us that whatever differences are found in these error statistics among various versions are indeed due to the differences in physical parameterizations and not some fortuitous or unspecified external influences. Likewise, any similarity between these error statistics for a particular case leads us to conclude that the statistic is insensitive to the differences between various versions.

It is, then, immediately obvious from Figure 3 that GWC84 becomes warmer, while GL-89 becomes cooler, in the middle troposphere, as time goes on. To be sure, the growth rates are greater in both versions in the January cases than in the June

cases, but the warming in GWC84 is greater than the cooling in GL-89 in both seasons. On the other hand, both versions show excessive warming in the top layers above tropopause in both seasons. Here, however, while GL-89 shows a greater warming than GWC84 in January, the opposite is true in June.

In PL-91 we find a mid-tropospheric warming whose magnitude is about the same as that of cooling in GL-89 in January, but much greater in June. The warming of PL-91 occurs in both seasons in the top layers, but the seasonal contrast is less.

While the forms of vertical profiles change because of changes in magnitude at individual levels, these same individual trends of either warming or cooling are also found in the Southern Hemisphere. We conclude, therefore, from Figure 3 that the principal effects of the differences among the versions are confined to the troposphere and that the warming in the stratosphere arises mainly from the common feature in these versions.

To see how these hemispheric biases are made up, we next turn to the corresponding zonal statistics as depicted in Figures 25-34 that show the latitude-pressure cross sections between 80 S and 80 N on days 3, 5, and 10 of the three model versions, averaged over all six cases in each season. We find in GWC84 that the warming is taking place universally except for two isolated small regions, one in the tropical boundary-layer region and the other in the arctic stratosphere above 200 mb, where cooling also intensifies with time. It is clear that the warming is most intense in the high middle latitudes in the winter hemisphere and the least in the equatorial troposphere.

In GL-89, on the other hand, we find that the low-latitude troposphere is totally dominated by cooling whose centers appear in the lower layers but above the boundary-layer region. The warming in the middle and high latitudes is greatly reduced both in intensity and in coverage. As to PL-91, we find that warming in the middle and high latitudes is similar to GL-89 in both intensity and coverage, but the cooling in the low-latitude troposphere in GL-89 is replaced by weak cooling in the equatorial lower troposphere. In particular, the maximum warming at 500 mb observed in both seasons in the hemispheric statistics is very well accounted for by

the distributions in these cross-sections. Finally, the warm bias in the stratosphere, found to be common to all versions in both seasons, is seen in these cross-sections to sit right above the Equator and extend more or less equally into both hemispheres.

We next examine Figure 4, which depicts the evolutions of forecast accuracies. In both seasons both GL-89 and PL-91 yield smaller values of RMSE than GWC84 throughout the whole depth of the troposphere. The largest reduction is found in the bottom layers in January and in the middle troposphere in June. The difference between GL-89 and PL-91 is more subtle; the magnitude is smaller than that of either from GWC84 and varies not only from case to case but also from level to level.

The distributions of the ensemble averages of the corresponding zonal statistics are depicted in Figures 25-34. It is evident that in all versions, values of RMSE are smallest in the equatorial region and increase toward the centers in high latitudes. We find major contributions toward reducing the hemispheric RMSE in GL-89 and PL-91 come from two sources: extension of coverage by smallest RMSE in the equatorial region and decrease in the value of the maximum RMSE in the high-latitude centers.

To bring out more detail in the error statistics, we have chosen to employ a different presentation, as shown in Figures 5-22. In each of these figures, each frame depicts the time variations of one of the error statistics for individual cases for one of the three versions at one of three pressure levels, representing the low, middle and high troposphere, respectively. The corresponding distributions of zonal statistics are presented in Figures 25-34.

In wind speeds, we show only RMSE (Figures 5-10), since in all cases magnitudes and variations of biases are so much smaller than those of RMSE (see, for example, Figures 25-28) that we consider them to be of little value for the purpose of comparison. Three features may be noted in these figures, where u is shown on top and v at bottom. First, RMSEs in the two wind components are nearly equal at all times. Secondly, the RMSEs increase with elevation as mean winds do in all versions. Finally, there is little difference among the three versions, with a sole exception at 200 mb where GWC84 clearly yields larger values. It is apparent that

there is little discernible effect on the wind speed errors produced by the differences among the three versions. The corresponding cross-sections, Figures 27 and 28, show uniformly that the centers of maximum RMSE are located in the cores of jet streams and confirm the conventional notion that the greater the wind speed, the greater the error in wind speed.

In relative humidity, we present bias at the top and RMSE at the bottom in each figure (Figures 17-22). Here, we find wide variations and large differences from level to level and from version to version in bias, but a great uniformity among cases and small differences among versions in RMSE. Gradual drying in the low and middle tropospheres of GWC84 and steady moistening in middle and upper tropospheres of GL-89 are evidently consistent from case to case. On the other hand, the dryness found in the low troposphere of PL-91 and in the upper troposphere of GWC84 is more of a static than evolutionary nature. Apparent fluctuations and variabilities observed in biases are the result of magnified scales employed to emphasize differences among cases. Aside from the trends of bias noted above, these figures show that GL-89 produces the largest RMSE and GWC84 and PL-91 are nearly equal in the middle and high tropospheres. In the lower troposphere, however, GWC84 and PL-91 are comparable and produce smaller RMSEs than GL-89.

By comparing values of RMSE in wind, temperature, and relative humidity and adapting a simple rule of selecting a version or versions with the smallest RMSE, in which a small margin is allowed for equivalence, we attempted to score relative merits of the three versions with respect to each variable and each layer. The result is summarized in Table 4, where "X" denotes a version or versions deemed best. It should be added here that all forecasts in a 10-day period were weighted equally in comparing RMSE values over the entire period. Regarding all the variables and two seasons equally, we would then find PL-91 to have the greatest number of "Xs" and thus be considered the most desirable version of all.

Table 4. A Score Card on Northern Hemisphere Error Statistics

	GWC84			GL-89			PL-91		
	L	M	H	L	M	H	L	M	H
January									
V	X					X	X		X
T				X		X	X	X	X
RH			X	X				X	X
June									
V	X					X	X		
T						X	X		X
RH			X		X	X			

Turning to Figures 23 and 24, which present the time variations of the 500 mb height anomaly correlation, we find that all three versions show skill up to Day 6 in the Northern Hemisphere and that there is no statistically significant difference among them before Day 6 in both seasons. It is also noted that PL-91 yields the highest correlation, with substantial difference from the others beyond Day 6 in both seasons. Although not shown in figures here, we also found from the results that all versions showed poorer skill in the other two zones (up to Day 4) and that the equatorial zone showed larger differences and wider variations among different versions than the higher latitude zones.

In Section 4.1.3, we presented hemispheric maps depicting the geographical distributions of systematic errors of the PL-91 forecast model. Generally, the results show that although areas of systematic wind speed forecast errors do occur, they are geographically diverse and are of modest magnitude. This appears to be consistent with the systematic temperature errors, in conformity with the thermal wind relation. The latter are seen to be geographically confined and not arranged in definite geographic patterns. However, we do notice a pattern of predominance of near-

surface systematic temperature errors occurring over land surfaces, and most of these are wintertime warm biases in the Northern Hemisphere mid-latitudes. In the summer season, warm and cold biases appear at low levels over a number of land surfaces with no clear geographic pattern. Only at 500 mb in the June forecasts, where a significant warm bias covers much of the low latitudes, is there a well defined location for the temperature errors. In contrast, the widespread nature of the relative humidity biases suggest a tendency to take moisture from certain levels of the model atmosphere and deposit it at other levels. No similar model tendency to redistribute momentum or heat (with the exception of 500 mb in June in the tropics) to certain model levels was observed.

We next study the figures described in Section 4.1.4 for the implications. Figure 46 presents the time history of temperature error biases in the Central Pacific window at 850, 700, 500, and 300 mb levels of the three model versions in all 12 cases of the experiment. Figure 48 does the same for the North American window. We find two notable features that are common to all panels in both figures. The first is that GL-89 is most negatively or, equivalently least positively, biased of the three versions. The other is that PL-91 remains in parallel with and positively biased from GL-89. Both support very well the findings of the hemispheric statistics for the window-sized regions shown in Figure 3. On the other hand, while GWC84 also is consistently biased positively from GL-89, its difference from either GL-89 or PL-91 is less uniform among cases and across levels. As a result, correspondence of the difference between GWC84 and GL-89 or PL-91 between regional and hemispheric statistics is less obvious than that of the difference between GL-89 and PL-91.

We attribute this contrast in the differences of temperature error biases to the difference in degree of change between, say, pair GWC84 and GL-89 and pair GL-89 and PL-91. For example, it is evident from Table 1 that there have been more substantial modifications introduced between GWC84 and GL-89 than between GL-89 and PL-91. We think, furthermore, that the ubiquitous and uniform nature of the difference between GL-89 and PL-91 reflects directly the changes made from GL-89 to PL-91; that is the radiation and moist convection schemes. In contrast, the less

well-defined difference of either GL-89 or PL-91 from GWC84 represents a complicated synthesis of effects from many more components of change brought into the newer versions.

In considering the difference between GWC84 and GL-89, we see in Figures 82 and 83, that there is in the amount of rainfall a 4 to 1 ratio in the CP window and 2 to 1 ratio in the NA window between GL-89 and GWC84. In spite of these additional sources of latent heat for warming the middle troposphere in both windows and in both seasons, GL-89 is considerably cooler and gets colder with time than GWC84 throughout the troposphere. We believe the main cause of the difference is the University of Utah's 1-deck (high-cloud) radiation scheme introduced in GL-89. The scheme reduces the amount of solar radiation reaching below the high cloud. The larger difference found in the NA window in January is most likely due to a greater cloudiness in the middle latitudes in winter.

With regards to the difference between GL-89 and PL-91, we observe in Figure 83 that the change from MODKURO to the ECMWF's mass-flux scheme in moist convection parameterization results in greater (10-20 percent) convective precipitation confined in the equatorial region, but nowhere else. The increase in the global total (Figure 82) is nearly equal in the two seasons (0.9 mm/day). The additional source of latent heat from the increased precipitation contributes toward the warm bias of PL-91 relative to GL-89 in the CP window. Tiedtke¹⁶ showed that the mass-flux convective scheme produced somewhat excessive midtropospheric heating and drying in a simulation over the Marshall Islands. However, the main source of the difference between PL-91 and GL-89, which remains relatively constant among levels and indifferent to season, is the change in the radiation scheme from the 1-deck to 3-deck algorithm (see Table 1).

In Figures 47 and 49 we find the time history of accuracies of temperature forecasts as measured by the regional RMSEs for the three model versions represented in the same fashion as in Figures 46 and 48. The corresponding hemispheric statistics in a different format are shown in Figures 11 and 12. The most obvious feature common to both figures is that RMSE is greater by a factor

ranging from 2 to 4 in the NA window than in the CP window at all levels and in all cases, but the RMSEs in the various versions are not so different between the two windows. We also readily concede that, unlike Figures 46 and 48, it is hard to discern consistency across cases and levels of relative orientations of the three versions. Both factors make it difficult to judge the relative merit of the three versions on the basis of RMSE. When we use a similar strategy as the one used in creating Table 4 for abstracting the results shown in these figures, we obtain Table 5. The table makes obvious some of the features implied in the figures, such as poor performance of GL-89 in the lower levels in the CP window, but not in the NA window, and unsound performance of PL-91 at the 500 mb level in both windows which was also evident in Figure 4. It also shows that "benefits" from the new parameterizations are clearly evident in the NA window at all levels, but are more confined to the upper troposphere in the CP window.

Table 5. Number of Cases Where a Version is Selected as Best Temperature Forecast

	Central Pacific			North America		
	GWC84	GL-89	PL-91	GWC84	GL-89	PL-91
850 mb	7	0	9	3	4	11
700	10	0	7	3	10	7
500	6	7	1	5	11	4
300	2	7	6	4	8	11

Another measure of accuracy of model simulation is provided by the correlation coefficient between a simulation and the corresponding analysis. Figure 50 presents the time variations of such coefficients of the three models in the two windows on each of three levels, 850, 500, and 300 mb, in each of the 12 cases for temperature (top) and height (bottom) on the surfaces. They illustrate the difference in the way in which correlation coefficient and RMSE measure accuracy. We recall how much greater the RMSEs and their differences among the models were in the NA window than in the CP window. In contrast, the correlation coefficients and their differences

among the models show greater ranges of variability in the CP window. There is hardly any indication here of unsoundness in PL-91 at the 500 mb level in the CP window, nor any sign of poor performances by GL-89 at the 850 mb level. Furthermore, even a cursory survey of the figures reveals that PL-91 surpasses the other two on all levels and in both windows. This, indeed, is what happens when one introduces a more quantitative way of scoring individual cases.

We also studied errors in other variables such as relative humidity and horizontal wind speeds in these windows. We were particularly interested in knowing whether a "better" forecast--as measured by these statistics--in one variable is necessarily better in another. We have found, on the basis of this experiment, that there is no unequivocal answer within the bound of the experiment. We illustrate the point by presenting Figures 51 and 52 that show the time history of the regional error biases in relative humidity for the CP and NA windows, respectively. They correspond to Figures 46 and 48 for temperature.

Gridpoint-based evaluations of PL-91 performance further detailed errors depicted on hemispheric maps. We selected five gridpoints in geographically diverse locations that were closely supported by radiosonde data in the analysis for this evaluation. Furthermore, we focused on the three lowest model layers to represent PL-91 boundary layer performance, and chose the layer closest to an observational report level to present as the verification in Figures 55-72. For the gridpoint 1 (Denver), for example, the average pressures corresponding to those σ levels were 728 mb, 718 mb, and 703 mb, respectively, as seen in Table 6. Therefore, the time series from the FGGE III-b analysis at those three layers were actually interpolated from the same two analysis pressure levels, that is, 700 and 800 mb. Consequently, the time series at $\sigma = 0.960$ are presented in Figures 55 through 60 because of their proximity to 700 mb. In Figures 55-72, we denote forecast time in units of 12-hour forecast intervals, where in each case a forecast was begun at 1200 UTC.

Table 6. Height and Pressure Data for the Five Reference Gridpoints

Gridpoint No. (nearest station)	$\sigma = 1$		$\sigma = 0.995$		$\sigma = 0.981$		$\sigma = 0.960$	
	Z*(m)	p.(mb)	h(m)	p(mb)	h(m)	p(mb)	h(m)	p(mb)
1 (Denver)	2698	732	41	728	152	718	327	703
2 (Omaha)	582	947	42	943	155	929	333	910
3 (Hawaii)	223	990	44	985	162	972	349	951
4 (Alert)	753	918	38	914	140	900	304	882
5 (Amundsen)	2986	668	35	665	132	656	285	642

p. = mean model surface pressure at model surface height Z; h = height above Z, and p = pressure for lowest three σ layers

One of the significant features in the time series of temperature (Figures 55 and 56) is the warm bias at Denver. This feature is an example of the positive mean errors of temperature (T) in the lower atmosphere over the western United States (Figure 40). Another significant feature is the obvious diurnal variation in June. The temperatures at 0500 local time (1200 UTC) were generally lower than the temperatures at 1700 local time (0000 UTC). The analyzed temperatures had a diurnal oscillation with smaller amplitudes than the predictions. The temperatures at 1700 local time at Denver were probably not the daily maximum temperatures. The actual amplitudes of diurnal oscillations for both analyzed and predicted temperature may be larger than those indicated in Figure 56. When we plotted the Denver radiosonde surface temperatures against the PL-91 $\sigma = 0.995$ temperatures, we found that the diurnal amplitudes were indeed larger than shown here at $\sigma = 0.960$, and agreed quite well, especially in June. Finally, we note that in most cases

the PL-91 forecasts fail to represent many of the longer term (presumably synoptic-scale) warming and cooling episodes evident in the analysis. The forecasts project persistence of average conditions resulting in the greatest warm or cold biases during warming and cooling episodes.

Figures 57 and 58 illustrate the time series of specific humidity (q) for Denver. The model prediction was generally too moist in January and too dry in most of the June cases. Figures 59 and 60 give the time series of windspeed (V) and wind direction (WD) for Denver. They indicate that there is little resemblance between predicted and analyzed wind speeds and directions. The model appears to be unable to replicate the synoptic-scale variations present in the analyses. As expected, we note that agreement with analyzed wind direction is best when analyzed and predicted wind speeds are greatest, and are poorest at low wind speeds. We observe that the mean error map of the wind speed at 700 mb (Figure 37) also did not reveal any systematic error over this region.

The time series of T , q , V , and WD for Hawaii are presented in Figures 61-66. The model generated a warm bias as shown in Figures 61 and 62. There was hardly any diurnal signal in the prediction, in contrast to the clearly evident signal in the analysis. This may be due to the island heating effect that the observation contributed to the analysis, whereas the prediction gridpoint was treated as an ocean point (where sea surface temperature is held constant). In Figures 63 and 64, we note that PL-91 fails to capture the major synoptic-scale drying and moistening episodes evident in the analysis, while correctly predicting the climatological mean state. Figures 65 and 66 suggest a positive wind speed bias in June. Notice that there are corresponding areas of positive temperature errors (Figures 39 and 42) and positive wind speed errors (Figure 37) around Hawaii in those maps. Hence, we believe that the gridpoint time series reveals temporal detail of the global model's performance at a particular location.

Figures 67-72 serve as another example of PL-91 performance, depicting a gridpoint near Alert. Temperature is better predicted in June than in January as judged by these cases. The specific humidity predictions tend to be too dry in

January and too moist in June (Figure 69 and 70). We should be careful, however, to evaluate the humidity predictions in polar regions since humidity measurements are considered suspect at low temperatures. In January, the model often predicted a high wind speed episode that was not evident in the analysis time series (Figures 71 and 72). However, no clear systematic wind forecast error is evident from the 12 cases shown in these figures.

A point of qualification is in order in the Denver and Alert verifications. As previously mentioned, we interpolated the FGGE III-b analysis to the model sigma structure dictated by the silhouette topography to arrive at the curves referred to as "F3B" in Figures 55-72. As seen in Table 6, this means that for Denver, the 700 mb and 800 mb analysis levels were used to interpolate values of T, u, v, and q to the pressure level corresponding to $\sigma = 0.960$, nominally about 703 mb. According to Table 6, the $\sigma = 0.960$ level is 327 m (29 mb) above the model terrain surface ($\sigma = 1$), yet the 700 mb radiosonde report level (which we found to have a major influence on the 700 mb analysis value at the gridpoint, which in turn played the major role in the interpolation to $\sigma = 0.960$) is about 130 mb above the actual surface (surface elevation = 1625 m, roughly 830 mb). Thus, we are effectively comparing a forecast value about 30 mb above the model surface with a verification based on an observation about 130 mb above the actual ground surface. The latter is probably above the boundary layer, most certainly so in January. Since the pressure about 30 mb above the actual surface is about 800 mb, we plotted the temperature time series of the Denver radiosonde at 700 and 800 mb to see how close these values are to the "F3B" and "PL-91" curves in Figure 55. The 700 mb radiosonde time series closely matched the "F3B" curve, and the 800 mb radiosonde time series was much closer to the "PL-91" curve than was the "F3B" curve. We conclude from this that proximity of an atmospheric level to the ground greatly influences the values of boundary layer temperature. This may be true for moisture and wind as well. Similarly at Alert, the $\sigma = 0.960$ level at 304 m (36 mb) above the model terrain, contrasted with a radiosonde report level at 850 mb (closest level to 882 mb), some 150 mb above the actual ground surface (surface elevation = 63 m, roughly 1005 mb). In this case, the

pressure some 35 mb above the actual surface is about 970 mb. Though we did not look at the Alert radiosonde time series as we did at Denver, we suppose that the resulting values would show less of a difference with respect to PL-91 values than do the "F3B" curves shown in Figures 66-72. At Hawaii, the differential between model and actual terrain was not substantial, so the terrain proximity factor was not an issue. However, this problem points out the difficulty of trying to use conventional observations (or analyses based on those observations) to verify boundary layer forecast values. It appears that, in the boundary layer, height (or pressure) above the respective ground surfaces should be used as the independent variable in verifications.

From the PL-91 performance at those gridpoints as discussed above, several points can be emphasized as a summary of this sub-section.

- a. PL-91 produced a systematic warm bias in both seasons at Hawaii, and failed to depict temperature change episodes at Denver.
- b. PL-91 appeared to reproduce correctly the phase of diurnal temperature variations, but with too small of amplitude over the ocean (Hawaii).
- c. PL-91 produced seasonal specific humidity bias of opposite sign at Denver and Alert, and produced no noticeable bias of moisture at Hawaii (but failed to capture major humidity change episodes).
- d. Accurate point predictions of wind speed and direction in the boundary layer appear to be very difficult for the model to achieve, although systematic wind prediction errors were modest (Hawaii) or non-existent (Denver and Alert).
- e. It is difficult to find a systematic trend or pattern of error in the boundary layer, where the error is dominated by the random component.

The new treatment of topography and the land surface parameterization in PL-91 has utilized the enhanced (silhouette) topography. Another addition to the PL GSM in PL-91 is a variable soil and vegetation classification based on Wilson and Henderson-Sellers³⁰ and Matthews³¹. The impacts of the silhouette topography

³⁰Wilson, M.F., and Henderson-Sellers, A. (1985) A Global Archive of Land Cover and Soils Data for Use in General Circulation Climate Models, *J. Climate*, 5:119-143.

and the land surface parameterization on the PBL predictions are presently subjects of investigation at PL.

In Section 4.3, we introduced map plots of weather predictions produced by GWC84 and PL-91 for the 1200 UTC 12 January 1979 case. Figure 73 compares the 72-hour forecasts of mean sea level pressure and 500 mb height with the verifying analysis. In this case, both model versions reproduced the major troughs and ridges fairly well. We made the following observations when we watched the six-day forecast color animation of this case.

- a. PL-91 performed well in predicting intensity and location of several surface lows.
- b. PL-91 generally predicted mean sea level pressure better than GWC84.
- c. Both versions failed to cut-off troughs and ridges in 500 mb height, and incorrectly split an intense north Pacific 500 mb trough.
- d. PL-91 did not predict the 500 mb height field noticeably better than GWC84.
- e. PL-91 produced an overall better prediction of 200 mb jet magnitude and location than GWC84, particularly over the north Pacific.

We show only one case of tropical weather prediction in Figures 76 and 77, for the 1200 UTC 10 June 1979 case. On the basis of this single case, it appears that PL-91 better preserved the north-south mean sea level pressure gradient over the Indian Ocean (Figure 76), which may account for its ability to better represent the higher 850 mb wind speeds (Figure 77) in this region. As a result, the oval-shaped closed circulation south of India (as the Indian monsoon develops) is better represented by PL-91.

The balance of the weather prediction maps shown depict the predicted humidity fields for 12 January over the Northern Hemisphere (Figures 74 and 75) and for 10 June over the tropical Eastern Hemisphere (Figures 78-81). In January, both versions tend to produce reduced RH at 850 mb over much of the hemisphere (this

²¹Matthews, E. (1983) Global Vegetation and Land Use: New High Resolution Data Bases for Climate Studies, *J. Clim. Appl. Meteor.*, **22**:474-487.

is better seen in the color-filled graphics²⁷). This is not as evident in the q forecasts, where we see the dry and moist features well reproduced by both versions. At 300 mb, both versions produce RH forecasts that are more moist than the verification (Figure 75). Again, the color-filled graphics make this more clear, showing PL-91 only slightly less moist than GWC84. Finally, the tropical case (Figures 79-81) shows that the PL-91 version's tendency to be too dry at 850, too moist at 700, and too dry at 400 mb is widespread, not concentrated in certain geographic locales.

6. SUMMARY AND RECOMMENDATIONS

In this section, we summarize the major findings that resulted from our experimentation with various versions of the PL GSM. We focus our summary on the three versions GWC84, GL-89, and PL-91, which were the most completely scrutinized in this report. In this way, we summarize the progress made during the 10-year process culminating in PL-91. Also, we included in this summary only the features revealed by more than one of the scales of investigation discussed in Section 5.

A major feature of the GWC84 forecasts was the pervasive tropospheric warm bias that was especially prominent in the winter hemisphere. We found that this warm bias tended to grow seemingly without limit through the 10-day forecast period. We attributed this bias to a lack of a radiation parameterization, which tends to produce a net cooling in the atmosphere. GL-89 produced a more modestly growing cold bias in the mid-troposphere, primarily relegated to the tropics, but also apparent over North America. The introduction of a new convective scheme and a reduction of the radiative cooling in PL-91 led to a modest mid-tropospheric warm bias that was larger in June than January. At very low levels, a warm bias was apparent over much of the Northern Hemisphere continents in both seasons. At high levels (above 200 mb) persistent warm bias exists in the forecasts of all three model versions, indicating a modeling shortcoming not addressed by the new physical parameterizations. We evaluated only the performance of PL-91 extensively in the

boundary layer. It seemed unable to capture synoptic scale warming and cooling episodes in the boundary layer. Overall, PL-91 appeared to have the edge in temperature forecast accuracy.

All three models generated a systematic error in humidity that was geographically widespread. In GWC84, a dry bias was found in the lower troposphere, a moist bias in the mid-tropospheric tropics, a dry bias in the mid-tropospheric extratropics, and a moist bias in the upper troposphere. GL-89 forecasts featured a moist bias in the mid and upper troposphere in the tropics, and a moist bias in the upper troposphere in the extratropics. In the PL-91 forecasts, the tropical bias had a vertical bimodal structure; dry at 850 mb, moist at 700 mb, dry at 400 mb, and significantly moist at 300 mb. This upper level moist bias was in fact present at all latitudes in PL-91. Low level moisture biases over land were seasonal, generally moist in January and dry in June. Although humidity prediction accuracy is lacking in all three model versions (synoptic scale variations were a problem in moisture forecasts, too), PL-91 was judged the best in January and GL-89 in June based on Northern Hemisphere statistics.

We found that wind prediction skill was difficult to judge, particularly in the boundary layer. In general, the bias in either wind component or the speed was small compared to the RMSE. Wind speed biases were very localized and appeared at different locations at different atmospheric levels. Overall, PL-91 forecasts appeared to have the smallest jet-level RMSEs in winds, particularly in the winter hemisphere. PL-91 also appeared to produce the smallest lower-tropospheric wind RMSEs, particularly in the tropics. The former improvement we attribute to the introduction of the gravity wave drag formulation, and the latter to the cumulus momentum drag formulation in the ECMWF convection parameterization. We found that PL-91 (and we expect the other versions as well) was generally unable to reproduce the variations seen in the analyzed winds in the boundary layer, most noticeably those of synoptic scale. However, we found no evidence of a systematic bias in boundary layer wind forecasts.

Weather pattern prediction assessment was limited to a single case. Even so, PL-91 seemed to represent surface pressure patterns better than GWC84, but was not noticeably better at 500 mb. We saw somewhat better jet positions and intensities in PL-91 than in GWC84. However, each model had its wide-spread and persistent moisture biases mentioned earlier that obscured pattern prediction.

On the basis of these preliminary assessments, we recommend that PL-91 be advanced as the new baseline version of the PL GSM. More innovative ways of using observations are needed to accurately evaluate the nature of both its systematic and random error. We recommend that the model be executed at a higher horizontal (and commensurate vertical) resolution, to represent state-of-the-art operational center resolutions. This will require that the optimization of the PL GSM be extended to the PL-91 version and then extensively tested. Such an effort is already underway at PL in a combined in-house and contractor effort.

As for improvements in PL-91, we recommend that the cumulus convection and boundary layer schemes be further tuned to reduce what appears to be excessive precipitation, especially in the tropics. The moisture biases in the model should be investigated as to their source and causative factors. Such an investigation is in process and will be reported on soon. We recommend that a cloud diagnosis scheme tuned for PL-91 (perhaps the Mitchell and Hahn¹⁹ scheme) be adopted for use in conjunction with the model's radiation parameterization in an attempt to further alleviate temperature biases. Another PL effort is currently underway to use the PL-91 version to attempt to develop an improved statistical cloud diagnosis scheme that can be developed from statistics any model may generate (that is, be model specific in its values but generic in design). Ultimately, we recommend that future versions of the PL GSM be considered for extension to prognostic cloud forecasting as the physical parameterizations of the model continue to improve.

References

1. Sela, J. (1980) Spectral Modeling at the National Meteorological Center, *Mon. Wea. Rev.*, **108**:1279-1292.
2. Brenner, S., Yang, C., and Yee, S. (1982) *The AFGL Spectral Model of the Moist Global Atmosphere: Documentation of the Baseline Version*, AFGL-TR-82-0393, Air Force Geophysics Laboratory, Hanscom AFB, MA. ADA129283.
3. Brenner, S., Yang, C., and Mitchell, K (1984) *The AFGL Global Spectral Model: Expanded Resolution Baseline Version*, AFGL-TR-84-0308, Air Force Geophysics Laboratory, Hanscom AFB, MA. ADA160370.
4. Ballish, B.A. (1980) *Initialization Theory and Application to the NMC Spectral Model*, Ph.D. Thesis, Dept of Meteorology, Univ. of Maryland.
5. Yang, C.-H., Mitchell, K., Norquist, D., and Yee, S.Y.K. (1989) *Diagnostics for and Evaluation of New Physical Parameterization Schemes for Global NWP Models*, GL-TR-89-0158, Geophysics Laboratory (AFSC), Hanscom AFB, MA. ADA228033.
6. Mahrt, L., Pan, H., Paumier, J., and Troen, Ib (1984) *A Boundary Layer Parameterization for a General Circulation Model*, AFGL-TR-84-0063, Air Force Geophysics Laboratory, Hanscom AFB, MA. ADA144224.
7. Soong, S.-T., Ogura, Y., and Kau, W.-S (1985) *A Study of Cumulus Parameterization in a Global Circulation Model*, AFGL-TR-85-0160, Air Force Geophysics Laboratory, Hanscom AFB, MA. ADA170137.
8. Kuo, H.-L. (1974) Further Studies of the Parameterization of the Influence of Cumulus Convection on Large-Scale Flow, *J. Atmos. Sci.*, **31**:1232-1240.

9. Liou, K.-N., Ou, S.-C., Kinne, S., and Koenig, G. (1984) *Radiation Parameterization Programs for Use in General Circulation Models*, AFGL-TR-84-0217, Air Force Geophysics Laboratory, Hanscom AFB, MA. ADA148015.
10. Mahrt, L., Pan, H.-L., Ruscher, P., and Chu, C.-T. (1987) *Boundary Layer Parameterization for a Global Spectral Model*, AFGL-TR-87-0246, Air Force Geophysics Laboratory, Hanscom AFB, MA. ADA199440.
11. Ou, S.-C., and Liou, K.-N. (1988) *Development of Radiation and Cloud Parameterization Programs for AFGL Global Models*, AFGL-TR-88-0018, Air Force Geophysics Laboratory, Hanscom AFB, MA. ADA202020.
12. Norquist, D. and Yang, C.-H. (1990) *Refinement and Testing of the Moist Convection Parameterization in the GL Global Spectral Model*, GL-TR-90-0285, Geophysics Laboratory (AFSC), Hanscom AFB, MA. ADA241684.
13. Hahn, D. and Chang, S. (1992) *Land-Surface Parameterization in the Phillips Laboratory Global Spectral Model*, to be published as a Phillips Laboratory Technical Report.
14. Vernekar, A.D., Zhou, J., and Kirtman, B. (1991) *A Comparison of Systematic Errors in AFGL and COLA Forecast Models*, PL-TR-91-2164, Phillips Laboratory, Hanscom AFB, MA. ADA244458.
15. Schattell, J. (1992) *Refinement and Testing of the Radiative Transfer Parameterization in the PL Global Spectral Model*, PL-TR-92-2169, Phillips Laboratory, Hanscom AFB, MA.
16. Tiedtke, M. (1989) A Comprehensive Mass Flux Scheme for Cumulus Parameterization in Large-Scale Models, *Mon. Wea. Rev.*, **117**: 1779-1800.
17. Norquist, D., and Yang, C. (1992) Comparing Model-produced Convective Cloudiness with Observations, *Mon. Wea. Rev.*, **120**: 770-786.
18. Mahrt, L., Ek, M., Kim, J., and Holtslag, A.A.M. (1991) *Boundary Layer Parameterization for a Global Spectral Model*, PL-TR-91-2031, Phillips Laboratory, Hanscom AFB, MA. ADA235310.
19. Mitchell, K. and Hahn, D. (1989) *Development of a Cloud Forecast Scheme for the GL Baseline Global Spectral Model*, GL-TR-89-0343, Geophysics Laboratory (AFSC), Hanscom AFB, MA. ADA231595.
20. Trapnell, R. (1992) *Cloud Curve Algorithm Test Program*, PL-TR-92-2052, Phillips Laboratory, Hanscom AFB, MA. ADA253918.
21. Crum, T.D. (1987) *AFGWC Cloud Forecast Models*, AFGWC Tech Note 87/001, AFGWC, Air Weather Service (MAC), Offutt AFB, NE.
22. Nehr Korn, T., Hoffman, R.N., and Louis, J.-F. (1990) *Design of an Enhanced Global Spectral Model*, GL-TR-90-0309, Geophysics Laboratory (AFSC), Hanscom AFB, MA. ADA232123.
23. Nehr Korn, T., Hoffman, R.N., Louis, J.-F., and Zivkovic, M. (1992) *An Enhanced Global Spectral Model*, PL-TR-92-2011, Phillips Laboratory, Hanscom AFB, MA. ADA251242.

24. Uppala, S. (1986) The Assimilation of the Final Level IIB Data Set at ECMWF, Part I. *Preprints, Scientific Results of the First GARP Global Experiment*, 14-17 January, 1986, Miami, FL. *Amer. Meteor. Soc.*, 24-29.
25. Shaw, D.B., Lonnerberg, P., Hollingsworth, A., and Uden, P. (1987) The 1984/1985 Revisions of the ECMWF Assimilation System, *Quart. J. Roy. Meteor. Soc.*, 113:533-566.
26. Illari, L. (1989) The Quality of Satellite Precipitable Water Content Data and Their Impact on Analyzed Moisture Fields, *Tellus*, 41A: 319-337.
27. Norquist, D. (1992) "Everybody talks about the weather, but...", *Vector View*, 5, March-April 1992, 8 pp. [Available from Phillips Laboratory Supercomputer Center, PL/SCI, Kirtland AFB, NM 87117-6008]
28. Jaeger, L. (1983) Monthly and areal patterns of mean global precipitation, in *Variations in the Global Water Budget*, A. Street-Perrott, M. Beran, R. Ratcliffe, Eds., D. Reidel, Dordrecht.
29. Slingo, J. (1987) The Development and Verification of a Cloud Prediction Scheme for the ECMWF Model, *Quart. J. Roy. Meteor. Soc.*, 113:899-927.
30. Wilson, M.F., and Henderson-Sellers, A. (1985) A Global Archive of Land Cover and Soils Data for Use in General Circulation Climate Models, *J. Climate*, 5:119-143.
31. Matthews, E. (1983) Global Vegetation and Land Use: New High Resolution Data Bases for Climate Studies, *J. Clim. Appl. Meteor.*, 22:474-487.
32. Mesinger, F. and Collins, W.G. (1987) Review of the Representation of Mountains in Numerical Weather Prediction Models, *Observation, Theory, and Modeling of Orographic Effects*, 15-20 September 1986, Volume 2, ECMWF, Shinfield Park, Reading, U.K.

APPENDIX A Topography Representations

There are three kinds of topography representation commonly used in global numerical models: (1) mean topography, h_1 , (2) envelope topography, h_2 , and (3) silhouette topography, h_3 . Their definitions are as follows.

$$h_1 = \frac{1}{N \cdot M} \sum_{j=1}^N \sum_{i=1}^M h(i, j)$$

where $h(i, j)$ is the actual terrain height at subgridpoints (i, j) for a grid box, and h_1 is the mean terrain height for which the standard deviation of the terrain height at that gridpoint is

$$\sigma_1 = \left\{ \frac{1}{N \cdot M} \sum_{j=1}^N \sum_{i=1}^M (h(i, j) - h_1)^2 \right\}^{1/2}$$

The envelope topography is

$$h_2 = h_1 + C\sigma_h$$

where C is a constant, usually between 1.0 and 2.0. The so-called silhouette topography (orography) is

$$h_3 = \frac{1}{2} \left[\frac{1}{N} \sum_{j=1}^N h_j + \frac{1}{M} \sum_{i=1}^M h_i \right]$$

where h_j is the maximum height of the subgrid terrain profile in each y-z plane, and h_i is the maximum height of the profile in each x-z plane in the grid box. M and N are the number of subgridpoints within a grid box in x and y directions, respectively.

In the early days of global numerical weather prediction, h_1 was used. The mean orography, h_1 , computed as an arithmetic average of points over the model grid was found to underestimate the blocking effects of high mountains. Later, the enhanced orography (envelope and silhouette orography) was introduced in order to overcome the deficiencies due to mean orography. Many researchers (for example, Mesinger and Collins³²) have described the impacts of the enhanced orography.

PL-91 adopts the silhouette orography, which was considered better than envelope orography in dealing with the gravity wave parameterization.¹⁴

³²Mesinger, F. and Collins, W.G. (1987) Review of the Representation of Mountains in Numerical Weather Prediction Models, *Observation, Theory, and Modeling of Orographic Effects*, 15-20 September 1986, Volume 2, ECMWF, Shinfield Park, Reading, U.K.